

**The Production and Characterization of an  
Intense Hyperthermal Beam of  
H<sub>3</sub> Molecules and of H Atoms**

Thesis by

James F. Garvey

In Partial Fulfillment of the Requirements  
for the Degree of  
Doctor of Philosophy

California Institute of Technology  
Pasadena, California

1985

Submitted March 15, 1985

© 1985

James F. Garvey

All Rights Reserved

To my parents, with all my love

## ACKNOWLEDGEMENTS

Any work requires the cooperation and assistance of many individuals whom at this time I would like to acknowledge for their help. I first would like to thank my advisor Aron Kuppermann for his attention to detail which has proven helpful in the analysis of the many technical problems which have plagued this project over the years. His constant encouragement and warmth throughout my years here has made the time tremendously fulfilling and will prove to be a inspiration for me in the future. I also wish to thank Professor Jack Beauchamp for the interest he has shown in my work and in my progress over the years. His friendship and timely suggestions have proved to be a great boon while I have been here.

My work on this project would not have been possible without the substantial help, both technical and spiritual, which I have recieved from the Chemistry machine shop personnel. Bill Schuelke, Tony Stark, Guy Durenberg, Delmar Dill and Ray Garcia have all at some time or another been responsible for the construction, design, and maintenance of the apparatus used in this experiment. Their constant help and attention when things were down (which has certainly been most of the time) is heartly appreciated. Believe me, I can't thank you guys enough for all you have done for me.

In addition to their help I must also thank the other personnel of the chemistry department: Jim Olsen and Jim Gangwer of the mechanics shop for keeping the pumps running on the beam long after they should have stopped, Tom Dunn and Jack Guledjian of the electronic shop for help with the mass spectrometer electronics in the detection system, Rich Ehrich for the detailed drawings for the construction of the inhomogeneous magnet, and Erich Siegel and the glass shop for the many 'emergency' jobs I've had over the years.

I also wish to thank all the members of the Kuppermann group for their assistance and friendship over the years. In particular I wish to acknowledge Kerry Walzl and Steven Cuccaro for their help in proofreading all of this thesis. I also wish to thank Jack Kaye who guided me through the Be + FH calculation and was indispensable in the interpretation of those results.

On the extracurricular side, I wish to thank Don and Wendy Caldwell for the great pleasure of doing Brigadoon and the Fantastics together and Peter Felker for the pleasure of appearing on the same stage with him twice in my life. I also would like to thank the Bobcats, old and new, for their friendship and support.

Lastly, I wish to thank my parents for all the love and support they have given to me my whole life. This thesis is dedicated to them.

**ABSTRACT**

The simplest bimolecular reaction involving neutral reagents is the reaction



This system, because of its simplicity and fundamental significance in chemical dynamics, has been the subject of extensive accurate *ab initio* theoretical quantum mechanical calculations and the results obtained have been used to test approximate theories of reaction dynamics. However, this system has proved difficult to study experimentally due to its high activation barrier ( $\sim .33$  eV) and its small reactive cross section ( $\sim 1 \times 10^{-16}$  cm<sup>2</sup>). Because of these factors, state-to-state reaction dynamics have only become feasible recently.

In order to study this reaction in a crossed molecular beam experiment, a means of generating an intense beam of H atoms is essential. This thesis documents the design and operation of a hydrogen arc discharge for generating such a beam. The method consists of using a high power arc discharge to create a high temperature ( $\sim 12,000$  K) plasma in which H<sub>2</sub> molecules can be dissociated into atoms. By using an arc source of the type developed by Kunth, a stable, intense, hyperthermal H atom beam has been successfully produced. Section 2 of this thesis discusses the design and operation of the apparatus and Section 3 of the thesis discusses the characterization of the hydrogen atoms within the beam. The laboratory energy distribution function of these atoms was determined approximately, and spans the range from 0.5 eV to about 12 eV. The total intensity of this beam is of the order of  $\sim 10^{22}$  atoms/sterad/sec. With such an intense and energetic beam, a wealth of chemical dynamical experiments may now become feasible.

In the course of developing this intense beam of hydrogen atoms, the source was found to also produce metastable  $H_3$  molecules. This is the first direct, unambiguous observation of such a specie in a molecular beam, and is discussed in Section 4. Translational energy analysis of this  $H_3$  molecule indicates an energy distribution similar to that of the H atoms, suggesting that the lifetime of  $H_3$  is of the order of 40  $\mu\text{sec}$  or longer. We also observed emission spectra from the Rydberg states of  $H_3$  identified previously by Herzberg. This is spectroscopic evidence for the presence of this neutral molecule in our beam. The only know state of  $H_3$  capable of having the long lifetime observed is  $2p\ ^2A_2''$ , the second excited state of this species.

In addition, we detected this molecule by a variety of other independent techniques. It has long been known that alkali metal atoms with low ionization potential will ionize upon collision with a metal surface having a high work function. The  $2p\ ^2A_2''$  state of  $H_3$  has an IP of  $\sim 3.7$  eV and is expected to behave in a similar way. As a result, surface ionization of metastable  $H_3$  has been observed for for a variety of metals and is reported in this thesis. From that low IP one would also expect that the metastable  $H_3$  should be photoionizable using an appropriate light source. In this thesis we report the generation of  $H_3^+$  through irradiation of the beam with the light from a high intensity mercury lamp. Lastly, since the metastable  $H_3$  is in a Rydberg state, it would be expected to exhibit a large total scattering cross section due to the diffuse nature of the Rydberg orbital. Such cross sections were measured by the attenuation of the  $H_3$  beam as it passed through a gas cell.

Section 5 describes the first observation of the electronic spectrum of WH. This emission spectrum was due to WH formed by the presence of the tungsten anode and cathode which are heated too close to its melting point by the arc discharge. Analysis of this spectrum has given rotational constants and bond distances for the electronic states of the mono-hydride involved

in the observed transisiton. Due to relativistic terms in the potential, the theoretical calculation of WH has proved difficult to date. Recently a reliable potential for W has been generated such that our experimental bond distances will provide an important empirical check for any further theoretical calculations performed on this system. Likewise, the arc source may be employed in the future as a means of generating new metal hydride emission spectra.

Appendix A of the thesis details the design and construction of the inhomogeneous magnet to serve in the future as a velocity selector for the hyperthermal hydrogen beam in our crossed beam experiment. Using such a Stern–Gerlach magnet as a velocity selector, the dynamics of the  $\text{H} + \text{H}_2$  reaction can be probed as a function of translational energy of the reactants. Appendix B grew out of an interesting Ch 227 project and will now become a theoretical paper. Exact quantum mechanical calculations of the collinear reaction  $\text{Be} + \text{FH}$  ( $v = 0, 1$ ) have been performed and the effects of reagent translational and vibrational excitation on reaction probabilities and product state distributions are examined. These quantum mechanical results are compared with those of quasi–classical trajectory calculations reported previously.

**TABLE OF CONTENTS****1. Prologue**

1.1	Introduction .....	1
1.2	Survey of Hyperthermal Beam Techniques .....	4
1.3	References .....	9

**2. Experimental**

2.1	Theory .....	13
2.2	Vacuum System .....	16
2.3	Source .....	21
2.4	Operation of the Source .....	30
2.5	Mass Spectrometer .....	36
2.5.1	Ionizer .....	37
2.5.2	Lens System .....	39
2.5.3	Filter Rods .....	42
2.5.4	Detection Electronics .....	44
2.5.5	Alignment .....	50
2.6	References .....	53
2.7	Figures and Captions .....	55

**3. Results and Discussion for H Atoms**

3.1	Effects of Electric Fields .....	66
3.2	Absolute Intensity Measurements .....	69
3.3	Energy Analysis .....	75
3.4	Emission Spectroscopy .....	79
3.5	Future Work .....	84
3.6	References .....	95
3.7	Figures and Captions .....	98

## 4. Results and Discussion for H<sub>3</sub> Molecules

4.1	Previous Work .....	113
4.2	Detection .....	122
4.3	Emission Spectrum .....	130
4.4	Surface Ionization .....	142
4.5	Photoionization .....	156
4.6	Total Scattering .....	163
4.7	Possible Alternative Origins of Detected H <sub>3</sub> .....	175
4.8	Future Work .....	185
4.9	References .....	189
4.10	Figures and Captions .....	199

## 5. Results and Discussion for WH and WD Molecules

5.1	Introduction .....	228
5.2	Results and Analysis .....	231
5.3	Future Work .....	244
5.4	References .....	246
5.5	Figures and Captions .....	249

## Appendix A: Magnetic Velocity Selector

A.1	Introduction .....	259
A.2	Theory .....	262
A.3	Design .....	267
A.4	Construction .....	272
A.5	References .....	281
A.6	Figures and Captions .....	284

**Appendix B: Quantum Mechanical Study of the Collinear****Reaction  $\text{Be} + \text{FH}(v = 0, 1) \rightarrow \text{BeF}(v') + \text{H}$** 

B.1	Introduction .....	296
B.2	Potential Energy Surface .....	298
B.3	Calculation Parameters .....	301
B.4	Results & Discussion .....	303
	B.4.1 $\text{Be} + \text{FH}(v) \rightarrow \text{BeF}(v') + \text{H}, v = 0, 1$ .....	303
	B.4.2 $\text{BeF}(v) + \text{H} \rightarrow \text{BeF}(v') + \text{H}, v > v'$ .....	307
B.5	Future Work .....	308
B.6	References .....	309
B.7	Figures and Captions .....	312

**Proposition I:** Investigation of  $\text{H} + \text{H}_2$  Reaction Dynamics as a Function of Collision Energy Using Sychrotron Radiation ..... 327

**Proposition II:** Study of Electronic to Vibrational Energy Transfer using Oriented Crossed Beams ..... 336

**Proposition III:** Bonding of  $\text{NH}_3$  and  $\text{H}_2\text{O}$  on Stepped Surfaces Investigated by ESDIAD ..... 345

**Proposition IV:** Effect of Magnetic Field on Organic Syntheses in the Plasma of Glow Discharges ..... 361

**Proposition V:** A Classical Determination of Vibrationally Adiabatic Barriers for the  $\text{H} + \text{H}_2$  as a Function of Delves' Angle ..... 374

## 1. Prologue

### 1.1 Introduction

The use of molecular beams to elucidate directly dynamics of molecular collisions has been widely demonstrated. Perhaps its most attractive potential is in reactive crossed beam experiments, in which the ultimate aim is the mapping of the potential surface where the reaction occurs. However, due to the high barrier heights of most reaction as well as small cross sections, only a limited number of systems have been studied<sup>1,2</sup> via this technique. It would therefore be attractive to be able to produce a beam which would have translational energy in the 1-20 eV energy regime, a regime which would embrace the dissociation energies of all chemical bonds and the activation energy of most reactions. This beam would also need to be quite intense since the small cross sections of most reactions will result in a very small amount of product molecules generated.

The simplest bimolecular reaction involving neutral reagents is



which has long been the major focus of many theoreticians<sup>3</sup>. Of all potential surfaces which have been calculated, the  $\text{H}_3$  potential is the most accurately known of any neutral reactive system<sup>4,5,6</sup>. Despite the attention this system has received theoretically, only until recently has it begun to be investigated experimentally by state-to-state studies. Part of the problem with the system is its large barrier ( $\sim 0.33$  eV) and its small reaction cross section ( $\sim 1 \times 10^{-16}$  cm<sup>2</sup>). As a result, fast and intense production of hydrogen atoms is

needed in order to observe any reaction. Recently, laser-photolysis of HI has been employed to produce fast H atoms ( $\sim 1.3$  eV) in a reaction cell. The H atoms which are generated then react with the  $D_2$  present to form HD. This product is then detected using laser nonlinear spectroscopic techniques before a significant number of secondary collisions can occur.<sup>7,8</sup> Product state distributions of HD are then observed and compared with theory.

Ideally one would like to do the experiment with crossed beams. Not only would the products certainly be formed in a collision-free environment but it would also be possible to look at the product produced as a function of the reagent translational energy. There have been only five beam studies reported to date. The earliest two studies, the  $D + H_2$  study<sup>9</sup> and the  $H + D_2$  study<sup>10</sup>, were severely hampered due to the high background pressure of interfering species. Through the use of differential pumping and advances in detector technology meaningful experiments on this system have since been performed: one for  $D + H_2$  at an average reaction energy of  $0.48$  eV<sup>11</sup>, one for  $H + T_2$  at an energy of  $0.7$  eV<sup>12</sup>, and the most recent study being  $D + H_2$  at an energy of  $1.0$  eV<sup>13</sup>. It should be noted that the energy is not the lab translational energy of the reagents but rather the average center of mass energy which results in reaction.

This thesis involves the development and characterization of an intense source of high energy hydrogen atoms. The ultimate goal of this work is to create a source of monoenergetic atoms whose translational energy would be continuously tunable from 1-10 eV. Once achieved it would be utilized in a crossed beam experiment and would enable direct and detailed comparisons with existing theory. Such a beam would enable the study of a wealth of hydrogen atom reactions. For example the reaction  $H + X_2$  where  $X_2$  is a halogen molecule is of great interest since the resulting X atom may be formed

in an excited state. By changing the translational energy of the H atoms the branching ratio for the process could be measured. What now follows is a brief survey of existing techniques for the generation of molecular and atomic beams at hyperthermal energies.

## 1.2 Survey of Hypersonic Beam Techniques

The most common method for producing hypersonic beams is the seeded beam technique<sup>14-17</sup>. A small concentration ( $\sim 1-5\%$ ) of a heavy species is mixed with a light, inert carrier gas. The heavy species is aerodynamically accelerated by the bulk flow rate of the light gas. The energy available to the heavy molecule, if it is accelerated to the same velocity of the lighter gas is

$$E = \frac{M_{beam}}{M_{carrier}} \int_0^{T_{nozzle}} C_p dT \quad (1.2)$$

where  $M_{beam}$  and  $M_{carrier}$  are the weights of the gas. However, some degree of "slip" may occur between the velocities of the light and heavy gas molecules. As a result it works best for small mole fractions of heavy molecules where the slip is quite small. For heavy molecules intensities of the order of  $\sim 10^{16}$  molecules  $\text{sr}^{-1} \text{s}^{-1}$  are usually attained. In the case of 1% argon expanded in room temperature hydrogen gas, the argon molecule achieves an energy of  $\sim 1 \text{ eV}$ <sup>16</sup>. However, this technique clearly will not work for hydrogen atoms, since hydrogen is the lightest gas.

Charge exchange sources also have been very useful in producing very high energy beams<sup>18-20</sup>. A well-focused ion beam is accelerated through a gas target of the neutral parent. Since the resonant charge transfer process cross section is larger than momentum transfer, the neutral species now generated retains its original direction and energy distribution. The maximum ion current that can be focused into a beam of divergence  $\gamma$  with energy  $E$  (in eV) is:

$$I_{max} = 4.67\pi\epsilon_0 \left(\frac{e}{2M}\right)^{1/2} \times E^{3/2} \tan^2 \gamma. \quad (1.3)$$

As can be seen by the above equation this technique will give weak intensities in the chemically interesting regime of 1-10 eV such that at 100 eV,  $10^{16}$  molecules  $\text{sr}^{-1} \text{s}^{-1}$  are possible but at 5 eV it falls to  $10^{12}$  molecules  $\text{sr}^{-1} \text{s}^{-1}$ . This is due to space charge effects which limit the density of the ion beam and the amount of focusing which is possible. Furthermore, at these lower energies the resonant charge transfer cross section may become smaller than the momentum transfer, such that the beam will diverge to a larger extent. As a result, charge exchange sources are of little use in the study of chemical reactions in the few eV translational energy range.

It is possible to utilize a shock-tube nozzle<sup>21-24</sup> to achieve the desired energy regime of 0-10 eV. The gas is heated upstream by means of a reflected shock wave such that the nozzle itself never becomes too hot. This transient heating creates dissociation and electronic excitation in the gas. The resulting beam can achieve intensities of the order of  $10^{21}$  molecules  $\text{sr}^{-1} \text{s}^{-1}$  at 2 eV energy. The drawbacks to this source are that it is not cw in that it provides a beam pulse of a few milliseconds duration but with a poor duty factor. There is the additional possibility that a metastable specie will be generated. Also, there is no simple way of creating hydrogen atoms with it.

A different technique consists of using microwaves (or r.f. discharge) to dissociate hydrogen molecules to atoms<sup>25,26</sup>. The source is mounted inside a resonant cavity where presumably the molecules dissociate due to electron bombardment. In the case of generating chlorine atoms<sup>27</sup>, 50 watts of power produced between 30 to 60 percent dissociation. However, instabilities in the microwave generation as well as low translational energies of the generated atoms make it unattractive. The oxygen atoms are dissociated by the microwave and the atoms are then accelerated by the lighter bath gas to the same bulk speed. The microwave source provides only dissociation

of the atoms. In the case of oxygen atoms in helium, oxygen atom fluxes of  $10^{17}$  atoms  $\text{sr}^{-1} \text{s}^{-1}$  with translational energies up to .33 eV have been generated.<sup>28</sup> Also being a non-equilibrium, non-specific source, the possibility of generating metastable species is also quite likely.

Hydrogen atoms can also be generated using a tungsten oven<sup>29,30</sup>. This has the great advantage of being perhaps the simplest technique of all and has had great success with the generation of many other different atomic beams<sup>31-33</sup>. Typically this is done by utilizing a hollow cylinder of tungsten where the gas is fed in at one end and heated electrically. Using  $\text{H}_2$  gas this source is then able to generate an intensity of  $\sim 10^{18}$  atoms  $\text{sr}^{-1} \text{s}^{-1}$ . However, with these sources an equilibrium is set up between H and  $\text{H}_2$  which at temperatures of 3000K achieves only 40% disassociation. This plus the fact that it produces atoms at average laboratory energies  $\leq .4$  eV makes it difficult for a general source to be used in reactive scattering.

Probably the best approach for the present application is that of a plasma jet technique<sup>34,35</sup>. Here the nozzle is arranged so that an arc may be generated in the nozzle and the effective stagnation temperature is raised to ten thousand degrees or higher. This source should be very effective in the generation of hydrogen atoms since at these high temperatures recombination of the atomic hydrogen to molecular hydrogen occurs less readily than at ordinary temperatures. For some systems aerodynamic acceleration can also be achieved. Using this technique Ar beams of 3 eV and intensities of  $10^{19}$  atoms  $\text{sr}^{-1} \text{s}^{-1}$  have been achieved<sup>34</sup>.

Despite the obvious advantages of these arc-discharges their operation is not straightforward. A large difficulty with these sources is corrosion of the anode and cathode surfaces, creating dimensional instabilities which occur at these high operating temperatures. With this problem in mind Knuth

and coworkers<sup>36-38</sup> developed an arc heater, which (a) had lower electrode erosion rates, (b) a more stable arc, (c) higher thermal efficiency, and (d) greater ease of construction and maintenance.

It was this type of source which Bernstein later used to generate a beam of atomic nitrogen<sup>39</sup>. Not only were intense beams of nitrogen atoms generated, but also the addition of dilute mixtures of CH<sub>4</sub> and C<sub>2</sub>H<sub>4</sub> to the nitrogen flow caused the organics to be pyrolyzed, creating atomic C as well as C<sub>2</sub> and CH. This nitrogen beam was later used to react with a number of halogen molecules indicating a "forward" scattering direction of product<sup>40</sup>. This type of atomic nitrogen discharge has recently been used again<sup>41</sup> to create metastable nitrogen atoms which react with HI and with HBr in a crossed molecular beam experiment. Fluorescence from the NH product formed is then observed directly.

In the generation of hyperthermal hydrogen atoms, early work was unsuccessful in sustaining a continuous H<sub>2</sub> plasma beam source with a DC discharge<sup>42</sup>. It was not until Stwalley<sup>43,44</sup> and coworkers had adapted the Knuth source to operate with H<sub>2</sub> that hydrogen atoms could be generated by this technique. Stwalley's operating conditions generated hydrogen atoms with an intensity of  $10^{17} - 10^{20}$  atoms sr<sup>-1</sup> s<sup>-1</sup> at energies going from 0 to 5 eV. Their method of producing the plasma consisted of striking the discharge first with argon and then slowly changing over to hydrogen. In this way a pure discharge of hydrogen could be sustained.

Despite the existence of this technique since 1976, only two experiments have been reported to date using this high-intensity source of hydrogen atoms. The first was by Stwalley<sup>45</sup> who collided the hydrogen atoms with lithium atoms and molecules observing the photon and positive ion production. The second experiment was a crossed molecular beam experiment recently per-

formed by Toennies<sup>13</sup> where D atoms were produced and reacted in a crossed beam experiment with H<sub>2</sub>. This experiment was performed using a very broad energy distribution centered at center of mass energies of 1.4 eV and with a relative velocity spread ( $\Delta v/v$ )  $\sim$  1.0.

In this thesis we report our work using this technique for generation of an intense beam of hyperthermal hydrogen atoms. We also report the design and construction of a velocity selector designed to allow translational energy selection of H atoms with a resolution of 0.1 to 0.2 eV at energies up to a few eV. This may allow reactive crossed beam experiments to be performed for a range of translational energies. By using this technique, quantum mechanical resonances, which have already been observed in the F + H<sub>2</sub> system<sup>46,47</sup>, may one day be directly observed in the D + H<sub>2</sub> system through crossed beam reactive scattering.

### 1.3 References

1. R. B. Bernstein, *Chemical Dynamics via Molecular Beam and Laser Techniques*, New York : Oxford University Press (1982).
2. M. A. D. Fluendy and K. P. Lawley, *Chemical Applications of Molecular Beam Scattering*, Chapter 8, London:Chapman and Hall (1973).
3. D. G. Truhlar, *Ann. Rev. Phys. Chem.*, **27**, 1 (1976).
4. G. C. Schatz and A. Kuppermann, *J. Chem. Phys.*, **62**, 2502 (1975), **65**, 4668 (1976).
5. A. B. Elkowitz and R. E. Wyatt, *J. Chem. Phys.*, **62** 2504 (1975), **63**, 702 (1975).
6. R. B. Walker, E. B. Stechel, and J. C. Light, *J. Chem. Phys.*, **69**, 2922 (1978).
7. D. P. Gerrity and J. J. Valentini, *J. Chem. Phys.*, **79**, 5202 (1983).
8. E. E. Marinero, C. T. Rettner, and R. N. Zare, *J. Chem. Phys.*, **80**, 4142 (1984).
9. S. Datz and E. H. Taylor, *J. Chem. Phys.*, **39**, 1896 (1963).
10. W. L. Fite and R. T. Brackmann, *Atomic Collision Processes*, edited by M. R. C. McDowell, North-Holland, Amsterdam, pp. 955-963 (1964).
11. J. Geddes, H. F. Krause, and W. C. Fite, *J. Chem. Phys.*, **56**, 3298 (1972).

12. G. H. Kwei and V. W. S. Lo, *J. Chem. Phys.*, **72**, 6265 (1980).
13. R. Gotting, H. R. Mayne, and J. P. Toennies, *J. Chem. Phys.*, **80**, 2230 (1984).
14. D. R. Herschbach, *Disc. Far. Soc.*, **33**, 149 (1962).
15. J. B. Anderson, R. P. Andres, and J. B. Fenn, in *Advances in Atomic and Molecular Physics*, D. R. Bates and I. Estermann, eds., Vol. I, Academic Press, New York (1965).
16. R. Klinelhofen and P. Lohse, *Physics of Fluids*, **7**, 379 (1964).
17. N. Abauf, J. B. Anderson, R. P. Andres, J. B. Fenn and D. G. H. Masrden, *Science*, **155**, 197 (1967).
18. N. G. Utterback, *Phys. Rev.*, **129**, 219 (1963).
19. N. G. Utterback and G. H. Miller, *Rev. Sci. Instrum.*, **32**, 1101 (1961).
20. N. G. Utterback and G. H. Miller, *Phys. Rev.*, **124**, 1477 (1961).
21. G. T. Skinner, *Physics of Fluids*, **4**, 1172 (1961).
22. G. T. Skinner and B. H. Fetz, in *Rarefied Gas Dynamics*, C. L. Brundin, ed., Vol. II, Academic Press, New York (1966).
23. T. V. Jones, in *Rarefied Gas Dynamics*, C. L. Brundin, ed., Vol II, Academic Press, New York (1966).
24. G. T. Skinner, *Proc. 7th Agard Colloquium on Advances in Aerothermochemistry*, Oslo (1966).
25. J. P. Toennies, W. Weley, and G. Wolf, *J. Chem. Phys.*, **61** 2461, (1974).

26. D. Bassi, M. DePaz, A. Pesis, and F. Tommasini, *Chem. Phys. Lett.*, **26**, 422 (1974).
27. L. Davis, B. T. Field, C. W. Zabel, and J. R. Zacharias, *Phys. Rev.*, **76**, 1076 (1949).
28. D. R. Miller and D. F. Patch, *Rev. Sci. Instrum.*, **40**, 1566 (1969).
29. J. Potjewyd, UTIAS Report #220, CNISSN 0082-5255, Institute for Aerospace Studies, University of Toronto, March 1978.
30. M. A. D. Fluendy, R. M. Martin, E. E. J. Muschlitz, and D. R. Herschbach, *J. Chem. Phys.*, **46**, 2172 (1967).
31. Y. T. Lee, P. R. Le Burton, J. D. McDonald, and D. R. Herschbach, *J. Chem. Phys.*, **51**, 455 (1969).
32. Y. T. Lee, J. D. McDonald, P. R. Le Burton, and D. R. Herschbach, *Rev. Sci. Instr.*, **40**, 1402 (1969).
33. M. A. D. Fluendy, D. S. Horne, K. P. Lawley, and A. W. Morris, *Mol. Phys.*, **19**, 659 (1970).
34. R. W. Kessler, and B. Koglin, *Rev. Sci. Instr.*, **37**, 682 (1966).
35. E. L. Knuth, *Applied Mechanics Rev.*, **17**, 751 (1964).
36. E. L. Knuth, UCLA Department of Engineering Report #66-19 (April 1966).
37. W. S. Young, W. E. Rodgers, and E. L. Knuth, *Rev. Sci. Instrum.*, **40**, 1346 (1969).
38. E. S. Young, UCLA Department of Engineering Report #69-39 (July

- 1969).
39. R. W. Bickes Jr., K. R. Newton, J. M. Herrmann, and R. B. Bernstein, *J. Chem. Phys.*, **64** 3648 (1976).
  40. R. L. Love, J. M. Herrmann, R. W. Bickes, Jr., and R. B. Bernstein, *J. Am. Chem. Soc.*, **99**, 8316 (1977).
  41. K. Tabayashi, S. Ohshima, and K. Shobatake, *J. Chem. Phys.*, **80**, 5335 (1984).
  42. G. Clausnitzer, *Nucl. Instrum. Methods*, **23**, 309 (1963).
  43. K. R. Way, S.-C. Yang, and E. C. Stwalley, *Abstracts of the IXth International Conference on the Physics of Electronic and Atomic Collisions*, Univ. Washington P., Seattle, 957 (1976).
  44. K. R. Way, S.-C. Yang, and W. C. Stwalley, *Rev. Sci. Instrum.*, **47**, 1049 (1976).
  45. J. B. Crooks, K. R. Way, S.-C. Yang, C.-Y. R. Wu, and W. C. Stwalley, *J. Chem. Phys.*, **69**, 490 (1978).
  46. R. K. Sparks, C. C. Hayden, K. Shobatake, D. M. Neumark, and Y. T. Lee in *Horizons in Quantum Chemistry*, K. Fukui and B. Pullman, eds., Reidel, Boston, pp. 91-105 (1980).
  47. D. M. Neumark, A. M. Wodtke, G. N. Robinson, C. C. Hayden, and Y. T. Lee, *Phys. Rev. Lett.*, **53**, 226 (1984).

## 2. Experimental

### 2.1 Theory

There will be no attempt to review the sizable amount of theory which has been developed to understand free jet expansions<sup>1-3</sup>. Considering the special nature of the plasma discharge many approximations will, of course, break down. However, it is useful to attempt to use these equations in order to understand what parameters are important to characterize molecular beams.

A jet of gas expanding into a very large evacuated chamber will produce shock waves which lower the intensity of the beam. A shock wave is a bulk gas phenomenon and will form only if the mean free path is small. Therefore, if an object is placed in the path of a free-jet expansion, the gas is stopped at the object, and in the neighborhood of that object a stagnation pressure is developed which the jet can't penetrate freely. Similarly, just as a solid object can create shock waves, residual gases in the chamber can also create shock waves as they become entrained in free-jet expansion and slow down the whole expansion process.

It is known how to calculate<sup>4</sup> where this shock barrier will appear. According to Bier and Schmidt<sup>5</sup>, the maximum diameter of the shock barrel occurs at approximately two-thirds the distance from the source orifice to the Mach disk as shown in the following equation;

$$\frac{x_b}{d^*} = .44 \left( \frac{p_o}{p_s} \right)^{\frac{1}{2}} \quad (2.1)$$

where  $p_s$  is the background pressure in the source chamber,  $p_o$  is the stagnation pressure,  $x_b$  is the distance of the appearance of the shock barrel relative

to the location of the skimmer, and  $d^*$  is the diameter of the nozzle opening. One can then relate the stagnation pressure,  $p_o$ , to the speed of the source chamber vacuum pump if one equates the mass-flow rate for the nozzle to the load on the source chamber

$$S \left( \frac{p_s m}{k T_s} \right) = \left( \frac{\pi d^{*2}}{4} \right) \left( \frac{p_o m}{k T_o} \right) \sqrt{\left( \frac{\gamma k T_o}{m} \right) \left( \frac{2}{\gamma + 1} \right)^{\frac{\gamma+1}{\gamma-1}}} \quad (2.2)$$

where  $T_o$  is the temperature of the beam,  $T_s$  is the temperature of the gas in the chamber,  $S$  is the speed of the source chamber pump, and  $\gamma$  is the specific heat ratio. We can eliminate the direct dependence on  $p_o$  by combining equations (2.1) and (2.2) to

$$x_b = .5 \sqrt{\frac{S m}{k T_s}} \sqrt[4]{\frac{k T_o}{m \gamma} \left( \frac{\gamma + 1}{2} \right)^{\frac{\gamma+1}{4(\gamma-1)}}} \quad (2.3)$$

Here one only needs to know the speed of the source chamber vacuum pump, the stagnation and source temperature and the specific heat ratio in order to predict the location of the maximum diameter of the shock barrel. For our current design one should insert these approximate values:  $T_o \sim 10,000\text{K}$ ,  $T_s \sim 300\text{K}$ ,  $S \sim 1500 \text{ l/s}$ , and a specific heat ratio  $\gamma$  of  $7/5$ . The heat ratio is an attempt to take into account the additional degree of freedom due to the electronic excitation of the hydrogen atom. Using these parameters  $x_b$ , the nozzle to skimmer distance for the appearance of the first Mach disc, is 8.8 cm.

It is possible to make crude estimations for the Mach number by using the semi-empirical expression derived by Sherman<sup>6</sup>

$$\frac{x}{d^*} = \sqrt{\left( \frac{\sqrt{\gamma(\gamma-1)}}{2.2} \right)} \left[ \left( \frac{1}{\sqrt{M}} \right) \frac{1 + M^{\frac{2\gamma-1}{\gamma}}}{\left( \frac{\gamma+1}{2} \right)} \right]^{\frac{\gamma+1}{4(\gamma-1)}} + \frac{.75}{(\gamma(\gamma-1))^{\frac{1}{2}}} \quad (2.4)$$

where  $x$  is the nozzle to skimmer distance. Taking  $x$  as 4 cm and  $d^*$  as 0.1 cm gives a Mach number of 16. This number is highly unreasonable considering the high pressures within the source chamber during the operation of the arc.

We can now see that attempting to use these equations to calculate a Mach number for our beam can lead to misleading results since so many of the quantities needed such as  $\gamma$ ,  $T_o$ , and  $S$  are only known approximately. We can get a much more realistic Mach number from Stwalley's work<sup>7</sup>. In the development of a hydrogen arc discharge source similar to the one we use he characterized his beam by measuring its velocity distribution. This was done through measuring the deflection of the hydrogen atoms via an inhomogeneous magnet. These deflection patterns were summed with a weighting factor based on the velocity distribution for a supersonic expansion

$$F = (1 + 2.316 \times 10^{-13} v^2) \left[ v \left( \frac{3 + M^2}{6RT} \right)^{\frac{1}{2}} \right]^3 \quad (2.5)$$

$$\times \exp \left( \frac{-(3 + M^2)}{6RT} \left[ v - \left[ 5RT \left( \frac{M^2}{3 + M^2} \right) \right]^{\frac{1}{2}} \right]^2 \right)$$

where  $F$  is the relative amount of energy from atoms with velocity between  $v$  and  $v + dv$ ,  $T$  is the stagnation chamber temperature and  $M$  is the Mach number. Using this model, Stwalley was able to determine a Mach number between 0.3 and 3 for his hydrogen discharge.

## 2.2 Vacuum System

One can see from the previous equations that in order to have high beam intensities as well as a stable arc-discharge, it is necessary for the source chamber vacuum pump to be able to have a high pumping speed at a relatively high pressure. The entire vacuum system is shown in Figure 1. A 20" diameter oil diffusion pump is used along with a 6" oil diffusion booster pump, which share a common oil reservoir, to pump the source chamber [VC1]. The diffusion pumps were originally roughed by a Kinney DVD 8810 mechanical pump, but due to its advanced years this pump was retired. The current roughing pump is a Welch model 1398 Duo Seal<sup>©</sup> mechanical pump with a rated speed of 50 ft<sup>3</sup>/min. The diffusion pumps a measured combined pumping speed of 10,000 l/sec at 10<sup>-5</sup> torr and 4000 l/sec at 10<sup>-4</sup> torr. The pumps require 5 gallons of Convoil 20<sup>©</sup> oil. Upon operation of the pumps the oil turns black after one year of operation. This is either due to some corrosion within the diffusion pumps themselves or perhaps to the high amount of hydrogen gas which is pumped through the system. In any case the oil must be changed periodically in order to ensure reliable operation. An ultimate pressure of 1 x 10<sup>-6</sup> torr is achievable with no load applied to the system, but, with the beam operating, the pressure in VC1 will rise to as high as several hundred millitorr, for periods ranging from a few minutes to several hours. In spite of this high pressure the diffusion pumps do function, since turning them off noticeably affects the appearance of the arc discharge plume.

The diffusion pumps are mounted to a movable pump stand which in turn is connected to the mechanical roughing pump, also mounted to a movable base, via eight feet of 6" diameter flexible tubing. These movable stands were

built to facilitate the eventual move of the source chamber from its present location, attached to the small bell jar [VC2], to being attached to the 50" bell jar of a crossed molecular beam apparatus located on the other side of the lab. In the past a 6" ball valve was fitted to the discharge side of the booster to isolate the roughing pump from the diffusion pump, but a crack in its seal has recently made it unusable. Because of the age of the valve a replacement seal could not be located and the valve itself was removed.

The arc source chamber has the shape of an L, and is built from mild steel tubes having diameters of 24" and 10", as shown in Figure 1. It is connected to the diffusion pump by a 10" ID flange having an O-ring seal. Looking down from above the chamber toward the skimmer, to the left of the L is a 10" diameter flange which is used to service the source and to the right is a 6" flange [P1] which is fitted with a quartz window to permit viewing of the operation of the source. Along the top of the L are three 2 3/4" conflat feedthroughs which are used to pass electrical power (for the arc and magnet), cooling water, and gas into the source. On the front of the L there is a 6" diameter exit port with a Varian conflat flange. On the inside of the L the aluminum water-cooled base of the skimmer [S] is mounted to this end via an O-ring seal, so that the nozzle and the skimmer are in alignment with the center of the 6" exit port. It is through this exit port that the L is mated with the 20" bell jar (VC2) via 7.47" of 6" flexible tubing [F].

Upon first successful operation of the arc source utilizing hydrogen gas as the plasma medium, it was observed that the front of the L became excessively hot, so much so that the outer metal surface became visibly reddened. It was realized that continued running of the source would require cooling coils on the outside of the chamber. Quarter-inch copper tubing was wound around the outside of the L; however, there was not enough surface contact with the

chamber to ensure efficient cooling. Since actual welding of the cooling tubes was not possible at the time, the copper coils were secured to the outside of the chamber using a high temperature heat transfer cement called Thermon<sup>©</sup>. While aesthetically unattractive it provides good thermal contact to the outer surface with the cooling coils, thus circumventing the problem.

The 20" bell jar, which contains all the diagnostic equipment to study the beam, is mounted on a movable stand which is physically attached to the pump stand of the oil diffusion pump via unistrut struts, which create one secure assembly. The bell jar is mounted to the top of a mercury diffusion pump and is trapped by a freon baffle as well as a liquid nitrogen trap. The pump may be isolated from the bell jar via a 6" gate valve. The pump speed of this overall system has been measured at 125 l/sec and is capable of giving an ultimate vacuum of  $2 \times 10^{-6}$  torr. The bell jar itself sits on a base of twenty 2 3/4" flanges which are used to allow electrical connections inside the bell jar. The seal between the bell jar and the base is achieved with a Viton O-ring<sup>©</sup>. The bell jar itself has four 6" conflat flanges, the first being mated to the source chamber, the second being 90° away having a quartz window to view the inside of the chamber, and the third directly in front of the entering beam and has a EAI Quad 300 mass spectrometer mounted to allow analysis of the entering beam. There is a fourth flange mounted at a 45° angle to the top of the bell jar, which is currently not being used. The bell jar can be moved independently of its base via perpendicular push-pull screws mounted to the base. This permits movement of the mass spectrometer relative to the incoming beam to provide alignment between the nozzle and skimmer in the source chamber, and the mass spectrometer itself. The floor of the 20" bell jar has a circle of tapped holes on the floor of the pump chamber surrounding the pump hole. These holes hold threaded rods which in turn support the

chopper, beam flag and deflection plates, all of which will be discussed later.

To protect the various VC1 pumps from damage or accidental misuse, an interlock-control system is used to protect the system. This unit is designed to shut off the arc power or any of the pumps if any failures occur in the other components of the system. Each stage of the interlock is enabled only when the preceding stage is made operational. The first stage in the past controlled the Kinney mechanical pump. For the pump to operate the cooling water to the pump body had to be turned on. However, now with the Welch pump, which needs no cooling water, this stage of the interlock is superfluous. Once the Welch pump is on and water is flowing through the diffusion pump for VC1, then the heater power for its diffusion pumps may be turned on. Both a thermal cut-out switch and an over-pressure switch are provided to protect the diffusion pump and switch off the heater power should either condition occur. The pressure sensor used is a Schulz-Phelps gauge and controller (Granville-Phillips). Only after the roughing and diffusion pumps are on can the arc power be turned on.

Within the vacuum chamber there are two separate water cooling lines. One line cools only the anode and cathode parts of the arc source. The second line first cools the center of the magnet which holds the source, then cools the magnet itself and finally the aluminum base of the skimmer. A major frustration is caused by water leaks occurring while the system has been under vacuum. These leaks have varied in magnitude from minor drips, to an actual filling of the chamber itself. In a sense these are somewhat unavoidable due to the high temperatures of the source and surrounding metal, and the need to use polyethylene tubing to electrically insulate the cathode from the rest of the chamber. In an attempt to minimize these accidents the flow out of both water lines is monitored by McDonnell flow switches. When flow rate

drops, either due to a leak in the system or a drop in the total flow of water into the lab, an alarm sounds. This in turn triggers the interlock system discussed in the preceding paragraph and shuts off the arc power as well as power to all the diffusion pumps.

### 2.3 Source

Following the design of Knuth, *et al.*<sup>8-10</sup> an arc-heated source was constructed. A cutaway schematic view of it is shown in Figure 2. The concept of the source is a simple one in that gas is introduced into the area between a fixed anode [2] and a movable cathode tip [10]. Placing the source within a vacuum chamber will cause the gas to flow through the nozzle [1] into the chamber due to the large pressure differential. Striking a high voltage pulse between [2] and [10] will create a plasma flame which, due to the expansion of gas through the nozzle, extends beyond the anode itself, thus carrying away some of the heat generated. As described later, this arc produces very high temperatures which require efficient cooling of metal surfaces of the source to avoid their destruction.

In the original use of this design we achieved little success in creating and sustaining a reliable hydrogen plasma. It has only been in recent years that these difficulties were surmounted by a total redesign of the source as well as a new understanding as to what parameters are important in creating a stable discharge. What follows is a description of the evolution of the system.

The cathode portion of the source is shown in Figure 3 and physically consists of a hollow brass tube [A] with a 1 1/8" diameter tip cathode rod [B] attached to the front. This rod is made of 2% thoriaed tungsten and is capable of withstanding temperatures in excess of 3000 K. Many different shapes for the tip of the rod have been tried, with the best one having the end rounded. However, during running of the source it tends to erode such that tungsten sputtered off the rod sometimes clogs the nozzle. After an extended run the tip of the rod is shaped to a sharp point from this sputtering. This

cathode rod is attached by a set screw [C] to the base of the hollow brass tube in a way which allows for water cooling of the tube [A], as well as the tungsten rod. This tube is fitted inside of a support structure [D] in such a way that it can move  $3/4''$  with respect to the latter. A brass bellows [E] is silver soldered between the tube and the support structure to maintain a vacuum tight assembly. Once set, the position of the tube may be held in place via the outside casing [F].

Two gas inlets are drilled at sharp angles through the cathode support structure [D] on opposite sides of the chamber located between the cathode and the anode. This has the effect of causing the gas to swirl around inside the source creating a more stable flow through the nozzle thereby stabilizing the arc. It has been observed that, when one side of the inlets is clogged, the arc will not operate. This is probably due to gradients in the gas flow making the discharge medium less uniform and unstable. This clogging sometimes occurs due to the fact that the inlet lines are soft soldered to the cathode housing, such that, if the casing becomes too hot, the solder will run into the inlets. This problem has now been alleviated by building the entire cathode section out of stainless steel. Not only is this a more rugged device, but the gas inlets are welded in and do not become loose at the temperatures generated.

The anode assembly, as seen in Figure 4, consists of a large cylindrical brass piece [D1 & D2] which has six water cooling channels bored into it. The front of the device holds the nozzle assembly through which the gas passes and to which the arc is struck. It appears now that part of the problem that existed in the past with creating a stable discharge was due to the arc confined to the small region between the tip of the cathode and the nozzle. What apparently occurred is that, once the arc was struck between the cath-

ode tip and the anode nozzle, it would migrate to the anode housing creating an internal arc which would subsequently damage the source. To circumvent this problem it was decided that the anode section of the source should be electrically insulated from the cathode everywhere except at the exit point of the nozzle. This entailed machining an elaborate piece of Macor<sup>©</sup> ceramic which looked like a pair of coaxial cylinders with different diameters. The smaller diameter cylinder surrounded the cathode rod and the larger diameter one surrounded the hollow tube which holds that rod. This shielded the cathode assembly from the support structure, confining the discharge to the small volume between the tip of the cathode rod and the anode nozzle. This proved successful in that for the first time in this lab a hydrogen discharge was sustained. However, in the actual operation of the discharge, the narrow ceramic tube would become damaged due to heating and the arc would fail. This coupled with the expense in machining the Macor<sup>©</sup> made us look for a new solution. A different approach was tried in which the insulating assembly was made out of aluminum which was then black-anodized creating a nonconductive coating around the aluminum. However, the heat of the arc melted the anodization off the edges of the assembly and the device immediately shorted out to the source body.

Our last attempt was to eliminate the smaller diameter ceramic cylinder and to use just a simple larger diameter Macor<sup>©</sup> cylinder closed at one end but with a hole through the closed surface, which allowed the tungsten rod to stick through it. This is the current design and is shown as part [E] of Figure 4. That figure shows the other parts of the anode assembly in a disassembled configuration. In this design, the arc still remains limited to the small region between the cathode tip and anode. After prolonged use the only damage to the cylinder is a slight charring at the exit hole. The drawback of this

geometry is that the arc will sometimes strike along the inside area of the nozzle (Figure 4, part c) causing severe erosion of its surface.

Since much heat is generated at or near the exit aperture of the nozzle, this part is designed for easy replacement. Ideally, a material which is highly conductive electrically and thermally would make an excellent nozzle. We initially followed Stwalley's<sup>7</sup> example of using a copper nozzle which simply screwed into the front of the anode. Using this design we quickly encountered the same problem he had, namely, that during a typical run the nozzle opening would enlarge from an initial 2 mm diameter to as much as a 6 mm opening. We tried, as Stwalley, to use molybdenum as material for the nozzle but it melted too easily. After many attempts with these materials we eventually came to the conclusion that the nozzle would have to be made out of tungsten. In the case of the cathode it had been simple to make it out of this material. This had been accomplished by cutting a 1/8" welder's rod nearly to the desired length and rounding the tip on a grinder. In the case of the anode nozzle, because of the grave difficulties in machining tungsten, a much simpler design was necessary. Also because of the poor thermal conductivity of tungsten, efficient cooling was critical in order to avoid having it open up as all the others nozzles had done. The eventual design chosen involved cutting a 1/8" thick disk of tungsten from a .375" welder's rod. A 1.2 mm hole is then drilled into this disk with a carbide drill. This disk is shown in Figure 4, part B. It is held in place by two copper pieces (parts C and D) which are threaded into the the anode base. These copper pieces provide excellent thermal contact between the tungsten nozzle and the water-cooled base of the anode body. We have had great success with this design and are able to run repeatedly (5 to 8 times, several hours each time) using the same nozzle, with little erosion occurring.

When assembled, the anode and cathode are joined by six teflon screws. The anode and cathode are electrically separated by a teflon spacer and a Viton O-ring<sup>©</sup> which also serves to provide a vacuum seal between these two components. Great care must be taken in achieving such a seal since otherwise, even though the correct amount of gas is entering the vacuum chamber, less of it is going through the nozzle than usual. As a result, the plasma will become excessively hot, thereby damaging the anode. Likewise, when tightening the six teflon screws it is necessary that the cathode rod remain centered with respect to the anode body. If the rod should be off axis, damage will occur to the copper pieces which retain the tungsten nozzle, and the nozzle hole itself will enlarge in an asymmetric fashion; i.e., it will open up in the region to which the rod is pointing.

Once the system is assembled, the space between the cathode tip and the anode nozzle forms a small chamber (Figure 2 [4]) into which the gas may be introduced via the inlet lines (Figure 2 [3]). To ensure that the cathode is insulated from the rest of the chamber (thus preventing any shorts) all water lines to it are made of 1/4" polyethylene tubing, and the metal gas inlet line contains a glass spacer to insulate it as well from the anode and the rest of the chamber.

When assembled the 'cathode tip-anode nozzle' distance can be adjusted by compressing the cathode bellows (Figure 2 [7]), measuring the distance from the tip of the rod to the threaded copper nozzle holder (Figure 4C) with the nozzle disk (Figure 4B) removed with a set of calipers, and fixing the cathode assembly in place at the appropriate location with teflon retainer screws. Trial and error have shown the optimum gap between the tip of the cathode and the surface of the anode disk to be 0.5mm, for, if it is smaller than that value, the nozzle hole will immediately short out to the cathode

rod, but if it is too large the arc will be extinguished during the changeover from argon to hydrogen. This distance appears to be fundamental to the stable operation of the system. For example, Toennies<sup>11</sup> has recently developed a beam similar to the one described here and had great difficulty maintaining a stable discharge until he began to run using the parameters just described.

Power for our arc source is provided by a Westinghouse type WS variable current arc welder supply. This unit can supply a maximum current of 180 amperes and an open circuit voltage of 90 VDC. Since the arc welder runs on 440 voltage, a step-up transformer is used to provide the necessary power for the welder from the 220 line currently available in our lab. The level of the regulated output current from the welder can be remotely adjusted by means of a servo motor built into the power supply. This servo changes the position of a tap which connects to the secondary of the transformer in that supply. A Westinghouse 0-150 VDC meter is used to monitor the output voltage, while a 0-250 ADC ammeter is used to monitor the current. The arc itself is started by using a 200 amp lamp starter (Hanovia model 29912) which generates a high voltage pulse. All of this is part of the interlock system discussed in section 2.2, such that, if any of the segments of the interlock fail, the arc power will immediately be shut off.

Figure 5 shows a schematic top view of the entire machine, with the arc source [AS] installed. This source is mounted into the center of a 6" diameter by 1.4" thick electromagnet [M]. This device has no magnetic core and is formed by wrapping approximately 450 turns of 14 gauge armored polythermaleze antenna wire (Belden, 8009-500) around an aluminum support structure. A cross sectional drawing of this electromagnetic is shown in Figure 6. Because of the heat generated by this electromagnet it is water-cooled in two ways. The first way is by 2 layers of 3/16" copper tubing which

are wound within the wire windings. The magnet is also cooled by a brass cooling channel which is set in the center of the magnet, as shown in Figure 6. It is within this cooling channel that the assembled arc source sits during the operation of the discharge. During operation of the magnet, water flows through both the brass channel and the copper tubing. Typically, the magnet will be operated at 20 volts and 20 amperes, the power being supplied by an HP Harrison 6269A DC power supply. This current will typically result in a one-kilogauss field in the center of the magnet as measured with a Bell "120" gaussmeter. This field is of critical importance in stabilizing the plasma by providing a perpendicular force on any ions which try to leave the beam, directing them instead to remain in the center of the free jet expansion. In our apparatus we have changed the position of the source with respect to the magnet. In Stwalley's<sup>7</sup> and Knuth's<sup>8-10</sup> original design the nozzle was placed at the exit of the magnet, while in our design we have located it in the center of the magnet. This appears to give the magnetic field a greater influence on the plasma, such that by decreasing that field to about 600 or 700 gauss one can visually observe a spreading of the beam to a larger diameter. Likewise, the effect is reversible in that by increasing the applied field the beam become more narrower and well defined.

Of all the separate parts of the apparatus the electromagnet becomes the hottest during operation of the arc despite the cooling system previously described. As a result of this heating the current through and voltage across the magnet windings will drop as a function of time, until leveling out at 12 amperes and 12 volts. After one year of use the polythermaleze insulation will melt off the wire, shorting the coils out, and a new magnet has to be wound. To help circumvent this problem in the future, additional copper cooling coils should be welded to the front and the back of the magnet to provide additional

cooling. Alternatively, a permanent magnet could eliminate this problem due to the absence of the energizing current.

As shown in Figure 5, the magnet [M] is mounted on a movable rail track so that once the arc is operating, the arc source and the magnet may be jointly moved closer to the downstream skimmer [S] via a mechanical vacuum feedthrough [T] mounted on a 10" flange. By simply turning the outside knob control of that feedthrough, the whole assembly [TA] can be moved back and forth. Care must be taken in the initial placing of the heat-sensitive polyethylene cooling lines such that in the moving of the arc source they in no way get in contact with the hot body of the magnet, nor with any of the hot surfaces of the source.

The skimmer [S], as shown in Figure 7, consists of a two-piece copper assembly which is threaded into a conical aluminum base. The base itself is sealed with the help of an O-ring to the front of the L chamber (Figure 1 [VC1]). As shown in Figure 7a the first part of the skimmer is a conical copper mount which screws into the aluminum base. The actual skimmer as shown in Figure 6b screws into the copper mount in Figure 7a. This allows for easy replacement of the skimmer should it become damaged during the operation of the arc source. The skimmer has an exterior angle of  $28^{\circ} 30'$  and an interior angle of  $16^{\circ} 30'$  and an orifice diameter of .04". We have tried making this piece out of Macor<sup>©</sup> but because of that ceramic material's poor heat conductivity, bringing the source closer than 6 cm. from the skimmer caused the latter to soften and seal its aperture. Using copper for the skimmer the source is able to get as close as 2 cm without deforming the skimmer. It has been observed that the closer the skimmer to the nozzle, the higher is the measured hydrogen atom intensity. Of course, one wishes to get the source as close as possible to the skimmer to achieve high intensity. By slowly moving

the source closer to the skimmer, the skimmer retains its shape unless some hot tungsten sputters out of the nozzle, hitting the former. If the source is brought up too quickly, not allowing the excess heat to equilibrate with the water cooling, the skimmer can deform and close up.

The aluminum base (as shown in Figure 7a) has an aluminum 1/4" tubing wrapped around and welded to it to provide water cooling for it and for the copper skimmer. Due apparently to some electrolytic reaction, the interior of the aluminum tube is slowly eaten away leaving what appears to be a white oxide residue. As a result, after about 9 months of running the tubing will start to become clogged up and after one year's use the tubing itself will begin to leak. When this occurs the only solution is for new tubing to be rewelded to the aluminum cone. To circumvent this problem in the future that base might be made out of stainless steel and 1/4" stainless tubing can then be welded to it. Though its thermal conductivity may be poorer, it should be much more resistive to the type of corrosion just discussed.

## 2.4 Operation of the Source

What follows is a brief summary of the typical ignition of the argon plasma and its changeover to a hydrogen arc. Any attempt to start the discharge in pure  $H_2$  will result in the destruction of the source and anything within its vicinity due to melting<sup>10</sup>. It has been found that a safe, reliable way to generate a hydrogen beam is first to start the plasma with argon and then gradually switch over to hydrogen<sup>13</sup>. This technique is so delicate that Stwalley and coworkers filmed the changeover in an attempt to document the operation<sup>13</sup>. A second-by-second table of the values of flow rates, voltage, and source pressure with some pertinent description is available<sup>14</sup>. Our system, being different from Stwalley's, has caused a somewhat different technique to evolve over the years.

After allowing VC1 and VC2 to pump down (Figure 1), a flow of argon is established. The flow is regulated by a leak valve until a constant flow of 7 SCFH air, as measured by the flow meter on the gas line, is achieved. For a typical nozzle this corresponds to a stagnation pressure of about 340 torr as measured by the 0 to 1 atmosphere Wallace & Tiernan gauge on the inlet line. At this point the pressure in VC1 will rise to 50 microns, while the pressure in VC2 will rise to  $4 \times 10^{-4}$  torr. The water lines for the source, the magnet-skimmer, and the exterior of VC1 are then turned on, and the pressure is carefully monitored to verify whether there are any minor water leaks within the chamber. Once the gas pressure has stabilized, the current to the magnet and to the arc welder are turned on. The portion of the secondary winding tap of the welder's power supply controlled by the servo-motor is set to a position which should produce a 100 ampere current once the arc strikes

(the normal reading of this position is 130 amp).

The argon arc is now initiated by throwing the switch on the Hanovia lamp starter which provides the voltage pulse between the anode and the cathode, initiating the discharge. Should the discharge successfully commence, the welder will supply 15 volts and 100 amperes. Once every twenty or thirty times the discharge will, instead of striking between the cathode tip and the anode disc, strike between the cathode power cable and the interior of the vacuum chamber close to where the former enters the latter. This can be observed through the sparks and discharge light emitted as viewed through P1, Figure 1. The cables to the anode and cathode are shielded from each other and from the inside of the VC1 (Figure 1) chamber by insulating material and ceramic spacers, and their connection to the feedthrough is insulated with teflon tape. Despite these precautions, 'external discharges' continue to occur once in a while. When they do, the power is manually turned off as quickly as possible and typically little damage is caused such that another attempt may be made at starting the discharge. Usually by making a small change in the stagnation pressure, or by moving the source back and forth with the help of the mechanical vacuum feedthrough T (Figure 5), a successful ignition will take place without its being necessary to break the vacuum.

It is in the initial ignition of the argon arc that the greatest damage to the nozzle and the cathode tip occurs. For 5 to 10 seconds after the start of the discharge, streams of sparks will sometimes be emitted from the nozzle. Eventually the discharge will ignite and a stable intense light blue plume will be observed. At this point the arc is being run at 15 volts and 100 amperes.

Once the discharge appears stable, hydrogen gas is **slowly** mixed into the argon flow. The gas is introduced into the system via a Granville-Phillips variable leak valve (series 203). No visible change appears in the plasma until

approximately 24 torr partial pressure of hydrogen has been introduced. At this time there is a dramatic change in the appearance of the plume: it becomes much reduced in size and turns a less intense but beautiful crimson red. The hydrogen flow is continuously increased until the hydrogen pressure reaches 150 torr. The intensity of the plasma emission continues to decrease as the hydrogen flow increases. This procedure takes approximately ten minutes.

Once this hydrogen pressure has been reached the argon flow is slowly turned off, which unless otherwise modified results in a decrease of the arc current and an increase in its voltage. It is, however, vital that during this changeover the current be kept at a constant value of 100 amperes or the discharge will be extinguished. This is accomplished by changing via the servo motor the position of the welder's secondary winding tap. During this decrease in the argon flow the emission will get progressively brighter while the cooling water will become progressively hotter. It is at this point that the greatest chance of losing the discharge exists. Sparks from the nozzle can many times be seen at this time as well as various types of anomalous behavior, as discussed below.

A) Often, the plasma will turn into an emerald color which is due to copper sputtering off the inside of the nozzle holder (Figure 4 [C]). A subsequent examination shows that copper has eroded from the inside of this part sometimes covering the entire exterior of the tungsten nozzle disc. This seems to be caused by the discharge migrating from the tungsten nozzle disc to the inside copper nozzle holder. When this green color is observed this anomaly can often be rectified by rapidly increasing the argon flow to its previous level and then repeating the above turn-off procedure. However, the nozzle will have to be replaced after the run is over.

B) Sometimes the plasma will suddenly become quite dim. This is usually

caused by a sizable piece of tungsten eroding off the cathode tip, and reducing the size of the nozzle aperture. When this occurs there is little hope of getting the beam started up again. However, allowing it to run for a while at a low hydrogen stagnation pressure sometimes heats the nozzle sufficiently to clear its orifice. If this does not work it is necessary to break vacuum and redrill the nozzle aperture.

C) Occasionally the plasma will begin to oscillate in a circular fashion around the center beam line or likewise begin to pulse from an intense plasma to a dull plasma. This type of periodic behavior appears to be due to the cavity between the anode and cathode's becoming irregularly shaped as the rod and/or nozzle are unevenly etched, causing the discharge to rotate in the discharge gap. This sometimes can be corrected by momentarily increasing the current to the electromagnet. This higher magnetic field tends to "realign" the discharge. Then by slowly reducing that current back to its normal value the discharge may return to a stable configuration. If this does not work, reducing the power to the source sometimes will also fix this condition.

D) The most recent disaster which has occurred is that at some random time during the changeover the color of the plasma will change to a very bright yellow-white color accompanied by a shower of sparks causing severe destruction. Shutting off the discharge at this point one notes that the pressure in the source chamber has increased to greater than 1 torr. After waiting approximately 15 minutes the system will pump itself back to its original pressure. This accident has occurred because a small water leak has opened up in the system. This type of leak is particularly diabolical since it will not leak except at the high temperatures of the discharge. This is due to the leak being caused by a small fracture now expanding open due to the high temperatures yet remains closed at room temperature. These fractures

have appeared in the cooling line in the magnet windings and in the threads of the brass anode housing which holds the nozzle assembly in place. The method to find this tiny crack is to vacuum leak check all cooling lines and, once the crack is located, to reseal it before attempting to use the discharge again.

E) The worst situation which can occur is that the plasma emission becomes far brighter than normal for the stagnation pressure being used. That indicates in general that there is a leak somewhere in the arc source and not enough hydrogen is getting through the nozzle. If the changeover is continued the discharge will become excessively hot and massive damage to the arc source will occur.

Should none of these unfortunate occurrences happen, the argon is slowly turned off over the span of ten minutes. If the current is kept at a constant value of 100 amperes, the voltage will rise from the initial 15 volts to 45 volts when the argon is fully turned off. At times the current will be observed to oscillate, usually because the changeover is occurring too quickly. Lowering the current to 90 amperes and then raising it back to 100 amperes sometimes cure this.

Once the argon flow has been totally turned off and the electric current and hydrogen gas flow have stabilized, a brilliant diffuse crimson red plume is now observed at about a 150 torr stagnation pressure. According to Stwalley<sup>7,12</sup>, who calls the discharge at this time the 'standard' discharge, reducing the H<sub>2</sub> pressure but keeping the input power constant will produce a more intense beam of hydrogen atoms. Indeed, by slowly lowering the H<sub>2</sub> pressure the plasma is observed to go into this 'pencil' mode where the plasma now becomes a very intense white beam surrounded by a diffuse dull red plume. Once the beam is in this mode a much higher flux of hydrogen

atoms is observed, and the pressure in VC2 (Figure 1) is  $\sim 2 \times 10^{-5}$  torr while in VC1 it will be anywhere from 100 microns to one torr, depending on how much use the nozzle has had, and how much it may have changed during the current run. Under these conditions the beam becomes quite stable and may be run indefinitely in this present mode, 5 hours being the longest we have kept it on before deciding to turn it off. After running for about 25 minutes the voltage to the source will appear to drop to a value of  $\sim 30$  volts, and stay at that value for the rest of the run.

Up to this point the beam is operated far away ( $\sim 17$  cm) from the skimmer. Once the plasma has been stabilized the source may be brought closer to the skimmer manually. After it gets within 8 cm there is a dramatic increase in the observed hydrogen atom intensity, which steadily increases as the source is brought closer. This effect is clearly shown in Figure 8 where the neutral  $m/e = 1$  signal is monitored in VC2 (Figure 1) as a function of the skimmer-nozzle separation. Two cm. is the closest the source has ever been to the skimmer without the latter clogging. Normally it is operated 3 to 4 cm. away. However, if the beam is returned to the 'standard' mode, it is possible to get the source much closer without fear of deforming the skimmer. This is undoubtedly due to the plasma temperature's being much lower when there is more gas flowing through the discharge, with the power input remaining constant.

The procedure which has been outlined above provides a reliable routine which 60% of the time (when everything is operational) results in a stable high temperature (pencil) arc source.

## 2.5 Mass Spectrometer

Since the principal method of detection of the neutral species in the beam produced by the arc discharge is by mass spectroscopy, we will now describe the mass spectrometer used in detail, especially since important modifications in its use have been made. The device used was an EAI Quad 300 residual gas analyzer, which ionizes and mass analyzes any species which enter the ionizing region. The quadrupole head assembly [QMS], depicted in Figure 5, performs the function of ionization, mass filtering and ion detection, while the electronics assembly [MSE] provides the necessary voltages to the head. This head is inserted into the bell jar [VC2] where a pressure of  $10^{-5}$  or less is maintained. All electronic connections to the head assembly are made through a 4-inch ID flange containing feedthroughs connecting the inside of VC2 to the outside. These feedthrough are shielded on the external side of the flange by a metal shield in order to minimize any noise pickup.

### 2.5.1 Ionizer

A tungsten filament, .005" in diameter, is heated by a DC power supply which causes it to emit a stream of electrons as shown in Figure 8a. These are accelerated and bombard the species in the region producing positive ions (both parent and fragmented ions) as well as electronically excited species. This source operates at a relatively low ionization efficiency of the order of  $10^{-6}$ . A large percentage of these ions are collected, accelerated and focused by the set of electrostatic lenses (Figure 8b) into the quadrupole rod assembly.

The neutral molecules can enter the ionization region either through the open aperture in the front of the mass spectrometer or through either of the open sides of the hexagonal ionization chamber which has a volume of approximately .4 cm<sup>3</sup>. The beam of electrons is formed by passing through the tungsten wire a DC current of about 1.5 A. The electrons emitted by this resistively heated filament are attracted into the ionization region due to the field produced by biasing the Faraday cage surrounding the ionization region. The energy of these electrons can be controlled by changing the voltage to the filament block. This energy is normally in the 80-90 eV range. In the present setup there are two filament assemblies which face each other outside of the ionization chamber such that, if a filament should break due to high current, high pressure or age, the other filament may be used immediately without having to break vacuum for replacement.

The ionization chamber region has been recently modified in order to allow surface ionization measurements to be made. Two ceramic blocks have been fixed to opposite sides of the ionization chamber such that a metal wire may be suspended down the middle of the ionization region. This wire is

electrically insulated from the rest of the system. As a result the wire in no way impairs the normal operation of the mass spectrometer. When surface ionization measurements are to be made the electron impact filament and the electron accelerating voltage are turned off. The surface ionization wire can now be resistively heated to a temperature which desorbs molecules from it, thereby cleaning it. With only this hot wire in the region, any ions formed must be due to a surface ionization process.

### 2.5.2 Lens System

The Faraday cage operates at a voltage,  $V_c$ , 0 to 40 volts DC with respect to ground. The ionizer assembly and associated electronics are shown in Figure 8a. The ionizing chamber is surrounded on all sides by this Faraday cage. The electronics which supplied the voltage to the cage has been modified such that a negative bias may be applied in the event one should wish to extract and mass analyze negatively charged ions. In addition the circuitry has been modified such that one can completely turn off this power supply such that there is no extraction of ions from this region. When operated in this mode it is possible to substitute an external power supply to provide the potential to the faraday cage. This change was necessary due to wanting to utilize the mass spectrometer to give a crude energy spectrum of the species in the beam (as is explained later in this thesis).

The focusing lens is mounted adjacent to the cage and is electrically insulated from it. Its potential,  $V_f$ , is provided by the ionizer controller and may be varied from 0 to  $-100$  volts with respect to ground. The circuitry for this lens has also been modified to allow the user to change the polarity and hence collect negatively charged ions.

The exit lens is mounted adjacent to the focus lens and is at ground potential. Any ions which pass through it lose  $E_F$ . The system formed by the Faraday cage, the focusing lens and the exit lens extracts the positive ions from that cage, imparts to them a kinetic energy  $E_c = eV_c$  and focuses them on to the axis of the quadrupole rod system. Their final energy as they enter the quadrupole assembly is  $E_c$  plus whatever translation and internal energy they had after being ionized. Ions whose direction make an angle of

as much as  $30^\circ$  with that axis will be properly mass-analyzed, leading to a high transmission efficiency.

For most of the measurements made in this work the mass spectrometer was operated with the potentials to both the focus lens and the Faraday cage (with respect to ground) being set to zero. The reason for this is, since the beam is entering the mass spectrometer axially, all the neutral species in the beam already have a high forward translational energy due to the plasma heating. Hence the neutral beam molecules which are ionized in the mass spectrometer ion source will already be leaving the ionization region with a significant velocity and will need less additional acceleration from the Faraday cage than otherwise. This is to be contrasted with any thermal background gas molecules which are moving in random directions in the bell jar, the most abundant molecule being  $H_2$ . When these background molecules are ionized by the mass spectrometer ionizer, they will have little chance of getting to the quadrupole rods unless they are collected and focused by the lens system. As a result, by having the lens system turned off, all ions stemming from that thermal background are repressed. This is very useful since the mass spectrometer in this system is operated at relatively high pressures, typically  $5 \times 10^{-5}$  torr with the arc source on. The beam signal would otherwise be swamped by such a large background. Working with the ion optics turned off, and the chopper turned on, the ion signal has no AC component showing that this signal originates entirely from species in the beam with no contribution from background molecules.

It should be noted that since we operate the mass spectrometer at a high pressure the lens surfaces, the quadrupole rods, and the ionizer blocks become increasingly dirty with continued use. As a result the signal intensity as well as the mass resolution fall off as a function of time. This necessitates that

at five-month intervals the mass spectrometer be disassembled and cleaned. Such cleaning is done by using a slurry of aluminum oxide and methanol to rub away any colored deposits. Once this is accomplished, the parts are cleaned by ultrasound in a solution of 10% hydrogen peroxide and 10% formic acid. This is then followed by repeated ultrasound rinses in deionized water and in acetone.

### 2.5.3 Filter Rods

The dimension of the quadrupole rods are as follows: length = 125mm, diameter = 6mm. Ceramic spiders or supports electrically separate and define the space between the rods. One can't overemphasize the importance of handling these supports with great care during the assembly and disassembly of the mass spectrometer, since it is their shape and dimensions which completely define the geometry of the cavity formed by the cylindrical rods, and ultimately the mass analysis and resolution. A DC voltage,  $V_1$ , and a superimposed RF voltage,  $V_0$ , are applied to the rods generating an electrostatic field between them given by

$$\Phi = \frac{(V_1 + V_0 \cos \omega t)(x^2 - y^2)}{r_o^2} \quad (2.6)$$

where  $r_o$  is the distance from the pole system axis to the axis of each pole and  $x$  and  $y$  are coordinates of a point with respect to a system of Cartesian axis whose directions are parallel to lines connecting the centers of adjacent poles. These poles are shown in Figure 8a. As the ions pass through this field they will undergo spiralling trajectories defined by appropriate Mathieu equations. The effect is that for some ions the radius of the trajectory increases without bound until it collides with a metal surface and is removed from the system. However, ions with constant radii will traverse the pole region, and emerge. By shifting the parameters of the field one can filter the ions in order of increasing atomic mass.

The mass analysis may be run in two modes, auto and manual. In the auto mode a DC sawtooth potential is applied to the rods such that a series of masses are scanned, the width and starting position of the spectrum being

determined by the settings of the RF-DC generator. The manual mode is used to continuously monitor a single peak, the mode in which most quantitative measurements were made in these experiments. In this mode the RF-DC generator provide constant RF and DC voltages. Ions of only a particular mass are then selected through the quadrupoles. The DC ion signal that will be observed is proportional to the intensity of that molecular species in the beam. As one changes the center mass control of the RF-DC generator, the observed DC level undergoes changes as each successive mass peak is selectively tuned.

## 2.5.4 Detection Electronics

### *2.5.4a Electron Multiplier*

The ion detector is a 16 stage windowless beryllium-copper electron multiplier and consists of 15 multiplying dynodes and a final electron collector anode. Positive ions which make it through the mass analyzer strike the first dynode, and if they have sufficient energy will cause electrons to be emitted from it. This process is repeated through 15 successive stages, the net result being the production of a large number of electrons for each positive ion which originally struck the first dynode such that gains of the order of  $10^6$  are easily achieved. The first dynode is typically operated at  $-2.2$  kV with respect to ground and the voltage drop between successive dynodes is approximately 214 volts, thus creating this electron cascade.

The multiplier we used originally had been exposed to air for extensive periods of time. Even with its poor sensitivity, it had to be operated at a reduced voltage ( $\sim 2$  kV) due to the high intensity of the beam. Eventually its gain dropped sufficiently for it to become unusable. Upon removal it was observed that the first dynode was severely discolored, probably due to ion sputtering.

The multiplier was replaced with an ITT F5074 one, and it was with this device that the majority of the measurements described in this thesis were made. Its gain and dark current characteristics are listed in Table I. The increased sensitivity of this multiplier proved to be a hindrance due to its ability to act as a 15 stage photomultiplier with the first dynode operating as a UV sensitive cathode. Since the plasma acts as a bright light source the multiplier was being saturated by the light that was able to get through the

**TABLE I****Characteristics of Electron Multiplier (as of 8/28/80)**

Voltage Applied (V)	Gain	Dark Current (A)
2000	$3.0 \times 10^5$	$1.6 \times 10^{-13}$
2300	$1.4 \times 10^6$	$7.0 \times 10^{-13}$
2600	$5.0 \times 10^6$	$2.1 \times 10^{-12}$
2900	$1.2 \times 10^7$	$6.0 \times 10^{-12}$
3200	$4.2 \times 10^7$	$1.5 \times 10^{-11}$

skimmer and subsequently pass through the mass spectrometer. As a result, it was necessary to physically offset the axis of the multiplier from the center axis of the mass spectrometer. Light then was not able to directly strike the first dynode, but the ions would still be attracted by the negative potential placed on it. Offsetting it by approximately 2 cm proved to significantly decrease the DC background due to the light without significantly decreasing the ion signal. However, there was still a background signal attributed to light entering the multiplier enclosure and scattering within that enclosure in a way that permitted a small amount to still strike the first dynode. This last problem was finally alleviated through the mounting of a 1 cm<sup>2</sup> piece of lucite<sup>©</sup> painted black where the first dynode had been. Any light which now enters this chamber strikes the black plastic and is absorbed.

With this new multiplier installed the electronics were slightly modified such that it could now operate in two modes. The first is the normal mode by which the multiplier acts as a high-gain amplifier. The second allows for the direct measurement of current to the first dynode through the use of a Keithley 602 solid state electrometer. By measuring this current with the mass spectrometer operating in the manual mode, one can directly measure the ion current impinging on that dynode and can from this information get an absolute number density of a particular molecular species present in the beam, as described in Section 3.2 .

#### *2.5.4b ESA 75 Electrometer*

This electrometer is a solid-state electrometer amplifier attached to the anode (i.e., last dynode of the electron multiplier) and is capable of measuring currents from  $10^{-4}$  to  $10^{-12}$  A (Figure 5, PA). The input stage consists of a differential J-FET, which provides high input resistance ( $10^{14}$  ohms or

greater) to the signal being measured. Typically operated, a signal of  $10^{-10}$  A will produce a 100 mV signal at the output. Care must be taken to avoid excessively large input currents since its transistors will then burn out, as occasionally happened. Also the electrometer should be firmly mounted since it will act as a microphone and any small vibration will create observable noise in the output signal.

#### *2.5.4c Lock - In Amplifier*

All the AC measurements reported in this thesis were made using a Princeton Applied Research precision lock-in amplifier model HR-8 attached to the exit of the electrometer (Figure 5, LI1). This amplifier is essentially a detection system capable of operating with an extremely narrow equivalent noise bandwidth. Its function is to select a narrow band of frequencies from a signal spectrum applied to its input and to convert it to a DC signal proportional to the amplitude of the AC signal at the selected frequency. The basis element of the amplifier is a phase-sensitive reference. In our case the synchronous reference is provided by the output of a photo diode facing the mechanical chopper which chops the beam at a frequency of  $\sim 8$  hz. Opposite that diode, on the other side of the chopper, is a small photon-coupled diode emitter, which provides the light input to that photo diode. By using a time constant for the lock-in output of  $\sim 3$  sec the effect of input noise on that output is made very small. As a result, the output becomes a dc level proportional to the fundamental component of the input signal at the chopping frequency with the noise averaging to zero. This achieves a large signal-to-noise ratio improvement. In our case it permits us to distinguish the molecules in the beam from background since they are the only species being chopped at the frequency to which the amplifier is tuned.

#### *2.5.4d Time Averaging Computer*

For the later experiments reported in sections 4.4, 4.5, and 4.6 of this thesis all the results were taken using a Varian Associates C-1024 Time Averaging Computer (CAT) (manufactured by Technical Measurement Corp.) in lieu of the lock-in amplifier. The CAT operates as follows: when a spectrum of interest is swept repeatedly the signal accumulated into memory channels in proportion to the number of sweeps, while the random noise is proportional to the square root of the number of sweeps. Thus, the signal-to-noise ratio of the information in the memory is increased proportionally to the square root of the number of sweeps. The reason that the noise component increases more slowly than the signal is due to its inherent randomness.

Normally this type of device is used to increase the sensitivity of an NMR or EPR experiment. We have adapted it to our system to increase the speed of our mass spectroscopy measurements. Normally, when using the C-1024 with an NMR or EPR spectrometer, a search ramp voltage is generated to sweep the field such that the computer samples 1024 voltages while scanning its memory on a linear time basis. Each new sweep adds signal to the stored information. Thanks to a circuit built by Tom Dunn of our electronics department, we were able to slave the C-1024 to the sweep of the mass spectrometer. The C-1024 is then sequenced to sweep concurrently with the mass spectrometer sweep, and the time-versus-spectrum coherence is maintained for both. As a result, instead of sitting on one peak (in the manual mode) and measuring the ac signal via the lock-in amplifier (as we had done previously), the entire mass spectrum may now be scanned repeatedly with the same gain in signal-to-noise that was previously achieved by using a large time constant with the lock-in and sitting on a single peak. Now these measurements may be performed much more rapidly with the added

advantage of always being able to observe all the mass peaks of interest.

### 2.5.5 Alignment

One of the largest problems concerning the use of this arc-heated beam has been the alignment of the different elements of the apparatus. Due to the temporary nature of the bell jar and test stand which supports it (see Figure 1), it is difficult to preserve the alignment of the device for long periods. Part of the problem is in the flex tubing which connects the bell jar to the source chamber. While the two stands of Figure 1 are firmly clamped together the bell jar, sitting on top of an O-ring seal, may rotate around its vertical axis during successive openings and closings of the system due in part to that tubing's flexibility. In an attempt to control this motion, adjustable retaining rods are placed around the flex tubing to prevent any bending during the initial pump down. Despite these precautions the entire system still needs to be realigned on a regular basis. The difficulty of this alignment is increased when using the gas chamber discussed in Sections 4.5 and 4.6, because the beam must be threaded through the apertures of that chamber before arriving at the mass spectrometer.

The alignment procedure consists of removing the cathode assembly from the arc source but leaving the nozzle assembly inside the magnet. By placing a mirror inside VC1 (Figure 1) it is then possible to sight directly through the nozzle and skimmer apertures and into the bell jar chamber. A high intensity lamp is hung in the bell jar chamber to provide illumination of the interior. A precision optical surveying instrument, the Wild N 3, is used to do all the sighting. The Wild N 3 is set to a horizontal position and is then sighted on the skimmer and the nozzle through the mirror. While the skimmer is fixed to the wall of the VC1 chamber by an O-ring seal, the nozzle may be

moved with respect to the fixed skimmer. This crude motion (Figure 5, TA) is provided by two adjustable screws upon which the end of the translator stage sits. By adjusting these screws one can move the nozzle up and down and side to side with respect to the skimmer. However, this adjustment is quite crude and time consuming. Once the source is used in conjunction with the 50-inch bell of the crossed molecular beam apparatus, it will be necessary to redesign this assembly to provide a more reliable means of alignment.

Once the scope, the nozzle, and the skimmer are aligned, then these parts are removed and it is now possible to sight directly into the bell jar region itself. By lifting up that bell jar (Figure 5, VC2) it is possible to manipulate the flag, chopper, deflection plates (which are attached to the base of the jar) and align them with the scope. The mass spectrometer itself however is directly fixed to the bell jar itself through one of the six inch ports. When pumped down the bell jar will be in contact with the metal surface of the base but at atmospheric pressure it will ride on the O-ring. As a result, with the O-ring in place the mass spectrometer will appear higher than it will actually be under vacuum. To perform the alignment of the mass spectrometer the bell jar is first lowered into place with the O-ring absent to compensate for the additional height. The mass spectrometer is then aligned with the sighting scope by moving the stand itself via its adjustable legs. Once this is accomplished the bell jar is again lifted and the O-ring is now put into place. The bell jar is then lowered again and the test stand is securely fixed to the diffusion pump stand. The mass spectrometer can now be aligned in the other two dimensions by push-pull screws which are mounted on top of the stand. Through the use of these screws it is possible to move the bell jar, with respect to the fixed stand, which is now rigidly fixed, since it is still riding on top of the O-ring, making the bell jar quite easy to move.

The last part of this procedure is to replace the nozzle and skimmer in VC1 and check that the scope is still sighted along their apertures. This ensures that the scope has not been moved during the course of the alignment of the rest of the instrument. This completes the alignment and the system may be closed up to be pumped down. Despite precautions, many times there will be movement of either the bell jar or of some object within it during the pump down. This is detected as a reduced signal at the mass spectrometer even though the discharge beam appears operational. When this occurs the entire alignment procedure must be done again.

## 2.6 References

1. E. L. Kunth, N. M. Kuluva, and J. P. Callinan, *Entropie*, **18**, 38 (1967).
2. W. L. Fite, Research Note #1, Extranuclear Laboratories Inc., January 1971.
3. J. B. Anderson, R. P. Andres, and J. B. Fenn, in *Advances in Chemical Physics*, J. Ross, ed., Vol. X, Chapter 8, Interscience Publishers, N. Y. (1966).
4. E. L. Kunth and N. M. Kuluva, *Recent Advances in Aerothermochemistry*, May 16, 1966.
5. K. Bier and B. Schmidt, *Z. fur angewandte Physik*, **13**, 493 (1961).
6. F. S. Sherman, Technical Report, Fluid Mechanics 6-90-63-61, Lockheed Missles and Space Co., Sunnyvale, Ca., May 23, 1963.
7. K. R. Way, S.-C. Yang, and W. C. Stwalley, *Rev. Sci. Instrum.*, **47**, 1049 (1976).
8. E. L. Kunth, *Applied Mechanics Rev.*, **17**, 751 (1964).
9. E. L. Kunth, UCLA Department of Engineering Report #66-19 (April 1966).
10. W. S. Young, W. E. Rodgers, and E. L. Kunth, *Rev. Sci. Instrum.*, **40**, 1346 (1969).
11. R. Gotting, H. R. Mayne, and J. P. Toennies, *J. Chem. Phys.*, **80**, 2230 (1984).

12. K. R. Way, S.-C. Yang, and E. C. Stwalley, *Abstracts of the IXth International Conference on the Physics of Electronic and Atomic Collisions*, Univ. Washington P., Seattle, 957 (1966)
13. K. R. Way, S.-C. Yang, and W. C. Stwalley, *Operation of a Superthermal Arc-Heated Hydrogen Atom Source*. This film may be rented from Media Library Audio Visual Center, University of Iowa, Iowa City, IA 52242, Catalog No. U-30354.
14. K. R. Way, S.-C. Yang, and W. C. Stwalley, United States Energy Research and Development Administration Report COO-2326-11 (11 February 1976). Alternatively, see AIP document No. PAPS RSINA 47-1049-17 for 16 pages of arc documentation material.

## 2.7 Figures and Captions

Figure 1. A side view of the vacuum system: VC1, vacuum chamber one, the source chamber; P1, viewport; P2, viewport and gas pipe support; unistrut, mechanical coupler; VC2, vacuum chamber 2, the diagnostics chamber.

Figure 2. Cutaway view of arc-heated source: 1, exit aperture; 2, anode housing; 3, water cooling inlet/outlet/ ports; 4 source gas chamber; 5 O-ring insulator and vacuum seal; 6 cathode support; 7, flexible bellows; 8, cathode; 9 cathode water cooling channel; 10 cathode tip.

Figure 3. Scale drawing of cathode assembly: A, hollow tube; B, tungsten cathode rod; C, set screw; D, support structure; E, bellows; F, outside casing. The view of the cathode is a cross-sectional cut permitting a view of both sets of teflon screw holes in the support structure. Originally the assembly was made out of brass but is now made out of stainless steel.

Figure 4. Exploded view of anode assembly: A, threaded copper top; B, tungsten anode; C, threaded copper bottom; D (1 and 2) brass anode housing; E, macor<sup>©</sup> cylinder.

Figure 5. A schematic view of the top of the machine: VC1, vacuum chamber one; AS, anode assembly; A, anode; C, cathode; M, magnet; Sm, water-cooled copper skimmer; TA, translation assembly; T, translator; P1, viewport; L, optical lens; C2, 150 Hz chopper; monochromator, 0.5 m Jarrell-Ash monochromator; PM, photomultiplier; CP, current preamp; L12, lock-in amplifier; SCR2, strip chart recorder; VC2, vacuum chamber

2; C1, 10 Hz chopper; D, electric field deflectors; F, mechanical flag; QMS, quadrupole mass spectrometer; P2, port; PA, EAI preamplifier (ESA-75); LI1, lock-in amplifier; MSE, mass spectrometer electronics; SCR1, strip chart recorder.

Figure 6. a) Water-cooled aluminum base mounted to side wall of VC1 with copper mount in place in aluminum base. Side wall is shown by slanted lines b) Copper skimmer which is mounted on aluminum base via the copper mount.

Figure 7. Cross section of electromagnet showing cooling coils. The anode (nozzle) sits snugly in the center of the magnet with the nozzle positioned roughly in the middle.

Figure 8. AC  $m/e = 1$  signal measured by mass spectrometer in VC2 as a function of skimmer-nozzle distance in VC1. Ion signal is the difference of the signal with the electron impact ionizer on and off at each nozzle skimmer distance. Stagnation pressure = 70 torr.

Figure 9. a) Combined semi-schematic and pictorial diagram showing the axial beam ionizer and the filter rods of the Quad 250A Analyzer. b) Schematic of ionizer assembly showing gas molecules entering the Faraday cage.

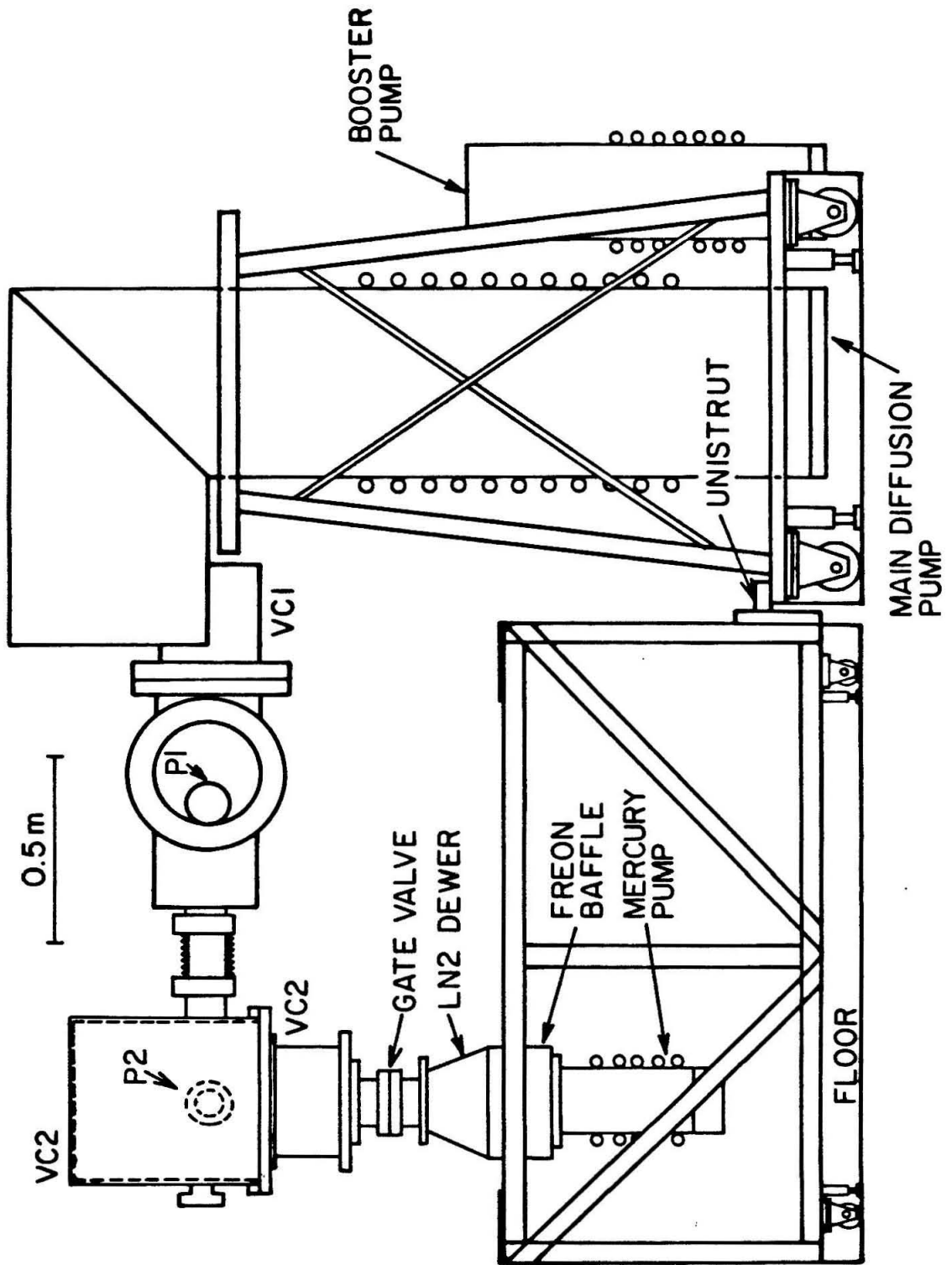


Figure 1

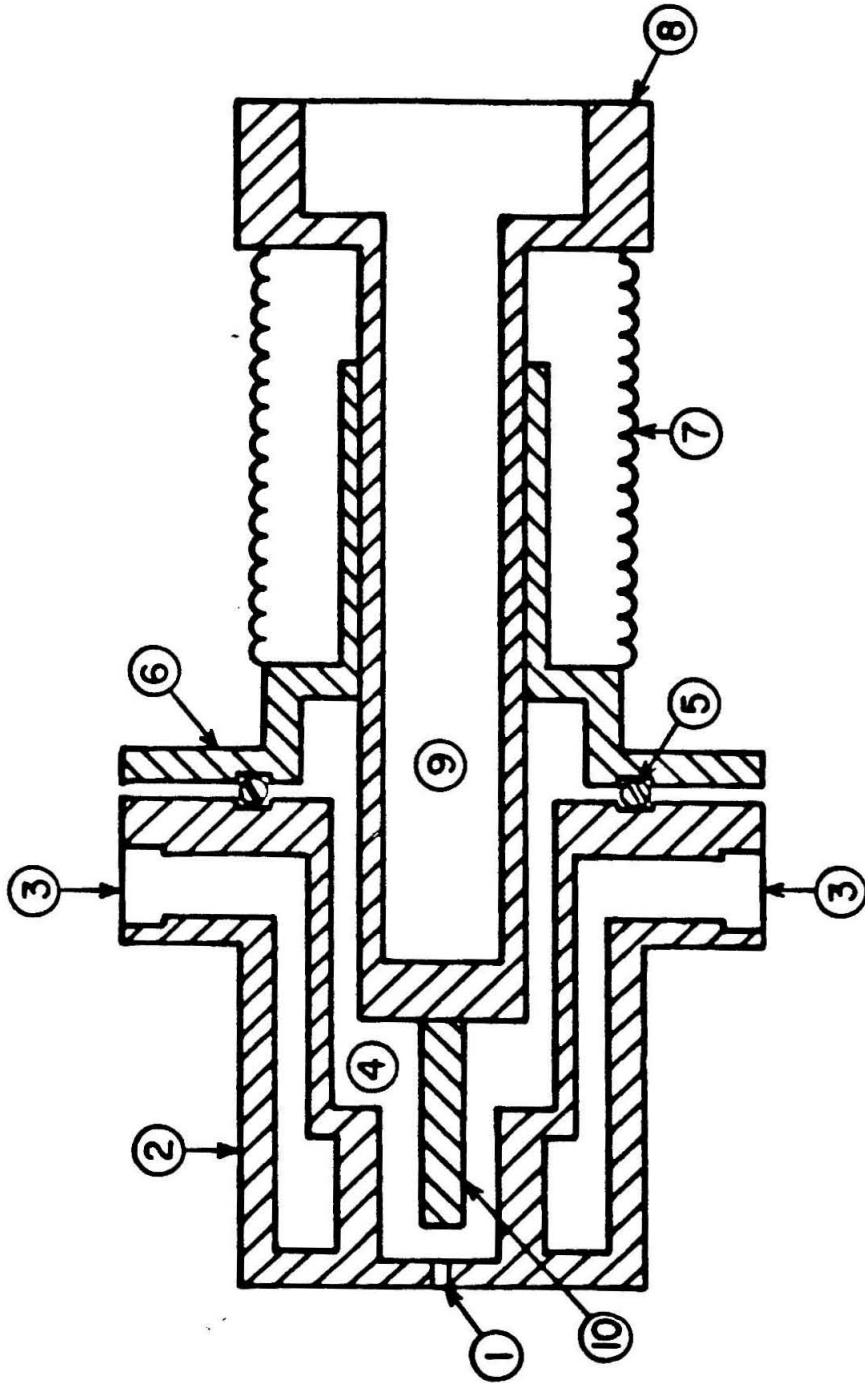


Figure 2

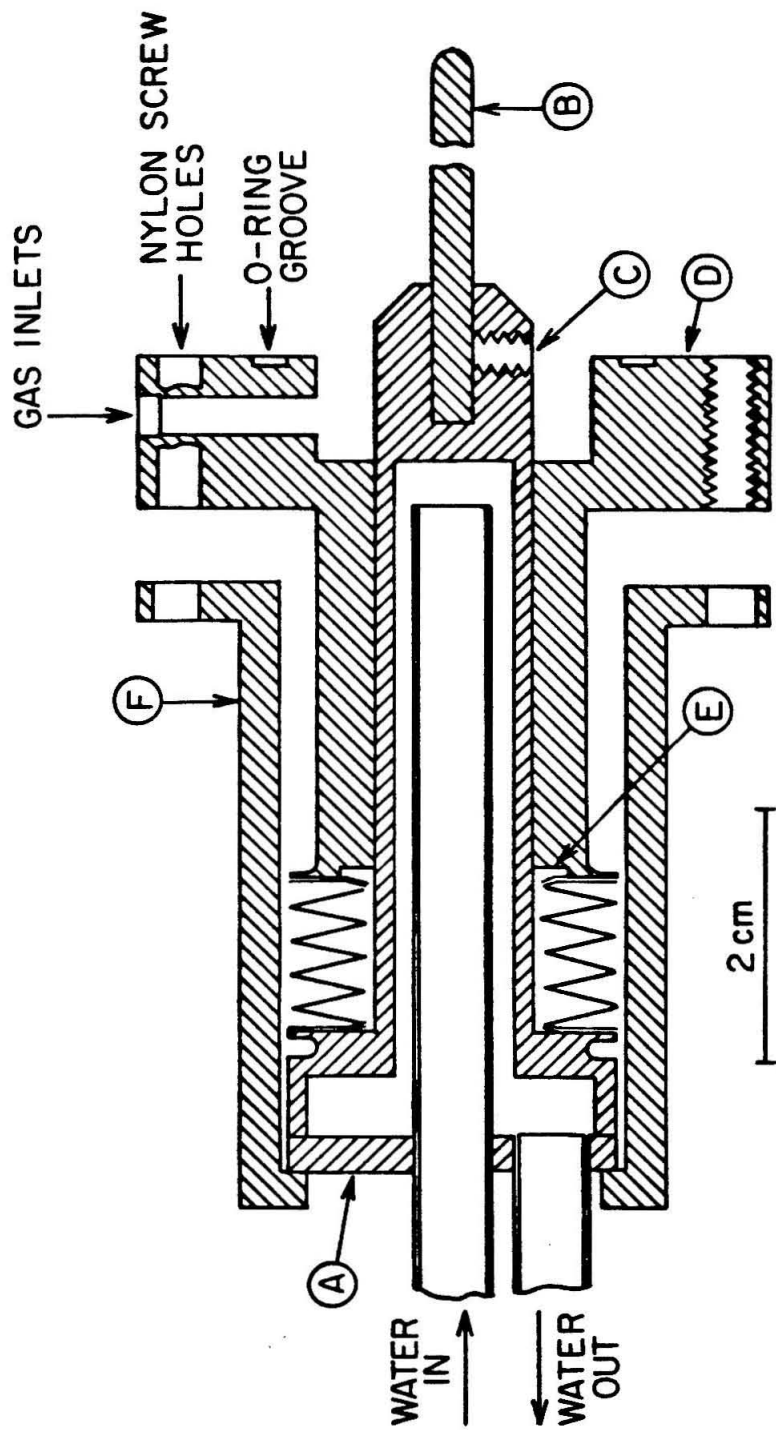


Figure 3

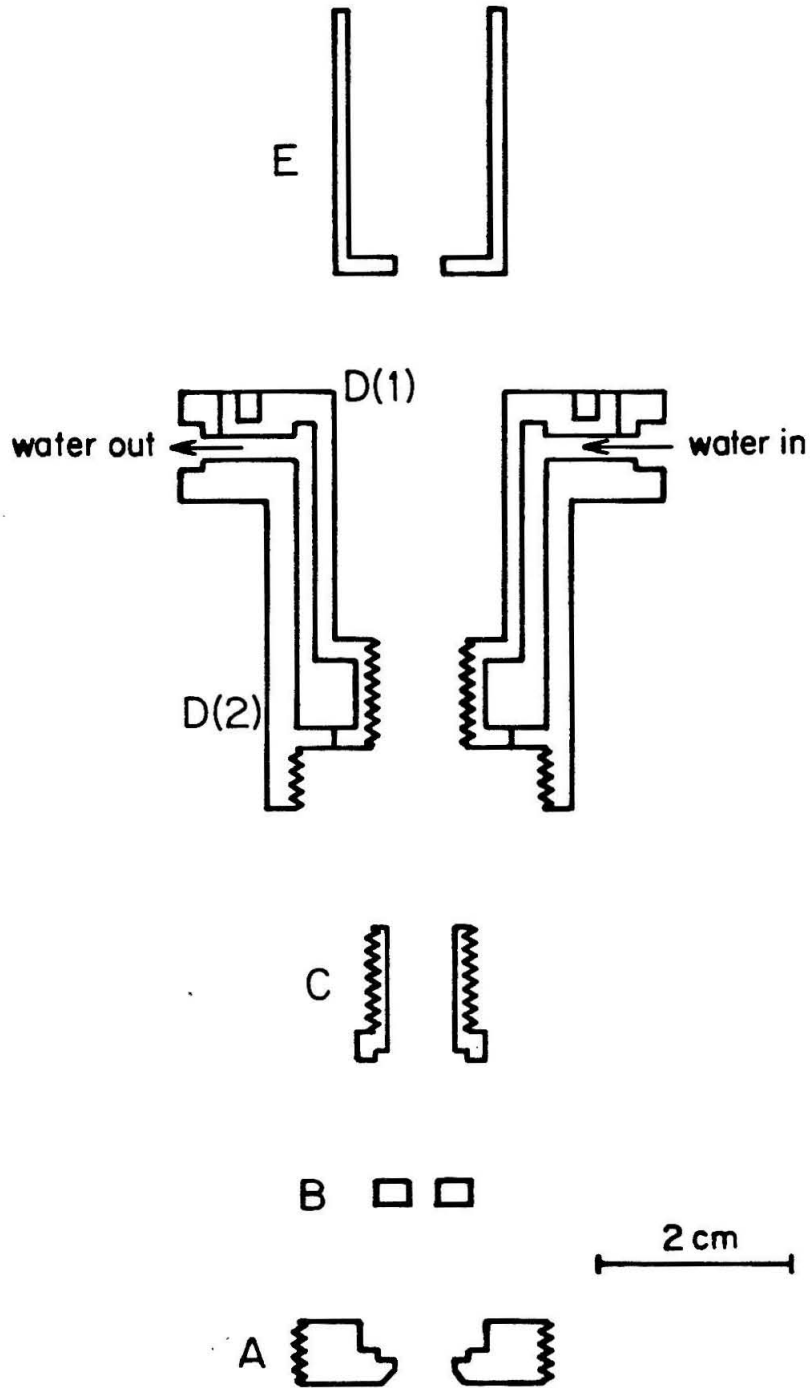


Figure 4

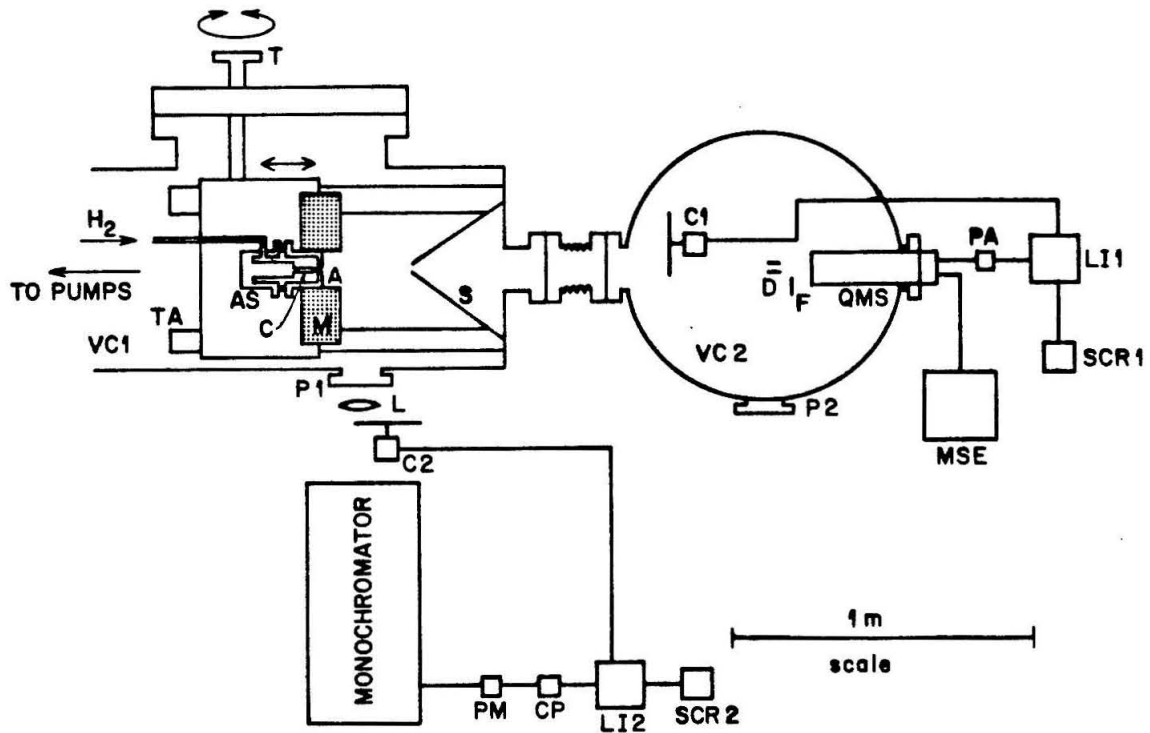


Figure 5

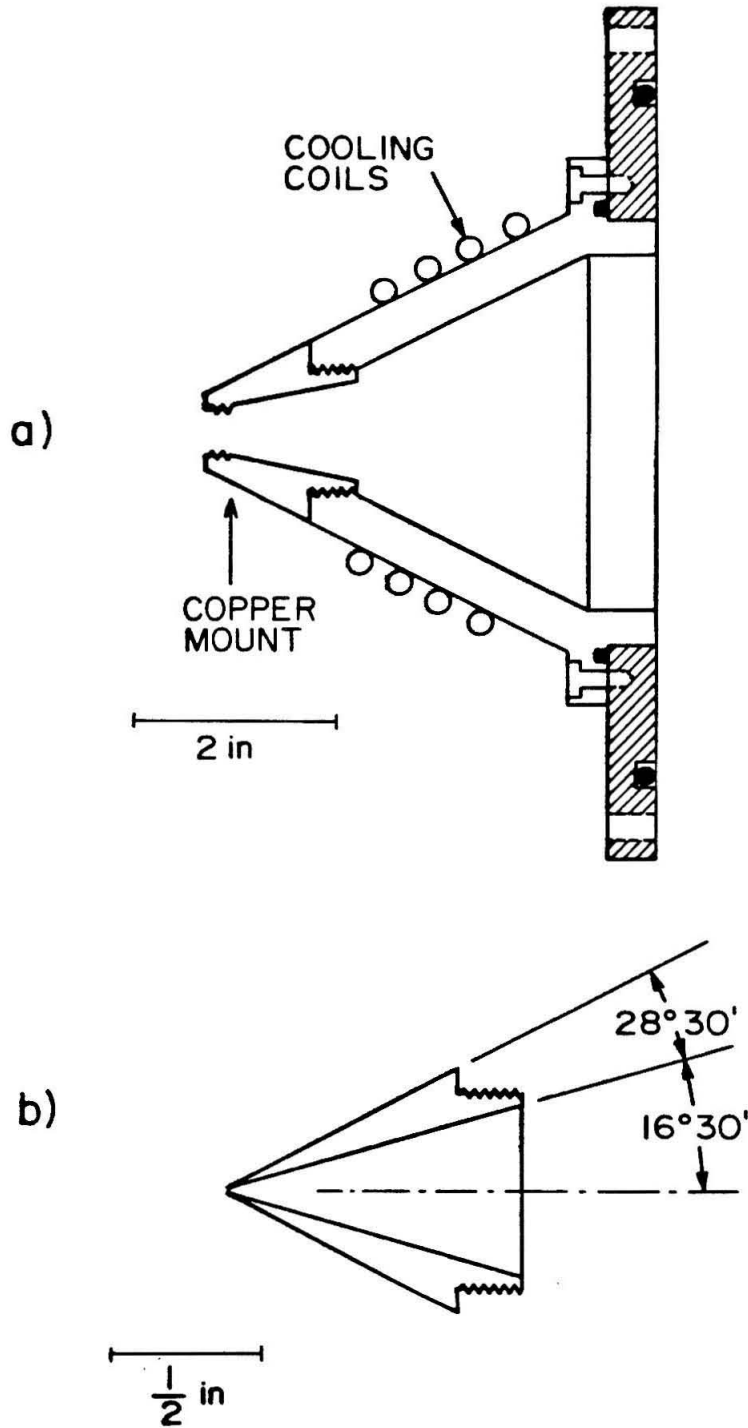


Figure 6

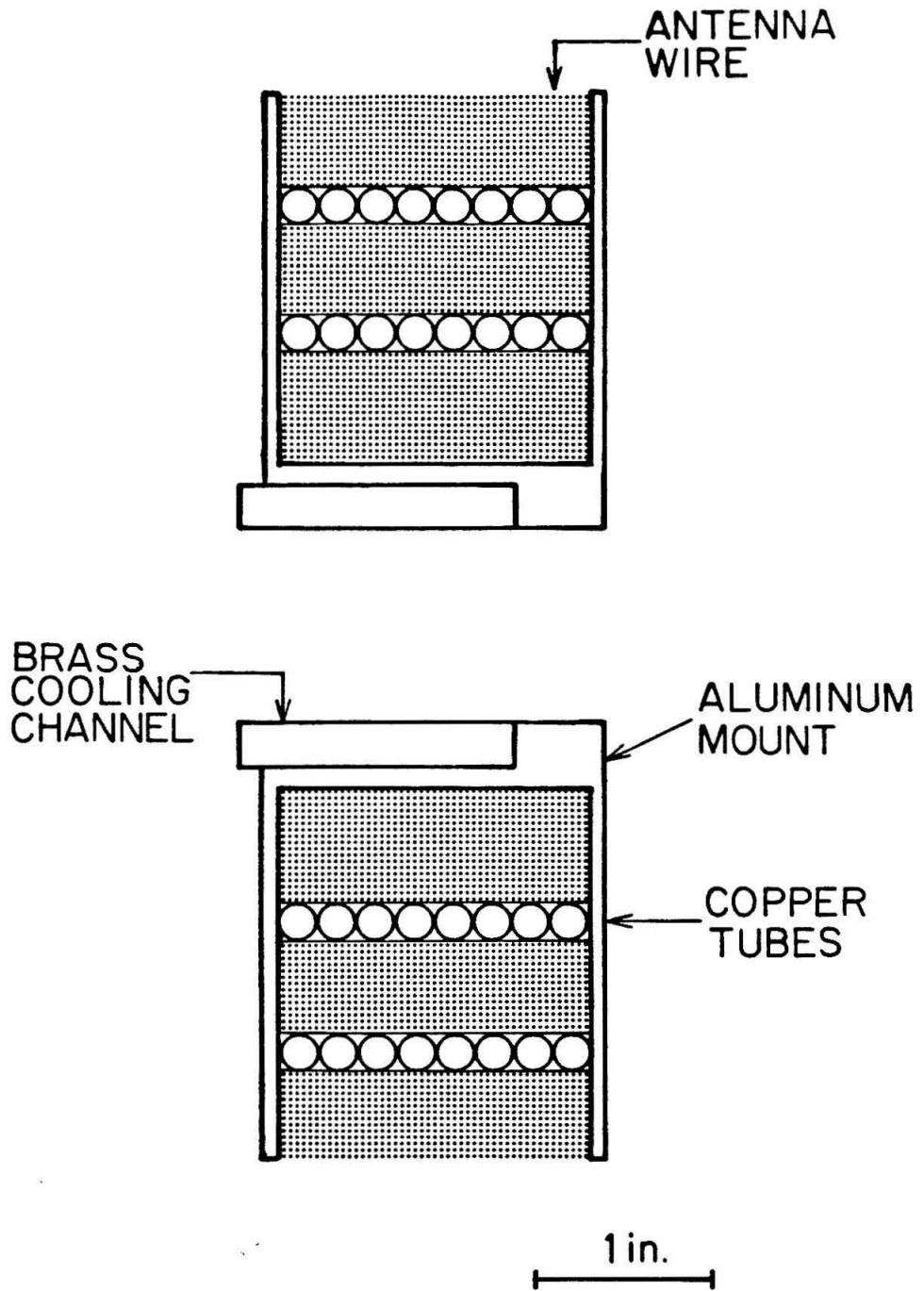


Figure 7

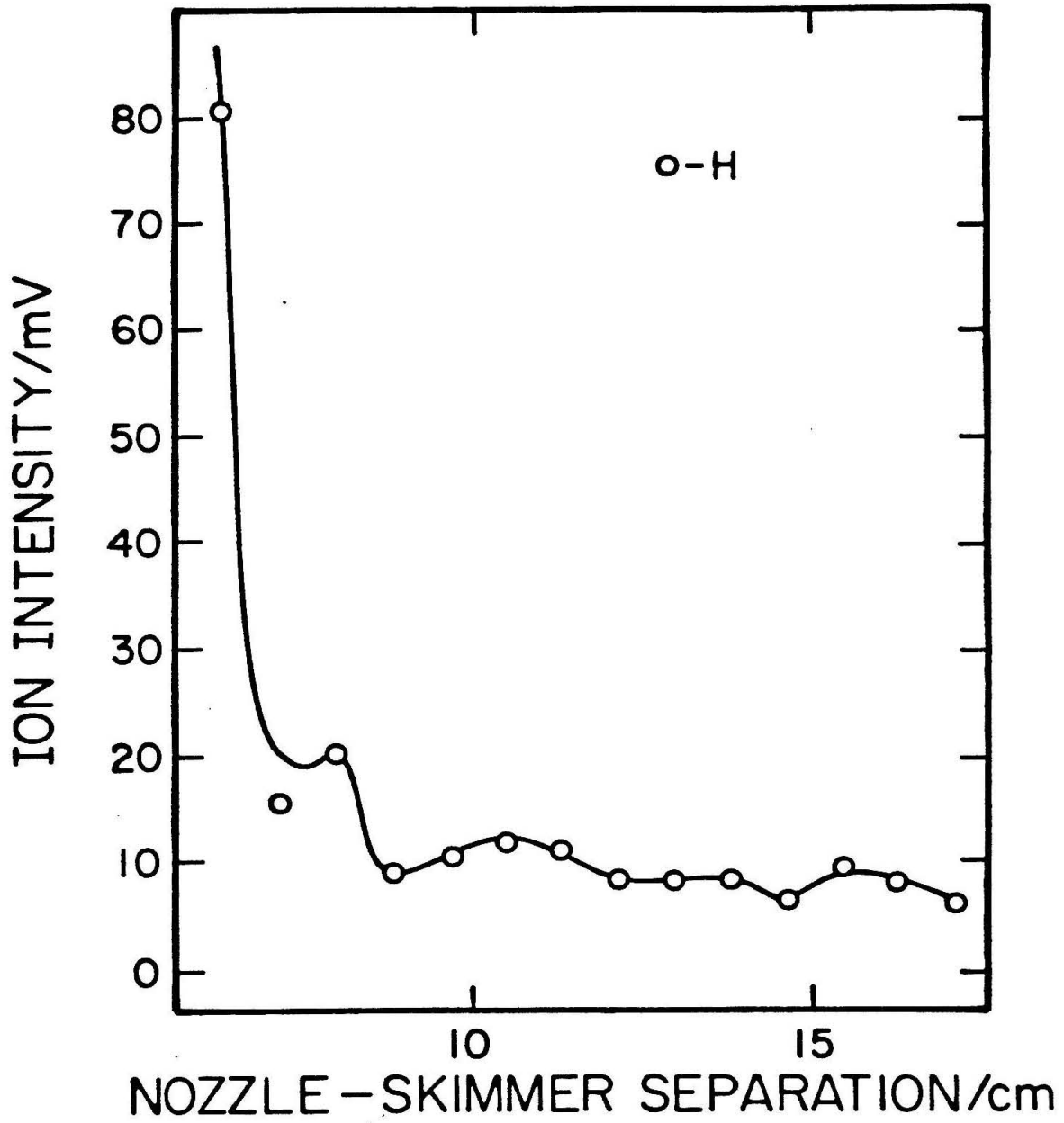


Figure 8

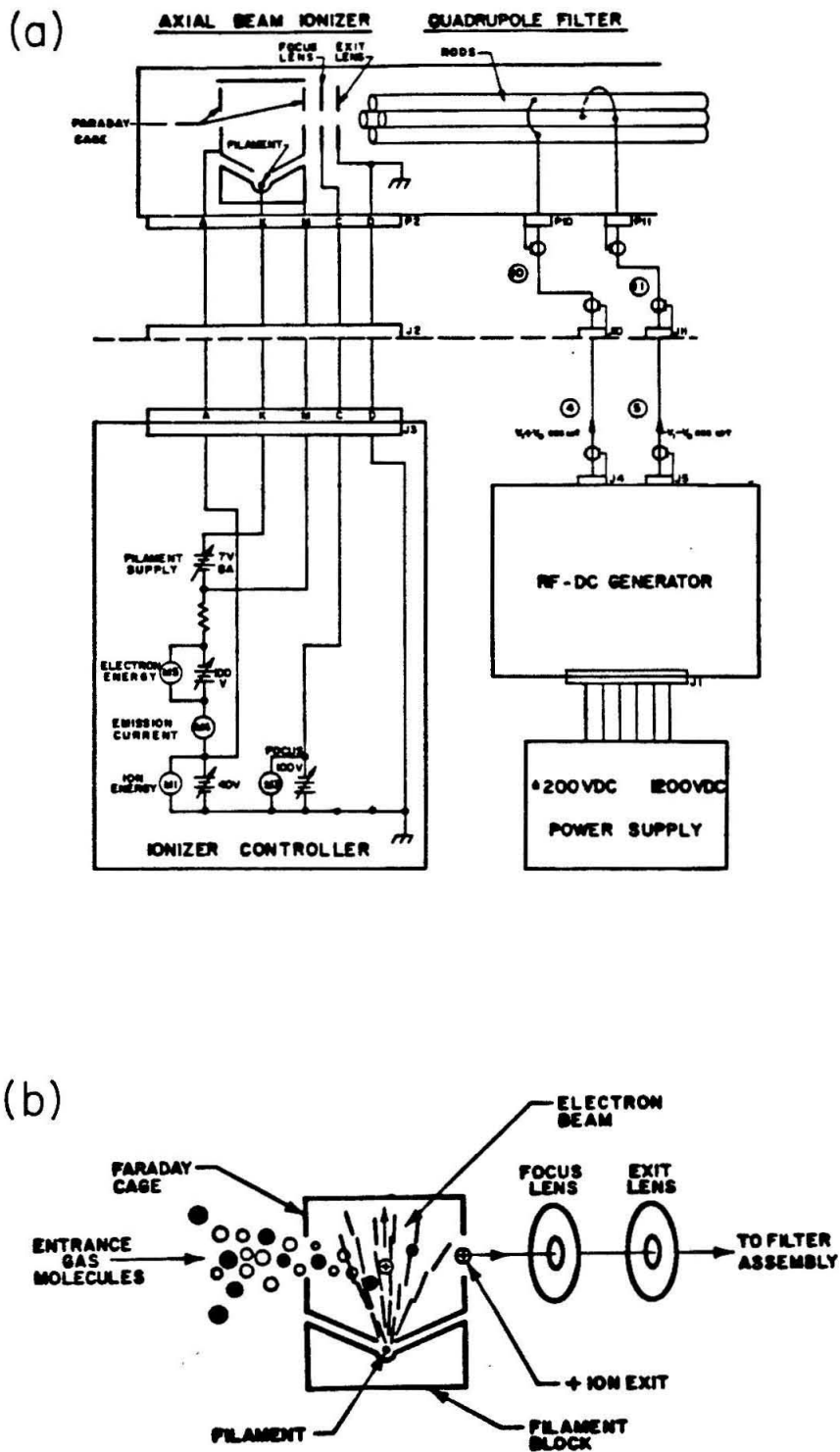


Figure 9

### **3. Results and Discussion for H Atoms**

#### **3.1 Effects of Electric Fields**

The presence of any ions in the beam will present severe difficulties in the use of a mass spectrometer to characterize the beam. This is due to the fact that approximately only 1 in every  $10^6$  neutral molecules is ionized in the mass spectrometer electron bombardment ion source and subsequently detected while every ion present in the beam before entering the mass spectrometer will also be detected and therefore the ion to neutral relative detection sensitivities is about  $10^6 : 1$ . As a result, it is easier for the signal due to external ions to mask that due to the neutral specie. In order to effectively eliminate the ions from the beam before they reach the mass spectrometer, an electrostatic field perpendicular to the beam direction is placed in the path of the beam. This field is produced by a pair of deflection plates and their position is indicated in Figure 1d (size of plates not to scale but exaggerated in the drawing for clarity). They consist of two pieces of .005" thick copper having dimensions of .450" by 1", and are separated by a 0.5 cm gap through which the beam passes.

Any species having a charge  $e$  passing through a field  $\Phi$  experiences a force in the direction of that field given by

$$F = e\Phi. \quad (3.1)$$

This results in a deflection of ions in the beam equal to

$$x = \frac{1}{2} \frac{eV}{md} \left( \frac{l}{V_t} \right)^2 \quad (3.2)$$

where  $V$  is the potential difference between the plates,  $l$  is the length,  $d$  is the gap between them,  $V_t$  is the translational velocity of the ions and  $m$  the mass of the ions. For our conditions this results in

$$x = .1249 \frac{m\Phi}{E} \quad (3.3)$$

where  $m$  is the mass of the species (in units of the hydrogen atom mass),  $E$  is the energy of the ion in eV,  $\Phi$  is the deflection field in volts/cm and  $x$  is the deflection in cm. For example, a proton with an energy of 25 eV passing through a field of 800 V/cm will have undergone a deflection of 1 cm away from the beam axis by the time it emerges from the deflection plates, indicating that a major fraction of the ions should be eliminated from the beam.

This field will also quench any metastable 2s hydrogen atoms which may also be in the beam, as the Stark effect from the electric field mixes the  $2^2S_{1/2}$  and the  $2^2P_{1/2}$  states of the H atom. Thus the atom can radiate to the ground  $1^2S_{1/2}$  via the P state. Though Stwalley reported not observing any metastables<sup>1</sup> the fields we used are large enough to quench any which may be generated.

To measure how effective these deflection plates are in cleaning ions out of the beam the DC ion intensity at  $m/e = 1, 2,$  and  $3$  was monitored as a function of applied field. The mass spectrometer was operated in the manual mode and tuned to a particular mass peak with the ion energy lens and the focus lens turned off to discriminate against the thermal background signal. The intensity of the peak was then recorded as a function of deflection field and is shown in Figures 2, 3, and 4. In the case of  $m/e = 1$  and  $3$  the same effect is observed, a rapid drop-off in intensity until approximately 500 V/cm, after which the intensity decreases much more slowly with increasing fields.

(The origin of the peak at  $m/e = 3$  is extensively discussed in Section 4.) Apparently after this point a majority of the ions have been swept out of the beam leaving the signal due mainly to neutral species. Fields greater than 1000 V/cm are not possible with the present set-up due to the relatively high pressure in VC2 which causes electric breakdown and arcing between the plates. By measuring the intensity of the ions with and without the electron impact ionizer on we can estimate the amount of ions in the beam, assuming that 100% of the ions are detected. From this assumption we are able to infer that positive ions compose less than .01% of the total beam composition, even before ion clean-up by the deflection field.

### 3.2 Absolute Intensity Measurements

An estimate of the total H-atom neutral beam intensity was made by measuring the  $m/e = 1$  DC ion current to the first dynode of the Cu-Be electron multiplier detector of the quadrupole mass spectrometer. This was done with the mass spectrometer operating in the manual mode and tuned to the mass peak of interest. Background was corrected for by either tuning off the peak and noting the drop in intensity, or inserting a mechanical flag into the path of the beam. The intensity of the  $H_2$  molecules in the beam is small and does not significantly contribute to the observed  $m/e = 1$  ion current. This current on occasion could be made as strong as a nanoampere but was usually operated in the  $\sim 1-5 \times 10^{-10}$  ampere range. The experimental conditions which pertained during these measurements are tabulated in Table I. The translational energy distribution function of these H atoms was crudely measured by a retardation potential measurement as described in Section 3.3, and extends from thermal energies to beyond 10 eV. For normal operating conditions (Figure 6b) its peak is at about 8 eV.

The mass spectrometer has a single-pass electron bombardment ionizer and is not very efficient. From the values contained in Table I we obtain a current of neutral H atoms into the ionizer of the mass spectrometer of

$$I_H = \frac{\pi v d I_+}{4 \sigma I_e} = 9.1 \times 10^{16} \frac{\text{H - atoms}}{\text{sec}} \quad (3.4)$$

where  $I_+$  is the measured ion current,  $d$  is the diameter of the neutral beam in the ionizer region,  $I_e$  is the electron beam current,  $E_e$  is the electron beam energy,  $v$  is the average velocity of the H atoms, and  $\sigma$  is the cross section for ionization of the H atoms by electron impact. The ionizer is at a distance of

**TABLE I****Intensity Measurements**

$I_+$	=	ion current at $m/e = 1 : 5 \times 10^{-10}$ A
$d$	=	diameter of H beam in mass spectrometer ionizer region : 3.2 mm
$I_e$	=	electron beam current : 70 $\mu$ amp
$E_e$	=	electron beam energy : 80 eV
$v$	=	velocity of H atoms at average energy of 8 eV : $3.9 \times 10^6$ cm/sec
$\sigma$	=	ionization cross section of H atoms by 80 eV electrons <sup>2</sup> : $0.66 \times 10^{-16}$ cm <sup>2</sup> .

1.0 m from the skimmer. The entrance aperture into that ionizer of 3.2 mm diameter therefore subtends a solid angle of  $8.0 \times 10^{-6}$  steradians as viewed from the skimmer aperture (whose own diameter is 1 mm). The resulting H atom beam flux per unit solid angle is

$$j_{\Omega} = 1.3 \times 10^{22} \frac{\text{H-atoms}}{\text{sec} \times \text{sterad}}. \quad (3.5)$$

If, instead of an H atom average energy of 8 eV we used 1 eV, this estimated average flux would still be  $4.6 \times 10^{21}$  H-atoms/sec $\times$ sterad. These measurements were performed over a period of several months, and fluxes of this order of magnitude were systematically obtained.

This value of  $j_{\Omega}$  is extremely high and merits some discussion. The number density of H<sub>2</sub> molecules at 70 torr pressure is  $2.4 \times 10^{18}$  molecules/cm<sup>3</sup>. Assuming all of these molecules, in the vicinity of the nozzle aperture, to have been dissociated (so their number density would be about  $4.9 \times 10^{18}$  atoms/cm<sup>3</sup>) and assuming that they have the speed given in Table I the rate at which they strike a 1 mm<sup>2</sup> aperture is  $1.9 \times 10^{23}$  atoms/sec. This is an estimate of their rate of effusion through that aperture. The focusing effect of the electromagnet and, to a certain extent the hypersonic nature of the expansion into the area between the nozzle and the skimmer, tends to produce significant collimation. The glow from the plume in that region suggests that a major fraction of the atoms is emitted within a cone whose half-angle is 50°, corresponding to a solid angle of 0.35 sterad. Assuming that half of the H atoms are emitted isotropically into that cone gives an intensity per unit solid angle of  $2.7 \times 10^{23}$  H-atoms/sec $\times$ sterad into that forward cone, indicating that our measured value of equation 3.5 is not absurdly high. Stwalley and coworkers<sup>1</sup> determined a lower bound of  $4 \times 10^{17}$  hydrogen atoms sr<sup>-1</sup>

$\text{s}^{-1}$  and an upperbound of  $10^{20}$  hydrogen atoms  $\text{sr}^{-1} \text{s}^{-1}$  for their beam conditions. The lower limit was set by their bolometer detector condition while their upper limit was set by their input  $\text{H}_2$  rate. Likewise Toennies and co-workers<sup>3</sup> determined their D atom intensity to be typically  $4 \times 10^{19}$  atoms  $\text{sr}^{-1} \text{s}^{-1}$ , though they did not explain how this intensity was measured.

We can indicate the reasonability of our intensity measurement by measuring the flow rate of hydrogen gas into the system while the arc discharge is running and comparing it with the measured intensity at the mass spectrum. While running the arc discharge at a stagnation pressure of 60 torr the flow rate of hydrogen gas into the system was measured to be 2 SCFH as measured by a Dwyer flowmeter. Assuming that all the hydrogen is dissociated, this translates to  $2.6 \times 10^{21}$  H-atoms  $\text{s}^{-1}$  being generated in the chamber. As a result our measured H atom signal at the mass spectrometer accounts for .003% of these atoms.

A possible source of error in the intensity measurements could lie in underestimating the ionization efficiency of the mass spectrometer used in the measurements. If more of the neutrals were being ionized this would give the high ion currents we have observed, but with a much lower beam intensity. This possibility can be ruled out since the mass spectrometer (with the ion focusing lens on) gives an  $m/e = 2$  signal in the nanoamperes region with  $10^{-5}$  torr  $\text{H}_2$  in VC2. This ion intensity is consistent with the ionization efficiency we have calculated for our mass spectrometer.

We can also see that the pressure in the mass spectrometer chamber (VC2) is consistent with the beam intensity measured by the mass spectrometer. At  $10^{-5}$  torr the mercury diffusion pump on the VC2 operates at a pumping speed of roughly  $100 \text{ l s}^{-1}$ . This corresponds to  $2.1 \times 10^{17}$  atoms  $\text{s}^{-1}$  being pumped out of the system which is two times greater than the

current of neutral H atoms measured by the mass spectrometer.

The reasons for two orders of magnitude difference between our intensities and those published by Stwalley<sup>1</sup> and Toennies<sup>3</sup> does not appear clear. Our operating conditions are different in that our discharge is hotter than the previous ones. Also as described in Section 2.3 our nozzle is set further into the electromagnet than Stwalley's; this appears to result in a higher collimation of the beam due to the focusing of the plasma by the applied magnetic field. The nature of these discharges can apparently change significantly from what would otherwise be considered simple modifications. Toennies' source (private communication) first typically achieved 60% dissociation of D<sub>2</sub> but after redesigning and "cleaning" it up that dissociation dropped to 20% for the same operating conditions. This behavior of that source is currently not understood, and he is introducing "contaminants" such as water into the hydrogen inlet lines, in an attempt to achieve the dissociation previously observed. All this goes in saying that, while it is disturbing we achieve higher intensities than have been observed in the past, it may not be surprising once one considers how apparently sensitive these sources are to operating conditions. The conclusion of these remarks is that the behavior of arc sources of this type is sufficiently obscure for significant differences in operating intensities to be consistent.

Taking the values of equation 3.5 to be realistic, it implies a neutral current density of H atoms at a distance of 1 m from the nozzle of  $3.2 \times 10^{17}$  H-atoms cm<sup>-2</sup> s<sup>-1</sup> and a number density (for 8 eV atoms) of  $8.3 \times 10^{10}$  H-atoms cm<sup>-3</sup>, which is a number density of a gas at 300 K and  $2.3 \times 10^{-6}$  torr pressure.

For reference purposes a mass spectrum of the beam obtained using the chopper and lock-in amplifier is displayed in Figure 5 with the ion current

ordinate normalized by the DC ion current measurement to the first dynode described in this section.

### 3.3 Energy Analysis

The original purpose of this beam source was to provide an intense hyperthermal source of hydrogen atoms. In the previous section we have shown that the beam is indeed quite intense; however, we need some way to measure the translational energy of the neutral specie in the beam. Originally this experiment was to be performed using the magnetic velocity selector described in Appendix A of this thesis. Delay in design and construction of this device have unfortunately required that we postpone these experiments.

However, we are able to achieve a crude energy analysis with the help of the electrostatic lens within the mass spectrometer. For most of the measurements reported in this thesis the mass spectrometer was operated with the potential of both the focusing lens and the Faraday cage set to zero. This was done to discriminate against thermal background molecules since the ions generated from the electron bombardment of the beam molecules have the translational energy produced by the plasma heating and will not need the additional acceleration normally provided by the Faraday cage to enter the quadrupole rod mass analysis region.

It is also possible to achieve a crude energy analysis of the species in the beam by application of a negative potential to the faraday cage. Only ions having a translational energy sufficient to overcome the negative potential applied to the cage will be able to pass through the mass analysis system and be detected. By scanning the negative potential applied and measuring the corresponding decrease in intensity of a particular mass, one can measure an integral of the energy distribution function.

It should be noted that this measurement is quite crude since the lens

system was not designed for this particular use and a change in its potential can affect the transmission efficiency of the ions that do make it through. This method can at best give a crude energy distribution function and the results should only be used in a qualitative manner.

Typically the arc source is run with  $H_2$  and once the plasma has stabilized the ion deflection plates are turned on (1000 kV/cm) and the usual mass spectrum of neutral specie in the beam is observed. The velocity analysis determination was performed by placing the mass spectrometer in the manual mode and tuning a particular mass. The chopper was turned on, the lock-in amplifier was tuned to the frequency of the chopper, and the AC signal measured. Normally a time constant of 3 sec was used for these measurements to achieve a reasonable signal to noise ratio. A negative voltage was then applied to the Faraday cage, and the AC intensity of that mass specie measured as a function of that voltage.

The data thus obtained are an integral of the translational energy distribution function of that mass species. To get the distribution function itself one must take the derivative of that curve.

Figure 6 shows the energy distribution function for  $m/e = 1$ . With a stagnation pressure of 55 torr (Figure 6a) corresponding to the 'pencil' mode, and an arc voltage and current of 40 V and 100 A, respectively, it shows a maximum at  $\sim 13$  eV. It is very asymmetric but its shape may be due in part to the way the measurement is made and not reflect the true shape. The width of the high energy peak occurring at 13 eV is  $\sim 5$  eV.

By contrast, Stwaller's<sup>1</sup> distribution in the pencil mode, measured by an inhomogeneous magnetic field energy analysis and bolometric detection, has a maximum at 5 eV and a width of 5 eV. Again this difference is consistent with the conclusion made in the previous section that our discharge is much

hotter than previously reported arc sources.

Figure 6b shows the energy distribution function of the H atom with the stagnation pressure increased to 70 torr (still the pencil mode), with the arc voltage and current conditions the same as those for Figure 6a. The peak in the distribution is observed to shift down to  $\sim 8$  eV and the width is reduced to  $\sim 3$  eV. Increasing the stagnation pressure decreases the average translational energy of the hydrogen atoms generated. It is observed that the intensity of the H atoms generated and the intensity of the visible emission from the discharge plume also decrease with increasing stagnation pressure. Each of these observations is consistent with the assumption that increasing the stagnation pressure while keeping the power to the source constant decreases the effective temperature of the plasma. At increased stagnation pressure there is less energy per molecule, so that the translational energy of the H atoms decreases. As a result, stagnation pressure may be used as a crude means of altering that energy.

Figure 6c shows the energy distribution function obtained when the arc source was operated at the same stagnation pressure and arc electrical conditions as for Figure 6a but with 5 torr of Ar added to the inlet gas. The peak of that distribution has, as in Figure 6b, shifted down to  $\sim 8$  eV with a width of  $\sim 5$  eV, analogous to that for Figure 6a. It is interesting to note that such a small amount of Ar added to the beam significantly affects the translational energy distribution. This suggests that the Ar, due to its electronic structure, affects the plasma and effectively decreases the temperature of the medium.

These experiments were attempted on the  $m/e = 2$  species but their intensity was too small for any reliable measurements to be made. However, such measurements were made on the  $m/e = 3$  species and are shown in Figure 7. Figure 7a shows the  $m/e = 3$  species distribution function for a

stagnation pressure of 75 torr. The peak of the distribution occurs at  $\sim 7$  eV and has a width of  $\sim 7$  eV. Comparing with the H translational energy distribution, we see that they have roughly the same translational energy at the same stagnation pressure, suggesting that they are both heated to the same extent in the plasma. However, the width of the  $m/e = 3$  distribution is approximately twice that of the H atom distribution.

Increasing the stagnation pressure to 95 torr causes the peak of the translational energy distribution function for the  $m/e = 3$  species to decrease to  $\sim 3$  eV and its width to  $\sim 5$  eV. This is consistent with our previous conclusion that higher stagnation pressures at constant arc power dissipation decreases the temperature of the plasma. Attempting to put Ar into the beam reduced the intensity of the  $m/e = 3$  species to such an extent that these energy measurements could not be made. The nature of this  $m/e = 3$  species will be discussed in greater length in Section 4 of this thesis.

### 3.4 Emission Spectroscopy

To further characterize the discharge, the bright plume directly in front of the nozzle was spectroscopically analyzed. Figure 1 shows a schematic of the apparatus. The nozzle was fully pulled back from the skimmer to permit an unobstructed view of the plume light through P1. That light was focused onto the slits of a 0.5 meter Ebert scanning Jarrel-Ash monochromator by lens L, after being chopped at  $\sim 100$  Hz by C2. That spectrometer was calibrated before use with light from a Fe-Neon cathode discharge. The light after dispersion by the monochromator is detected by a photomultiplier tube whose output current is amplified by a Princeton Applied Research model 181 current sensitive preamplifier. The signal is then processed by a Princeton Applied Research model HR-8 lock-in amplifier which has been tuned to the chopping frequency of the chopper. The use of the lock-in provides excellent discrimination against any background or stray light. The output of the lock-in is finally fed to a strip chart recorder while the monochromator smoothly scans the desired spectral region. The signal intensity was so large that there never existed any difficulty in achieving good signal-to-noise resolution.

Figure 8 shows the emission spectrum from 390 to 490 nm for an Ar arc at a stagnation pressure of 340 torr, with the arc conditions being set at 10 V and 100 A. All the lines in this figure were assigned using Striganov's line positions<sup>4</sup> and are listed in Table II. Figure 9 shows the emission spectrum of a mixture of 340 torr Ar plus 23 torr of H<sub>2</sub>. The Balmer series of H atom lines can now be seen superimposed on the argon emission spectrum. As the H<sub>2</sub> partial pressure is increased to 38 torr the plume shows a dramatic color change and its spectrum is recorded in Figure 10. Though the argon to hydrogen ratio is now of 9:1, almost all the argon lines have disappeared.

Figure 11 shows the emission spectrum for a 'pencil' mode of pure hydrogen at a stagnation pressure of 60 torr and the lines showed are assigned in Table III. A crude estimate for the temperature of the plasma may be calculated by taking the ratio of the  $\beta$  and  $\gamma$  Balmer line intensities. Assuming a Boltzmann distribution of electronic states (which may be a poor assumption considering the discharge environment) a temperature of  $\sim 12,000$  K is calculated. It was also possible to record a spectrum of the discharge while the plasma was out of control and copper and tungsten were melting from the nozzle (Figure 12). In this case the expected Balmer series is superimposed on a number of atomic lines due to the excited metals spewing forth from the nozzle. These lines are unassigned.

TABLE II

## Assigned Argon Transitions

Wavelength (Å)	Transition
4917.8	4p(2 1/2)←10d(2 1/2)
4883.2	4p(2 1/2)←7d'(2 1/2)
4876.2	4p(1/2)←7d(1 1/2)
4867.8	4p(2 1/2)←11d(3 1/2)
4836.6	4p(1/2)←9s(1 1/2)
4768.6	4p(1/2)←6d'(1 1/2)
4752.9	4p(1/2)←8d(1/2)
4746.8	4p(1/2)←8d(1/2)
4709.5	4p(1/2)←10s(1 1/2)
4702.3	4s'(1/2)←5p(1/2)
4647.4	4p(1/2)←9d(1/2)
4642.1	4p(1/2)←9d(1 1/2)
4628.4	4s'(1/2)←5p(2 1/2)
4596.0	4s'(1/2)←5p(1 1/2)
4589.2	4s'(1/2)←5p(1 1/2)
4522.3	4s'(1/2)←5p(1/2)
4510.7	4s'(1/2)←5p(1/2)
4345.1	4s'(1/2)←5p'(1 1/2)
4335.3	4s'(1/2)←5p'(1/2)
4333.5	4s'(1/2)←5p'(1 1/2)

TABLE II cont.

Wavelength (Å)	Transition
4300.1	$4s(1\ 1/2) \leftarrow 5p(2\ 1/2)$
4272.1	$4s(1\ 1/2) \leftarrow 5p(1\ 1/2)$
4266.2	$4s(1\ 1/2) \leftarrow 5p(1\ 1/2)$
4259.3	$4s'(1/2) \leftarrow 5p'(1/2)$
4251.1	$4s(1\ 1/2) \leftarrow 5p(1/2)$
4200.6	$4s(1\ 1/2) \leftarrow 5p(2\ 1/2)$
4198.3	$4s(1\ 1/2) \leftarrow 5p(1/2)$
4191.0	$4s'(1/2) \leftarrow 5p'(1\ 1/2)$
4190.7	$4s(1\ 1/2) \leftarrow 5p(2\ 1/2)$
4181.8	$4s'(1/2) \leftarrow 5p'(1/2)$
4164.1	$4s(1\ 1/2) \leftarrow 5p(1\ 1/2)$
4158.5	$4s(1\ 1/2) \leftarrow 5p(1\ 1/2)$
4054.5	$4s(1\ 1/2) \leftarrow 5p'(1\ 1/2)$
4044.4	$4s(1\ 1/2) \leftarrow 5p'(1\ 1/2)$

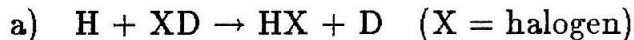
TABLE III

## Assigned Hydrogen Transitions

Wavelength ( $\text{\AA}$ )	Transition	Designation
4861.3	$2p \ ^2P \leftarrow 4d \ ^2D$ etc.	$\beta$
4340.4	$2p \ ^2P \leftarrow 5d \ ^2D$ etc.	$\gamma$
4101.7	$2p \ ^2P \leftarrow 6d \ ^2D$ etc.	$\delta$
3970.0	$2p \ ^2P \leftarrow 7d \ ^2D$ etc.	$\epsilon$

### 3.5 Future Work

What follows are descriptions of types of experiments which would be interesting to perform with the high intensity hydrogen atom beam we have developed. Coupling this beam with the velocity selector described in appendix A will provide a unique opportunity to study reaction dynamics over a wide range of reagent energies with a continuously tunable monoenergetic hydrogen atom beam.



The exchange reactions  $\text{H} + \text{XD} \rightarrow \text{HX} + \text{D}$  where X is a halogen atom have received significant experimental<sup>5-7</sup> and theoretical<sup>8-11</sup> attention. In particular, for X = F it was thought that this process might play a role in the deactivation of vibrationally excited FD or FH in the hydrogen-fluorine chemical laser.<sup>12</sup> High-quality *ab initio* calculations of the ground electronic state potential energy functions for these systems have indicated that the barriers for these exchange reactions are in excess of 40 kcal/mole for HFH and 20 kcal/mole for HClH<sup>8-11</sup>.

Although older experiments suggested that these barriers were much smaller, some more recent results are consistent with these larger values<sup>13,14</sup>. These reactions involving the transfer of a hydrogen atom have had a major role in the development of chemical kinetics<sup>15</sup>. Many of the results have been contradictory in nature especially the issue of whether the abstraction process is faster than the exchange process<sup>16,17</sup>. A molecular beam study has been performed which gave reaction cross sections for the two processes and showed that in the exchange reaction most of the available energy went into

product translation<sup>7</sup>.

The experiments with the fluorine system usually involve vibrationally excited HF or DF molecules. However, since these exchange processes are nearly symmetric, translational energy is frequently more effective than vibrational energy in overcoming the reaction barrier. This is known, for example, from collinear quantum mechanical calculations for the H + H<sub>2</sub> system<sup>18</sup>. Recent collinear quantum calculations for the HFD system<sup>19</sup> on a potential energy surface with a realistic barrier height of 40 kcal/mole indicate that the phenomenological threshold of the reaction probability for ground vibrational state reagents yields a good estimate of the barrier for exchange, whereas that for vibrationally excited states does not. This suggests the desirability of an experimental investigation of the dynamics of the H + XD → HX + D reaction and its reverse as a function of reagent translational energy. However, if the barrier of this reaction is indeed of the order of 40 kcal/mole or higher, direct studies of this kind require the availability of a sufficiently energetic and intense beam of H or D atoms. The beam described in previous sections of this thesis is ideally suited for such experiments. Coupling this beam with the magnetic velocity selector described in Appendix A will provide the energy resolution need to elucidate the dynamics of this reaction.

Using a crossed beam configuration it should be possible to study the dynamics of the



and



exchange reactions. We can initially consider a 2.5 eV beam of H atoms (which have been velocity selected by our inhomogeneous magnet) crossing a

beam of thermal or slightly supersonic DF molecules. To examine how this experiment will be performed it is necessary to construct Newton diagrams for this system as well as for the H + HF system (since there is always a certain amount of HF impurity in the incident DF beam). An analysis of these diagrams indicates that, if we detect the HF reactive product from reaction (3.6) in the laboratory angle range of  $33^\circ$  to  $66^\circ$  (with respect to the incident reactant DF beam), there will be negligible contributions due to the HF impurity scattered elastically by more than  $20^\circ$  in the center of mass or scattered inelastically to form HF ( $v = 1$ ) at CM scattering angles less than  $160^\circ$ . There is the possibility of a small contribution from rotationally inelastic scattering of the HF impurity, but it can be determined from separate studies in crossed H and HF beams and its effect may then be corrected for.

The laboratory scattering angle range of  $33^\circ$  to  $66^\circ$  for the HF reactive product corresponds to a CM scattering angle range of  $90^\circ$  to  $180^\circ$ . This range corresponds to most of the product being backward- or sideward-peaked. Even if it is forward-peaked, we should have no difficulty in extending the FH measurements to a laboratory angle of  $120^\circ$  with respect to the DF beam which will take us over the entire CM scattering angle range.

The main question remaining is whether the expected signal intensities are sufficiently high. How the magnetic velocity selector will affect the beam and how fine the energy resolution will be is still unknown. After velocity selecting the hydrogen atom beam we can however make a worst-guess estimate for the intensity of the beam after passing through the magnet, which is that the beam will be lowered by a maximum of 4 orders of magnitude. This will leave a hydrogen atom intensity of  $1.3 \times 10^{18}$  atoms  $\text{sr}^{-1} \text{s}^{-1}$ . This flux, passing through a  $1 \text{ mm}^2$  aperture at 1 m from the nozzle, gives a current density of  $3.3 \times 10^{13}$  atoms  $\text{cm}^{-2} \text{s}^{-1}$ . For 8 eV H atoms this results in a

number density of  $8.3 \times 10^6$  atoms  $\text{cm}^{-3}$  corresponding to a partial pressure of  $2.3 \times 10^{-10}$  torr.

For the thermal DF beam we can assume a pressure of  $10^{-4}$  torr in the beam resulting in a number density for DF of  $3 \times 10^{12}$  molecules  $\text{cm}^{-3}$ . For thermal DF traveling at  $1 \times 10^5$   $\text{cm s}^{-1}$  this corresponds to a current density of DF of  $3 \times 10^{17}$  molecules  $\text{cm}^{-2} \text{s}^{-1}$ .

Assuming now that the beams cross in a scattering volume of  $10^{-3} \text{cm}^3$  and that the cross section for reaction (3.6) at these elevated energies is  $\sim 10 \text{ \AA}^2$  then there will be a flux of  $2 \times 10^6$  HF  $\text{s}^{-1}$  produced. If we assume that the HF product is concentrated in the CM scattering range of  $160^\circ$  to  $180^\circ$  (i.e., that it is backward-peaked, as was observed in the  $\text{D} + \text{XH} \rightarrow \text{DX} + \text{H}$  reaction at an average relative energy of 0.4 eV for  $\text{X} = \text{Cl}$ ,  $\text{Br}$ , or  $\text{I}$ , for thermal beams<sup>7</sup>) for a mass spectrometer ionization efficiency of  $8 \times 10^{-3}$ , this will result in a signal of about 3000 counts/sec at  $m/e = 20$ . As long as the background at this mass does not exceed  $10^4$  counts/sec, this is a sufficiently large signal for measurements. Such backgrounds are attainable at the ion source pressures of the order of  $10^{-10}$  torr at which we operate the mass spectrometer in our crossed molecular beam apparatus. In addition, since the product HF laboratory velocity is about ten times the thermal one, we may be able to decrease the background signal by using a slight retardation potential on the ions, as has been described in section 3.3 of this thesis in the measurement of the velocity distribution function for the H atoms. These calculations were made assuming the worst case in the velocity selection of the H beam. It may turn out that higher fluxes of monochromatic hydrogen atoms may be obtained by operating at the appropriate stagnation pressures. In this case the amount of DF generated would be greater.

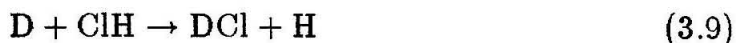
The reverse reaction of  $\text{D} + \text{HF}$  is more favorable because the HF target

has only a small natural abundance DF impurity and the mass spectrometer background at  $m/e = 21$  at which the DF reactive product is detected is about an order of magnitude lower than that at  $m/e = 20$ .<sup>20</sup> The DF signal may be sufficiently large and the background sufficiently low for us to perform a correlation chopper analysis of the velocity of the DF product.

It therefore appears that a good candidate for a first study to be performed on the crossed molecular beam apparatus<sup>21,22</sup> utilizing the H atom beam is an investigation of reactions (3.6) and (3.7) at various relative energies. These initial studies should be particularly interesting not only because the barrier for these exchange processes is greater than 40 kcal/mole, but also because the potential energy function at the saddle point configuration seems to be almost independent of the HFH bend angle<sup>11</sup>. This suggests that the angular distribution of the products might be governed by phase-space considerations, which tend to favor perpendicular rather than collinear collisions. It would also be interesting to extend this work to the

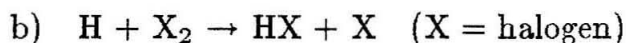


system. The barrier for this exchange reaction may be on the order of 20 kcal/mole<sup>8,9</sup>. The reaction



(as well as its Br and I counterparts) has been studied in a crossed molecular beam using thermal D and ClH beams at an average relative kinetic energy of 0.4 eV<sup>7</sup>. The DCl signal measured was quite intense, and the estimated cross section for the reaction was in the 1 to 10 Å<sup>2</sup> range. These results seem at first glance to be inconsistent with a potential surface barrier of the order of 0.9 eV. However, the D atoms were generated in a thermal

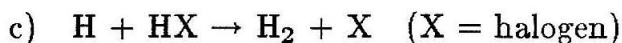
oven at 2800 K and were found to have a Maxwellian velocity distribution. As a consequence, about 30% of these atoms have relative energies which exceed the most probable one by more than 0.5 eV, and we cannot use these experiments to infer a low barrier height. Therefore, it would be very desirable to make a direct measurement of the phenomenological exchange reaction threshold. A similar analysis as that used for the HFD system shows that the corresponding crossed beam experiment for HClD is feasible. However, the mass spectrometric background at the  $m/e = 39$  peak at which the DCl product would be detected is relatively high, but nevertheless, signals of the order of  $10^3$  to  $10^4$  counts/sec can be measured at this peak<sup>7</sup>.



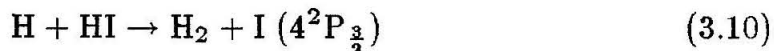
Reactions of hydrogen atoms with halogens have proved of great interest in the past due to the exoergicity of the reaction. As a result, there is a wealth of gas phase kinetic studies investigating these reactions<sup>23-27</sup>. Because of the exothermicity of these reactions it has also been possible to study them spectroscopically and to determine how the excess reaction energy is partitioned among the products. The  $\text{H} + \text{X}_2$  reaction is ideal for this type of spectroscopic study due to the radiative lifetime of the HX product as well as the wide quantum spacing<sup>28-32</sup>. Through these studies it was shown that these reactions exhibit a comparatively low fractional conversion of the total available energy into internal excitation of the new molecule. This relatively inefficient conversion of reaction energy into product vibration is thought to arise from the 'repulsive' nature of the potential surface<sup>30,32</sup>. The natural evolution of these studies has led to crossed molecular beam experiments<sup>33,34</sup>. These experiments have proved possible due to the low activation energy of this type of reaction; thus thermal reagent beams suffice in producing enough HX product to be detected. These experiments have shown that the reaction occurs in a direct fashion with the product HX being scattered mainly in the  $\text{X}_2$  direction<sup>33,34</sup>.

Past theoretical models for reactions of  $\text{H} + \text{X}_2$  have always assumed a strong directional preference for the reaction to occur in a collinear configuration. These molecular beam experiments<sup>34</sup> have shown that the product angular distributions show a striking shift as the transferred halogen atom changes from Cl to Br to I. This change in the HX angular distribution points to the reaction favoring a more bent configuration as the transferred halogen atom becomes larger. By studying the effect of reagent energy on the

reaction dynamics for this system and observing how the excess energy is channeled into the product, one should obtain detailed information of the nature of the reactive surface. With our monoenergetic hydrogen atom beam this system could be studied in our crossed molecular beam chamber and the product HX observed either through mass spectrometric detection or by spectroscopic detection of the fluorescence of the excited HX.



This class of reaction is very interesting due to the possibility that the halogen atom might be produced in an electronically excited state. In the case of  $\text{X} = \text{I}$  there are two possible channels;



This occurs because the reaction is exoergic by 1.5 eV but the spacing between the ground  $4^2\text{P}_{\frac{1}{2}}$  state and the first excited state, the  $4^2\text{P}_{\frac{3}{2}}$  state, of the iodine atom is by 0.9 eV. This allows for the possibility that some of the excess energy from the reaction may become channeled into electronic energy of the products. Since the other higher electronic states of the iodine atom are many eV higher, there is the interesting possibility that the product atom may be formed in the  $4^2\text{P}_{\frac{3}{2}}$  and  $4^2\text{P}_{\frac{1}{2}}$  states. This branching ratio for this reaction has been measured in bulk by measuring the infrared chemiluminescence of the excited iodine atom<sup>35</sup>.

It would be of interest to study this system in a crossed beam experiment. In particular, it would be interesting to measure the branching ratio for the two possible electronic states of I and see how it changes with respect to the translational energy of the hydrogen atom beam. The branching ratio can be studied by measuring the translational energy distribution of the iodine atom produced from the reaction.

In order to investigate the feasibility of distinguishing the two different electronic states on the basis of translational energy, it is necessary to do a kinematic analysis of the expected velocity distribution of the halogen atom products. This analysis consists of comparing the product distribution with the spectrum of recoil vectors allowed by the conservation laws for energy

and linear momentum<sup>36-38</sup>. Constructing the Newton diagrams for the  $H + HX$  reaction it becomes immediately clear that the experiment would be unfeasible for  $X = F, Cl,$  and  $Br$  due to the small separation between the ground and first excited state of the halogen atom. However, the case of  $X = I$  seems well suited to this type of analysis. The experiment would be performed by crossing the already described velocity-selected  $H$  atom beam with a beam of  $HI$  formed by expansion through a glass capillary array in the 50" bell jar<sup>39</sup>. The iodine atoms generated by the reaction will be analyzed by a quadrupole mass spectrometer which can be rotated in and out of the plane of the beams. The translational energy analysis of the iodine atoms will be performed by a correlation chopper mounted in front of the mass spectrometer. The chopper should have 256 teeth and will be operated in the range of 400 to 600 hz. This method will provide sufficient resolution to differentiate between the two electronic states of the iodine atom.

One severe problem with this experiment is in differentiating between the  $I$  product and the  $HI$  which is elastically scattered. In the only crossed beam experiment performed on this system<sup>14</sup> it was found that the  $H_2$  was backward scattered, but in this experiment the  $I$  was not detected. As a result it is impossible to say if the  $I$  will be scattered in an angle range which will be free from the  $HI$  elastic background. If this is not true it might be possible to distinguish the product  $I$  from the thermal background through a retardation potential applied to the lens of the mass spectrometer as described in section 3.5.1.

In the future it may also be possible to study reactions where  $X = Br,$   $Cl,$  and  $F$ . By using the quadrupole mass spectrometer as the detector, one could use multi-photon ionization instead of the conventional electron impact ionizer. In this case the laser light would be delivered to the ionizing

region of the mass spectrometer through a fiber optic array, such that the mass spectrometer could still be rotated as a function of the fixed reagent beam. The ground and excited state of the halogen atom could then easily be distinguished by simply scanning the available frequency range with a dye laser. Then one might be able to measure the branching ratio for this whole class of reactions as a function of H atom velocity.

### 3.6 References

1. K. R. Way, S.-C. Yang, and W. C. Stwalley, *Rev. Sci. Instrum.*, **47**, 1049 (1976).
2. L. J. Kieffer, and G. H. Dunn, *Rev. Mod. Phys.*, **38**, 1 (1966).
3. R. Gotting, H. R. Mayne, and J. P. Toennies, *J. Chem. Phys.*, **80**, 2230 (1984).
4. A. R. Striganov and Sventitskii, *Table of Spectral Lines of Neutral and Ionized Atoms*, (trans. from the Russian), IFI/Plenum, N.Y. (1968).
5. M. R. Levy, *Progr. React. Kinet.*, **10**, 1 (1979).
6. F. S. Klein and I. Veltman, *J. Chem. Soc. Faraday Trans.*, **74**, 17 (1978).
7. J. D. Mc Donald and D. R. Herschbach, *J. Chem. Phys.*, **62**, 4740 (1975).
8. P. Botschwina and W. Meyer, *Chem. Phys.*, **66**, 2752 (1977).
9. T. H. Dunning, Jr., *J. Chem. Phys.*, **66**, 2752 (1977).
10. C. F. Bender, B. J. Garrison, and H. F. Schaefer III, *J. Chem. Phys.*, **62**, 188 (1975).
11. W. R. Wadt and N. W. Winter, *J. Chem. Phys.*, **67**, 3068 (1977).
12. J. F. Bott, *J. Chem. Phys.*, **65**, 1976 (1976).
13. F. E. Bartoszek, D. M. Manos, and J. C. Polanyi, *J. Chem. Phys.*, **69**, 933 (1978).

14. W. Bauer, L. Y. Rusin and J. P. Toennies, *J. Chem. Phys.*, **68**, 4490 (1978).
15. S. W. Benson, *The Foundations of Chemical Kinetics*, Mc Graw Hill, N. Y., pp. 314-343 (1960).
16. A. E. De Vries and F. S. Klein, *J. Chem. Phys.*, **41**, 3428 (1964).
17. H. Y. Su, J. M. White, L. M. Raff, and D. L. Thompson, *J. Chem. Phys.*, **62**, 1435 (1975).
18. D. G. Truhlar and A. Kuppermann, *J. Chem. Phys.*, **56**, 2232 (1972).
19. A. Kuppermann, J. A. Kaye, and J. P. Dwyer, *Chem. Phys. Lett.*, **74**, 257 (1980).
20. R. K. Sparks, private communication.
21. A. Kuppermann, R. J. Gordon, and M. J. Coggiola, *Faraday Discuss. Chem. Soc.*, **55**, 145 (1973).
22. M. Keil, J. R. Slankas, and A. Kuppermann, *J. Chem. Phys.*, **70**, 541 (1979).
23. J. B. Levy and B. K. W. Copeland, *J. Chem. Phys.*, **72**, 3168 (1968).
24. R. G. Albright, A. F. Dodunov, G. K. Lavrovskaya, I. I. Morson, and U. L. Talnoye, *J. Chem. Phys.*, **50**, 3632 (1969).
25. H. G. Wagner, U. Welxbachor, and R. Zellner, *Berichte der Bunsen*, **80**, 902 (1976).
26. K. H. Homann, H. Schewinfurth, and J. Warnaty, *Berichte der Bunsen*, **81**, 724 (1977).

27. R. A. Fass, *J. Phys. Chem.*, **74**, 984 (1970).
28. P. E. Charters and J. C. Polanyi, *Disc. Faraday Soc.*, **33**, 107 (1962).
29. K. G. Anlauf, P. J. Kunts, D. H. Maylotte, P. D. Pacey, and J. C. Polanyi, *Disc. Faraday Soc.*, **44**, 183 (1967).
30. J. C. Polanyi, J. J. Sloan, and J. Wagner, *Chem. Phys.*, **13**, 1 (1976).
31. J. P. Sung and D. W. Setser, *Chem. Phys. Lett.*, **58**, 98 (1978).
32. K. G. Anlauf, P. S. Horne, R. G. MacDonald, D. H. Maycotte, J. C. Polanyi, W. J. Skrlac, D. C. Tardy, and K. B. Woodall, *J. Chem. Phys.*, **53**, 4091 (1970).
33. J. Grosser and H. Haberland, *Chem. Phys.*, **7**, 442, (1970).
34. J. W. Hepburn, D. Klimek, K. Liu, J. C. Polanyi, and S. C. Wallace, *J. Chem. Phys.*, **69**, 4311, (1978).
35. P. Cadman and J. C. Polanyi, *J. Phys. Chem.*, **72**, 3715, (1968).
36. D. R. Herschbach, *Vortex*, **22**, 348 (1961).
37. D. R. Herschbach, *Disc. Faraday Soc.*, **33**, 149 (1962).
38. G. H. Kwei, J. A. Norris, and D. R. Herschbach, *J. Chem. Phys.*, **43**, 247 (1965).
39. M. Keil, Ph.D thesis, CIT (1978).

### 3.7 Figures and Captions

Figure 1. A schematic view of the top of the machine: VC1, vacuum chamber one; AS, anode assembly; A, anode; C, cathode; M, magnet; Sm, water-cooled copper skimmer; TA, Translation assembly; T, translator; P1, viewport; L, optical lens; C2, 150 Hz chopper; monochromator, 0.5 m Jarrell-Ash monochromator; PM, photomultiplier; CP, current preamp; L12, lock-in amplifier; SCR2, strip chart recorder; VC2, vacuum chamber 2; C1, 10 Hz chopper; D, electric field deflectors; F, mechanical flag; QMS, quadrupole mass spectrometer; P2, port; PA, EAI preamplifier (ESA-75); LI1, lock-in amplifier; MSE, mass spectrometer electronics; SCR1, strip chart recorder.

Figure 2. DC ion intensity of the  $m/e = 1$  peak as a function of electric field of the deflector plates. The electron impact ionizer is on with a current of  $150 \mu\text{A}$ .

Figure 3. DC ion intensity of the  $m/e = 2$  peak as a function of electric field of the deflector plates. The electron impact ionizer is on with a current of  $150 \mu\text{A}$ .

Figure 4. DC ion intensity of the  $m/e = 3$  peak as a function of electric field of the deflector plates. The electron impact ionizer is on with a current of  $150 \mu\text{A}$ .

Figure 5. AC ion current as a function of  $m/e$ . In each panel the lower curve in the AC background obtained with the electron beam turned off, and the upper curve is the AC ion current signal shifted upwards by 0.2

$\times 10^{-10}$  A for convenience of display. Electron impact current:  $100 \mu\text{A}$ . Electron accelerating voltage: 60V. Ion source pressure:  $2.1 \times 10^{-5}$  torr measured by an uncalibrated ion gauge.  $\text{H}_2$  in the molecular beam source. The stagnation pressure in the molecular beam source was 60 torr.

Figure 6. Derivative (with respect to energy) of AC signal of  $m/e = 1$  signal as a function of repeller voltage applied to ion energy lens. Operating conditions of discharge: 100 A and 35 V power, (a) beam is operated at 55 torr stagnation pressure of  $\text{H}_2$ , (b) beam is operated at 70 torr stagnation pressure of  $\text{H}_2$ , (c) beam is operated at 55 torr stagnation pressure of  $\text{H}_2$  and 5 torr stagnation pressure Ar.

Figure 7. Derivative (with respect to energy) of AC signal of  $m/e = 3$  as a function of repeller voltage applied to ion energy lens. Operating conditions of discharge: 100 A and 35 V power, (a) beam is operated at 75 torr stagnation pressure of  $\text{H}_2$ , (b) beam is operated at 95 torr stagnation pressure of  $\text{H}_2$ .

Figure 8. Emission spectrum from 4900 Å to 3900 Å of an argon arc at a stagnation pressure of 340 torr.

Figure 9. Emission spectrum from 4900 Å to 3900 Å of an argon-hydrogen arc at a stagnation pressure of 360 torr.

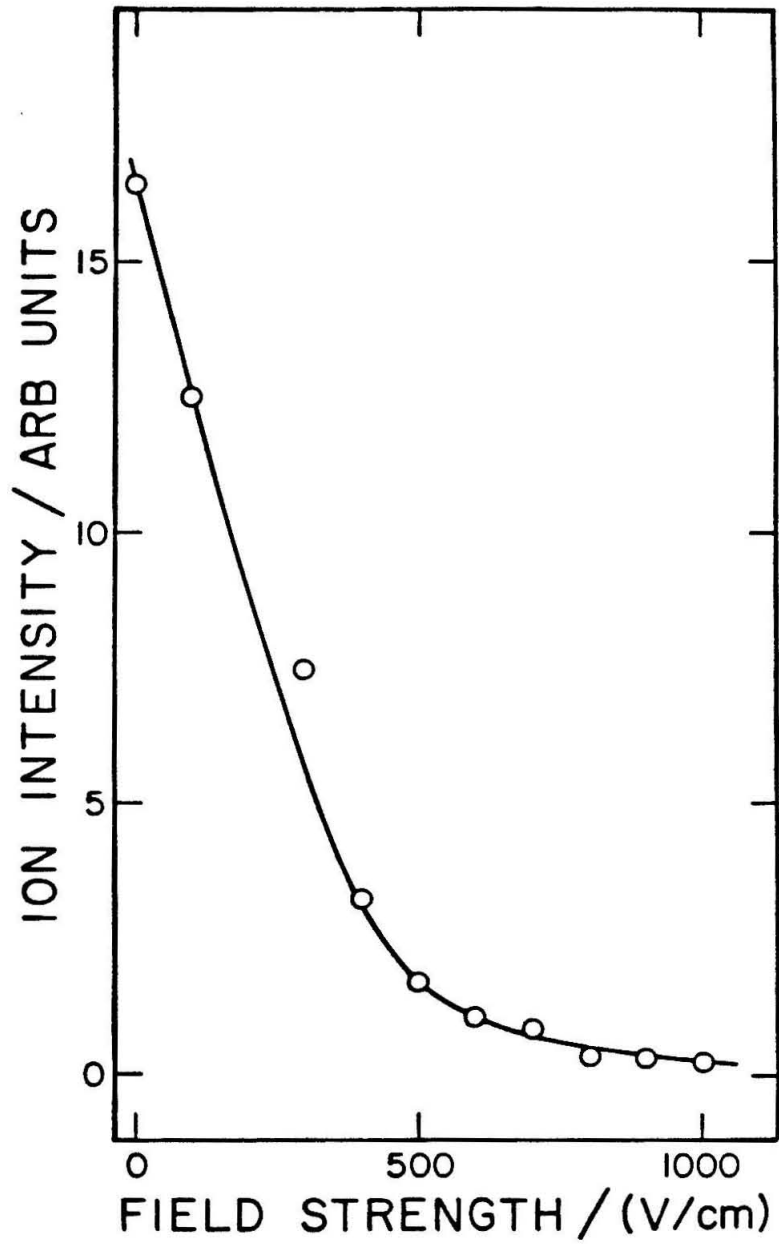
Figure 10. Emission spectrum from 4900 Å to 3900 Å of a argon-hydrogen arc at a stagnation pressure of 380 torr.

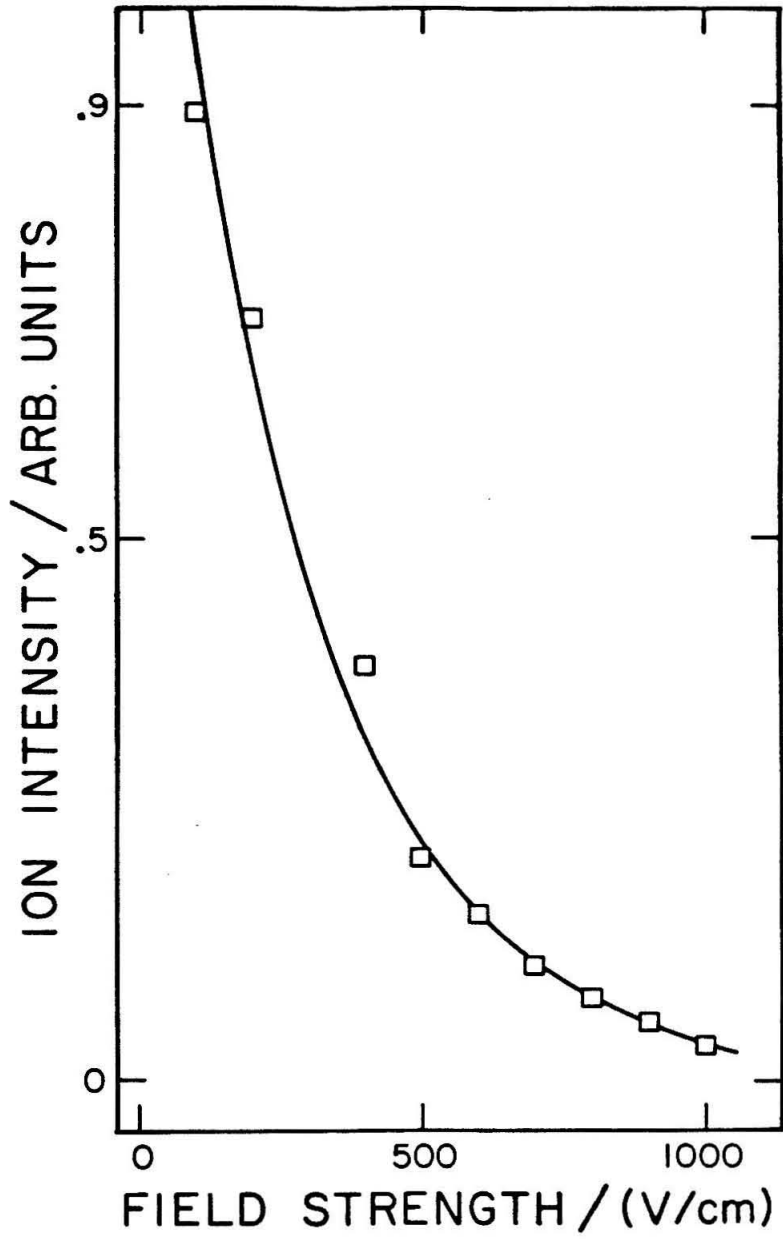
Figure 11. Emission spectrum from 4900 Å to 3900 Å of a hydrogen arc at a stagnation pressure of 60 torr ('pencil' mode).

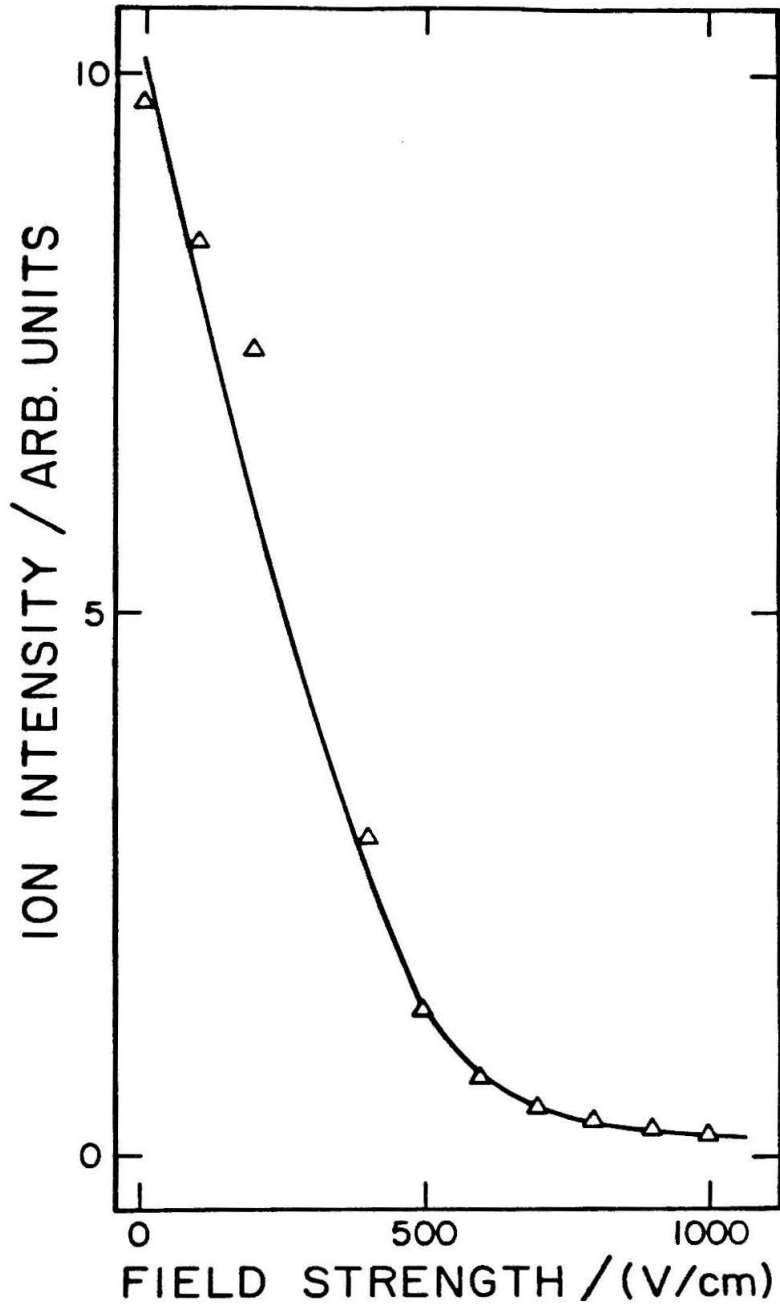
Figure 12. Emission spectrum from 4900 Å to 3900 Å of a hydrogen arc in

'pencil' mode malfunctioning.



**Figure 2**

**Figure 3**

**Figure 4**

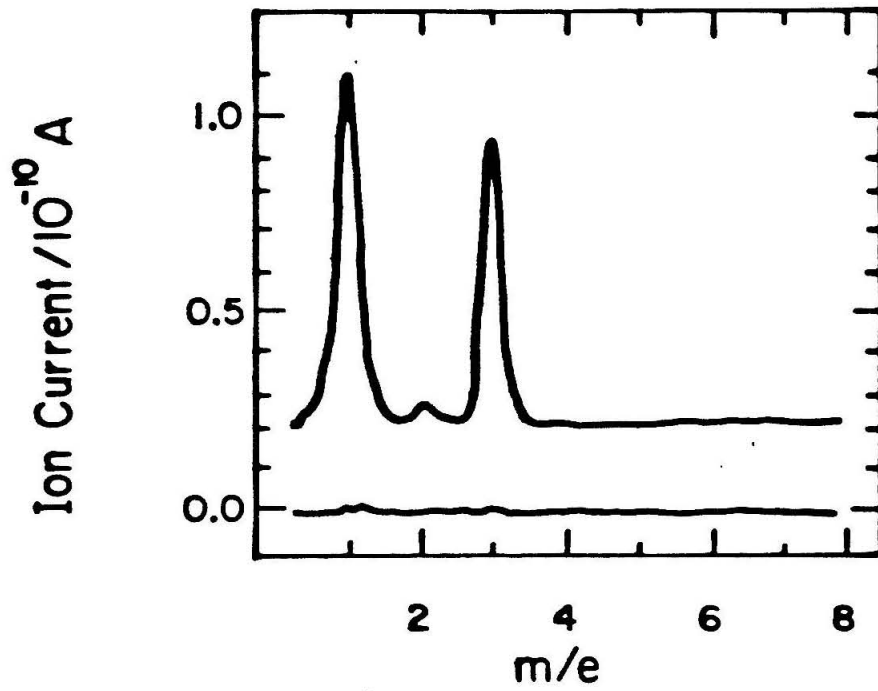


Figure 5

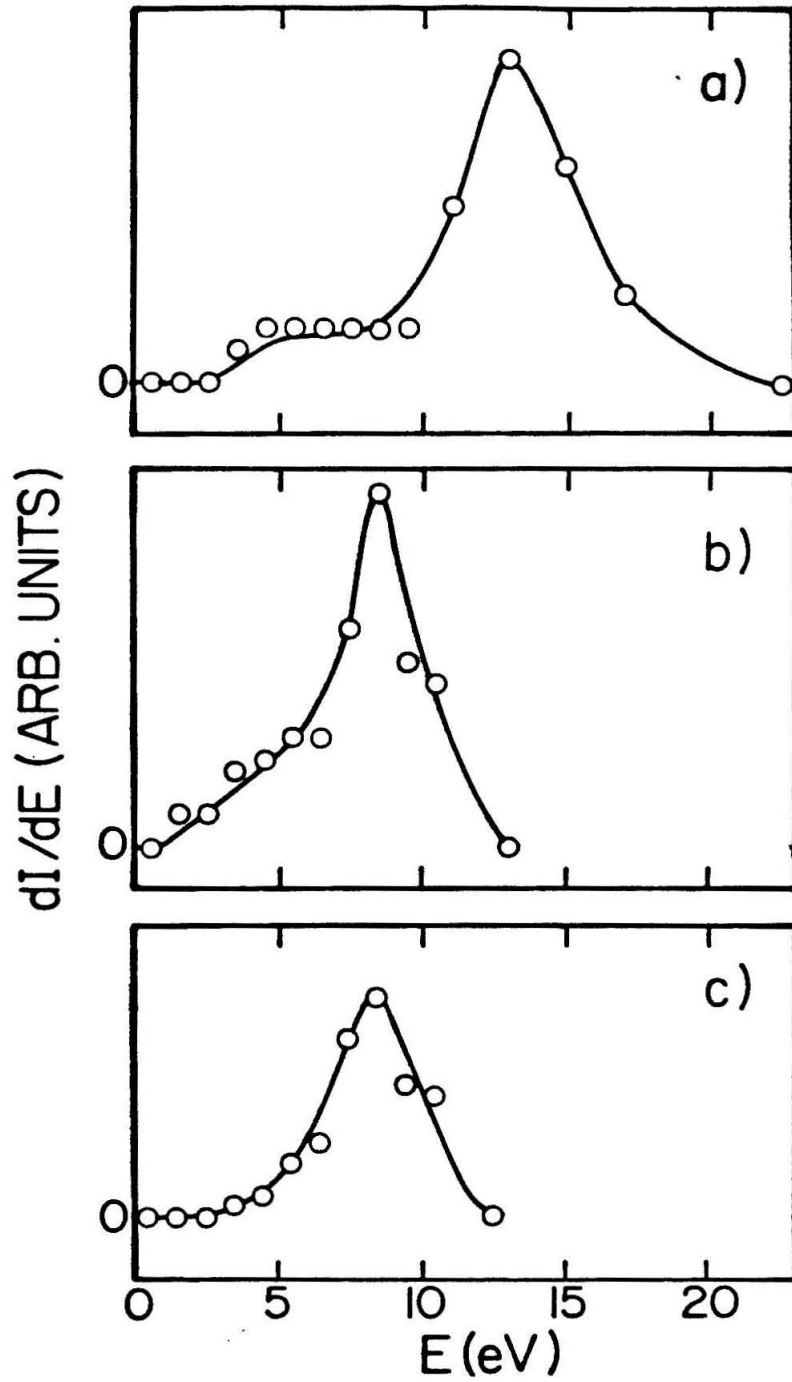


Figure 6

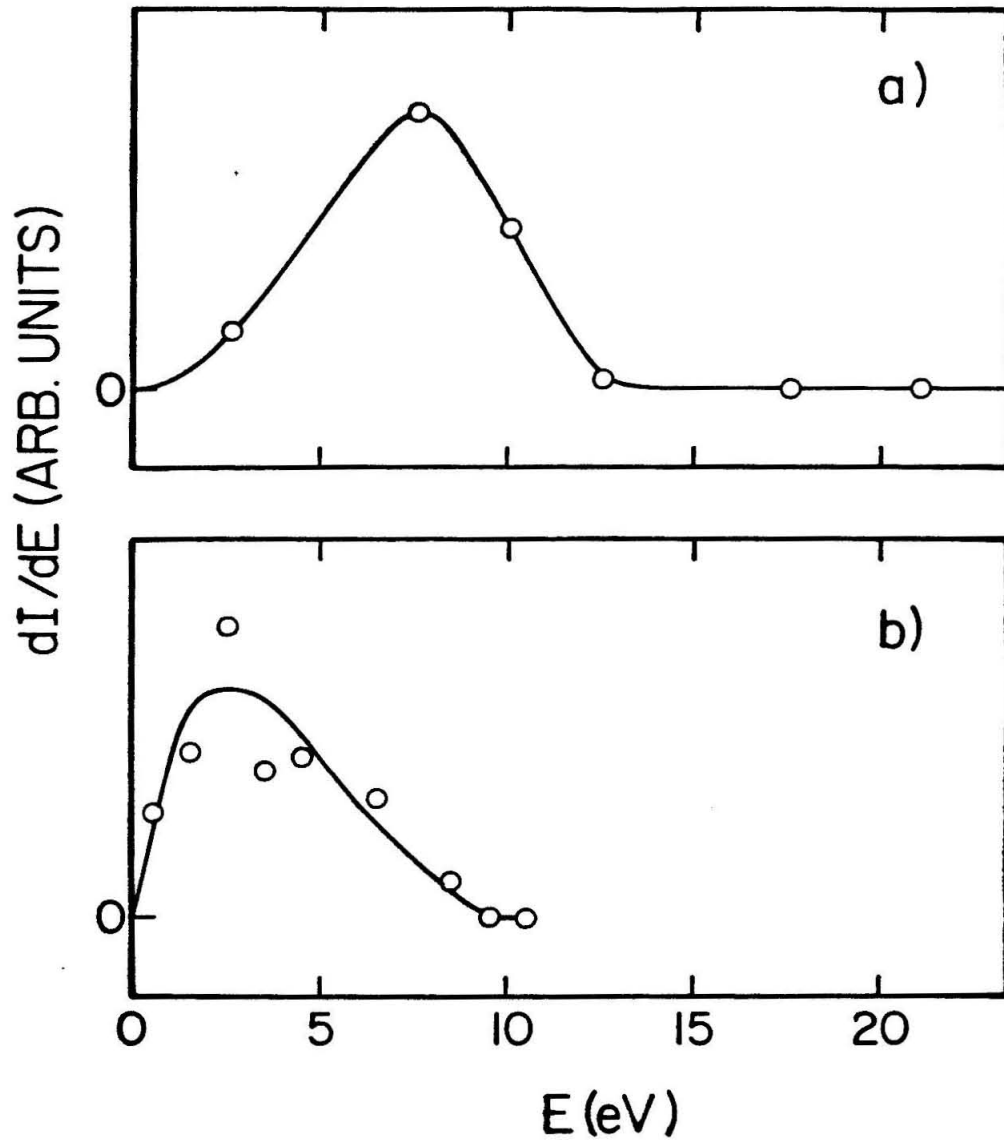


Figure 7

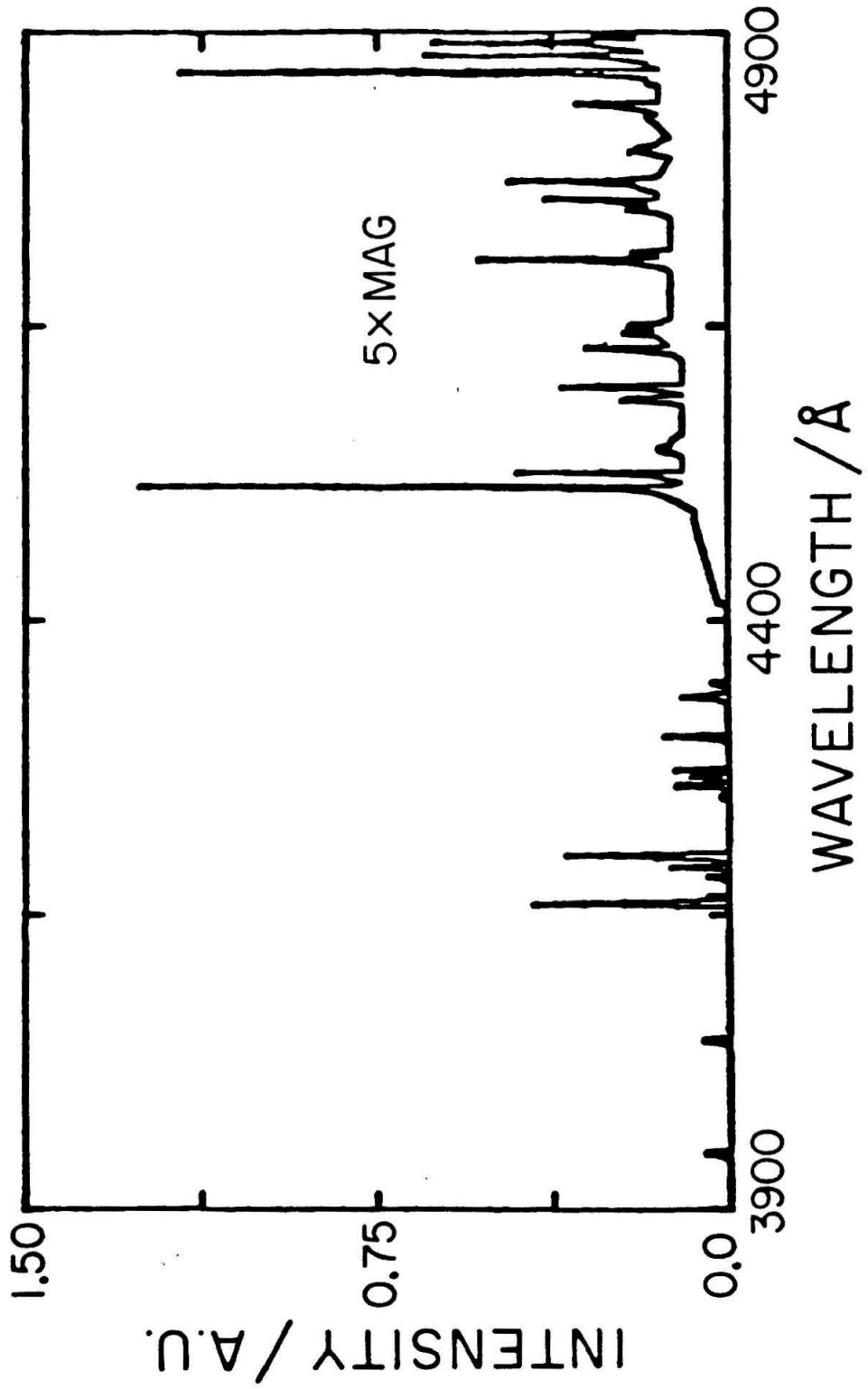


Figure 8

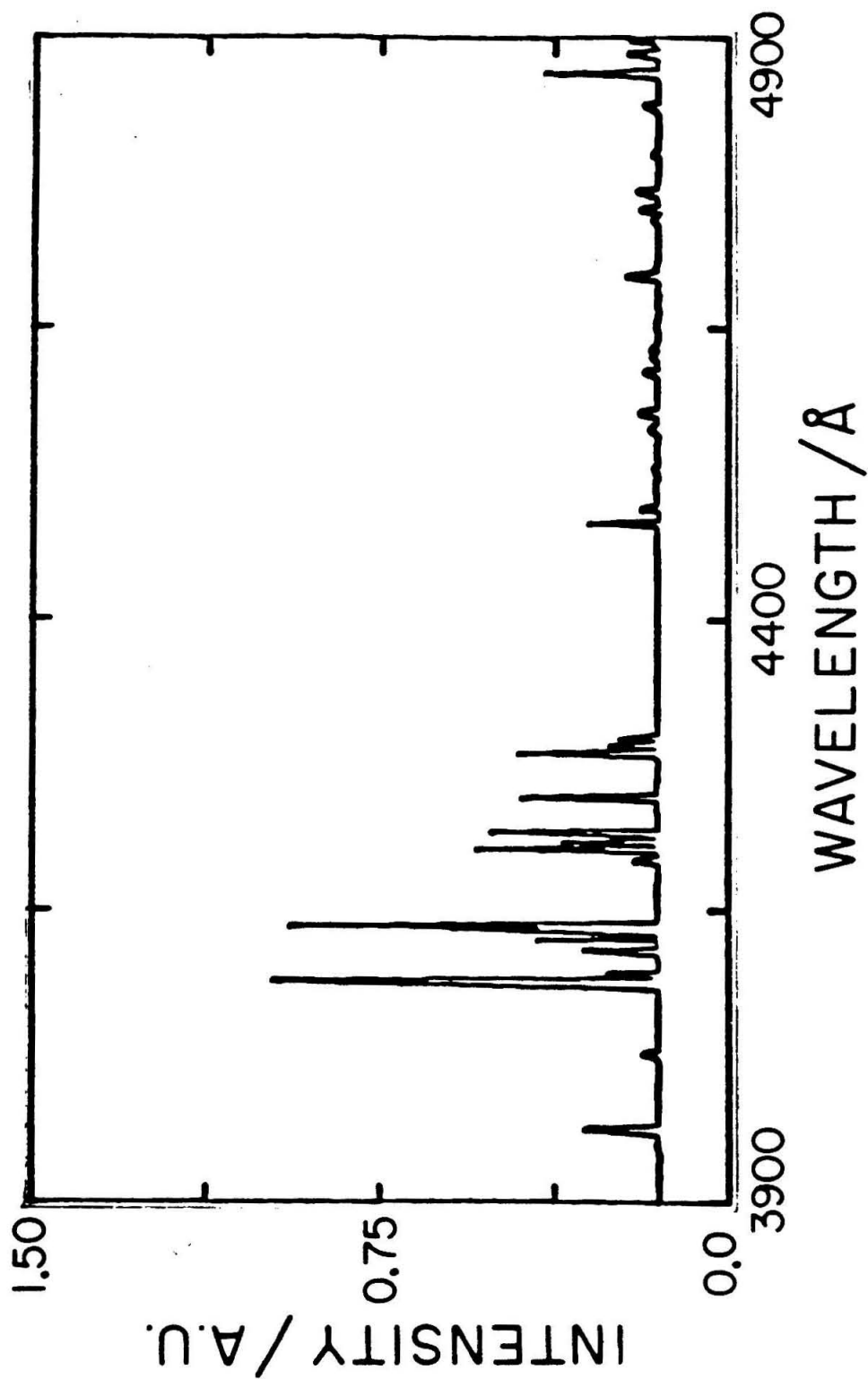


Figure 9

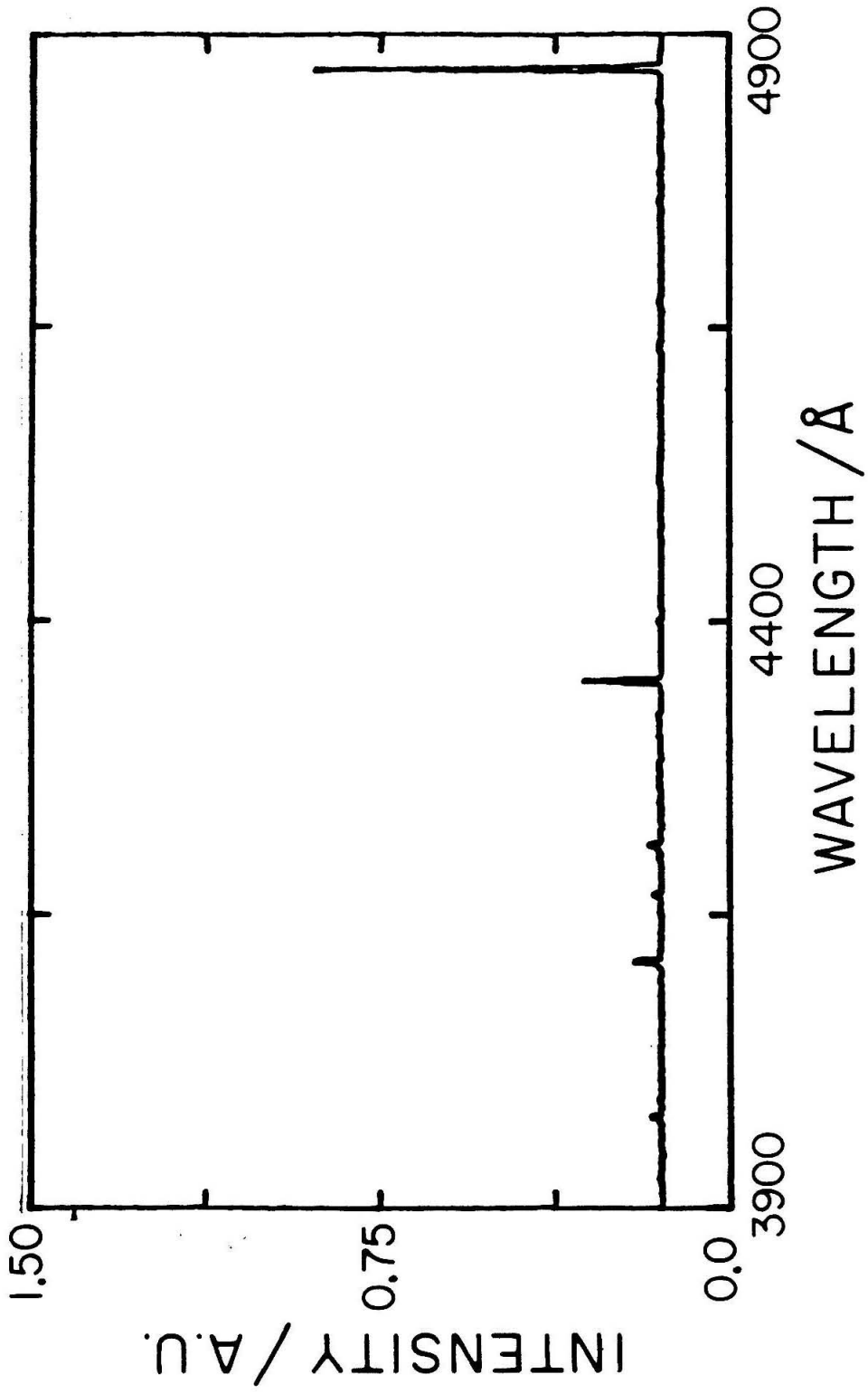


Figure 10

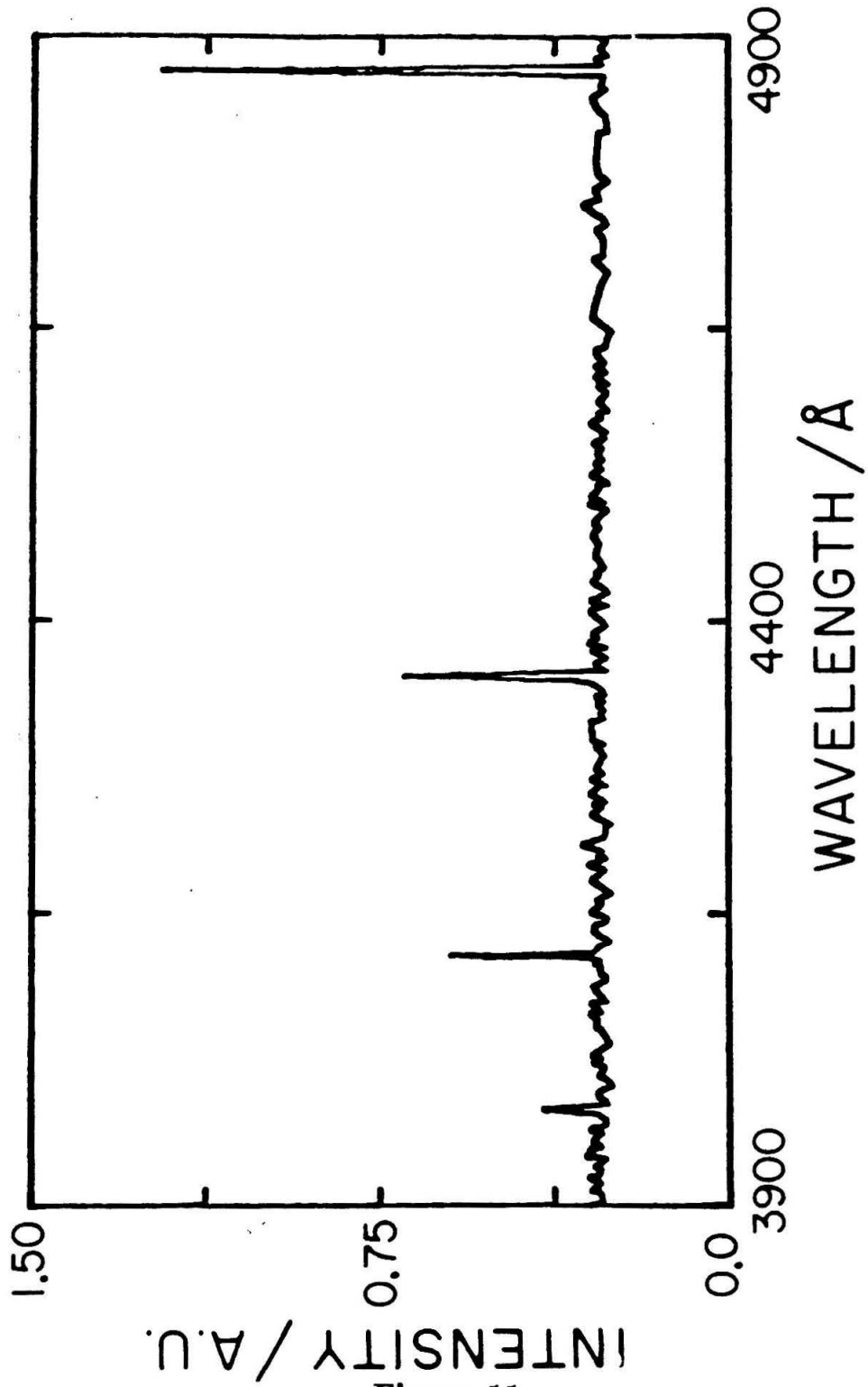


Figure 11

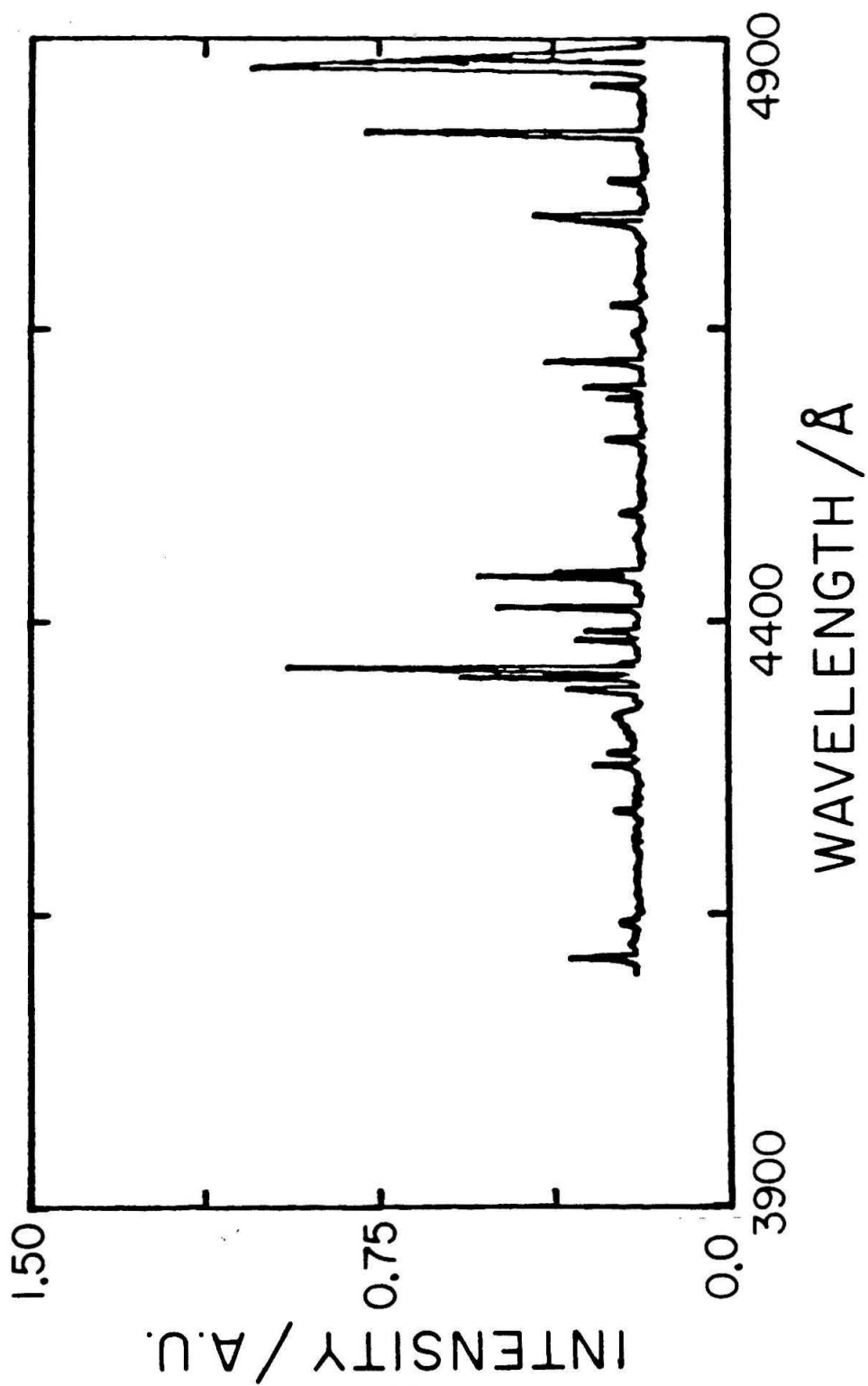
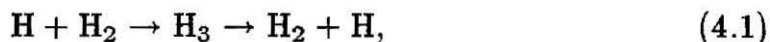


Figure 12

## 4. Results and Discussion for H<sub>3</sub> Molecules

### 4.1 Previous Work

What follows is a review of the experimental and theoretical work concerning H<sub>3</sub>. For the past forty years the simplest triatomic system, the triatomic hydrogen radical, has been the subject of extensive investigation. The ground state potential energy surface of this species, relevant to the symmetric hydrogen exchange reaction



has been calculated by many workers by a variety of techniques dating from the first Eyring and Polanyi calculations<sup>1</sup> to the present<sup>2-4</sup>. A very thorough account of the history of these calculations is given by Truhlar and Wyatt<sup>5</sup>. That surface has no minima. Thus the compound H<sub>3</sub>, in its electronic ground state, is very unstable with a life-time of about 10<sup>-12</sup> sec. before dissociation into H<sub>2</sub> + H.

In apparent conflict with this theoretical result, several workers have reported the detection of a stable form of H<sub>3</sub>. The very first report of the existence of such a species came from Devienne in an experiment where a double charge-exchange sequence was responsible for the observation of H<sub>3</sub><sup>6-10</sup>. In his experiments a beam of stable H<sub>3</sub><sup>+</sup> molecular ions is sent through a gas target such that electron-capture processes give rise to the production of a neutral beam of triatomic hydrogen. Devienne observed the neutral to exist with appreciable intensity for flight times as long as a fraction of a microsecond. The experiment is performed by taking a high energy (1.5 -

12.0 keV) beam of  $\text{H}_3^+$  which is neutralized by charge-exchange with a gas cell filled with  $\text{H}_2$ . As a result several different molecular species may be generated:



The neutral  $\text{H}_3$  (as well as other ionic and neutral molecular species) leaves the charge-exchange cell and exists for some time until it is reionized by collision with target gases, or (in a different experiment) with a beam of helium ions (12.0 keV)



The re-formation of ions with a mass to charge ratio of 3 (as measured by deflection of the ions by an electromagnet) is interpreted as evidence that some neutral  $\text{H}_3$  molecules survived for the time between the first charge-exchange and the second charge-exchange. The resulting  $\text{H}_3^+$  ions are then detected with a Faraday cup.

A short time later Gray and Tomlinson<sup>11</sup> investigated the HeH system using a method exactly like Devienne's and found HeH molecules with a lifetime of at least  $10^{-8}$  sec. However, when they attempted to neutralize and re-ionize either  $\text{D}_2\text{H}^+$  or  $\text{D}_3^+$  they observed no signal, suggesting that no neutral species had been generated. With this result, it appeared that Devienne's result was not neutral  $\text{H}_3$  but rather due to the presence of HD. It was thought that in Devienne's experiment an unavoidable contamination of deuterium in the hydrogen of the accelerator source produced  $\text{HD}^+$  ions since the intensity of the observed signal  $\text{H}_3^+$  signal was of the same order of magnitude of the

intensity expected from the natural abundance of HD in hydrogen gas. Since  $\text{HD}^+$  can not be distinguished from  $\text{H}_3^+$  electromagnetically at the resolution used by Devienne, his results were attributed to the HD contamination.

It was not until 1972 that Barnett and Ray<sup>12</sup> also reported the observation of  $\text{H}_3$ . They claimed to have identified this species in an experiment identical to Devienne's, where the second charge-exchange process was now replaced by electric field ionization. In their experimental procedure they took several precautions to minimize the contamination of the  $\text{H}_3^+$  beam by any  $\text{HD}^+$  and concluded that, despite the fact that the HD and  $\text{H}_3$  would both behave similarly in the electrostatic-stripping field, the signal they observed was due solely to the generation of an  $\text{H}_3$  neutral species.

That same year Nagasaki and co-workers<sup>13</sup>, in contrast to Gray and Tomlinson's result, reported the generation of a neutral  $\text{D}_3$  molecule. By generating 183 keV  $\text{D}_3^+$  ions and using the same successive charge-exchange technique (here using  $\text{N}_2$  as a target gas) they were able to identify the  $\text{D}_3$  molecule with an estimated half life longer than  $10^{-7}$  sec. In this case the only contamination which could contribute to the observed signal was  $\text{C}^{+2}$ , and that signal could easily be distinguished energetically by the detector. In this paper they noted the apparent conflict between their estimated life time which was  $10^6$  times larger than the theoretically estimated life time of the ground state of  $\text{D}_3$ . In attempting to reconcile this disagreement they were the first to note that the neutral species they had experimentally observed may indeed be in an excited electronic state of  $\text{H}_3$ , possessing a different lifetime from the ground state. In 1970, two years prior to Nagasaki's result, the first theoretical study of the potential energy surfaces of excited electronic states of  $\text{H}_3$  was carried out by Frenkel<sup>14</sup>. He performed restricted Hartree-Fock calculations in order to interpret collision experiments of  $\text{H}_2$  with metastable

2s H atoms<sup>15</sup>. His calculation showed deep minima in the excited energy surfaces for  $H_3$  (using  $D_{3h}$  symmetry) which could therefore support bound states.

The technique of neutralization and reionization of  $H_3^+$  in order to study  $H_3$  was not again employed until 1981 when Castro de Faria and co-workers<sup>16</sup> reported the observation of  $H_3$  by neutralizing and reionizing 1.2 MeV  $H_3^+$  ions through collisions with an argon target. However, the past difficulty of discriminating between the ion products  $HD^+$  and  $H_3^+$  was circumvented by using gold foil in front of their solid state detector. In this way they were able to discriminate between the two ions by means of their different energy losses and were able to unambiguously prove that the neutral  $H_3$  molecule had been generated and was not the result of a spurious contaminant. From their work they were also able to show the lifetime of  $H_3$  was greater than .1  $\mu\text{sec}$ . By also measuring the dissociation cross section of the ion produced it is possible to estimate the excitation of the original neutral molecule. For example, in the case of  $H_2$ , fitting the transmission measurements yields a dissociation cross section of  $\sim 5 \times 10^{-16} \text{ cm}^2$  for the  $H_2^+$  produced by reionization of the  $H_2$ . This value is two times larger than the cross section measured for  $H_2^+$  produced from the accelerator with the same translational velocity. This implies that the reionization of  $H_2$  produces ions that are more vibrationally excited than the  $H_2^+$  produced by the accelerator. In the case of  $H_3$ , the  $H_3^+$  produced from it exhibits a dissociation cross section of  $\sim 4.7 \times 10^{-16} \text{ cm}^2$ . This is approximately the same value measured for the  $H_3^+$  ion of the same translational energy. From this analysis it would appear the  $H_3^+$  ions resulting from ionization of  $H_3$  are not excited. This indicates that the  $H_3$  was in a Rydberg state since the capture or removal of an electron into or from a Rydberg state should leave the  $H_3^+$  core unperturbed. This is also sup-

ported by the ionization cross section measured for  $\text{H}_3 \sim 7.3 \times 10^{-16} \text{ cm}^2$  (in contrast with the ionization cross section measured for  $\text{H} \sim 2.5 \times 10^{-16} \text{ cm}^2$ ).

The most recent use of this technique has been by Gaillard and co-workers<sup>17</sup>. By placing an electric field between the neutralization and reionization gas cells they were able to show that for fields of 1.5 to 50 kV/cm a large fraction of the neutral triatomic molecules are destroyed. This indicates that the  $\text{H}_3$  is in a weakly bound state with  $n < 10$  (where  $n$  is the principal quantum number) and that the  $\text{H}_3$  Rydberg states are formed in a narrow band of  $n$  and  $l$  values. This result will be discussed in greater detail in section 4.7 .

A different approach has entailed beam studies where the neutral particles  $\text{H}_3$  dissociation products were detected directly rather than the ions generated by the  $\text{H}_3$  colliding with a gas target. Vogler<sup>18,19</sup> used a time-of-flight difference method and observed the spontaneous dissociation products of  $\text{H}_3$  which are formed by the non-resonant neutralization of 10 keV  $\text{H}_3^+$  with  $\text{H}_2$ . The H- $\text{H}_2$  fragment pairs are detected by two separate detectors operating in a coincidence mode. From the position of the two detectors and the flight-time difference of the two fragments, the vector velocities of the fragments may then be determined. The relative translational energy distribution of  $\text{H}_2$  and H fragments were observed to group into two distinct features. The first, centered at about 2.7 eV was narrow and structureless, while the second was broad and highly structured, spanning the energy range of 3.8 - 5.85 eV. The first feature was explained as coming from  $\text{H}_2$ -H fragments produced from the dissociation of  $\text{H}_3$  in the repulsive ground state. In contrast, the second was interpreted in terms of a predissociation of a bound excited state of  $\text{H}_3$ . The vibrational quanta and zero-point energy observed

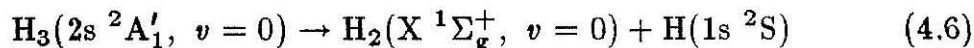
from the structured second energy distribution agree with the calculation done by Porter<sup>20</sup>. On the basis of Porter's calculation, Vogler proposed an interpretation in terms of semidiscrete vibronic levels in the upper sheet of the Jahn-Teller double potential surface of the ground  ${}^2E'$  electronic state of  $H_3$  for creating the structure in his observed high energy distribution.

This technique was then used by Cisneros and co-workers<sup>21</sup> where he observed the angular distribution of the dissociation products  $D_2$  and  $D$  following electron transfer from  $Cs$  to  $D_3^+$  at collision energies ranging from 1.0 - 7.0 keV. In this case the relative translational energy of the fragments corresponded roughly with the 3.8 - 5.85 eV range observed by Vogler. However, the structure observed by Vogler was absent in the Cisneros experiment. This difference may be due to the lower angular resolution of the Cisneros experiment. Porter *et al.*<sup>22,23</sup> have also attempted this kind of experiment, producing  $H_3$  by electron transfer from  $Mg$  to 4 keV  $H_3^+$ . Ionic and neutral species are then counted by a electron multiplier having a 2 keV threshold. This detector can be moved along a line perpendicular to the projectile beam axis. In this experiment the observed relative translational energy of the  $H_3$  dissociation products corresponded roughly to the low energy feature of the distribution observed by Vogler. As a result, while Vogler interpreted his results in terms of an electronically excited  $H_3$  molecule, Porter<sup>22,23</sup> interpreted his results as due to  $H_3$  formed in its lowest energy configuration, the repulsive ground state. However, in none of the above experiments<sup>18,19,21,22</sup> was there any evidence seen for a long-lived state of  $H_3$ .

At roughly the same time new experimental evidence for  $H_3$  came from a novel experiment by Herzberg. In an attempt to observe and characterize the ro-vibrational spectrum of  $H_3^+$  Herzberg used an ordinary hollow cathode discharge tube to observe the emission spectrum. While we were running  $H_2$  in

it at 1 torr a different spectrum was obtained at the cathode end than at the anode end. Subtraction of the two spectra resulted in a series of broad bands in the visible region that could be assigned to  $\text{H}_3$  electronic transitions<sup>24-28</sup>. Strangely enough, other configurations of hollow cathode sources had failed to give the spectrum observed by Herzberg<sup>26</sup>. These emission band spectra, due to Rydberg to Rydberg transitions of  $\text{H}_3$ , will be discussed later in section 4.3.

The findings of Herzberg stimulated theoretical calculations<sup>29-36</sup> which successfully describe the rotation band spectra of Herzberg. Recently, Mayne and co-workers<sup>37</sup> have calculated the absorption spectra of transition state configurations of  $\text{H}_3$ . Other theorists have already begun to extrapolate to larger systems and have performed calculations on Rydberg states of  $\text{H}_4$ <sup>38</sup> and  $\text{H}_5$ <sup>39</sup>. Because of this theoretical effort some interpretations of previous experiments have been changed. Watson<sup>40</sup> re-evaluated Vogler's past result<sup>18,19</sup> and suggested that the structured energy distribution observed was not due to a Jahn-Teller sheet, as proposed by Vogler, but rather a predissociation from a Rydberg state of  $\text{H}_3$ . Watson noted that the lowest excited  $\text{H}_3$  state was a Rydberg state which can be described as a  $2s \ ^2A'_1$  state. The King and Morokuma calculation shows that the predissociation process



is exothermic by approximately 5.57 eV. On the basis of this theoretical result Watson proposed that Vogler's product energy distribution was due to the above predissociation, thereby making Vogler's work the first experimental determination of the energy of a known electronic state of  $\text{H}_3$  relative to the dissociation products of  $\text{H}_2$  and H.

In light of Herzberg's results and because of a private communication

of our own results, Porter repeated his charge-exchange experiments in an attempt to observe a long-lived species of  $H_3$ . By increasing the angular resolution of his apparatus<sup>41</sup> as well as using K instead of Mg as the charge-exchange target, he was able now to observe a metastable state of  $H_3$ <sup>42</sup>. This result will be discussed in greater detail in Section 4.7.

As a result of Herzberg's work, a great deal of interest has been generated recently in the spectroscopy of  $H_3$ . Freeman *et al.*<sup>43</sup> attempted to stimulate  $H_3$  emission by pulsing 1 torr of  $H_2$  with high energy (0.53 MeV) electrons, in an attempt to understand why the conditions of a hollow cathode discharge would favor the formation of  $H_3$  as observed by Herzberg<sup>24-28</sup>. However, the experiment failed to detect any such emission. A much more successful effort has been made in employing laser spectroscopy to study the hollow cathode discharge of  $H_3$ . Figger and co-workers<sup>44,45</sup> performed this experiment by first observing the emission from a DC discharge in flowing  $D_3$ . Then by setting this discharge tube, vacuum-tight, in the tuning arm of a color-center laser, they observed the discharge emission at a selected line of  $D_3$ , as a function of laser frequency. Thus by observing the laser induced change in the emission, this method is sensitive to population changes in the upper level of the transition, as directly monitored by the monochromator. In this way the assignment of the lines they observe is simplified since the upper level is defined by the monochromator setting. This type of color-center laser intracavity spectroscopy has proved extremely helpful in the observing and assigning of new spectral features of  $D_3$ .

The most recent work on  $H_3$ , and perhaps the most exciting, is spectroscopy on beams of the metastable species. Figger *et al.*<sup>46</sup> have begun to perform spectroscopy on beams of  $D_3$  created by charge-transfer of 5 keV  $D_3^+$  with alkali metals. In the charge-exchange process the  $D_3$  molecules are

produced in excited states, such that after leaving the alkali metal cell they emit light in a collision free region, which is then measured spectroscopically. To date only transitions between the Rydberg states  $n = 3$  and  $n = 2$  have been observed. However, all the lifetimes measured by this technique are in good agreement with the *ab initio* calculation by King and Morokuma<sup>29</sup>. The fact that transitions from the higher-lying states are not observed is an indication that the  $n = 3$  state is more efficiently populated by the direct charge-exchange process than by cascading from higher Rydberg levels. Experiments are planned by this group to excite higher Rydberg states in the  $D_3$  beam by laser radiation and detect the excitation of the higher state via electric field ionization of the excited state.

In this section of the thesis we report the first direct observation of a hyperthermal beam of metastable  $H_3$  molecules, intense enough for scattering and absorption spectroscopy experiments<sup>47</sup>. The following section will discuss the generation and characterization of this molecular species and possible explanations for its long lifetime.

## 4.2 Detection

Through characterization and development of an arc-discharge source for the production of hyperthermal hydrogen atoms, it was observed that this plasma source was capable of generating other novel molecular species. The source and its operation have already been described in Section 2 of this thesis. The beam apparatus is depicted schematically in Figure 1. The discharge source is similar to that described previously<sup>48-50</sup>. It is placed in a vacuum chamber [VC1], pumped by a 20" Westinghouse oil diffusion pump, and is connected by a flexible bellows to a test stand consisting of a bell jar [VC2] pumped by a system comprising a 6" mercury diffusion pump, a freon-cooled chevron baffle and a liquid nitrogen trap. Differential pumping between these two chambers is provided by a skimmer [S] with an orifice diameter of about 1 mm with a knife-sharp edge. Chamber VC2 contains a beam flag [F], a beam chopper which modulates and allows ac detection of the beam [C1], a pair of electric deflector plates which eliminate ions from the beam [D], and an EAI 300 quadrupole mass spectrometer with an electron bombardment ion source [QMS].

The CW arc discharge in the H-atom source can be run continuously for many hours with a H<sub>2</sub> stagnation pressure of 50-100 torr such that the pressure in chamber VC1 is of the order of 10<sup>-2</sup> torr and the pressure in chamber VC2 is of the order of 10<sup>-5</sup> torr. The source [AS] can be moved with respect to the skimmer with the help of a translation stage [TA] such that the apparatus can be operated in two modes. The first mode, in which the nozzle is far away (~ 10 cm) from the skimmer (as depicted in Figure 1), allows spectroscopic observation of the intense red emission of the plasma

plume in front of the nozzle. The second mode involves moving the nozzle to within 4 cm of the skimmer to maximize the intensity of the H-atom beam as detected by the mass spectrometer. Despite grave initial difficulties in running the source it is now capable of producing a reliable, intense beam of hyperthermal hydrogen atoms (as described in Section 3 of this thesis).

It was during the initial successful running of this hydrogen atom source that an ion signal at  $m/e = 3$  was first observed. Through use of the chopper it was ascertained that both the signal at  $m/e = 1$  and 3 were chopped at the same frequency ( $\sim 8$  Hz). From this it would appear that both signals were due to species which were generated within the beam and not due to some background contaminant present in the bell jar.

Due to use of the ion deflection plates it was ascertained that the signal which is observed is not due to ions initially present in the beam. Figure 4 in section 3.1 of the thesis shows the behavior of the  $m/e = 3$  signal with increasing ion deflection field. As in the case of the  $m/e = 1$  species (Figure 2, Section 3.1) it is observed that at fields sufficiently large the mass signal levels out indicating that all ions have been swept out of the beam before they have a chance to reach the mass spectrometer.

Perhaps the most convincing proof that the  $m/e = 3$  signal is due to a neutral species is shown in Figure 2. Here the ac signal from the mass spectrometer electronics was monitored by a PAR lock-in amplifier as a function of mass. By slowly scanning that mass, a mass spectrum is generated. The upper curve shows the signal obtained with the ionizing current of the mass spectrometer turned on. As described previously in Section 2.5.2 of this thesis, the mass spectrometer ion focusing lens voltages are turned off in order to discriminate against the  $H_2$  background present in the bell jar chamber. As a result only the neutral species in the beam, with translation energy in the

axial direction of the quadrupole rods, will be observed. In the case of using  $\text{H}_2$  gas in the discharge, as shown in the top curve of Figure 2a, virtually all of the  $\text{H}_2$  is dissociated to produce  $\text{H}$  and  $\text{H}_3$ . When the ionizer is turned off any observed signal will be due to ions which were able to get through the deflection plates because they have sufficiently high kinetic energy, or due to ions produced in the ionizer region from energetic collisions between background molecules and species in the beam. As shown in the lower curve of Figure 2a, with the ionizer off the ac signal virtually vanishes.

Using  $\text{D}_2$  in the arc discharge (figure 2b) a  $m/e = 6$  signal is observed, presumably due to a  $\text{D}_3$  neutral species. As before virtually all the  $\text{D}_2$  is dissociated to produce  $\text{D}$  at  $m/e = 2$  or  $\text{D}_3$  at  $m/e = 6$ . The small signal at  $m/e = 1$  is due to dissociation of the unavoidable  $\text{HD}$  contamination present in the  $\text{D}_2$  used. Again, as in Figure 2a, turning the electron beam off causes the mass signal to disappear almost completely. Finally, using a 50 : 50 mixture of  $\text{H}_2$  and  $\text{D}_2$  in the source, the expected mixture of  $\text{H}_3$ ,  $\text{DH}_2$ ,  $\text{HD}_2$ , and  $\text{D}_3$  is observed in Figure 2c. As before, turning off the electron beam causes the signal virtually to vanish. In these measurements, using a calibrated electrometer (as was described in Section 3.2 of this thesis), an  $\text{H}_3$  intensity of the order of  $10^{20} - 10^{21}$  molecules/sterad/s is observed.

We observed in this work that the proportions of  $\text{H}$  and  $\text{H}_3$  strongly depend on the source's stagnation pressure. This relationship is illustrated in Figure 3 where the dc signal for  $m/e = 1, 2,$  and  $3$  is plotted as a function of stagnation pressure at constant arc power (40V, 100A). As can be seen in Figure 3, at high stagnation pressure the  $\text{H}$  signal is small and no signal is observed at  $m/e = 2$  or  $3$ . As the stagnation pressure is decreased the  $m/e = 1$  and the  $m/e = 3$  signals rise rapidly. What appears to be happening is that the decrease in stagnation pressure at constant power increases the

effective temperature of the plasma. At lower stagnation pressures there is a lower density of molecules, and more energy is available per molecule. This is in keeping with other empirical observations: the most damage occurs at the nozzle at the lower stagnation pressure (melting of nozzles, shorts between the anode and the cathode, etc.), the brightness of the plasma emission increases, and the translational energy of the beam species rises (Section 3.3). Thus, increasing the temperature of the plasma enhances the amount of dissociation of  $H_2$  and as a consequence increases the formation of  $H_3$ . In fact, the rapid onset of both curves with decreasing stagnation pressure might be interpreted as a threshold effect, such that only above a certain energy density (or below a certain stagnation pressure) does the  $H_2$  start to dissociate to a large extent to form H atoms and then only at even higher temperatures does  $H_3$  start to form. As a result, we may use the stagnation pressure to control the relative amount of  $H_3$  with respect to H.

At very low stagnation pressure the mass signal of both  $m/e = 1$  and  $3$  is observed to decrease to some extent. This may be an artifact due to the changing geometry of the nozzle at such high temperatures. However, it may also be due to the fact that at such high temperatures many more charged species are being formed in the plasma. If the ion density increased by a large extent, the 'focusing' effect of the magnet might be negated by space charge effects. Thus these ions would repel each other out of the field and lower the intensity of the neutrals observed downstream.

A crude energy analysis of the  $H_3$  species was performed through the use of ion-retarding elements in the optics of the mass spectrometer, as explained in Section 3.3 of this thesis. These results indicate that a major fraction of the  $H_3$  has laboratory translational energies in the range of 0 - 10 eV. From these measurements it is possible to estimate flight times and obtain a

lower bound for the lifetime of the observed  $H_3$  species on the order of 40 - 100  $\mu s$ . Comparing the translational energies of H and  $H_3$  formed at the same stagnation pressure (Figures 6b and 7a, Section 3.3), it is seen that they are roughly equal with the energy distribution of  $H_3$ , being considerably broader than that of the hydrogen atoms. That both species have similar average translational energies is not too surprising since both are formed in the same medium and should be heated to about the same temperature. Increasing the  $H_2$  stagnation pressure from 75 torr to 95 torr (Figure 7a and 7b, Section 3.3) decreases the laboratory translational energy of  $H_3$  from a peak value of 7 eV to a peak value of 4 eV. This effect shows again that an increase in the stagnation pressure decreases the temperature of the plasma and as a result the translation energy of the species generated within it. Previously it had been observed that a small addition of Ar to the  $H_2$  flow through the source shifted the H atom translational energy to lower energy, presumably due to seeding or perhaps to some quenching effect the Ar has on the plasma. Attempting to do this with  $H_3$  decreased the  $H_3$  signal to such an extent that it was not possible to measure the translational energy. Again the Ar appears to affect the discharge by cooling the plasma to such an extent that the generation of  $H_3$  is suppressed.

The only other origin for the observed  $m/e = 3$  signal would be that some ion-molecule reaction in the ionizer region of the mass spectrometer could form  $H_3^+$ . Since  $H_2^+$  is created in the ionizer region of the mass spectrometer, from the  $H_2$  present in the beam, the ion could react with neutral background gas to form



The product  $H_3^+$  would then be detected by the mass spectrometer and give a signal which would be consistent with our observations. However, this pos-

sibility is precluded by observing that the expected signal from that potential source is less than  $10^{-3}$  the observed  $m/e = 3$  signal. A simple experiment to disprove this was suggested to us by Prof. J. Beauchamp. The experiment consists of filling the bell jar chamber with  $2 \times 10^{-5}$  torr of  $D_2$  while the beam was operating and detecting any change in the mass spectrum of the beam. If the  $m/e = 3$  signal was in any way due to ion-molecule reaction, the  $m/e = 3$  signal should have dropped and signals at  $m/e = 4, 5$  should have been observed due to



Under these conditions we observed no change in the mass spectrum, thereby ruling out that the  $m/e = 3$  signal was created by reaction with background gas in the ionizer region of the mass spectrometer. This topic will be treated in greater detail in Section 4.7 of this thesis. It should be noted that neither Stwalley<sup>51</sup> nor Toennies<sup>52</sup>, who have both employed similar sources in the past, have not reported the observation of a neutral  $H_3$  species. Stwalley has informed us that he operated at less power than we do, and that his nozzle was positioned at the exit of the axial magnet (in contrast to our location in the center of the magnet). He reported<sup>52</sup> that his magnetic field in no way influenced his plasma and that he could operate his hydrogen plasma with it either on or off. This is in contrast with the results of Bernstein<sup>53</sup> who, in the operation of a nitrogen plasma (using a device very similar to that of Kunth<sup>48</sup> and of Stwalley<sup>50</sup>) showed his source temperature to rise from 6650 K to 17000 K after turning on the axial electromagnet (750 gauss). Varying the magnetic field he was able to continuously change the nozzle source temperature, which he used as a simple means for varying the translational

energy of the N atom beam. No explanation was suggested for the effect, but clearly the magnetic field increased the arc temperature by well over a factor of three. Likewise, he observed that the magnetic field increased the intensity of N atoms produced by a factor of three.

In the operation of our source we have found it impossible to generate a hydrogen discharge without a magnetic field of at least 1000 G. At lower fields the source immediately shorts out upon the introduction of hydrogen gas into the argon discharge. If there are any instabilities in the magnetic field they produce instabilities in the discharge (sparking, oscillation of the plume, etc.) While running a pure hydrogen discharge in the source, it is possible to see dramatic changes in the shape of the plasma plume with magnetic field. By increasing the current through the electromagnet, the 'pencil' plasma becomes much more intense as well as narrower. It is our personal feeling that this focusing effect of the magnet on the plasma discharge may be the major reason for our beam appearing more intense as well as for the generation of the metastable  $H_3$  beam. Clearly the focusing of the plasma will increase the intensity of the beam since more molecules will make it through the skimmer than for a simple effusive source. In addition, if this effect increases the interaction time of the particles within the high-temperature plasma, perhaps this accounts for the mechanism for the generation of  $H_3$  (ie., three-body collision, ion-molecule reaction, neutral-excited species reaction, etc.) becomes that much more probable. Whatever the actual mechanism for the generation of  $H_3$  in the plasma is, it appears a high temperature as well as a high magnetic field is essential to its creation. Also, because of the difference between our experimental conditions and those of Stwalley's and Toennies (effect of magnetic field, our redesign of the geometry of the source, pumping capacity, etc.), it would appear that one should indeed be able to generate

beams having different characteristics.

We conclude that our high-temperature source for hydrogen atoms can, under the appropriate conditions, become a source of a metastable neutral  $H_3$  species. How metastable  $H_3$  molecules with such long lifetimes can be formed, and what electronic state could be responsible will be addressed in the next section.

### 4.3 Emission Spectrum

As mentioned in the introduction, Herzberg and co-workers<sup>24-28</sup> have been studying the light emitted from the cathode region of a hollow cathode discharge through hydrogen or deuterium at about 1 torr pressure and temperatures down to that of liquid nitrogen (cooling greatly strengthens the intensity of the emission observed). While the emission glow in the anode side gave only spectra of  $H_2$ , the glow in the cathode column gave spectra of  $H_2$  and discrete spectra of triatomic hydrogen. They observed bands at 5600, 6025, and 7100 Å. A detailed analysis of these bands led to their assignment as due to transitions between Rydberg states of  $H_3$  which are spin doublets with  $A'_1$ ,  $A''_2$ ,  $E'$ , or  $E''$  symmetry, with the Rydberg electron being in a 2s, 2p, 3s, 3p or 3d type state. What follows is a detailed review of this work and its conclusions concerning the possibility of a metastable species of  $H_3$ .

The  $H_2$  visible spectrum has been the subject of much work, and at one time part of this spectrum was suggested to be due to the  $H_3$  molecule<sup>54-57</sup>. However, as more and more lines were identified as belonging to  $H_3$ , culminating in the tables published by Dieke<sup>58</sup>, not a single line observed in various discharges in hydrogen was assigned to any species other than  $H_2$ . It was a great surprise then when Herzberg observed new spectra in his discharge tube. By increasing the pressure to 1.0 torr and lowering the temperature to that of liquid nitrogen, a considerable enhancement is observed in the  $H_3$  spectrum relative to that of  $H_2$ . Attempts to date to observe this spectrum in other types of sources have failed. What has been a great aid in the assignment of these features is that the  $H_3$  spectrum in the positive column of the hollow cathode discharge is absent. Indeed, the comparison of the spectra of the

negative glow in the hollow cathode and the positive column of the same discharge provides a reliable indication whether the line was due to  $H_2$  or  $H_3$ . To aid in this identification Herzberg superimposed a negative print of the anode spectrum on the original of the cathode spectrum. In this way the  $H_2$  lines are more or less eliminated and all that remains are features due to  $H_3$ .

The lines of the 5600 and 7100 Å bands of  $D_3$  are very broad, with the corresponding  $H_3$  bands being four times as broad. The fact that they have the same width suggested not only that they shared the same lower state but that the state was strongly predissociated ( $\sim 0.8 \times 10^{-12}$  s), the lower state being the first excited state of  $H_3$ . This assignment has since been confirmed with the 5600 Å band attributed to the parallel transition  $3d \ ^2A_2'' \rightarrow 2s \ ^2A_1'$  and the 7100 Å being due to the perpendicular transition  $3p \ ^2E' \rightarrow 2s \ ^2A_1'$ . The 7100 Å transition is indicated by arrow 1 in figure 4.

However, the bands at 6025 Å of  $H_3$  are much sharper than those of the 5600 band (yet still broader than the  $H_2$  lines in that region). As a consequence the band was assigned as the  $3d \ ^2E'' \rightarrow 2p \ ^2A_2''$ , the lower state of this transition being the second excited state of  $H_3$ .

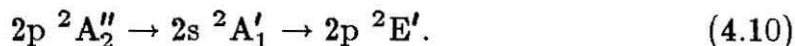
As a result, from these bands rotational constants may be derived and bond distances calculated. The  $2s \ ^2A_1'$  state has an  $r_o = 0.8453$  Å while the second excited state, the  $2p \ ^2A_2''$ , has an  $r_o = 0.8667$  Å. Unfortunately, there are not a great deal of experimental bond distances for  $H_3^+$  to compare to these values. The experiments of Gaillard *et al.*<sup>59</sup> using foil-induced dissociation of an  $H_3^+$  beam obtained an experimental value of  $r_o = 0.97 \text{ Å} \pm 0.03 \text{ Å}$  for  $H_3^+$  which is somewhat larger than the theoretical value, due probably to vibrational excitation. A recent experiment by Oka<sup>60</sup> in which the infrared spectrum of  $H_3^+$  was observed found  $r_o = 0.88 \text{ Å}$  for  $H_3^+$ <sup>42</sup>. From this result

it is evident that the excited states of  $H_3$  have a contracted geometry  $\sim .02-.04 \text{ \AA}$  from the ground state of  $H_3^+$  while retaining the  $D_{3h}$  symmetry. This contracted geometry may be due to the diffuseness of the Rydberg electron interacting with the  $H_3^+$  core.

If we now consider the lifetimes of the  $2s \ ^2A'_1$  and  $2p \ ^2A''_2$  states, the  $2s \ ^2A'_1 \rightarrow 2p \ ^2E'$  predissociation, as shown in Figure 4, arrow 2, is forbidden by electronic considerations. It is known that forbidden transitions can have intensity due to vibronic coupling. Using symmetry considerations, it is usually assumed that there is some symmetrical, equilibrium internuclear configuration for the molecule. However, molecules are undergoing vibrations and the molecular symmetry can change considerably. Forbidden electronic transitions may become allowed by certain vibrational modes, but usually not by all. Symmetry considerations for  $H_3$  would indicate that the predissociation of the  $2s \ ^2A'_1$  state into the  $2p \ ^2E'$  state becomes allowed by vibronic interaction through a normal mode of species  $e'$  which transforms  $A'_1$  into  $E'$ . If the Franck-Condon factor is large, these predissociations will be strong. However, there is no vibrational motion in  $H_3$  which can transform  $2p \ ^2A''_2$  into  $E'$ . Only ro-vibronic interaction can induce predissociation and the predissociation of the  $2p \ ^2A''_2$  state must occur through a rotational motion about an axis perpendicular to the symmetry axis of the molecule. This conclusion has been confirmed by line width measurements; since the widths of the  $6025 \text{ \AA}$  band are about two orders of magnitude sharper than the  $5600 \text{ \AA}$  band<sup>25</sup>. It should be mentioned that they are also twice as wide as the corresponding  $H_2$  and  $D_2$  ones. This residual broadening may be due to a Doppler effect associated with possibly large kinetic energies of the thermalized  $H_3^+$  or  $D_3^+$  ions whose recombination with electrons, in the cathode discharge, is assumed to be responsible for the formation of the neutral ex-

cited  $H_3$  or  $D_3$ . Herzberg deduces an effective translational temperature of 3000 K for the  $2s \ ^2A'_1$  state of  $D_3$  formed in his discharge. Under these conditions, the line widths of emissions of translational thermalized Rydberg states to the  $2p \ ^2A''_2$  one could be even narrower than what was observed in his experiments. Therefore, the emission coefficients for the  $2p \ ^2A''_2 \rightarrow 2p \ ^2E'$  are expected to be small, as the transition is forbidden by electronic selection rules. Although the lifetime of the  $2p \ ^2A''_2$  state of  $H_3$  or  $D_3$  is not experimentally known, these considerations indicate that it could be very large, perhaps in excess of 1  $\mu\text{sec}$ .

Since spontaneous emission to the ground state is strongly forbidden, the only other means for the state to relax radiatively from this state is via the process



From the King and Morokuma calculations<sup>29</sup> one can calculate an Einstein emission coefficient of  $\sim 1.2 \times 10^4 \text{ s}^{-1}$  for the  $2p \ ^2A''_2 \rightarrow 2s \ ^2A'_1$  process. This results in the lifetime for that transition being  $\sim 87 \mu\text{sec}$ <sup>42</sup>.

On the basis of these considerations we feel the  $2p \ ^2A''_2$  state is the most likely candidate for the metastable  $H_3$  molecule which we have observed in our arc-heated beam. With a bond distance some .02 Å smaller than  $H_3^+$ , the metastable molecule may be pictured as an  $H_3^+$  core in an equilateral triangle geometry, with the Rydberg electron (which makes it neutral) in a  $2p$  orbital perpendicular to the plane of the triangle. As a result, the triangle contracts slightly to accommodate the additional electron. Figure 5 shows a representation of this molecule with a hydrogenic  $p_z$  orbital (perpendicular to the plane of the nuclei) representing the  $2p$  Rydberg orbital of  $H_3$ . Further evidence for the assignment of the metastable  $H_3$ 's being in the  $2p \ ^2A''_2$  state comes from the recent experiments performed by Porter and co-workers<sup>41,42</sup>

and will be discussed in Section 4.7 of this thesis.

In order to obtain further and independent evidence concerning the presence of neutral  $H_3$  in our discharge, we looked at the light emanating from the region between the nozzle and the skimmer of the arc source, in the wavelength region between 5000 Å and 7500 Å through a Jarrell-Ash 0.5 m monochromator. The experimental set-up is described in section 3.4 of the thesis. Our feeling was that, if the generation of  $H_3$  was through the metastable state  $2p \ ^2A''_2$ , then it must be populated from higher Rydberg states of  $H_3$  which are excited initially by the high temperature conditions of the discharge. If this is the case, then it would be reasonable to assume that emission from the plasma should contain bands which Herzberg has already reported.

Figures 6 and 7 show the typical emission spectrum observed while running a pure hydrogen (deuterium) arc at 60 torr. The sharp reproducible structure is due to emission of  $H_2$  or  $D_2$ . In the case of  $H_2$  we are able to assign the majority of these peaks based on the assignments of Dieke<sup>58</sup>, and the assignments are shown in Table I. As can be seen from these transitions many of the peaks are due to highly excited states of  $H_2$ , again showing that the plasma is indeed electronically a very hot medium.

As was already discussed, Herzberg was able to differentiate his spectrum from the  $H_2$  continuum by merely subtracting the anode spectrum from the cathode spectrum. We, of course, cannot do this in our experiment; hence the many  $H_2$  transitions serve to obscure the broad, diffuse  $H_3$  bands which lie underneath. Looking in the 5500 Å to 6100 Å emission region of our plasma for  $H_3$  features proved fruitless due the number of  $H_2$  transitions obscuring it. However, in the 7100 Å region we were able to observe some broad bands which may be directly compared to the bands observed by Herzberg.

TABLE I

## Assigned Hydrogen Molecule Transitions

Wavelength (Å)	Transition Assignment
6995.2	$3d\ ^3\Sigma (v=0) \rightarrow 2p\ ^3\Pi (v=1)$ , R6
7059.7	$3p\ ^1\Sigma (v=4) \rightarrow 2s\ ^1\Sigma (v=1)$ , R3
7071.2	$3d\ ^1\Sigma (v=3) \rightarrow 2p\ ^1\Pi (v=2)$ , Q2
7091.0	$(2p\sigma)^2\ ^1\Sigma (v=4) \rightarrow 2p\ ^1\Sigma (v=1)$ , P6
7128.7	$3s\ ^1\Sigma (v=0) \rightarrow 2p\ ^1\Pi (v=0)$ , R2
7146.3	$4d\ ^3\Delta (v=0) \rightarrow 2p\ ^3\Pi (v=4)$ , P3
7157.2	$2p\ ^3\Pi (v=0) \rightarrow 2s\ ^3\Sigma (v=1)$ , P2
7162.0	$3d\ ^3\Sigma (v=2) \rightarrow 2p\ ^3\Pi (v=3)$ , Q4
7166.2	$3d\ ^3\Sigma (v=3) \rightarrow 2p\ ^3\Pi (v=4)$ , Q1
7168.2	$3p\ ^3\Pi (v=1) \rightarrow 2s\ ^3\Sigma (v=2)$ , P5
7170.6	$3d\ ^3\Sigma (v=0) \rightarrow 2p\ ^3\Pi (v=1)$ , P5
7187.9	$3p\ ^3\Pi (v=1) \rightarrow 2s\ ^3\Sigma (v=2)$ , Q4
7254.5	$3p\ ^3\Pi (v=3) \rightarrow 2s\ ^3\Sigma (v=4)$ , R1 $3d\ ^1\Delta (v=0) \rightarrow 2p\ ^1\Sigma (v=7)$ , P4

TABLE I cont.

## Assigned Hydrogen Molecule Transitions

Wavelength (Å)	Transition Assignment
7257.5	$3p \ ^3\Pi (v=2) \rightarrow 2s \ ^3\Sigma (v=3), Q4$
7262.5	$3p \ ^1\Pi (v=1) \rightarrow 2s \ ^1\Sigma (v=1), R2$ $3p \ ^3\Sigma (v=1) \rightarrow 2s \ ^3\Sigma (v= ), R3$
7267.6	$3p \ ^3\Pi (v=2) \rightarrow 2s \ ^1\Sigma (v=3), Q5$
7274.1	$3p \ ^3\Pi (v=2) \rightarrow 2s \ ^1\Sigma (v=2), R3$
7281.0	$3p \ ^3\Pi (v=2) \rightarrow 2s \ ^3\Sigma (v=3), Q6$
7289.9	$4d \ ^1\Sigma (v=0) \rightarrow 2p \ ^1\Pi (v=2), R2$
7299.1	$3p \ ^1\Pi (v=0) \rightarrow 2s \ ^1\Sigma (v= ), Q2$

Figure 8 directly compares our emission spectrum at 60 torr (7b) with Herzberg's spectrum (7c). It should be noted that the Herzberg spectrum is a photometer curve with the sharp  $H_2$  peaks removed for ease of observing the underlying  $H_3$  structure. As assigned by Herzberg this band corresponds to a perpendicular transition of  $3p \ ^2E' \rightarrow 2s \ ^2A'_1$  (Figure 4, arrow 1). As can be seen from Figure 8, our emission spectrum corresponds well with the band positions of Herzberg's spectrum. However, the intensities of the bands do appear different. This may be due to the differences between the hollow cathode discharge and our arc discharge. It should also be noted that we are observing the emission some 5 cm downstream from the nozzle where the discharge is sustained. As a consequence, this part of the plasma is probably 'colder' than directly at the nozzle; hence the spectroscopy observed at both points should be different. In the current configuration of the apparatus it is impossible to view at any point closer to the nozzle. But the detection of a band similar to that independently observed by Herzberg gives direct evidence that neutral  $H_3$  in high Rydberg states are formed in the region of the plasma. It is not unreasonable to assume that the lower lying metastable states can be formed either as a result of emission from higher Rydberg states directly into the metastable state and perhaps also by a direct three-body  $H_3^+ + e^-$  recombination into that state.

Figure 8a shows the emission at 100 torr stagnation pressure. In this figure all features attributed to  $H_3$  have disappeared. If we monitor the 7120 Å band as a function of stagnation pressure (Figure 9) we see the intensity fall as a function of pressure, such that the strongest signal is observed at low stagnation pressure while at higher pressure the features virtually disappear. This indicates a lower electronic temperature at higher pressures and a correlation between the forming of high Rydberg states of  $H_3$  (as detected by the

light emission) with the appearance of the lower metastable  $2p\ ^2A_2''$  state (as detected by the mass spectrometer). We have already seen in this thesis that, at constant power, reducing the stagnation pressure increases the amount of hydrogen atoms produced (Section 3.2) as well as their translational velocity (Section 3.3). This was interpreted that at lower stagnation pressure the temperature of the plasma increases significantly. We have also seen that the amount of  $H_3$  also increases with decreasing stagnation pressure (Section 4.2). It is now possible, in light of the emission results, to unambiguously see how stagnation pressure affects the electronic temperature of the plasma. As a result, we conclude that lower stagnation pressure increases the number of high Rydberg  $H_3$  molecules produced, of which some, while relaxing, get trapped in the metastable  $2p\ ^2A_2''$  state, increasing the amount of  $H_3$  produced.

In the case of  $H_3$  we attempted to look for other broad feature in the visible spectrum which might also be due to  $H_3$  transitions but may not have been observed by Herzberg. The only feature found was a very weak band at 7480 Å which is shown in Figure 10a. The position of this band corresponds to the frequency calculated by King and Morokuma<sup>29</sup> for the transition  $2s\ ^2A_1' \rightarrow 2p\ ^2E'$  and is depicted in Figure 4 by arrow 2. This assignment is consistent with the unusually large width ( $\sim 50$  Å) of the band due to the repulsive character of the the  $2p\ ^2E'$  ground state. It should be noted that all other assignments from the King and Morokuma calculation<sup>29</sup> compare very favorably with the spectra observed by Herzberg. If this assignment is correct, then the width of this band is related to the shape of the  $2p\ ^2E'$  potential energy surface in the Franck-Condon region. As a result this band could give detailed information on the saddle point region of the  $H + H_2$  reaction, or, conversely, since the ground surface is well known from *ab initio* calculations, the band width could provide information about the geometry of the upper state from which the emission emanates, serving to verify if the upper state

is indeed the  $2s\ ^2A'_1$  state.

Observing how this band behaves with stagnation pressure (Figure 10b), it is seen that behavior is converse to that of the 7100 Å. The intensity of the 7480 Å band increases with increasing stagnation pressure as opposed to the 7100 Å which increases with decreasing pressure. This is consistent with the fact that at higher pressure the electronic temperature of the plasma is reduced. One could then imagine at these colder temperatures that the upper Rydberg states are not as populated. Since these higher states are not populated, there is a far lesser chance for them to cascade into the metastable state,  $2p\ ^2A''_2$ . As a result, at these colder temperatures the intensity of the 7100 Å band decreases and there is less  $H_3$  produced in the beam. Since these upper states are not being populated, then the first excited state, the  $2s\ ^2A'_1$  state, no longer has to compete with the rest and can be populated to a larger extent. This increase in the population with increasing pressure results in a rise in the intensity of the 7480 Å emission.

Despite the agreement with King and Morokuma's calculation<sup>29</sup> and the large width which we observe for that 7480 Å band, upon communication of our result Herzberg did not think the 7480 Å band would be due to the  $2s\ ^2A'_1 \rightarrow 2p\ ^2E'$  transition since the  $2s\ ^2A'_1$  state is predissociated<sup>61</sup>. This has been concluded previously by Herzberg<sup>25</sup> from the unusually large widths of Rydberg bands which end in that state which he observed (5600 Å and 7100 Å bands). However, this predissociation reported by Herzberg is only possible due to the vibronic mixing of the  $e'$  vibration. The other vibrational mode of  $H_3$ , the  $a'$ , will not result in predissociation of the  $2s\ ^2A'_1$  state. This vibration corresponds to the symmetric in-plane stretch of  $H_3$ . If this vibrational state was populated in our  $H_3$  beam, it might be expected that emission from the  $2s\ ^2A'_1$  state to the  $2p\ ^2E'$  state could be observed. The predissociation which Herzberg observed may be caused due to collisional

relaxation to the  $e'$  vibrational level which could occur in his hollow cathode discharge but may not occur in our hyperthermal beam. The  $2s\ ^2A'_1$  state then would have a much longer lifetime, and emission from it might indeed be what we have observed, despite Herzberg's reservations. From this analysis it appears that our original assignment of the 7480 Å transition might be correct, and is certainly consistent with our experimental data.

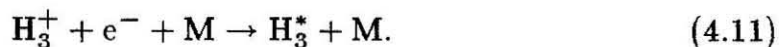
One future experiment which would assign this transition with certainty is to do laser excitation of that  $2s\ ^2A'_1$  state of  $H_3$  resulting in ionization of  $H_3^+$ , and then to detect the product  $H_3^+$  ion. Shining the laser directly into the nozzle would ensure that the beam would be irradiated. However, this  $H_3^+$  ion would be difficult to detect to the presence of it already in the beam. This problem could be circumvented by chopping the laser beam and use of lock-in technique to detect the  $H_3^+$  generated. If this experiment worked, it would show that some vibrational levels of the  $2s\ ^2A'_1$  state had not predissociated, thereby showing one could observe emission from it.

The only other possibility for the 7480 Å band is that it could be a vibrational progression of the 7100 Å band, such that the transition was now ending in the  $v = 1$  level of the  $2s\ ^2A'_1$  state. But if this is the correct assignment, then it is hard to reconcile it with the observation of increasing intensity with increasing stagnation pressure.

In the case of observing the emission spectrum of  $D_2$  none of Herzberg's features were observed; they was probably obscured by the large number of  $D_2$  peaks. A progression of broad bands were observed in the expected region (Figure 7). These results were communicated to Herzberg who commented<sup>61</sup> that, while unusual in their large width and regular progression, he did not feel they were due to  $D_3$  but must be due to some other molecular species. The origin of these bands have yet to be assigned.

At this point it is necessary to interject some possible mechanisms for the

production of  $H_3$  as a function of stagnation pressure. To produce metastable  $H_3$  one might first think of a neutralization reaction of  $H_3^+$  such as



This process could occur in the plasma discharges; however, it should not exhibit such an increase at decreased stagnation pressure. What appears to be important in the production of  $H_3$  is the temperature of the plasma. Mechanisms such as



or even



might account for the behavior of the  $H_3$  production with stagnation pressure since at higher temperatures there would be more  $H^*$  and  $H_2^*$  formed, thereby increasing the amount of  $H_3$  formed. Any argument for a mechanism for the production of  $H_3$  must at this time remain as speculation due to the complexity of the plasma discharge where, due to the high temperatures and pressures, many different types of processes may become possible.

#### 4.4 Surface Ionization

When gaseous atoms hit a hot metal surface, an electron from the atom may be transferred to the metal. The process, known as surface ionization, was first discovered by Langmuir and Kingdom<sup>62</sup> in 1923. Since that time it has become a useful tool for ionizing molecules in mass spectrometers<sup>63</sup>, for sources of ion beams<sup>64</sup>, and as a detector for molecular beams<sup>65</sup>, particularly those containing atoms of low IP such as alkalis<sup>66</sup>.

The ratio of the number of ions ( $n_+$ ) to atoms ( $n_a$ ) evaporating from a surface with which they are in equilibrium is given by the Saha-Langmuir equation<sup>67-69</sup>

$$\frac{n_+}{n_a} = \left( \frac{1 - r_+}{1 - r_a} \right) \frac{\omega_+}{\omega_a} \exp \left[ \frac{e(\Phi - I)}{kT} \right] \quad (4.16)$$

where  $r_a$  and  $r_+$  are the reflection coefficients for atom and ion;  $\omega_+/\omega_a$  the ratio of the statistical weight;  $I$  the ionization potential of the atom;  $\Phi$  the thermionic work function of the surface and  $e$  the electronic charge. Being an equilibrium relation, its useful temperature range is limited to that over which neutral atoms do not permanently condense on the surface. A beam hitting the surface is not necessarily equivalent to an equilibrium situation and the state of the evaporating particle (ion or molecule) is determined not only by equation (4.16) but also by the probability that the beam atom will reach equilibrium with the surface<sup>65</sup>. This is taken into account by the inclusion of a reflection coefficient,  $r_i$ , for the incident atom (which is not necessarily the same as  $r_a$  since the beam atoms may not be at the filament temperature). The surface ionization efficiency of an atom traveling within a beam is then given by

$$I_{\text{eff}} = \frac{n_+}{n_a} = (1 - r_i) \left[ 1 + \left( \frac{1 - r_a}{1 - r_+} \right) \frac{\omega_a}{\omega_+} \exp \left( \frac{-e(\Phi - I)}{kT} \right) \right]^{-1}. \quad (4.17)$$

One can see then that the atoms in the beam will surface ionize if they have a low IP and if they impinge on a hot filament with a high work function.

This process has been of great interest to theoreticians for a long time<sup>70-77</sup>. It was through the early work of Gurney<sup>78</sup> that it was shown that the interaction of the atom with the metallic surface causes a broadening and a shifting of the energy levels of the atomic electrons<sup>79</sup>. As explained by Gadzuk<sup>80</sup>, the valence energy level of the atom shifts upward and broadens because of the interaction with the free electrons in the metal. This interaction lowers the ionization energy of the atom. A resonance transition of the valence level to an empty metal state (above the Fermi level) is now possible when the IP becomes lower than the work function of the metal.

The use of surface ionization revolutionized the field of reactive scattering when it was found that this process could be used as an extremely sensitive technique for measuring the flux of alkali metal beams. The usual form of this type of detector consists of a hot filament of either tungsten or platinum (typically operated at  $\sim 1870$  K for tungsten and  $\sim 1290$  K for platinum) which is suspended under spring tension between two insulating mounts. The work functions of these metal are 4.58 eV and 5.36 eV, respectively. The ends of the filament are connected to the D. C. power supply. The ends of the wire are usually shielded to prevent the colder regions of the wire from sampling the beam flux. The ions generated in this way are detected by a collector which is biased at 40 volts negative with respect to the filament and attracts the ions, creating thereby a current which is measured by an electrometer. For alkali metal beams such as Cs, Rb, Na, and K, the ionization efficiency can vary from 60 to 100%. As a result this detector has received much attention in molecular beam work<sup>81,82</sup>.

The ionization efficiency versus temperature<sup>65</sup> curves have in common a relatively steep rise in efficiency at a fairly definite temperature and a tendency

to decline at a higher temperature. This decline is attributed to formation of a stable adsorbed layer of the alkali metal concerned on the filament surface. This adsorbed layer then serves to decrease the work function of the surface and consequently lowers the efficiency of the surface ionization.

The translational energy of the atom beam can strongly influence the efficiency of the surface ionization. Thermal beams of alkali atoms are easily ionized by hot filaments of tungsten and platinum, but for very fast alkali beams ( $> 3$  eV) the efficiency of the detector drops off quickly. This presumably is caused by reflection effects at the surface due to the high collision energy. However, it has been found that these energetic alkalis can be surface ionized with cold filaments of high work function<sup>83</sup>. As observed by Helbing and co-workers<sup>84</sup>, a change in ionization efficiency occurs between threshold ( $\sim 7$  eV) and 50 eV, above which the efficiency becomes relatively constant ( $\sim 100\%$ ). Unity efficiency for positive ionization has also been observed by Overbosch and co-workers for sodium atoms ( $E \sim 100 - 400$  eV) colliding with W(110) surfaces<sup>85,86</sup>. So for neutral alkali atoms above 50 eV a cold filament is an excellent detector since there is virtually zero background signal. An additional advantage is that this cold detector has a very quick response time ( $< 0.1 \mu s$ ) and may be utilized in time-of-flight experiments. However, for energies between 3 eV and 50 eV neither hot nor cold filaments have very great efficiency for hyperthermal alkalis. The loss of sensitivity arising from the increased reflection of neutral particles for both hot and cold surfaces can be partly circumvented by using a detector which allows multiple collisions with the ionizing surface<sup>87</sup>. This detector operates by placing a tungsten cylinder around a niobium wire and by using the cylinder as the ionizer and the wire as the collector of the ions. Incident atoms which are not ionized by the first collision with the cylinder are prevented from leaving the region of space enclosed by that cylinder and will eventually ionize when they again

hit the ionizing surface. Depending on the atom of interest, this can result in a multiplication factor of 30 in the detected signal when compared with a simple cold wire.

Up to now the discussion has been limited to atoms with low ionization potentials but it is also possible to surface ionize molecules as well. Alkali metal compounds such as halides can be ionized on tungsten and somewhat less effectively on platinum<sup>65</sup>. In these cases the molecule is dissociated and the alkali metal is emitted as an ion, though the mechanism for the dissociation is not clear. The tungsten surface is approximately equally effective at ionizing alkali metals and their halides whereas the platinum surface at temperatures in the 1200 K region ionizes the alkali atoms almost exclusively. Thus by using both types of filaments one can measure the alkali halide flux when both alkali and alkali halide are present<sup>66</sup>. Trouw and Trischka were the first to realize that treatment of the surface of the filament strongly influences the surface ionization efficiency<sup>88</sup> such that it is possible to tailor the filament for the job in mind. For example, platinum filaments can have two different surface states; the first is the usual one with a high work function which can ionize alkali halides as well as alkali metals, and the other is mode N which can only ionize the alkali metals. Mode N is prepared by aging the platinum wire at 1520 K for several hours and then running it at 1600 K for a few minutes in methane or carbon monoxide at a partial pressure of  $\sim 5 \times 10^{-4}$  torr. The reasons for this are not understood, but clearly surface contamination is responsible for the change in the surface ionization. This particular treatment has proved very helpful in the detection of molecular beam experiments<sup>89</sup>.

It has been shown<sup>90</sup> that highly vibrationally excited alkali halides are also readily ionized on a platinum filament. The ionization efficiency varies exponentially with the excitation energy approaching 20% for the highest states. As a result this type of selective detector could be used as an internal

energy monitor for estimating the average internal energy of excited alkali halides.

It has also been shown that when superthermal beams of non-alkali-containing molecules strike an oxidized Re filament, positive ions are ejected. Litvak and co-workers<sup>91</sup> have shown that in the case of CH<sub>3</sub>I the majority of positive ions ejected from the surface were alkali contaminants in the filament and not ions of CH<sub>3</sub>I. This phenomenon has been termed kinetic surface ionization (KSI) since ejection of ions from the surface require substantial beam kinetic energy.

Lastly, surface ionization can be used in a reverse sense, in that an atom or molecule with a large electron affinity can interact with a hot wire of low work function to form a negative ion via electron transfer. F. Greene and co-workers<sup>92</sup> showed for CBr<sub>4</sub> on carburetted tungsten wire efficiencies of  $\sim 1 - 2\%$  were possible. This technique gives very low efficiencies depending on the molecules chosen and can range down to  $10^{-8}$  for I<sub>2</sub> on tungsten.

It was suggested<sup>93</sup> that our metastable H<sub>3</sub> has some similarities to an alkali atom in that they both have low ionization potentials ( $\sim 3.7$  eV for  $2p^2A_2''$  H<sub>3</sub> as calculated by King and Morokuma<sup>29</sup>) and an outer shell having one electron only. As a result H<sub>3</sub> may surface ionize when it encounters a heated filament with a high work function. Rubidium atoms have an IP (4.18 eV) close to that of H<sub>3</sub> and exhibit an ionization efficiency of 90% on platinum at 1200 K and 100% efficiency on tungsten at 1400 K<sup>65</sup>. If H<sub>3</sub> would surface ionize upon interaction with a hot filament, then surface ionization may prove to be a highly selective detector for the metastable triatomic radical.

To perform this experiment it was necessary to modify the mass spectrometer. The modifications have been described in Section 2.5.1 of this thesis. They consist of two ceramic blocks set on opposite sides of the mass spectrometer ionization chamber. From these blocks a filament is suspended through

the middle of the ionization region. This filament is electrically insulated from the rest of the electronics and is connected to a DC center grounded power supply. This wire does not affect the normal operation of the mass spectrometer ion source. This was verified by testing the mass spectrometer with just background gas. There was no observed change in the original mass spectrum with either a heated or cold surface ionization filament. This was true for both the tungsten and platinum filaments. However, using rhenium as a filament released a large amount of  $H_2$  which did not decrease with time ( $\sim 1$  hr.). When surface ionization measurements are to be made, the electron impact ionizer is turned off and the filament wire may be heated by passing a DC current (0 - 2.0 A) through it with an HP 6236A power supply. With only this hot wire in the mass spectrometer ionization region, any ions formed there and detected can be due only to a surface ionization process occurring on the filament.

By varying the current to the filament it is possible to control its temperature. However, it is necessary to be able to measure that temperature accurately. This was done using a micro-optical pyrometer (the Pyrometer Instrument Co., Bergenfield, N. J. Model 95, with a reported accuracy<sup>92</sup> between  $\pm 4^\circ$  at 1000 K and  $\pm 10^\circ$  at 2800 K).

It is possible to measure the ionization efficiency of any mass as a function of the temperature of the filament. The ionization efficiency can be measured since the intensity of the beam as a function of stagnation pressure is known (Section 3.2). Since in all cases the .005" diameter wire subtends  $\sim 5\%$  of the cross-sectional area of the beam in the ionizer region, it is possible to estimate the flux incident on the wire. By measuring the ion signal of a particular mass emanating from the hot filament and taking the ratio of the corresponding ion flux to the incident neutral flux of that mass, the ionization efficiency of that neutral species is obtained.

Figure 11 shows curves of ionization efficiency vs. filament temperature as a function of stagnation pressure using a tungsten filament. From Figure 11 a we see that the onset of  $m/e = 3$  ions occurs at approximately  $1100^{\circ}\text{C}$  and has a maximum value of  $\sim 10^{-6}$  at  $\sim 2000^{\circ}\text{C}$ . It is interesting to ask why such low ionization efficiencies were observed, since in the case of Rb atoms of similar IP efficiencies of 100% are observed for ionization by a tungsten filament. Since the  $\text{H}_3$  in our beam is an electronically excited species one should expect that the most likely process would be for the  $\text{H}_3$  to de-excite electronically when colliding with the metal surface. This deexcitation to the repulsive ground state would result in the production of neutral  $\text{H}_2$  and  $\text{H}$ . Our measurements indicate that surface ionization to  $\text{H}_3^+$  is a very weak channel in the interaction of  $\text{H}_3$  with a metal surface. However, this observation of the production of  $\text{H}_3^+$  ions is to the best of our knowledge the first reported observation of the surface ionization of a metastable molecule, the  $2p\ ^2A_2''$  metastable state of  $\text{H}_3$ . While obviously not an intense source of ions, surface ionization could prove to be in the future a unique and highly selective detector of molecules or atoms which are in excited metastable electronic states.

We have shown previously that decreasing the stagnation pressure of the arc source at constant power input results in an increased temperature plasma and translational energy of the molecular species generated within the plasma. By decreasing the stagnation pressure we are then able to probe what effect higher translational energies have on the surface ionization. Dropping the pressure from 80 to 75 torr (Figure 11b), we see that the onset of  $m/e = 3$  species decreases from  $1100^{\circ}\text{C}$  to  $500^{\circ}\text{C}$  and the inflection point decreases from  $1800^{\circ}\text{C}$  to  $1200^{\circ}\text{C}$ . Further lowering the stagnation pressure to 70 torr decreases the onset to  $150^{\circ}\text{C}$  and the inflection point to  $800^{\circ}\text{C}$ . At all stagnation pressures the maximum ionization efficiency observed is always approximately  $10^{-6}$ .

One interpretation for this observation is that the translational energy of  $H_3$  affects its ionization efficiency. At low translation energies of ( $\sim 2$  eV) surface ionization occurs only at high filament temperature. At high translation energies ( $\sim 7$  eV) surface ionization can occur at both low and high filament temperatures. From these results it would appear that there are two competing factors which influence the ionization efficiency of  $H_3$  on a hot tungsten filament: its translational energy and the coverage of adsorbed specie. From our results it follows that at high translational energy it dominates while at low energies the surface coverage is the dominant effect. Even though the onset of surface ionization is very much influenced by the translational energy of the  $H_3$ , the ionization efficiency at the inflection point appears to be approximately independent of translational energy.

It is possible that by replotting these data further information may be obtained on the  $H_3$  specie. An inspection of equations 4.16 and 4.17 reveals that a plot of the natural log of the ionization efficiency vs. the inverse of the temperature of the filament should result in a straight line whose slope is proportional to the difference of the work function of the filament and the ionization potential of the surface ionized specie. These types of plots have proved useful in determining work functions of surfaces by our studying the surface ionization of an atomic specie with a known ionization potential<sup>94</sup>.

By using this technique and a knowledge of the tungsten work function (4.58 eV) one should be able to evaluate the ionization potential of  $H_3$ . The data of Figure 11 were replotted and are shown in Figure 12, with the resulting ionization potential tabulated in Table 2. We first observe that the ionization potential increases with increasing stagnation pressure. Perhaps at low stagnation pressures the high translational energy of the  $H_3$  serves to lower the effective ionization potential since some of that translational energy may become available for surface ionization. If this is the case, then the more

**Table II****Effective Surface Ionization Potential (in eV) for a Tungsten Filament**

Pressure (torr)	H	H <sub>3</sub>
80	5.2	5.4
75	5.3	5.1
70	5.1	4.9

accurate ionization potential would be the one measured at a higher stagnation pressure, which would be 5.4 eV.

An inspection of the energy level diagram for  $H_3$  in Figure 4 shows that this ionization potential is some 1.7 eV too large to be originating from the  $2p\ ^2A_2''$  state. However, it agrees very well with the ionization potential from the  $2p\ ^2E'$  state (5.36 eV). We have already said that the most likely process for  $H_3$  interacting with a metal surface is to de-excite electronically. The deexcitation to the repulsive state would result in the production of neutral  $H_2$  and H. However, since the time scale for electron transfer ( $\sim 10^{-14}$  s) is faster than the motion of the nuclei ( $\sim 10^{-12}$  s) it is possible that the repulsive  $2p\ ^2E'$  state would surface ionize to form  $H_3^+$  before it could dissociate to form neutral  $H_2$  and H. Our measurements indicate that surface ionization to  $H_3^+$  is indeed a weak channel, which is consistent with this interpretation. If this is indeed the case it would appear that the majority of the  $2p\ ^2A_2''$   $H_3$  deexcites to the  $2p\ ^2E'$  repulsive state and a small fraction of those quickly surface ionize to form  $H_3^+$ . If this is indeed the case, then this is the first case of the measurement of the ionization potential of a repulsive state.

Due to the unusual nature of the ionization potential we wished to repeat the experiment using a filament with a different work function in order to see if the result was indeed consistent. A platinum filament ( $\Phi = 5.36$  eV) was used for surface ionization and the results are shown in Figure 13. An immediate difference which is observed between the tungsten and platinum filaments is their behavior with stagnation pressure of the beam. For platinum no surface ionization was observed at 80 torr. At 75 torr (Figure 13a) a small amount of  $H_3^+$  is observed to be formed. At lower stagnation pressure (65 torr, Figure 13b) the typical amount of  $H_3^+$  is formed. However, the amount of ions formed at this point appear insensitive to stagnation pressure with the onset ( $\sim 300^\circ C$ ) and threshold ( $\sim 1100^\circ C$ ) being constant (Figure 13 b & c).

One explanation for the contrast in behavior with the tungsten is that there is some specie adsorbed on the tungsten filament which is not adsorbed on the platinum filament, which then makes the surface ionization process much more sensitive to the translational energy of the  $H_3$ .

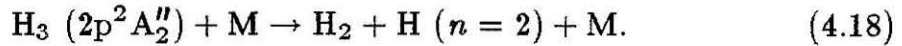
Figure 14 shows the Saha-Langmuir plots of the platinum surface ionization data. Table III shows the ionization potentials calculated from these data. Disregarding the result for 75 torr (since the signal was so weak) the platinum data give ionization potentials which support the conclusion that we surface ionize from the repulsive ground state of  $H_3$ .

It should be mentioned that in this series of experiments there was never any sign of the production of  $H_2^+$ , which is as expected, since  $H_2$  having an IP of 15.6 eV would not be expected to surface ionize on tungsten whose work function is 4.58 eV. It was very surprising then when at high tungsten filament temperatures the production of  $H^+$  was observed, as also shown in Figure 11. At all translational energies the onset and/or the  $m/e = 1$  ion is always  $\sim 400^\circ\text{C}$  greater than the onset  $m/e = 3$  and the inflection point for  $m/e = 1$  is always  $\sim 200^\circ\text{C}$  greater than the inflection point for  $m/e = 3$ . For the platinum filament (Figure 13) the production of  $H^+$  is somewhat greater than the production of  $H_3^+$  with the onset and threshold being about the same for both. One explanation is that we have produced in the source metastable hydrogen atoms which (due to high translation energy) do not decay by the time they exit the 1 kV/cm electric field (which serves to sweep ions out of the beam), and are surface ionized at the filament. Since the IP for H ( $n = 2$ ) is  $\sim 3.3$ , eV an excited hydrogen atom would be expected to surface ionize readily. This explanation must be discarded since the Saha-Langmuir plots (Figures 12 & 14) show the ionization potential to be on the average 5.26 eV. However, this ionization potential compares well with the average ionization potential of 5.30 eV which is calculated from the Saha-Langmuir plots for  $H_3^+$ .

**Table III****Effective Surface Ionization Potential (in eV) for Platinum Filament**

Pressure (torr)	H	H <sub>3</sub>
75	5.7	5.9
65	5.3	5.5
60	5.4	5.6

This suggests that the  $H^+$  production is due to the presence of  $H_3$  in the beam. One possible explanation is that these  $H^+$  ions are due to the dissociation of the  $H_3$  molecule (not unlike dissociation of alkali halides on hot filaments<sup>65,66,90</sup>). An interaction which might explain the production of  $H^+$  from  $H_3$  is



Though this process is endothermic by  $\sim 5.0$  eV, that energy could be supplied by the translation energy of the  $H_3$ . Then in a second step the electronically excited H atom formed on the filament could ionize and then desorb. Although this process is endothermic by  $\sim 5.0$  eV (Figure 4), that energy could be supplied by the translational energy of the  $H_3$ . Then in a second step the electronically excited H atom formed on the filament could ionize and then desorb. However, if this mechanism is the case, then one would expect it to exhibit an ionization potential of 3.33 eV and not the observed 5.26 eV. The only other explanation for the generation of  $H^+$  is that in the surface ionization of  $H_3$  to  $H_3^+$  some of the  $H_3^+$  which is now adsorbed on the surface dissociates to form  $H^+$  and  $H_2$  before it has a chance to desorb as  $H_3^+$ . This would then give the  $H^+$  the same effective ionization potential as the  $H_3^+$  since they both started from the same precursor,  $H_3$ . However, the dissociation of  $H_3^+$  to  $H^+$  and  $H_2$  is endothermic by some 4.3 eV. It is therefore difficult to understand how this process would occur on the surface unless in some unusual way this process is enhanced when the  $H_3^+$  is adsorbed to a metal surface.

In conclusion, from these experiments we are indeed able to observe surface ionization of  $H_3$  to  $H_3^+$  on both tungsten and platinum filaments. By observing the production of  $H_3^+$  as a function of filament temperature we are able to measure the effective ionization potential of  $H_3$  and are able to conclude that upon interaction with the metal surface the metastable  $2p^2 A_2''$  state first

decays to the  $2p \ ^2E'$  state which can then surface ionize to produce  $H_3^+$ . This process is consistent with the small number of  $H_3^+$  ions which are formed, since the greater part of  $H_3$  in the  $2p \ ^2E'$  state blows apart to form  $H + H_2$ .

We are unable to completely explain the observation of  $H^+$  ions. Further experiments are necessary to elucidate the mechanism for generating  $H^+$  at the hot filament. By velocity selecting the  $H_3$  beam one will be able to observe the effects of translational energy on surface ionization efficiency. If process (4.18) occurs, then at higher translational energies of  $H_3$  there should be an increased production of  $H^+$  while at energies below 5 eV it should totally disappear. Therefore, by observing the energetics of the surface ionization as a function of translational energy of the beam, it should be possible to elucidate the nature of the process. It should also be noted that our filaments were not treated or cleaned in any way. For any future work which is intended to be highly quantitative, greater care in the handling and preparation of the filament will be essential since, the effect being a surface phenomenon, any adsorbants will affect the work function of the metal and consequently the surface ionization.

## 4.5 Photoionization

Since surface ionization occurs with  $H_3$  due to the relatively low IP of its  $2p\ ^2A_2''$  state, it should be possible to photoionize  $H_3$  with light of an appropriate frequency ( $\lambda < 3300\ \text{\AA}$ ). To perform this experiment the bell jar was modified to accommodate a photoionization cell through which the beam can pass and be subjected to a source of ultraviolet light. The schematic of the set-up is shown in Figure 15, and a view of the cell is shown in Figures 16 and 17. Mounted in front of the entrance aperture are a pair of copper plates between which a field of  $1000\ \text{V/cm}$  can be produced. The purpose of this field is to remove ions from the beam before they can enter the cell. The inside of the pipe may then be illuminated by a light source exterior to the chamber by focusing the light through a quartz window into the cell. The light will then irradiate the beam, and what light is not absorbed will be reflected back by the spherical mirror fixed inside at the end of the cell, thus irradiating the beam twice. The light may excite or ionize some of the  $H_3$  passing through the cell. Since the momentum transfer for the ejected electron is extremely small, the ions formed will be deflected by a negligible amount and traverse the cell to be ultimately detected by the mass spectrometer located at the end of the bell jar on line with the neutral beam. The cell is made of aluminum and is black anodized. In addition, the entrance and exit apertures help decrease the amount of light from the mercury lamp entering the mass spectrometer and producing a background signal on the electron multiplier.

A top cross sectional view of the cell is shown in Figure 16. Its mounting flange is attached to a 6" diameter conflat flange (Figure 15, P2) and vacuum sealed by the two O-rings as indicated. For the initial alignment (with the system at atmospheric pressure) the cell may be moved in and out of the

chamber via the threads at the front of the cell. By rotating the ring at the front of the cell, the latter is translated (without rotations) either into or out of the VC2 chamber. This provides one of the degrees of freedom needed for alignment of the aperture axis with the beam. Once the desired translation is achieved the cell can be fixed to the inner mounting flange by tightening the set screw and locking ring indicated in Figure 16. The size of the aperture through which the beam must pass can be readily changed by having discs of different aperture sizes drilled and fitted into the aperture holders as shown in Figure 16. The holder is simply a 1/4" swagelock fitting that has been black anodized and fitted with an O-ring to provide a vacuum seal between the aperture disc and the holder itself. This holder can then be mounted on the entrance and on the exit sides of the cell. However, due to the alignment difficulties encountered these discs were not used and the opening of the holder acted as the aperture.

Figure 17a shows a cross-sectional side view of the photoionization cell by a plane perpendicular to the beam, and superimposed on it views of the deflection plates and entrance aperture. This view indicates how the beam must first pass between the copper deflection plates before entering the cell itself. This view also depicts the spherical mirror which is mounted inside at the rear of the cell. Its focal length is such that any light emitted by  $H_3$  as it passes through the cell would be reflected out onto the PMT positioned outside of the quartz window end of the cell (Figure 16). This was done in order to attempt to measure spontaneous emission from the metastable species (Section 4.7). It also serves in these photoionization experiments to reflect back the light from the mercury lamp once more through the cell, thus irradiating the species in the beam twice.

Figure 17b shows the front view of the photoionization cell as it appears from outside of the vacuum chamber. When open to atmosphere the cell may

be moved up-and-down and left-to-right via the 4 translator screws set around the flange. The pipe may also be rotated with respect to the outer mounting fixed flange via the rotator device as shown in the figure. These motions, plus the in-and-out motion provided by the cell threads, permit full flexibility in aligning it. Once the cell has been set in its desired aligned position it may be fixed in place by tightening the four central bolts pictured in Figure 17b and the set screw pictured in Figure 16.

Ideally a tunable laser source should be used to act as a light source in this experiment, since the amount of ionization as a function of the frequency of the light could give a great deal of information about the spectroscopy of the excited states of  $H_3$ . For the initial experiment it was decided to use a broad, intense source of excitation that would extend well into the UV. A Bausch & Lomb (cat. no. 33-86-36-01) 200-watt, short-arc, super-pressure mercury lamp which is enclosed in a quartz envelope was thus used for these experiments. It has a high luminance and an exceptionally high spectral radiance in the ultraviolet. This light source is known to give a continuous, fairly uniform intensity spectrum covering the UV, visible and infrared except for the very high-intensity discrete lines which are characteristic of the mercury arc spectrum. The arc has an average luminance of 25,000 candles per square centimeter and a luminous efficiency of 47.5 lumens per watt at a real power of 200 watts. Figure 19 shows the output spectrum from this lamp<sup>95</sup>. Taking the intensity of the 440 mercury line (as the most intense line in the output spectrum of the mercury lamp) we can calculate an intensity of that line of  $3.6 \times 10^{14}$  photon  $cm^2 s^{-1}$ .

Through the use of two quartz lens (one inside the mercury lamp unit [MP] and one exterior) the output of the lamp is focused directly into the cell which the neutral beam must pass before reaching the mass spectrometer. Figure 15 shows how the lamp is positioned on the exterior to the

vacuum chamber. Testing the mass spectrometer with the lamp on showed no change in the background signal, indicating that any stray light which may be escaping from the pipe does not interfere with the operation of the mass spectrometer.

Figure 19 shows the initial results for this experiment. Curve (a) in Figure 19A shows the electron impact spectrum for a stagnation pressure of 100 torr with the lamp off. As expected the signal is virtually all due to H, but it is very weak due to the reduced temperature of the plasma. Curve (b) shows the mass spectrum obtained with the ionizer of the mass spectrometer turned off. As expected there is no observed ion signal, since the deflection plates should have removed any ions from the beam before they could reach the mass spectrometer. Finally, curve (c) now shows the results under the same experimental conditions but with the mercury lamp turned on; as can be seen, no photoionization is detected.

For Figure 19B the stagnation pressure has been reduced to 95 torr. Curve (a) (the electron impact mass spectrum with the lamp off) shows the presence of some  $H_3$ , though the intensities of all species are still small due to the reduced temperature of the plasma. Curve (b) shows the mass spectrum with the ionizer turned off, and as for Figure 19B the ion signal drops to zero showing that no ions are present in the beam after passing through the deflection plates. Curve (c) corresponding to the mercury lamp turned on shows a small  $m/e = 3$  signal which we interpret as photoionization of metastable  $H_3$ . Lowering the stagnation pressure further to 90 torr (Figure 19C), we see in the electron impact spectrum (curve a) with the lamp off that all the ion signals have increased in intensity, due apparently to the increase in the temperature of the plasma. When the ionizer is turned off (curve b) a small ion signal is present presumably due to some high energy ions which are not significantly deflected by the plates. An analysis of the energy distribution of

the ions present in the beam (utilizing the same techniques discussed in section 3.3 of the thesis) indicates that the distribution extends all the way out to 40 eV (in contrast to the neutrals which tail off at  $\sim 20$  eV, under similar operating conditions). Currently it is not possible to employ higher fields ( $> 1000$  V/cm) because the high background pressure ( $\sim 5 \times 10^{-5}$  torr) in the bell jar during the operation of the discharge leads to electrical breakdown. This difficulty will not occur when the arc source is interfaced with our crossed molecular beam apparatus since the differential pumping will be significantly better allowing the deflection plates produce bigger electric fields. With the present setup, when we turn on the mercury lamp we see a sizable increase in the  $m/e = 3$  signal, approximately twice that of the background ion signal. We interpret this signal as the photoionization of the metastable  $H_3$ . Surprisingly, a very small increase in the  $m/e = 1$  signal is also observed, but this is probably not significant considering the signal-to-noise ratio of the experiments. Finally, lowering the stagnation pressure to 80 torr (Figure 19.D) further accentuates these effects. In summary, irradiation of the beam with the UV light at the lower stagnation pressures (80 torr) results in producing both  $H_3^+$  and  $H^+$  ions while at high stagnation pressure 95 torr (Figure 19B, curve (c)) only  $H_3^+$  ions are generated by the lamp.

To make these results clearer, for each of the stagnation pressures reported we have subtracted the background ion mass spectrum (obtained with the electron impact ionizer off) from the mass spectrum generated while the mercury light was on (and the electron impact ionizer still off). Any ion signal remaining must then be due to photionization of species in the beam by the UV light. These resulting difference curves are shown in Figure 20. We see no signal at 100 torr (Figure 20 (a)) as expected since there is no  $H_3$  being generated. At 95 torr stagnation pressure, where  $H_3$  is starting to be generated by the arc discharge (Figure 20 (b)), we clearly see an  $H_3^+$  photoion current of

$5 \times 10^{-13}$  A. This signal would roughly account for an ionization efficiency of  $10^{-8}$  of the  $\text{H}_3$  present in the beam. Further reducing the stagnation pressure to 90 torr increases the amount of  $\text{H}_3$  generated by the arc source by approximately a factor of 4 (Figure 19B curve (a) and Figure 19C curve (a)). We see that under these conditions the photoion current of  $\text{H}_3^+$  is also increased by a factor of approximately 4 (Figure 20 (c)). Decreasing the stagnation pressure to 80 torr (Figure 20 (d)) we see exactly the same effect as described above, the  $\text{H}_3^+$  ion current increasing by the same factor as the  $\text{H}_3$  has increased in the beam. Under these conditions we observe a photoion current which is due to  $\text{H}^+$ . There also appears a small bump at  $m/e = 2$ , but its intensity is of the same order as other fluctuations from the base line in the  $m/e < 1$  and  $m/e > 3$  regions of the spectrum.

The above results seem to indicate that indeed there are metastable  $\text{H}_3$  which are being photoionized by the light. This is consistent in that the magnitude of the photoion current of  $\text{H}_3^+$  is proportional to the intensity of neutral  $\text{H}_3$  in the beam. This then is the first direct observation of photoionization of metastable  $\text{H}_3$ .

It would also at first appear, on the basis of Figure 20 d, that metastable hydrogen atoms are also present, which are in  $n = 2$  or higher states and are being photionized by the UV light along with the metastable  $\text{H}_3$ . The fact that the  $\text{H}^+$  signal is only observed at low stagnation pressure is consistent with this conclusion. Only at these low stagnation pressures is the plasma hot enough to generate these metastable hydrogen atoms. This is due either to their greater translational energy which allows them to survive the deflection/quenching plate, or to a large increase in the fraction of hydrogen atoms excited to these metastable states such that more survive to make it through the pipe. However, this cannot be the case since any metastable hydrogen atoms should have been quenched by the electric field in front of the pipe. As has been

shown previously<sup>96,97</sup> a field of 1000 V/cm should lower the lifetime of the 2s metastable state to  $\sim 5 \times 10^{-9}$  s. For 8 eV hydrogen atoms traveling through the plates which are  $\sim 1$  cm long, they will remain in the field  $\sim 2.6 \times 10^{-7}$  s. This corresponds to approximately fifty lifetimes of the 2s state such that any metastable atoms should have all relaxed by the time they have left the field. As a result, our result cannot be explained by invoking photoionization of metastable hydrogen atoms and must remain unexplained for the time being. Future experiments should attempt to repeat this result and observe if the  $m/e = 1$  signal continues to increase with decreasing stagnation pressure which would suggest that the plasma heating is in some way responsible for this signal.

## 4.6 Total Scattering

Interesting information may be obtained by the study of the scattering of a beam of molecules by a gas target. From the measurement of the attenuation of the beam as it passes through the gas target, it is possible to derive a total collision cross section which gives a crude indication of the sum of the radii of the two molecules. Results of earlier investigation<sup>98-102</sup> showed the need to develop an appropriate theory to describe such measurements. Massey and Mohr were the first to develop an expression relating the elastic cross sections with the intermolecular potentials<sup>103</sup>. Bernstein and co-workers have used this attenuation technique to obtain total collision cross sections of alkali metals interacting with a variety of gases<sup>104-106</sup>.

The experiment consists in passing a beam of molecules through a scattering chamber containing a target gas. The intensity of the beam is reduced due to collision with the target molecules, and one measures the fraction of the beam which is transmitted. One varies the pressure in the scattering chamber and measures the decrease of the intensity of the beam as it passes through that cell. The schematic for this experiment is shown in Figure 21.

Since the metastable  $H_3$  would be expected to have a large radius, due to its being in a Rydberg state, we felt it would be informative to measure its total scattering cross section with a reference gas, such as argon. For the experiment we utilized the black anodized photoionization cell described in the previous section (Section 4.5) as a scattering chamber. The path length through that cell is 4.0 inches when the apertures are in place (Figure 17). By filling it with a target gas species, the molecules within the beam will undergo collisions and be scattered out of the the beam thus, lowering its intensity. By using the open aperture holders (to facilitate alignment) as the exit and

entrance apertures to the scattering chamber, approximately one and a half orders of magnitude pressure differential could be maintained between that chamber and the bell jar (VC2). Filling that chamber with  $5 \times 10^{-3}$  torr of Ar resulted in a rise of the pressure in the bell jar to  $\sim 1 \times 10^{-4}$  torr (while the arc discharge beam is on). Higher gas pressures in the scattering chamber were avoided in order to avoid damage to the mass spectrometer. That pressure was measured using an uncalibrated Schulz-Phelps gauge and a Granville-Phillips high-pressure ionization gauge controller (series 224). The intensity of the beam was measured as usual by electron impact mass spectroscopy. Figure 22 shows the logarithm of the transmittance  $I/I_0$  (beam intensity in the presence of the target molecules/beam intensity without scattering gas) of the H, H<sub>2</sub>, and H<sub>3</sub> as a function of the pressure of argon in the scattering cell. These points lie on a straight line as expected from theory.

From these results one wishes to obtain the effective total cross section,  $Q$ , and from it the interaction radii. The method of calculating  $Q$  which we employed is based on that of Rosin and Rabi<sup>99</sup> and is partially described in Levine and Bernstein<sup>107a</sup>. The probability that a beam molecule of laboratory velocity  $v_b$  will pass through a scattering chamber of length  $l$  without being deflected is given by

$$P(v_b) = \exp\left(-\frac{l}{\lambda}\right) \quad (4.19)$$

where  $\lambda$  is the mean free path. This means that the beam flux is an exponentially decreasing function of the length of the scattering path, a result similar to the Beer-Lambert law for the attenuation of a beam of light by absorption. The expression for  $\lambda$  is given by<sup>108</sup>

$$\lambda = \frac{\sqrt{\pi}(v_b/a_t)^2}{nQ\Psi(v_b/a_t)} \quad (4.20)$$

where

$$\Psi(x) = x \exp(-x^2) + (2x^2 + 1) \int_0^x e^{-y^2} dy \quad (4.21)$$

and

$$a_t = \sqrt{\frac{2kT_t}{m_t}}. \quad (4.22)$$

In these expressions  $n$  is the scattering gas concentration,  $k$  is the Boltzmann constant,  $m_t$  the mass of the target molecule and  $T_t$  the temperature of the target gas. To accurately calculate  $Q$  it is necessary to substitute  $\lambda$  from equation (4.20) into equation (4.19) and average over the beam velocity distribution. This requires a numerical integration.

It is somewhat simpler to note that the transmittance  $I/I_o$  is equal to the probability  $P(v_b)$ . Plots of  $\ln(I/I_o)$  versus the pressure of the scattering chamber are usually linear for  $I/I_o > 0.1$ . From the slope ( $S$ ) of such plots the total cross section ( $Q$ ) may be calculated using the Rosin-Rabi equation<sup>99</sup>, which is an approximation to the accurate one whose solution was just discussed. This equation is

$$Q = 2(\pi)^{\frac{1}{2}} J(z) \left( \frac{\ln(I/I_o)}{nd} \right) \quad (4.23)$$

where

$$J(z) = z^2 \int_0^\infty \left[ \frac{x^5}{\Psi(x)} \right] \exp(-zx^2) dx \quad (4.24)$$

$$z = \frac{m_b T_t}{m_t T_b} \quad (4.25)$$

$$x = \frac{v_b}{\left( \frac{2kT_t}{m_t} \right)^{\frac{1}{2}}}. \quad (4.26)$$

In these experiments  $m_b$  is the mass of the beam molecule,  $T_b$  is its temperature and  $d$  is the scattering path length. This equation is an approximation to the accurate one outlined in the previous paragraph. Bernstein and co-workers have shown that for  $I/I_o$  in the range of 0.1 to 1.0 the deviation between the approximate and exact equation is about 5% in the worst case<sup>105</sup>. The quantity  $J(z)$  is obtained by graphical interpolation of Rosenberg's table<sup>109</sup>.

We may now employ equation 4.23 to calculate the total cross section for scattering with argon (Figure 22). We first need to calculate the value  $J(z)$ . In the case of H scattering by room temperature argon

$$z = \frac{m_b T_t}{m_t T_b} = 7.569 \left( \frac{1}{T_b} \right) \quad (4.27)$$

where the lower-case b stands for the beam, the lower-case t stands for the argon target and  $T_b$  is measured in Kelvin. Assuming a  $T_b$  of 15,000 K this results in a  $z$  of  $5.04 \times 10^{-4}$ . Using Rosenberg's table<sup>109</sup> one obtains

$$J(z) \sim 0.282 = \frac{1}{2\pi^{\frac{1}{2}}}. \quad (4.28)$$

For our present measurements, substituting in the appropriate experimental values for our apparatus gives

$$Q (\text{\AA}^2) = 3.05 \times 10^{-18} \text{S}. \quad (4.29)$$

By using a least square fit of these data points of Figure 22 we can get values for S and Q for collisions of H, H<sub>2</sub>, and H<sub>3</sub> with Ar. These cross sections are listed in Table IV. The uncertainties in the Table represent 95 % confidence level.

Rothe notes in his thesis<sup>105</sup> that the cross sections are not accurately reproducible and could vary over 20%. However, the ratio of the cross sections of two different targets could be fairly reproduced on a day-to-day basis. This ratio seems to cancel drifts in his apparatus. Typically, angular resolution of the detector with respect to the target cell greatly influences the absolute cross sections measured. The attractive portion of the potential will favor small-angle scattering, and this will only be measured if the detector has good resolution, such that the better the angular resolution the larger the measured cross sections. This is determined by the angle subtended at the midpoint of the scattering path by the detector surface ionization wire ( $\sim 30''$ ).

Table IV

Total Scattering Cross Section with Argon Target,  $P_{stag} = 57$  torr

	H	H <sub>2</sub>	H <sub>3</sub>
Q (Å <sup>2</sup> )			
Experimental	1.7 ± 0.7	3.3 ± 0.9	17.3 ± 0.8
Theoretical			
Model		3.8	17.1
Q* <sub>X-Ar</sub>			
Experimental	1.0	1.9	10.2
Theoretical			
Model		2.2	10.0

There have been many experimental<sup>107,108</sup> and theoretical<sup>109</sup> studies on the absolute total cross sections for scattering of atomic hydrogen by argon. However, these studies were done at energies up to only 1 eV and cannot be directly compared with our result since this is the first scattering experiment using H atoms in the 5 eV to 15 eV energy range. It has been shown<sup>113</sup> that at high energies the major contribution to the elastic cross section comes from scattering by the repulsive core, such that a plot of the log of the cross section vs. the log of the velocity should be linear. If we extrapolate the linear dependence of the logarithm of the total elastic cross section on relative velocity for Ar + H given by Das and co-workers<sup>112</sup> to our energy, we obtain a cross section of  $4.4 \text{ \AA}^2$ . This differs from our total cross section of  $1.7 \text{ \AA}^2$  by a factor of 2.5. This difference can be attributed to our poor resolution, our broad hydrogen atom energy distribution (Section 3.3) and the fact that an extrapolation of the Das *et al.* data over more than an order of magnitude was involved.

We can also discuss our results in terms of relative cross section,  $Q^*$ , which is defined as

$$Q_{X-Ar}^* = \frac{Q_{X-Ar}}{Q_{H-Ar}} \quad (4.30)$$

where  $Q_{X-Ar}$  is the cross section of the beam specie X with Ar, and  $Q_{H-Ar}$  is the cross section of the H with Ar. Bernstein and Rothe<sup>104</sup> report that in atom-molecule total cross section measurements, while the absolute cross sections may vary over a range of  $\pm 10\%$ , the ratio of the cross section of two gases were reproducible to within  $\pm 3\%$ . In the case of our data for  $H_2$  we obtain a  $Q_{H_2-Ar}^*$  of 1.9.

This value can be rationalized on the basis of a very simple energy-dependent hard sphere radius model for argon. Taking the radius of H to be  $0.53 \text{ \AA}$ , the effective Ar radius (for high energy collisions) which will pro-

duce a value of  $Q_{H-Ar}$  of  $1.7 \text{ \AA}^2$  is  $0.21 \text{ \AA}$ . Using an effective radius for  $H_2$  as  $0.90 \text{ \AA}$  ( $\frac{1}{2}$  of the  $H_2$  internuclear distance plus the H radius), this yields a  $H_2-Ar$  hard sphere collision cross section of  $3.8 \text{ \AA}^2$  and a  $Q_{H_2-Ar}^*$  of 2.2. This is in reasonable agreement with the measured value of 1.9. Independently, the  $H_2-Ar$  collision cross section has been measured as a function of relative energy up to  $100 \text{ meV}^{114}$ . Extrapolation to  $\sim 13 \text{ eV}$  furnishes a value of  $12.4 \text{ \AA}^2$  and a  $Q_{H_2-Ar}^*$  with respect to the Das *et al.* results<sup>112</sup> of 2.8, which is not unreasonable, in view of the gross nature of the model and extrapolations used.

For  $H_3$  we calculate a  $Q^*$  of 10.2. This large size may at first appear surprising but really is not, considering that the  $H_3$  molecule is in an excited Rydberg state. For hydrogen orbital, the Bohr radius for an  $n = 2$  state is  $2.12 \text{ \AA}$ . Taking this as the radius of  $H_3$  in the  $2p \text{ } ^2A_2''$  state and the effective argon radius of  $0.21 \text{ \AA}$  obtained from the H scattering experiment, this furnishes a  $Q_{H_3-Ar}$  of  $17.1 \text{ \AA}^2$  and a  $Q_{H_3-Ar}^* = 10.0$ , in surprisingly good agreement with the measured values of  $17.3 \text{ \AA}^2$  and 10.2, respectively. From this simple analysis we see that it is quite reasonable for  $H_3$  to have a collision cross section with Ar an order of magnitude greater than that with a hydrogen atom.

We attempted to perform similar experiments with a higher stagnation pressure in the arc source. In Section 3.3 we have shown that increasing that pressure will lower the translational energy of the species in the beam and thereby should increase its scattering cross section. Figures 23 and 24 show data for scattering of H and of  $H_3$  generated at a 65 torr stagnation pressure with argon and also with propane. The calculated cross sections for both are shown in Table V and Table VI. The uncertainties listed represent a 95% confidence level. For the scattering of hydrogen atoms with argon we see that

Table V

Total Scattering Cross Section with Argon Target,  $P_{stag} = 65$  torr

	H	H <sub>3</sub>
Q (Å <sup>2</sup> )		
Experimental	2.9 ± 0.5	29.7 ± 6.3
Theoretical		
Model		20.4
Q <sub>X-Ar</sub> <sup>*</sup>		
Experimental	1.0	10.0
Theoretical		
Model		7.0

the cross section has increased by a factor of 1.7 as the stagnation pressure was increased from 57 to 65 torr.

Using the same analysis as before we calculate an effective Ar radius of .43 Å. Extrapolating again Das and co-workers<sup>112</sup> result to our energies to about 10 eV (which we get by linearly interpolating the results at 55 torr and 75 torr displayed in Figure 6 and 7 in Section 3), we get a cross section of 5.2 Å<sup>2</sup>. This is greater than our measured value of 2.9 Å<sup>2</sup> by a factor of 1.8, but is closer to the 65 torr result than the 57 torr ones. As expected, as the stagnation pressure increases (resulting in translational energies closer to the energies at which they performed their experiment) our cross sections move in the direction of the Das and co-workers<sup>112</sup> results.

For H<sub>3</sub> we see that the cross section for scattering with Ar has increased by a factor of 1.7 as well in going from 57 torr to 65 torr stagnation pressure. The fact that both the H<sub>3</sub> and H cross sections increased by the same factor is not unreasonable. In Section 3.3 we have shown that both H<sub>3</sub> and H have roughly the same translational energy at the same stagnation pressure, presumably because they are heated to the same extent in the plasma discharge. Under these conditions, their cross sections should be affected in a similar manner, as observed. Using the effective Ar radius and the radius of H<sub>3</sub> being 2.12 Å we calculate a scattering cross section for H<sub>3</sub> and Ar to be 20.4 Å<sup>2</sup> and a  $Q_{H_3-Ar}^*$  of 7.0. This is in reasonable agreement with our measured values of  $Q_{H_3-Ar} = 29.7 \text{ Å}^2$  and a  $Q_{H_3-Ar}^* = 10.0$

Lastly, we wanted to see what effect a larger scattering target would have on the cross sections. For this reason we choose to use propane as another scattering gas and the same stagnation pressure of 65 torr of the last argon scattering experiments. The results obtained are also shown in Figures 23 and 24 and listed in Table VI. We see the the H-propane cross section has increased by a factor of 7 compared to the H-Ar cross section at the same en-

Table VI

Total Scattering Cross Section with Propane Target,  $P_{stag} = 65$  torr

	H	H <sub>3</sub>
Q (Å <sup>2</sup> )		
Experimental	20.9 ± 2.7	25.4 ± 1.6
Theoretical		
Model		29.1
$Q_{X-Ar}^*$		
Experimental	7.1	8.6
Theoretical		
Model		10.0

ergy. An increase in the cross section is expected since the H atom is small compared to the target and will be very sensitive to a change in the size of the target gas. In contrast there is no change in the cross section of the H<sub>3</sub>-propane compared to H<sub>3</sub>-Ar. This as well is not unexpected since the large size of the metastable H<sub>3</sub> molecule will dominate the interaction, hence making it rather insensitive to a change in the target size.

Using the same analysis as for the argon experiment at 57 torr we can calculate an effective propane radius of 0.92 Å from the H plus propane scattering cross sections (using 0.53 Å as the radius for H). Using 2.12 Å as the radius of the H<sub>3</sub> molecule (as justified in the H<sub>3</sub> + Ar scattering analysis) and the effective propane radius we just calculated, we calculate a scattering cross section of 29.1 Å<sup>2</sup> for H<sub>3</sub> + propane at 65 torr stagnation pressure. Again, this compares very well with the measured value of 25.4 Å<sup>2</sup> for cross section. These values are listed in Table VI.

The reason for the similar cross sections for H<sub>3</sub>-Ar and H<sub>3</sub>-propane becomes obvious by comparing the 'true' sizes of the two scattering molecules. For solid Ar the average radius (half the distance between closest atomic centers) is 1.6 Å<sup>115</sup>. For propane, by adding together the appropriate bond distances<sup>116</sup> (taking into account the geometry of propane), we get a spherical radius of ~ 2.5 Å. The change in size in going from argon to propane is small compared to the radius of the H<sub>3</sub> but not of the H, suggesting that the scattering cross section of H<sub>3</sub> from those two molecules should be comparable in magnitude but the cross section of H should be significantly different, as observed.

In summary we have seen that the scattering cross section for H<sub>3</sub>-Ar is ten times larger than the cross section for H-Ar, in keeping with the large size of the metastable H<sub>3</sub> molecule. We have also evaluated total scattering cross sections for these neutral species at translation energies an order of magnitude

higher than have been previously observed. Going from Ar to propane as a scattering gas results in a large increase in the total cross section for hydrogen atom but no change for  $H_3$ . As a result, this experiment has barely begun to scratch the surface of interesting dynamics which may now be examined at these elevated energies. In addition, the large size of the  $H_3$  molecule may be expected to exhibit extremely unusual properties in additional investigations.

## 4.7 Possible Alternative Origins of Detected $H_3$

Because of the unique nature of the observed  $H_3$  metastable it is necessary that any other mechanisms which could account for the observed  $m/e = 3$  peak be ruled out. As a result a number of potential candidates have been considered.

### a) Ion-Molecule Reactions

One possible explanation of our result could be a spurious reaction which produces  $H_3^+$  ions in the mass spectrometer by a mechanism other than electron impact ionization of neutral  $H_3$ . Since in the region of the ionizer a large number of ions as well as electronically excited species are produced, it is then not unreasonable to consider that they might react with neutral molecules in the beam to form  $H_3^+$  which would then be extracted and detected by the mass spectrometer. This signal would then only appear when the ionizer was on and likewise give an AC signal when the beam was chopped, thus giving the appearance of a metastable species in the beam, when in actuality it was due to the ion product of a reaction involving totally different neutral species. Ion-neutral reactions tend to exhibit very large cross sections ( $\sim 100 \text{ \AA}^2$ )<sup>107b,117</sup> and therefore might indeed contribute to the observed signal.

The most likely ion-molecules reaction which may occur in the ionizer and produce  $H_3^+$  ions is



Let us estimate the ion current expected from this process. It is given by

$$I_{H_3^+} = I_{H_2^+} \sigma_{H_2^+ + H_2} \frac{p_{H_2}}{kT} l \quad (4.32)$$

where  $I_{H_2^+}$  is the experimentally observed ion current at  $m/e = 2$ ,  $5 \times 10^{-11}$  A,  $p_{H_2}$  is the pressure measured in the mass spectrometer chamber during

the operation of the arc-discharge beam, and  $l$  is the length of the  $\text{H}_2^+ + \text{H}_2$  interaction region which in this experiment is the length of the ionizer, 0.5 cm. Rate constants for this reaction have been experimentally<sup>118,119</sup> measured as well as calculated<sup>120</sup> and agree from 6 to  $20 \times 10^{-10} \text{ cm}^3 \text{ s}^{-1}$ . These rates are for a thermal process and, considering the high translational energy of the species in the beam, it is expected that the reactive cross sections will be reduced. The thermal cross section can be calculated from the relation

$$\sigma_{\text{rxn}} v^{\text{rel}} = k_{\text{rate}}. \quad (4.33)$$

At room temperature,  $v_{\text{H}_2}^{\text{lab}} = 1900 \text{ m/s}$ , but since we are interested in the velocity in the center of mass frame,  $v^{\text{rel}}$  will be related to  $v^{\text{lab}}$  by

$$v^{\text{rel}} = \sqrt{2} v^{\text{lab}}. \quad (4.34)$$

Using these numbers one can calculate a thermal cross section of  $\sim 75 \text{ \AA}^2$ . This cross section may now be scaled to the energies of the species in the beam. A number of workers<sup>120,121</sup> have shown that ion-molecule reactions for low energies (.1 - 10eV) exhibit the velocity dependence:

$$\sigma_{\text{rxn}} \propto \frac{1}{v^{\text{rel}}}. \quad (4.34)$$

We have shown in Figures 6 and 7 that a representative translational energy of the H and  $\text{H}_3$  species in the beam is 8 eV. Assuming this also to be the energy of the residual  $\text{H}_2$  in the beam, the corresponding  $\text{H}_2^+ + \text{H}_2$  cross section is  $6.6 \text{ \AA}^2$ . Substituting this value into (4.32) gives an expected  $m/e = 3$  signal of  $2 \times 10^{-14} \text{ A}$  which would be .004% of our observed  $m/e = 3$  of  $\sim 5 \times 10^{-10} \text{ A}$  signal when the beam is in operation. Even if the  $\text{H}_2$  molecules have an energy as low as 1 eV (which is very unlikely in view of the high temperature of the arc discharge), this figure would be about 0.01 %, which is still very

small. As a result, it can be concluded that this process contributes negligibly to the observed signal.

### b) Excited atom-molecule reaction

Since electronically excited H atoms can be formed in the electron bombardment ionizer, the reaction of these species with H<sub>2</sub> is another candidate for production of H<sub>3</sub><sup>+</sup>:



As before, we can estimate the H<sub>3</sub><sup>+</sup> ion current I<sub>H<sub>3</sub><sup>+</sup></sub> formed by this process by the expression

$$I_{\text{H}_3^+} = I_{\text{H}^*} \sigma_{\text{H}^* + \text{H}_2} \frac{p_{\text{H}_2}}{kT} l \quad (4.37)$$

where all the variables are as defined in equation (4.32) except for I<sub>H\*</sub> which is given by

$$I_{\text{H}^*} = \frac{I_{\text{e}^-} \sigma_{\text{H} + \text{e}^- \rightarrow \text{H}^* + \text{e}^-}}{v_{\text{H}} d} I_{\text{H}} \quad (4.38)$$

In this expression I<sub>e-</sub> is the measured electron beam current in the ionizer, 70 μA (i.e., 4 × 10<sup>14</sup> e<sup>-</sup>/s), v<sub>H</sub> is again the average translation energy of the 8.0 eV hydrogen atoms, 3.9 × 10<sup>6</sup> cm/s, I<sub>H</sub> is the current of the hydrogen atoms in the ionizer, 9.1 × 10<sup>16</sup> H-atoms/s, and lastly d is the diameter of the H beam in the region of the mass spectrometer ionizer region (3.2 mm). The cross section for the electronic excitation of H by 80 eV electrons (the energy used in our experiments) is a difficult number to obtain since it corresponds to formation of all excited states of a hydrogen atom by electron impact. Cross sections are known (both from theory and experiment)<sup>122</sup> for hydrogen atom excitation to the n = 2, 3, and 4 states. Graphing these cross sections as a function of inverse quantum number, they are observed to quickly fall off with increasing excitation. By fitting these cross sections with a straight line through the low n and summing along that line for many states (n = 1 -

20) we will get an upper limit to the cross section for total excitation which is  $\sim 1.5 \text{ \AA}^2$ . Substituting in these numbers into equation (4.38) gives the current of  $\text{H}^*$  formed in the ionizer as  $\sim 1.4 \times 10^{10} \text{ H}^*/\text{s}$ .

The ratio of the  $\text{I}_{\text{H}_3^+}$  ion currents produced from processes (4.31) and (4.36) can now be calculated by taking the ratio of equation (4.32) and (4.37):

$$\frac{\text{I}_{\text{H}_3^+}^{\text{H}^*+\text{H}_2}}{\text{I}_{\text{H}_2^+}^{\text{H}^*+\text{H}_2}} = \frac{\text{I}_{\text{H}^*}}{\text{I}_{\text{H}_2^+}} \frac{\sigma_{\text{H}^*+\text{H}_2}}{\sigma_{\text{H}_2^++\text{H}_2}}. \quad (4.39)$$

Substituting in our calculated value we get

$$\text{I}_{\text{H}_3^+}^{\text{H}^*+\text{H}_2} = 4.2 \times 10^{-14} \sigma_{\text{H}^*+\text{H}_2} (\text{\AA}^2). \quad (4.40)$$

The  $\text{H}^* + \text{H}_2$  reactive cross section is not known. This would mean that for this process to account for 10% of our observed signal, it would have to have a reactive cross section equal to  $1199 \text{ \AA}^2$ , a value which seems to us to be unrealistically large.

### c) Three-body recombination processes

Any 3-body recombination process of the type



can be ruled out. The pressure in the ionizer region is of the order of  $10^{-5}$  torr, resulting in a number density<sup>123</sup> of  $3.5 \times 10^{12}$  molecules  $\text{cm}^{-3}$ . It is difficult to calculate the number of triple collisions that occur in a gas, but a fairly good estimate should be obtained by setting the ratio of binary collisions  $Z_{12}$  to triple collisions  $Z_{123}$  equal to the ratio of the mean free path,  $d$ , and the molecular diameter  $\lambda$ :

$$\frac{Z_{12}}{Z_{123}} = \frac{\lambda}{d}. \quad (4.43)$$

E. Rabinsowitch<sup>124</sup> has shown that this ratio  $Z_{12}/Z_{121}$  closely parallels the rate constants of recombination reactions of halogen atoms where the efficiency of the reactions apparently depends on the number of triple collisions occurring. Applying this to our case where  $d \sim 10^{-8}$  cm and  $\lambda \sim 760$  cm,  $Z_{12}/Z_{123} = 7.6 \times 10^{10}$ . This crude calculation shows that at the low pressures VC2 operates at any 3-body collisions are highly unlikely.

As Professor J. Beauchamp suggested to us, an electron current can trap ions in the ionizing region of the mass spectrometer. As a result, the mean residence time of the ions being greater makes the likelihood of an ion molecule reaction greater. Professor Beauchamp proposed a simple check to see if this was occurring. By monitoring the  $H_3 : H$  ratio as a function of emission current, if the  $m/e = 3$  signal is due to ion-molecule as a result of ion trapping (contrasted to the  $m/e = 1$  signal resulting from electron impact ionization of H atoms) then the ratio should change as the emission current is reduced. Monitoring the ratio from 130 to 30  $\mu A$  there was no noticeable change in the ratio of the  $m/e = 3$  and  $m/e = 1$  signal. Thus it would appear both ion signals are the result of electron impact ionization.

In addition to the analysis of the mechanisms a), b), and c) perhaps the simplest proof that the species is not due to ion-molecule reactions comes from the results of an experiment again suggested to us by Professor J. Beauchamp. If the background gas in the mass spectrometer was  $D_2$  instead of  $H_2$ , and the signal was due to secondary reactions of beam species with background molecules, then additional peaks should be observed at  $m/e = 4$  and 5 due to the following possible processes:



This experiment has been tried by running the beam with  $\text{H}_2$  while doubling the pressure in the mass spectrometer chamber (VC2) with  $\text{D}_2$  ( $\sim 3 \times 10^{-5}$  torr). If the  $m/e = 3$  signal was due to ion-molecule reaction it should decrease and new peaks should grow. This experiment was performed (as explained in Section 2.5) with the ion lens turned off such that there would be no background signal due to the background gas. No peaks were observed under these conditions at  $m/e = 4$  or  $5$  and there were no detectable changes in the  $m/e = 1$  or  $3$  signals as a function of  $\text{D}_2$  pressure.

Thus from these experiments, as well as from the previous analysis, we are able to conclude that indeed the large  $m/e = 3$  signal observed cannot be explained on the basis of any secondary process which may occur in the ionizer region of the mass spectrometer. From this we are forced to conclude that this signal is indeed evidence of a neutral  $\text{H}_3$  species which is generated in the discharge itself.

Let us now examine the possibility that this  $\text{H}_3$  is due to population of an excited electronic state other than the  $2p \ ^2A_2''$  state. In recent years there has been a growth in the number of studies of atoms<sup>125-128</sup> in which the valence electron is excited to a state of high  $n$  (the principle quantum number). In these Rydberg states the electron is very weakly bound. Simple Bohr theory indicates that for  $n = 25$  the mean radius is approximately  $500 \text{ \AA}$  and the binding energy of the excited electron is only  $20 \text{ meV}$ . In a thermal collision there is more than enough energy available to result either in a change of state or ionization of the atom. However, in a collisionless environment these states are relatively long-lived. Quantum mechanical treatments<sup>128,129</sup> show that for  $n = 25$  the radiative lifetime can be anywhere from  $3$  to  $500 \mu\text{sec}$  depending on the value of the orbital angular momentum quantum number  $l$ . These long lifetimes are a consequence of poor overlap between the wave functions of the Rydberg state and the ground or lower excited states.

Due to these long lifetimes the possibility exists that the  $H_3$  we have observed is not in the  $2p \ ^2A''_2$  state as we proposed but some high-lying Rydberg states. To rule this out it is necessary to analyze the possibility the process of field ionization of these states.

When an atom is in a high Rydberg state it may be described to a good approximation as an ionic core with a single electron sufficiently far away from the core to be described by the single particle Hamiltonian<sup>130</sup>

$$H = -\frac{1}{2}\nabla^2 + V(r). \quad (4.47)$$

In the presence of a constant electric field  $\vec{E}$ , which is taken to lie along the  $z$  axis, a  $zE$  term must be added to the right-hand side of this equation. This field not only will perturb the atomic energy levels (Stark effect) but will cause a local potential maximum to appear on the "down-field" side of the atom. Therefore, in the presence of such an electric field there are no true stationary states and the electron will have a finite probability of tunneling through this potential barrier to the outside. As the field becomes high the barrier will become lower and narrower, thereby increasing the probability of the electron is being emitted. The penetrability of this barrier was first calculated by Lanczos<sup>131</sup> and this result has since been extended by many workers<sup>132-138</sup>. As a result, at low fields strong electron emissions occurs for electrons with binding energies smaller than the critical value

$$W_c \approx -24 [ E \text{ (kV/cm)} ]^{\frac{1}{2}} \text{ meV}. \quad (4.48)$$

If this simple hydrogenic model is assumed to hold for neutral atoms in general, then all Rydberg states with a principal quantum number greater than

$$n_C \approx 24 [ E \text{ (kV/cm)} ]^{-\frac{1}{4}} \quad (4.49)$$

are field ionized, where  $n_C$  is the quantum number and  $E$  is the strength of the applied field. This has been experimentally verified by a number of

workers<sup>138–140</sup>, so that hydrogenic theory provides a good model of highly excited Rydberg species in other species such as rare gases and alkalis atoms.

Though this hydrogenic model gives good agreement for highly excited states of such atoms it is expected to give only qualitative results for molecules. This is because the non-coulombic aspects of  $V(r)$  may be important far away from the core and a  $r^{-1}$  potential may be a poor approximation for even highly excited Rydberg states. Also, in molecules the ionic core is not “frozen” and energy transfer from core excitation to the Rydberg electron may occur<sup>136</sup>.

With these qualifications in mind, assuming that our  $H_3$  neutral will field ionize in a near-hydrogenic manner, the 1 kV/cm field which we currently use to sweep out ions can be expected to field ionize any  $H_3$  with  $n \geq 25$ . The ions generated in this manner will likewise be swept out and will not be detected by the mass spectrometer. We can therefore be certain that the species which we are detecting is not due to a highly excited Rydberg state.

Further evidence for this conclusion comes from work done by Gaillard *et al.*<sup>17</sup>. By using the neutralization-ionization method discussed in Section 4.1 they were able to study the sequence



By employing a field ionization cell (placed between their neutralization cell and their ionization cell) they could destroy a large fraction of the neutral triatomic molecules using fields of 50 kV/cm. By observing how the  $H_3$  population is depleted as a function of applied field and applying the hydrogenic frozen core model to their data they concluded that the  $H_3$  they generated were in  $n \leq 11$  states. To further prove this observation Gaillard measured the electron capture cross sections and saw that they were orders of magnitude smaller than the capture cross sections that have been measured by other workers for high- $n$  Rydberg states of atoms<sup>141</sup>. The small values as

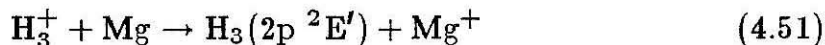
well as the unusual velocity dependence of the cross section can be explained by molecules in low Rydberg states spanning a few values of  $n$ .

With quenching of high Rydberg states accomplished by field ionization we still need to rule out the possibility of low-lying Rydbergs. To do this it is only necessary to look at the radiative lifetimes for states  $n \leq 25$ . As calculated from equations listed in Bethe and Salpeter<sup>128</sup>, as well as experimental data from Stebbings<sup>138</sup> and Allen<sup>142</sup>, states with  $n \leq 25$  should have lifetimes less than 10  $\mu\text{sec}$ . If  $\text{H}_3$  mimics these hydrogenic cases, any of these low-lying Rydbergs will have radiatively decayed before reaching the mass spectrometer detector in our apparatus.

From this analysis we can safely rule out the metastable of  $\text{H}_3$  we observe as being in high Rydberg in view of the field ionization produced by our ion deflector plates and the short radiative lifetimes of these states. Recently, further evidence for our assignment of our  $\text{H}_3$  metastable state comes from the work of Porter *et al.*<sup>41,42</sup>. After communicating our observation of a neutral species of  $\text{H}_3$  and our tentative assignment of its being in the  $2p\ ^2A_2''$  state, they repeated his earlier charge-exchange experiments where he had previously reported no evidence for a stable species of  $\text{H}_3$ . By increasing the angular resolution of his apparatus as well as now using K metal vapor in the collision chamber, instead of Mg, they were now able to see long-lived  $\text{H}_3$ .

They interpret the difference between their most recent<sup>41,42</sup> and previous results<sup>22,23</sup> as due to the target gas used. In the previous result Mg (whose IP is 7.7 eV) was used as the target gas to neutralize the  $\text{H}_3^+$ . Since it can be assumed that the electron transfer reaction in the velocity range of their experiment occurs vertically<sup>143</sup>, the  $\text{H}_3$  neutral produced in the repulsive  $2p\ ^2E'$  ground state would have initially the geometry of the ion (an equilateral triangle with  $r_o = 0.88\ \text{\AA}$ )<sup>60</sup>. The  $\text{H}_3$  ground state potential energy surface of Siegbahn and Liu<sup>4</sup> predicts the energy of the radical in this geom-

etry to be 3.1 eV above the ground state of  $\text{H}_2 + \text{H}^{4,18,19}$ . Since this agrees with their measured  $\text{H} + \text{H}_2$  relative translational energy, they conclude that the vertical electron process



is predominant, explaining why no metastable  $\text{H}_3$  neutrals were observed. This is not surprising since the  $\text{H}_3$  level with the smallest energy mismatch with respect to ionization of Mg is the  $2p \ ^2E'$  one, which should therefore be the ones most resonantly accessed in the  $\text{H}_3^+ / \text{Mg}$  reaction.

However, in their most recent results the kinetic energy released from the  $\text{H}_3$  produced in the  $\text{H}_3^+ / \text{K}$  reaction is almost 2 eV greater than that observed with the Mg target. The ionization potential of K is 4.2 eV. This indicates that a higher energy state of  $\text{H}_3$  is produced by electron transfer from the metal with a lower ionization potential. From theoretical calculations, the first two excited states of  $\text{H}_3$  (the closely spaced  $2s \ ^2A'_1$  and  $2p \ ^2A''_2$  states) are expected to be  $\sim 5.85$  eV above the separated dissociation products<sup>29-31</sup>. Comparing this theoretical value with their experimental value of 5.0 eV, Porter *et al.*<sup>42</sup> conclude that the electron-transfer reaction is dominated by the processes



These electron transfers of K to the first two excited states of  $\text{H}_3$  are nearly resonant and therefore should be the most accessible. Since this corresponds to the  $2p \ ^2A''_2$  state (which was described in Section 4.3) they attributed their observations to formation of this state and therefore to (4.53).

## 4.8 Future Work

The experiments performed to date on  $H_3$  have only scratched the surface of what is possible to learn from that molecule. The  $H_3$  can be considered an excited state of the  $H + H_2$  reaction and as such makes it an interesting species to study. The electronic energy of the  $2p \ ^2A''$  state of  $H_3$  is approximately 5.85 eV above that of  $H + H_2$  <sup>29,43</sup> whereas the potential energy of the  $2p \ ^2E'$  repulsive ground state is somewhat in excess of 2.65 eV. Therefore, upon a vertical transition to the ground state, the Rydberg will liberate about 3 eV of electronic energy, the balance to 5.85 eV becoming available as nuclear potential energy with respect to the  $H + H_2$  dissociated configuration. In a collision with another molecule, this energy could become available for reaction. Furthermore, the laboratory translational energy of these  $H_3$  molecules is, as pointed out previously, in the range of 0 to 12 eV, providing an additional source of energy. Therefore, this species can be expected to exhibit highly unusual dynamics in that it may indeed undergo novel chemical reaction as well as perhaps unexpected partitioning of the available energy into electronic, vibrational, rotational and translational energy of the products. Chemiluminescent processes are possible and electronic population inversions may be produced as well. Since the intensity of the  $H_3$  with respect to  $H$  in the beam can be controlled to some extent by regulation of the stagnation pressure, one should be able to deconvolute the dynamical properties of  $H$  from those of  $H_3$ .

What follows is a possible shopping list of future experiments which would involve utilizing the  $H_3$  species.

a) Spontaneous Emission from  $H_3$ : By viewing the light emitted by the  $H_3$  beam well away from the source, through a well-baffled large aperture

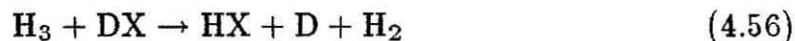
visible light monochromator, it may be possible to observe the metastable state decay spontaneously. Far enough away all electronically excited states of  $H_3$  should have decayed except for the  $2p \ ^2A_2''$  metastable one. The probability that it will decay during the few microseconds it remains in the view field of the optical detector depends on the lifetime of the  $2p \ ^2A_2'' \rightarrow 2p \ ^2E'$  continuum emission, but due to the large intensity of the incident beam, there is a good chance that the corresponding emission could be detected. Efforts to date to observe this emission using a simple PMT failed due to the large photon background in the chamber. By using better baffling as well as a more sophisticated detection system, it should be possible to observe this emission. Once this was observed, velocity selecting the beam and measuring the change in the emission band intensity would give information on the emission lifetime itself. The shape of the emission continuum band contains information about the shape of the of the repulsive  $2p \ ^2E'$  potential energy surface.

b) Collisionally Induced Chemiluminescence: Utilizing a gas cell and a series of rare gas target it should be possible to detect the  $2p \ ^2A_2'' \rightarrow 2p \ ^2E'$  emission induced by collisions between  $H_3$  and those gases. Crude measurements utilizing a photomultiplier tube failed to show any emission for the reasons mentioned above. However, a more sophisticated system of photon counting may permit its detection. If the signal-to-noise ratio permits it, it may be possible to repeat these measurements with velocity selected beams and to resolve the spectrum of the emitted light. This will provide information about the collisionally induced luminescence and its dependence on the target polarizability. The change in the shape of the emission band with respect to that of the spontaneous emission should give interesting information about the interaction potential between the metastable  $H_3$  and the rare gases.

c) Laser Spectroscopy: Electronically excited states lying above the  $2p \ ^2A_2''$  one

can be probed through the use of lasers. If, after excitation, the state produced cascades down to the repulsive  $2p\ ^2E'$  ground state and separate apart to form  $H + H_2$ , a drop in the  $m/e = 3$  peak intensity will be observed. By observing that signal as a function of laser excitation wavelength it should be possible to obtain detailed information about the spectroscopy of  $H_3$  in the collision-free environment of a molecular beam. Furthermore, if emission to states above the  $2p\ ^2E'$  one occurs in that time interval, one could detect such laser-induced fluorescence and obtain complementary information about the excitation process.

d) Reactive Collision Dynamics: Investigations of the reaction dynamics of metastable  $H_3$  should be very interesting. In certain respects the reaction of these molecules may resemble those of H atoms, since they can produce such atoms upon light emission or internal conversion to the  $2p\ ^2E'$  repulsive ground state. On the other hand, the available 3 eV of electronic energy plus 2.85 eV or so of potential energy make it potentially a highly reactive species. The availability of several eV of additional translational energy further broadens the range of chemical reactions that are energetically accessible. Examples of such reactions are:



Reactions (4.54) and (4.55) would not be possible with hydrogen atoms but may be possible with  $H_3$ . The next three reactions are the counterparts of hydrogen atom exchange and abstraction, with the  $H_2$  acting as a chaperone. Reaction (4.59) is analogous to an abstraction reaction and could occur via a harpooning mechanism analogous to that between  $M$  and  $X_2$  (where  $M$  is an alkali metal). Likewise, reactions (4.60) and (4.61) will not occur with hydrogen atoms in the absence of a third body. The  $H_3$  molecule may be thought of as a hydrogen atom carrying its own third body. As a result these reactions may indeed occur. Some of these reactions may be chemiluminescent or may likewise be studied by laser-induced fluorescence detection techniques. As a consequence of these studies new reaction dynamics may be discovered.

#### 4.9 References

1. H. Eyring and M. Polanyi, *Z. Phys. Chem*, **B12**, 279 (1931).
2. J. O. Hirschfelder, H. Eyring, and H. Rosen, *J. Chem. Phys.*, **4**, 121 (1936).
3. I. Shavitt, R. M. Stevens, F. L. Minn, and M. Karplus, *J. Chem. Phys*, **48**, 2700 (1968).
4. P. Siegbahn and B. Liu, *J. Chem. Phys.*, **68**, 2466 (1978).
5. D. G. Truhlar and R. E. Wyatt, *Ann. Rev. Phys. Chem.*, **27**, 1 (1976).
6. F. M. Devienne and J. C. Roustan, *C. R. Acad. Sci. Paris*, **263**, B-1389 (1966).
7. F. M. Devienne, *C. R. Acad. Sci. Paris*, **264**, B-1400 (1967); **267**, B-1279 (1968); **268**, B-1303 (1969).
8. F. M. Devienne, *Entropie*, **24**, 35 (1968).
9. F. M. Devienne, *Compt. Rend.*, **267**, 1400 (1967).
10. F. M. Devienne, *Sixth International Conference on the Physics of Electronic and Atomic Collisions*, MIT Press, Cambridge, p. 789 (1969).
11. J. Gray and R. H. Tomlinson, *Chem. Phys. Lett.*, **4**, 251 (1969).
12. C. F. Barnett and J. A. Ray, *Phys. Rev. A.*, **5**, 2120 (1972).
13. T. Nagasaki, H Doi, K. Wada, K. Higashi, and F. Fukuzawa, *Phys. Lett.*, **38A**, 381 (1972).
14. E. Frenkel, *Z. Naturforsch.*, **25a**, 1265 (1970).

15. F. J. Comes and U. Wenning, *Z. Naturforsch.*, **24a**, 1227 (1969).
16. N. V. de Castro Faria, M. J. Gaillard, J. C. Poizat, and J. Remillieux, *Ann. Israël Phys. Soc.*, **4**, 134 (1981).
17. M. J. Gaillard, A. G. de Pinho, J. C. Poizat, J. Remillieux, and R. Saoudi, *Phys. Rev. A*, **28**, 1267 (1983).
18. M. Vogler and B. Meierjohann, *J. Chem. Phys*, **69**, 2450 (1978).
19. M. Vogler, *Phys. Rev. A*, **19**, 1 (1979).
20. R. N. Porter, R. M. Stevens, and M. Karplus, *J. Chem. Phys.*, **66**, 2392 (1977).
21. C. Cisneros, I. Alvarez, R. Garcia G., C. F. Barnett, J. A. Ray, and A. Russek, *Phys. Rev. A*, **19**, 631 (1979).
22. P. M. Curtis, B. W. Williams, and R. F. Porter, *Chem. Phys. Lett.*, **65**, 296 (1979).
23. P. M. Curtis, Ph.D thesis, Cornell University, 1979. Available from University Microfilms, Inc., Ann Arbor, Michigan.
24. G. Herzberg, *J. Chem. Phys*, **70**, 4806 (1979).
25. I. Dabrowski and G. Herzberg, *Can. J. Phys.*, **58**, 1238 (1980).
26. G. Herzberg and J. K. G. Watson, *Can. J. Phys.*, **58**, 1250 (1980).
27. G. Herzberg, H. Lew, J. J. Sloan and J. K. G. Watson, *Can. J. Phys.*, **59**, 428 (1981).
28. G. Herzberg, J. T. Hougen and J. K. G. Watson, *Can. J. Phys.*, **60**, 1261 (1982).

29. H. R. King and K. Morokuma, *J. Chem. Phys.*, **71**, 3213 (1979).
30. R. L. Martin, *J. Chem. Phys.*, **71**, 3541 (1979)
31. M. Junger, *J. Chem. Phys.*, **71**, 3540 (1979).
32. G. Calzaferri, *Chem. Phys. Lett.*, **87**, 443 (1982).
33. J. Tennyson *Chem. Phys. Lett*, **86**, 181 (1982).
34. S. Raynor and D. R. Herschbach, *J. Phys. Chem.*, **86**, 1214 (1982).
35. S. Raynor and D. R. Herschbach, *J. Phys. Chem.*, **86**, 3592 (1982).
36. K. Hirao and S. Yamabe, *Chem Phys.*, **80**, 237 (1983).
37. H. R. Mayne, R. A. Poirier, and J. C. Polanyi, *J. Chem. Phys.*, **80**, 4025 (1984).
38. M. Jungen and V. Staemmler, *Chem. Phys. Lett.*, **103**, 191 (1983).
39. K. Kaufmann, M. Jungen, and V. Staemmler, *Chem. Phys.*, **79**, 111 (1983).
40. J. K. G. Watson, *Phys. Rev. A*, **22**, 2279 (1980).
41. G. I. Gellene, D. A. Cleary, R. F. Porter, *J. Chem. Phys.*, **77**, 3471 (1982).
42. G. I. Gellene and R. F. Porter, *J. Chem. Phys.*, **79**, 5975 (1983).
43. C. G. Freeman, T. I. Quickenden, and D. F. Sangster, *J. of Photochemistry*, **24**, 403 (1984).
44. H. Figger, H. Moller, W. Schrepp, and H. Walther, *Chem. Phys. Lett.*, **90**, 90 (1982).
45. W. Schrepp, H. Figger, and H. Walther, *Lasers & Applications*, **77** (July

- 1984).
46. H. Figger, M. N. Dixit, R. Maier, W. Schrepp, and H. Walther, *Phys. Rev. Letters*, **52**, 906 (1984).
  47. J. F. Garvey and A. Kuppermann, *Chem. Phys. Lett.*, **107**, 491 (1984).
  48. H. L. Kunth, *Appl. Mech. Rev.*, **17**, 751 (1964).
  49. W. S. Young, W. E. Rodgers, and E. L. Kunth, *Rev. Sci. Instrum.*, **40**, 1346 (1969).
  50. K. R. Way, S.-C. Yang, and W. C. Stwalley, *Rev. Sci. Instrum.*, **9**, 1049 (1976).
  51. W. C. Stwalley, private communication.
  52. R. Gotting, H. R. Mayne, and J. P. Toennies, *J. Chem. Phys.*, **80**, 2230 (1984).
  53. R. W. Bukes Jr., K. R. Newton, J. M. Herrmann, and R. B. Bernstein, *J. Chem. Phys.*, **64**, 3648 (1976).
  54. E. Gehrcke and E. Lau, *Sitzungsber. Preuss. Akad.*, **24**, 453 (1922).
  55. F. Horton and A. C. Davies, *Philos. Mag.*, **46**, 872 (1923).
  56. H. D. Smyth and C. J. Brasefield, *Proc. Natl. Acad. Sci. U.S.A.*, **12**, 443 (1926).
  57. G. Herzberg, *Ann. Phys. (Leipzig)*, **84**, 565 (1927).
  58. H. M. Crosswhite, *The Hydrogen Molecule Wavelength Tables of Gerhard Heinrich Dieke*, Wiley Interscience, New York, N.Y. (1972).
  59. M. J. Gaillard, D. S. Gemmell, G. Goldring, I. Levine, W. J. Pietsch, J.

- C. Poizat, A. J. Ratkowski, J. Remillieux, Z. Vager, and B. J. Zarbansky, *Phys. Rev. A.*, **17**, 1797 (1978).
60. T. Oka, *Phys. Rev. Lett.*, **45**, 531 (1980).
61. G. Herzberg, private communication.
62. I. Langmuir and K. H. Kingdom, *Science*, **57**, 58 (1923).
63. M. A. D. Fluendy and K. P. Lawley, *Chemical Application of Molecular Beam Scattering*, Chapman and Hall, London, p. 132 (1973).
64. J. H. Moore, C. C. Davis and M. A. Coplan, *Building Scientific Apparatus*, Addison-Wesley, p. 305 (1983).
65. D. Datz and E. H. Taylor, *J. Chem. Phys.*, **25**, 389 (1956).
66. K. T. Gillen, C. Riley, and R. B. Bernstein, *J. Chem. Phys.*, **50**, 4019 (1969).
67. I. Langmuir and K. H. Kingdon, *Proc. Roy. Soc. (London)*, **A107**, 61 (1925).
68. M. J. Copley and T. E. Phipps, *Phys. Rev.*, **48**, 960 (1935).
69. E. Ya. Zandberg and N. I. Ianov, *Usp. Fiz. Nauk.*, **67**, 581 (1959).
70. M. Remy, *J. Chem. Phys.*, **53**, 2487 (1970).
71. K. P. Wojciechowski, *Surface Sci.*, **55**, 246 (1976).
72. J. P. Muscat and D. Newns, *Surface Sci.*, **74**, 355 (1978).
73. R. K. Janev, *J. Phys.*, **B7**, 1506 (1974).
74. W. Bloss and D. Hone, *Surface Sci.*, **72**, 277 (1978).

75. E. G. Overbosch and J. Los, *Surface Sci.*, **108**, 99 (1981).
76. R. Brako and D. M. Newns, *Surface Sci.*, **108**, 253 (1981).
77. U. V. Gemmingen and R. Sizmann, *Surface Sci.*, **114**, 445 (1982).
78. R. M. Gurney, *Phys. Rev.*, **47**, 479 (1935).
79. R. Gomer and L. W. Swanson, *J. Chem. Phys.*, **38**, 1613 (1963).
80. J. W. Gadzuk, *Surface Sci.*, **6**, 133 (1967).
81. K. R. Wilson and D. R. Herschbach, *J. Chem. Phys.*, **49**, 2676 (1968).
82. K. T. Gillen, A. M. Rulis, and R. B. Bernstein, *J. Chem. Phys.*, **54**, 2831 (1971).
83. E. Hulpke and C. Schlier, *Z. Physik*, **207**, 294 (1967).
84. R. K. B. Helbing and E. W. Rothe, *J. Chem. Phys.*, **48**, 3945, (1968); **51**, 1607, 3628 (1969).
85. E. G. Overbosch, B. Rasser, A. D. Tenner, and J. Los, *Surface Sci.*, **92**, 310 (1980).
86. E. G. Overbosch and J. Los, *Surface Sci.*, **108**, 99 (1981).
87. J. Politiek and J. Los, *Rev. Sci. Instrum.*, **40**, 1576 (1969).
88. T. R. Trouw and J. W. Trischka, *J. Appl. Phys.*, **34**, 3635 (1963).
89. K. T. Gillen, A. M. Rulis, and R. B. Bernstein, *J. Chem. Phys.*, **54**, 2831 (1971).
90. K. T. Gillen and R. B. Bernstein, *Chem. Phys. Lett.*, **5**, 275 (1970).
91. H. E. Litvak, M. E. Gersh, and R. B. Bernstein, *Chem. Phys. Lett.*, **36**,

- 145 (1975).
92. E. F. Greene, A. Persky, and A. Kuppermann, *J. Chem. Phys.*, **49**, 2347 (1968).
93. R. B. Bernstein, private communication.
94. E. F. Green, J. T. Keeley and M. A. Pickering, *Surf. Sci.*, **120**, 103 (1982).
95. Oriel Corporation Catalog, Stamford, Conn., p. D30 (1979).
96. W. E. Lamb, Jr. and R. C. Retherford, *Phys. Rev.*, **79**, 549 (1950).
97. I. A. Sellin, *Phys. Rev.*, **136**, A1245 (1964).
98. W. Mais, *Phys. Rev.*, **45**, 773 (1934).
99. S. Rosin and I. Rabi, *Phys. Rev.* **48**, 373 (1935).
100. P. Rosenberg, *Phys. Rev.*, **55**, 1267 (1939).
101. I. Rabi, *Rev. Sci. Instr.*, **6**, 251 (1935).
102. K. Kodera and T. Tamura, *Bull. Chem. Soc. Japan*, **31**, 206 (1958).
103. H. S. W. Massey and C. B. O. Mohr, *Proc. Roy. Soc. (London)*, **A 144**, 188 (1934).
104. E. W. Rothe and R. B. Bernstein, *J. Chem. Phys.*, **31**, 1619 (1959).
105. E. W. Rothe, Ph.D thesis, University of Michigan (1959). Available from University Microfilms, Inc., Ann Arbor, Michigan
106. H. Schumacher, R. B. Bernstein, and E. W. Rothe, *J. Chem. Phys.*, **33**, 584 (1960).
107. R. D. Levine and R. B. Bernstein, *Molecular Reaction Dynamics*, Oxford

- University Press, New York (1974)., a) p.16 , b) p.86.
108. L. Loeb, *Kinetic Theory of Gases*, McGraw-Hill, New York (1934).
109. P. Rosenberg, *Phys. Rev.*, **61**, 528 (1942).
110. V. Aquilanti, G. Linti, F. Vecchio-Cattivi, and G. G. Volpi, *Chem. Phys. Lett.*, **15**, 305 (1972).
111. R. W. Bickes, Jr., B. Lantzsch, J. P. Toennies, and K. Walaschewski, *Faraday Discuss. Chem. Soc.*, **55**, 167 (1973).
112. G. Das, A. F. Wagner, and A. C. Wahl, *J. Chem. Phys.*, **68**, 4917 (1978).
113. R. D. Levine and R. B. Bernstein, *Reaction Dynamics*, Oxford University Press (1974).
114. J. Peter Toennies, W. Welz, and G. Wolf, *J. Chem. Phys.*, **71**, 614 (1979).
115. R. E. Dickerson, H. B. Gray, and G. P. Haight, Jr., *Chemical Principles*, W. A. Benjamin, Inc. p. 596 (1974).
116. A. Streitwieser, Jr., and C. H. Heathcock, *Introduction to Organic Chemistry*, Macmillan Publishing Co. (1976).
117. R. B. Bernstein, *Chemical Dynamics via Molecular Beam and Laser Techniques*, Oxford University Press (1982).
118. V. L. Tal'roze and E. L. Frankenvich, *Zh. fiz. Khim.*, **34**, 2709 (1960).
119. K. P. Warne, *J. Chem. Phys.*, **46**, 502 (1967).
120. G. Gioumouisis, and D. P. Stevenson, *J. Chem. Phys.*, **29**, 294 (1958).
121. K. R. Ryan and J. H. Furtell, *J. Chem. Phys.*, **43**, 3009 (1965).

122. K. Takayanagi and H. Suzuki, *Cross Section for Atomic Processes, Vol. I*, Research Information Center Institute of Plasma Physics, Nagoya University, Nagoya, Japan (1975).
123. J. H. Moore, C. C. Davis, and M. A. Coplan *Building Scientific Apparatus*, Addison-Wesley (1983).
124. E. Rabinowitsch, *Trans. Faraday Soc.*, **33**, 283 (1937).
125. S. A. Edelstein and T. F. Gallagher, *Advances Atomic Mol. Phys*, **14**, 365 (1978).
126. K. Takayanagi, *Comments Atomic Mol. Phys.*, **6**, 177 (1977).
127. R. F. Stebbings, *Science*, **193**, 537 (1976).
128. H. A. Bethe and E. E. Salpeter, *Quantum Mechanics of One-and Two-Electron Atoms*, Springer-Verlag, Berlin (1957).
129. J. R. Hiskes, C. B. Tarter, and D. A. Moody, *Phys. Rev.*, **133**, A424 (1964).
130. E. Fermi, *Nuovo Cim.*, **11**, 157 (1934).
131. C. Lanczos, *Z. Physik*, **68**, 204 (1931).
132. D. S. Boudreaux and P. H. Cutter, *Phys. Rev.*, **149**, 170 (1966).
133. M. G. Inghram and R. Gomer, *Z. Naturforsch.*, **10a**, 863 (1955)
134. E. W. Muller and K. Bahadur, *Phys. Rev.*, **102**, 624 (1956).
135. F. Kirchner, *Naturwiss*, **41**, 136 (1954).
136. R. Gomer, *J. Chem. Phys.*, **21**, 1869 (1953).
137. D. S. Bailey, J. R. Hiskes, A. C. Riviere, *Nucl. Fusion*, **5**, 41 (1965).

138. R. F. Stebbings, C. J. Latimer, W. P. West, F. B. Dunning and T. B. Cook, *Phys. Rev. A.*, **12**, 1453 (1975).
139. P. M. Koch, L. D. Gardner, and J. E. Bayfield, in *Fourth International Conference on Beam Foil Spectroscopy, Gatlinburg, Tenn.* Plenum, New York (in press).
140. D. K. Kleppner, M. G. Littman, and M. L. Zimmerman, in *Atoms and Molecules in Rydberg States*, eds. R. F. Stebbings and F. B. Dunning, Cambridge University Press, Cambridge, England (in press).
141. M. Breinig, S. B. Elston, S. Huldt, L. Liljeby, C. R. Vane, S. D. Barry, G. A. Glass, M. Schauer, I. A. Sellin, G. D. Alton, S. Datz, S. Overbury, R. Laubert, and M. Suter, *Phys. Rev. A.*, **25**, 3015 (1982).
142. L. Allen, D. G. C. Jones, and D. G. Schofield, *J. Opt. Soc. Am.*, **59**, 842 (1969).
143. G. I. Gellene, D. A. Cleary, R. F. Porter, C. E. Burkhardt, and J. J. Leventhal, *J. Chem. Phys.*, **77**, 1354 (1982).
144. K. C. Kulander and M. F. Guest, *J. Phys. B: Atom. Molec. Phys.*, **12**, L501 (1979).
145. M. Karplus and R. N. Porter, *Atoms & Molecules: An Introduction For Students of Physical Chemistry*, Benjamin/Cummings Publishing Co., p. 139 (1970).

#### 4.10 Figures and Captions

Figure 1. A schematic view of the top of the machine: VC1, vacuum chamber one; AS, anode assembly; A, anode; C, cathode; M, magnet; Sm water-cooled copper skimmer; TA, translation assembly; T, translator; P1, viewport; L, optical lens; C2, 150 Hz chopper; monochromator, 0.5 Jarrell-Ash monochromator; PM, photomultiplier; CP, current preamp; LI 2, lock-in amplifier; SCR2, strip chart recorder; VC2, vacuum chamber 2; C1, 10 Hz chopper; D, electric field deflectors; F, mechanical flag; QMS, quadrupole mass spectrometer; P2, port; PA, EAI preamplifier (ESA-75); LI 1, lock-in amplifier; MSE, mass spectrometer electronics; SCR1, strip chart recorder.

Figure 2. AC ion current as a function of  $m/e$ . In each panel the lower curve in the AC background obtained with the electron beam turned off, and the upper curve is the AC ion current signal shifted upwards by  $0.2 \times 10^{-10}$  A for convenience of display. Electron impact current:  $100 \mu\text{A}$ . Electron accelerating voltage: 60V. Ion source pressure:  $2.1 \times 10^{-5}$  torr measured by an uncalibrated ion gauge. (a)  $\text{H}_2$  in the molecular beam source; (b)  $\text{D}_2$  in that source; (c) and equimolar mixture of  $\text{H}_2$  and  $\text{D}_2$  in that source. For all the panels the stagnation pressure in the molecular beam source was 60 torr. (Nozzle conditions changed slightly.)

Figure 3. Average DC ion current as a function of pressure for  $m/e = 1, 2,$  & 3. Mass spectrometer electron impact current is  $100 \mu\text{A}$  and electron accelerating voltage is 60 V. Error bars represent 90% confidence limit.

Figure 4. Energy level diagram for  $\text{H}_3$ . In the figure the ground and excited

states of  $H_3$  are scaled with respect to their dissociation products as determined by ref. 25. The scaling of the ground state of  $H_3^+$  with respect to  $H_2 (X^1\Sigma_g^+) + H^+$  is taken from Ref. 144. On this energy level diagram  $H_2 (X^1\Sigma_g^+) + H (n = 1)$  is taken as the zero of energy. Arrows indicate some of the observed spectroscopic transactions.

Figure 5. Representation of  $H_3$  molecules in the  $2p^2A_2''$  state. The bond distance for the nuclei were taken from Ref. 26. The Rydberg orbital perpendicular to the plane of the nuclei is represented by a 90 % boundary surface of a hydrogenic  $2p_z$  orbital<sup>143</sup>.

Figure 6. Emission spectrum from 7000 Å to 7300 Å of a hydrogen arc at a stagnation pressure of 60 torr.

Figure 7. Emission spectrum from 7000 Å to 7400 Å of a deuterium arc at a stagnation pressure of 60 torr.

Figure 8. Emission spectrum viewed through port P1; (a) stagnation pressure = 100 torr, (b) stagnation pressure = 60 torr, (c) photometer tracing of 7120 Å band of  $H_3$  observed by Herzberg with sharp  $H_2$  removed.

Figure 9. (a) Emission spectrum of 7120 Å band as viewed through port P1, (b) Emission intensity of the  $H_3$  band as viewed through port P1 as a function of pressure.

Figure 10. (a) Emission spectrum of 7480 Å band viewed through port P1 at a stagnation pressure of 98 torr of  $H_2$  gas, (b) Emission intensity of the 7480 Å band as viewed through port P1 as a function of pressure.

Figure 11. Ionization efficiency ( $I_{eff}$ ) plotted as a function of tungsten filament efficiency temperature for the production of  $H^+$  and  $H_3^+$  ions, (a) stagnation pressure = 80 torr, (b) stagnation pressure = 75 torr, (c)

stagnation pressure = 70 torr.

Figure 12. The natural log of the ionization efficiency ( $I_{eff}$ ) plotted as a function of inverse tungsten filament temperature for the production of  $H^+$  and  $H_3^+$  ions, (a) stagnation pressure = 80 torr, (b) stagnation pressure = 75 torr, (c) stagnation pressure = 60 torr. Dashed line represents a least squares fit the points.

Figure 13. Ionization efficiency ( $I_{eff}$ ) plotted as a function of platinum filament temperature for the production of  $H^+$  and  $H_3^+$  ions, (a) stagnation pressure = 75 torr, (b) stagnation pressure = 65 torr, (c) stagnation pressure = 60 torr.

Figure 14. The natural log of the ionization efficiency ( $I_{eff}$ ) plotted as a function of inverse platinum filament temperature for the production of  $H^+$  and  $H_3^+$  ions, (a) stagnation pressure = 80 torr, (b) stagnation pressure = 75 torr, (c) stagnation pressure = 60 torr. Dashed line represents a least squares fit the points.

Figure 15. A schematic view of the top of the machine: VC1, vacuum chamber one; AS, anode assembly; A, anode; C, cathode; M, axial magnet; S, water-cooled copper skimmer; TA, translation assembly; T, translator; P1, viewport; VC2, vacuum chamber; P2, mounting port for photoionization cell; SM, spherical mirror; DP, electric field deflectors; L, quartz lens; ML, 200 watt high pressure mercury lamp; PS, power supply for mercury lamp; QW, quartz window; IG, ion gauge; QMS, quadrupole mass spectrometer; PA, EAI preamplifier (ESA-75); MSE, mass spectrometer electronics; CAT, time-averaging computer; X-Y, x-y recorder.

Figure 16. Top cross sectional view of photoionization cell with mounting flange. Hatched area of drawing indicates the pipe walls.

Figure 17. a) Side view of photoionization cell sighting through entrance aperture looking toward the mass spectrometer. The hatched areas indicate the cell walls. b) Front view of photoionization cell looking at it mounted on P2 (Figure 15).

Figure 18. Output spectra of a variety of high intensity lamps. The data are to be regarded as typical and are subject to variation from lamp to lamp. The instrument bandwidth is 2 nanometers.

Figure 19. Results for photoionization of  $H_3$ , (a) mercury lamp on, electron impact ionizer off, (b) mercury lamp off, electron impact ionizer off, (c) mercury lamp off, electron impact ionizer on. Figure 19 A is for a stagnation pressure of 100 torr, Figure 19 B is for a stagnation pressure of 95 torr, Figure 19 C is for a stagnation pressure of 90 torr, and Figure 19 D is for a stagnation pressure of 80 torr. The intensity scale appropriate for each of these figures is depicted in (c) for each. The same scale applies as well to (a) and (b) with the appropriate multiplicative factor.

Figure 20. Photoion current generated by irradiation of beam with mercury lamp as a function of  $m/e$ . Points represent the difference of Figure (a) and Figure (b) from Figure 19. a) stagnation pressure = 100 torr, b) stagnation pressure = 95 torr, c) stagnation pressure = 90 torr, d) stagnation pressure = 80 torr. Smooth curve through the points represent author's opinion of what is significant.

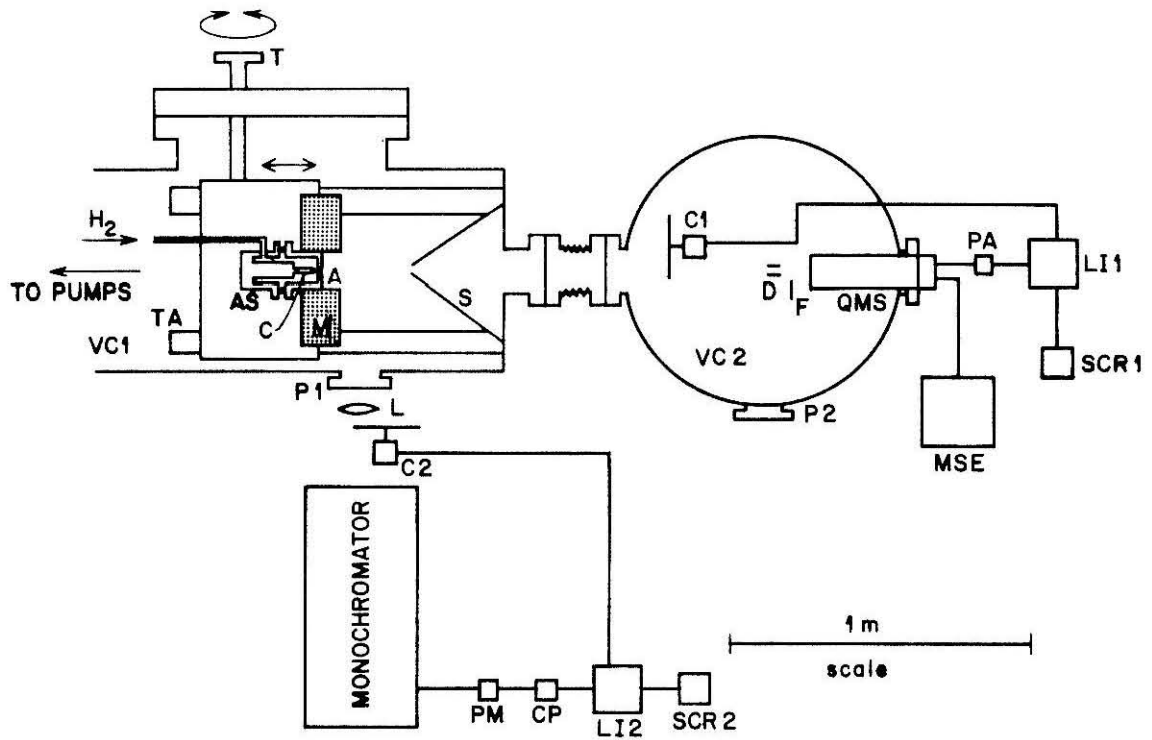
Figure 21. A schematic view of the top of the machine: VC1, vacuum chamber one; AS, anode assembly; A, anode; C, cathode; M, axial magnet; S, water-cooled copper skimmer; TA, translation assembly; T, translator; P1, viewport; VC2, vacuum chamber; P2, mounting port for black anodized pipe; SM, spherical mirror; DP, electric field deflectors; QW,

quartz window; IG, ion gauge; QMS, quadrupole mass spectrometer; PA, EAI preamplifier (ESA-75); MSE, mass spectrometer electronics; CAT, time-averaging computer; X-Y, x-y recorder.

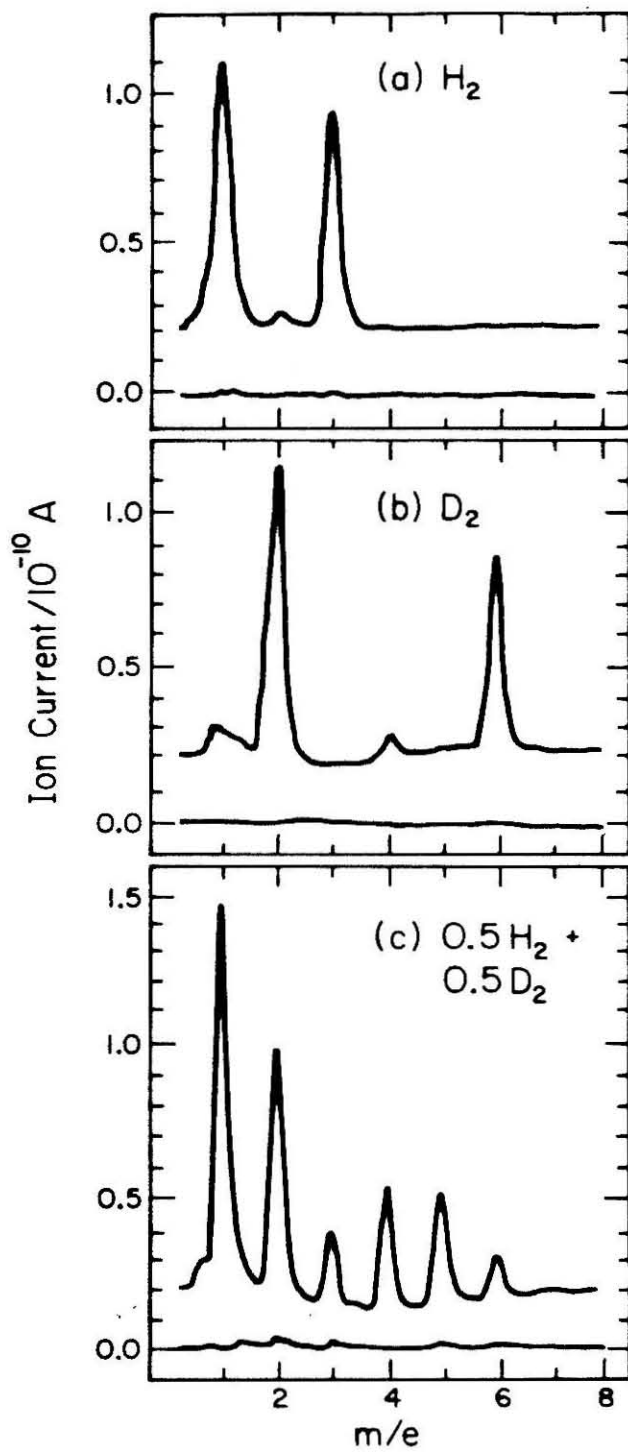
Figure 22. Attenuation of mass spectrometer signal plotted as a function of argon pressure within the stagnant gas cell for  $m/e = 1, 2,$  and  $3$ .  $I_0$  is intensity of that species with no gas in the cell and  $I$  is intensity of that species at that pressure. Dotted lines are least squares fit to points. Path length of gas cell is 4 inches. Beam stagnation pressure is 57 torr.

Figure 23. Attenuation of mass spectrometer signal plotted as a function of argon pressure within the stagnant gas cell for  $m/e = 1$ .  $I_0$  is intensity of that species with no gas in the cell and  $I$  is intensity of that species at that pressure. Dotted lines are least squares fit to points. Path length of gas cell is 2 inches. Beam stagnation pressure is 65 torr.

Figure 24. Attenuation of mass spectrometer signal plotted as a function of argon pressure within the stagnant gas cell for  $m/e = 3$ .  $I_0$  is intensity of that species with no gas in the cell and  $I$  is intensity of that species at that pressure. Dotted lines are least squares fit to points. Path length of gas cell is 2 inches. Beam stagnation pressure is 65 torr.



**Figure 1**

**Figure 2**

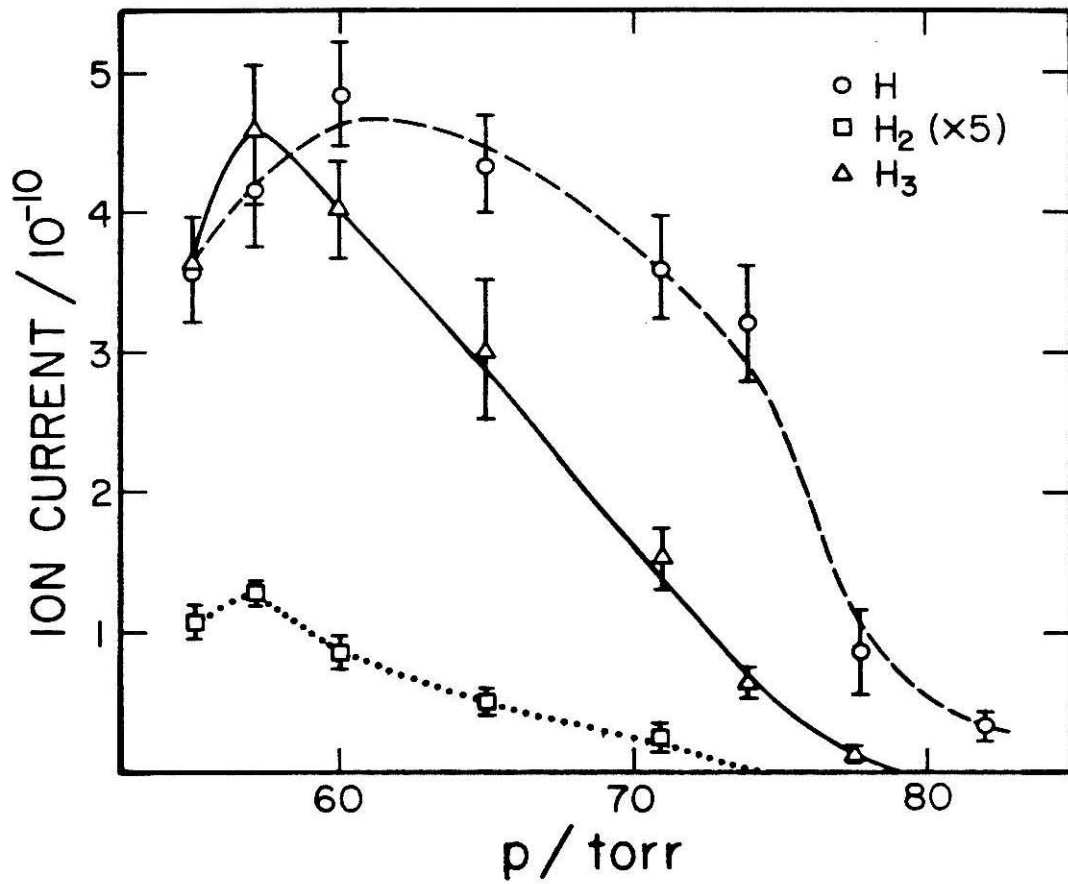


Figure 3

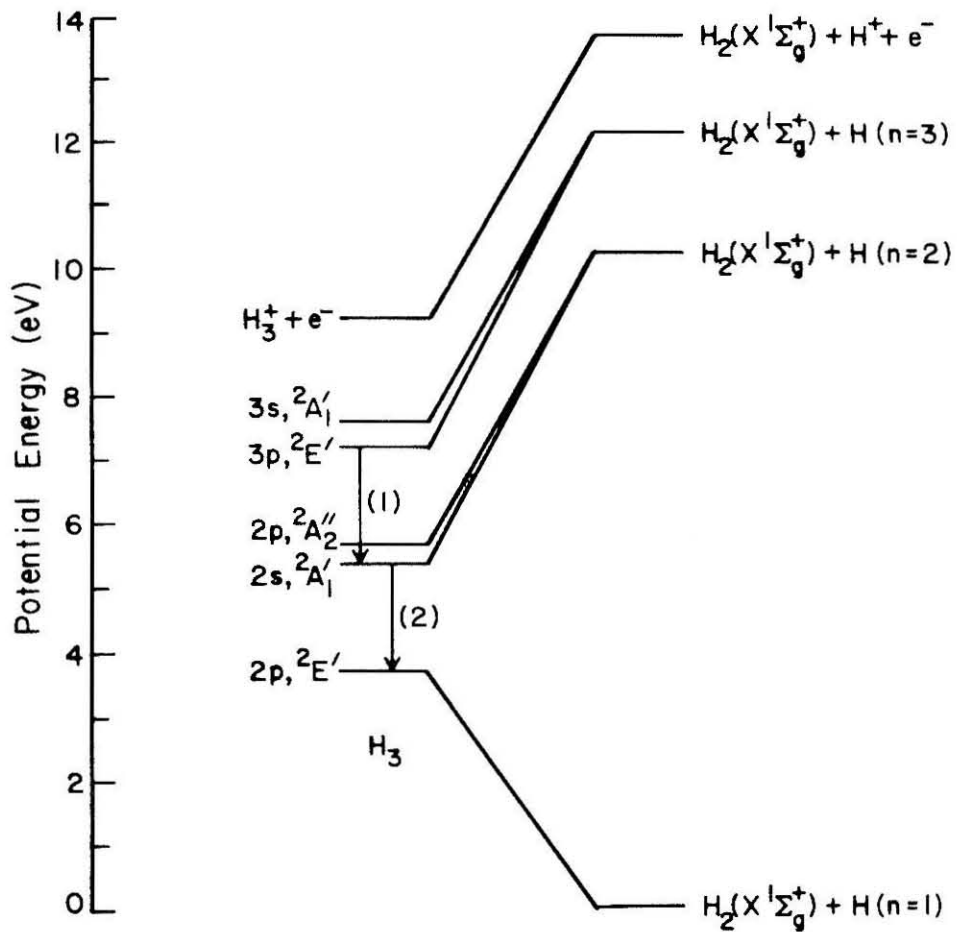


Figure 4

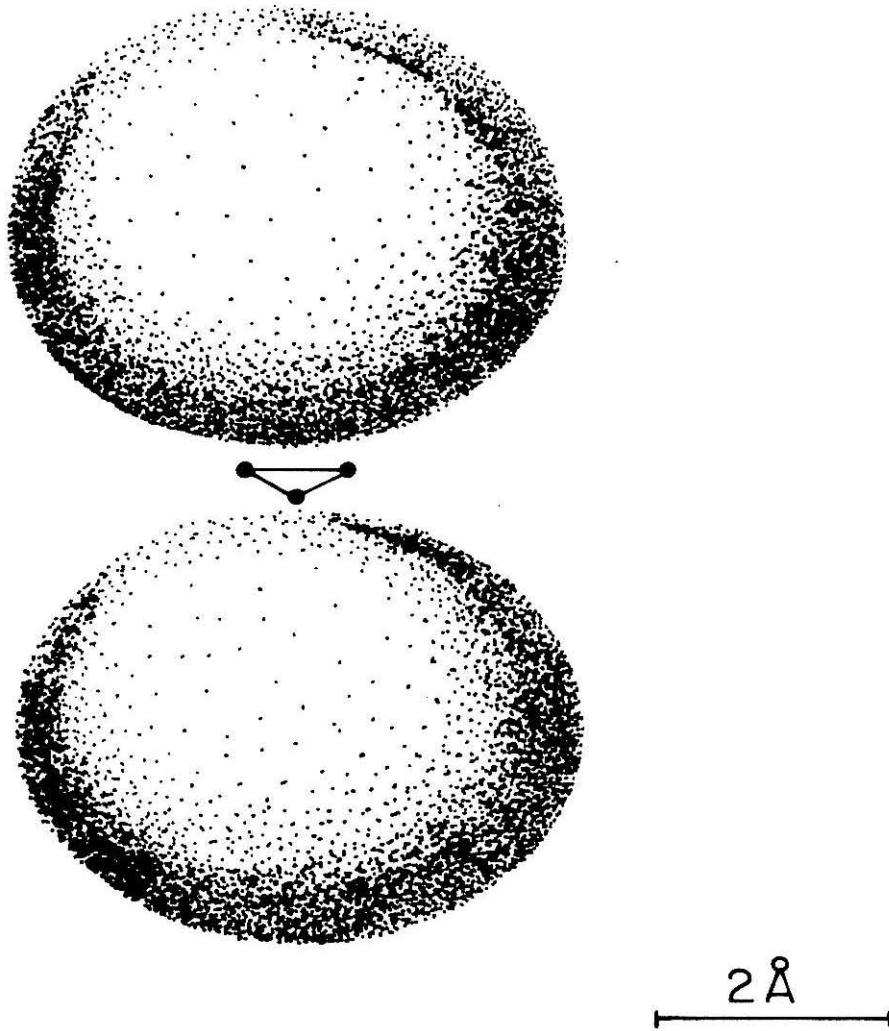


Figure 5

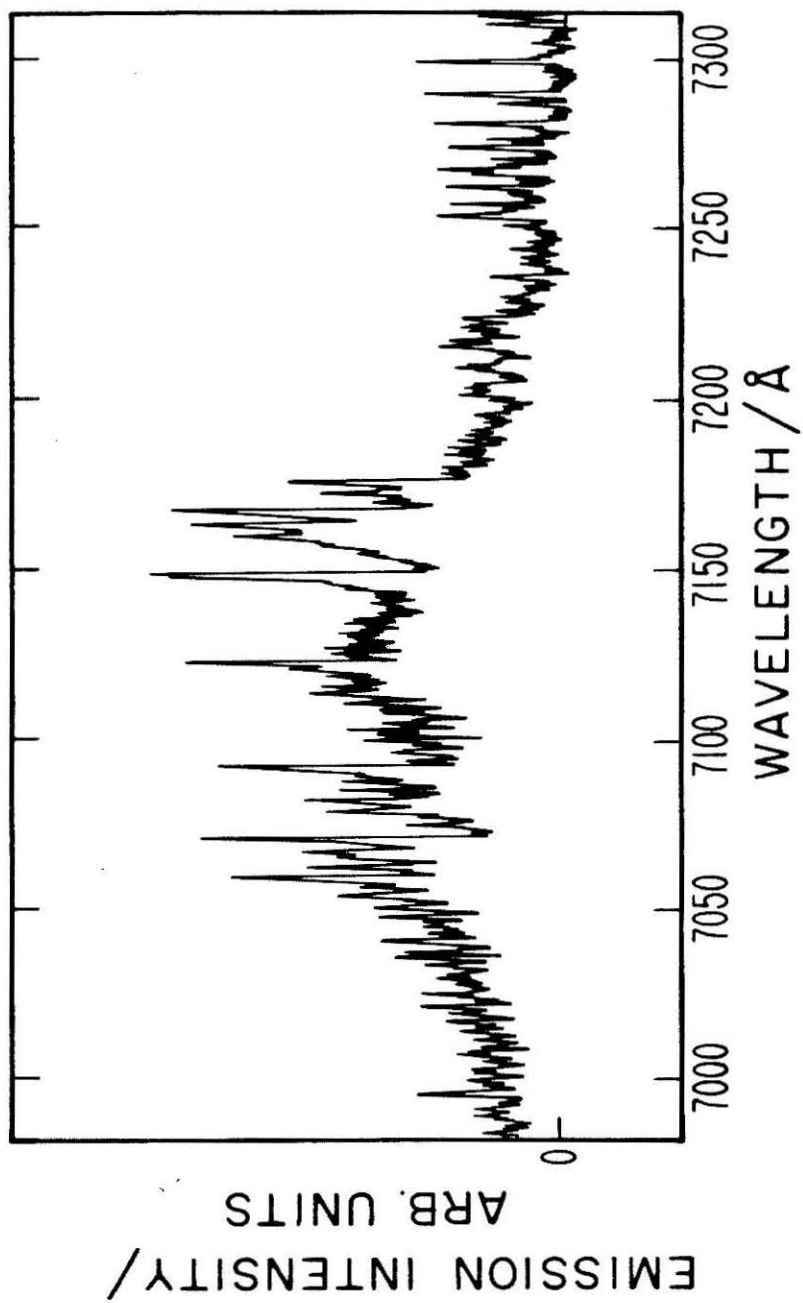


Figure 6

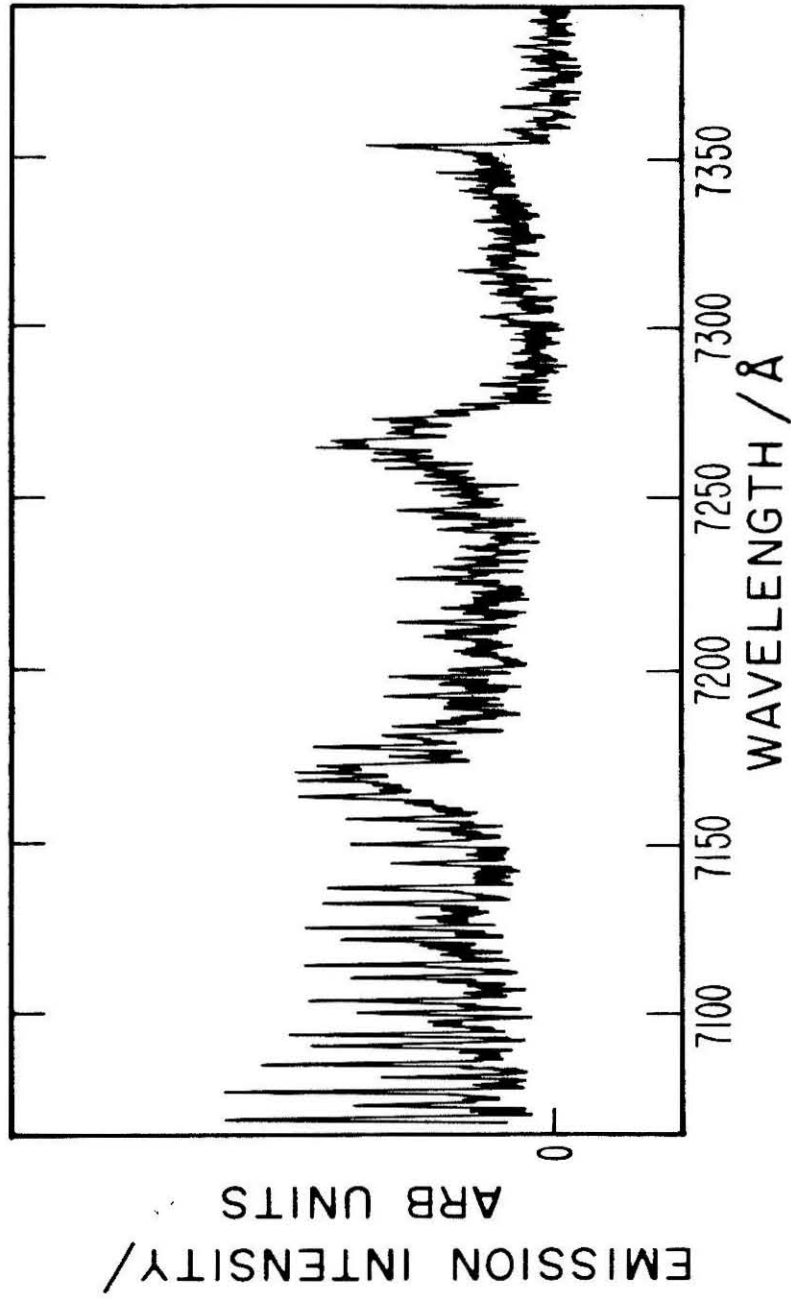


Figure 7

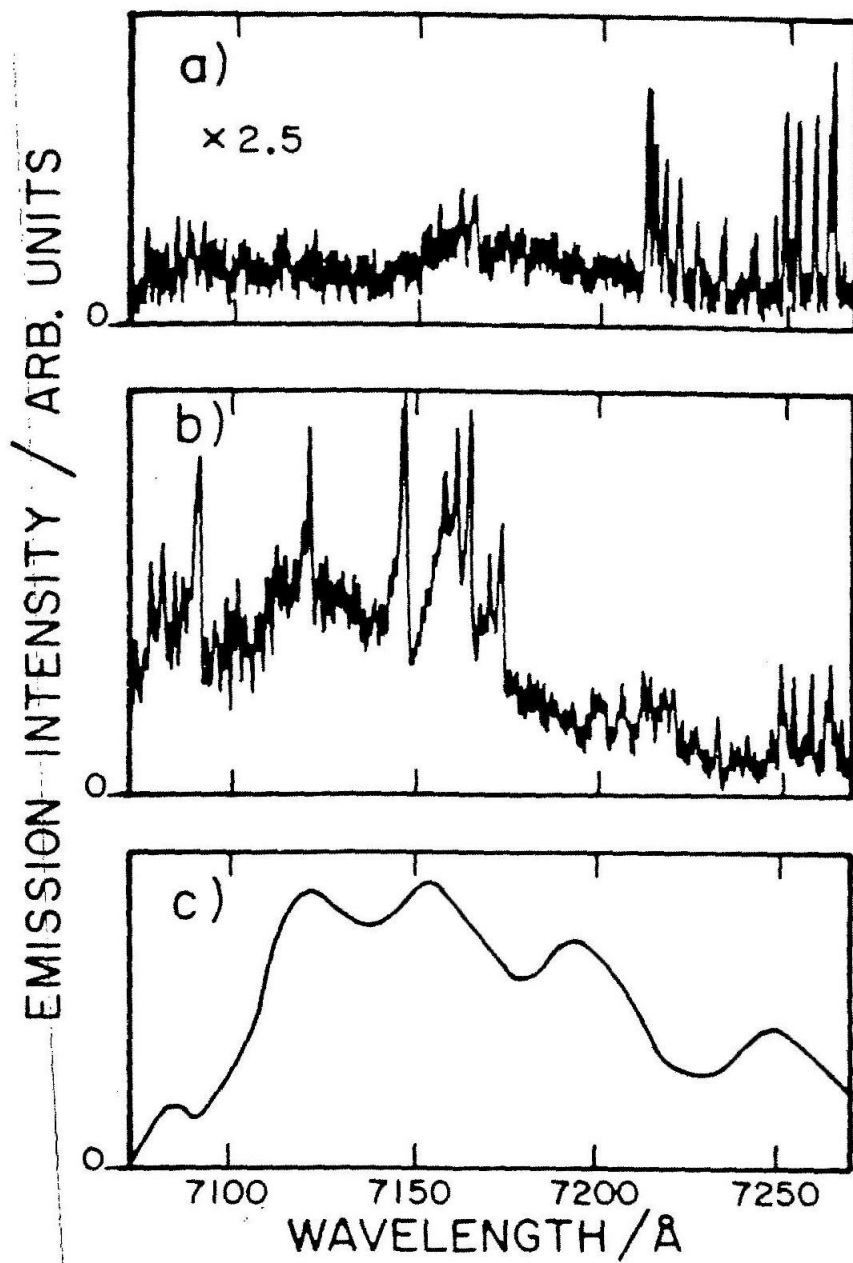


Figure 8

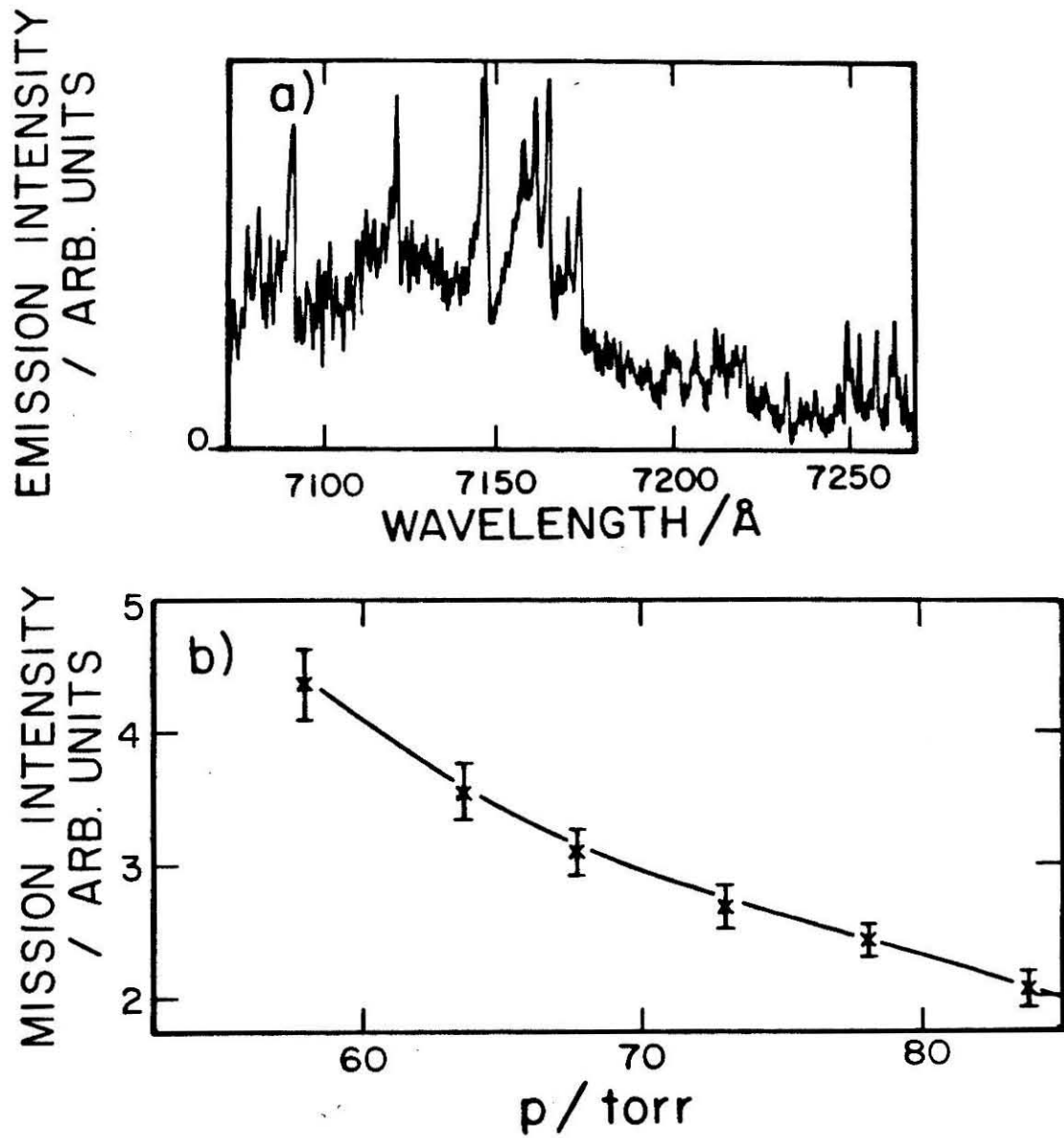


Figure 9

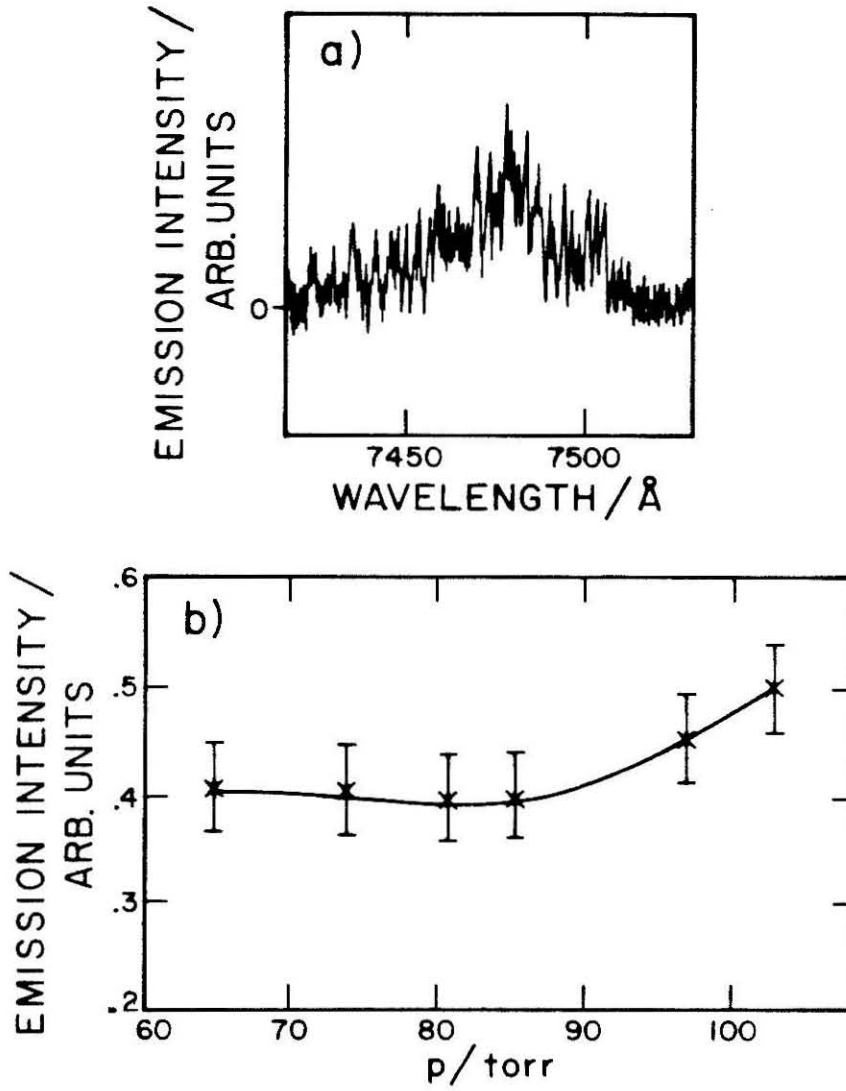


Figure 10

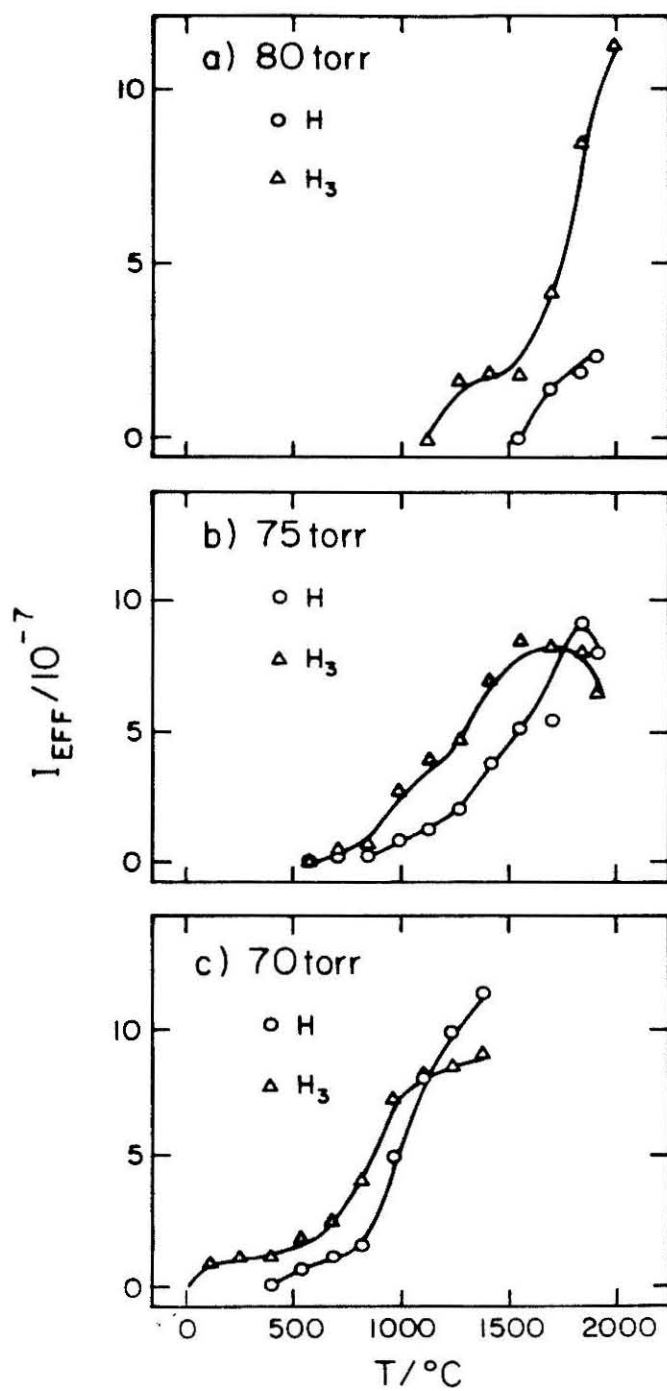


Figure 11

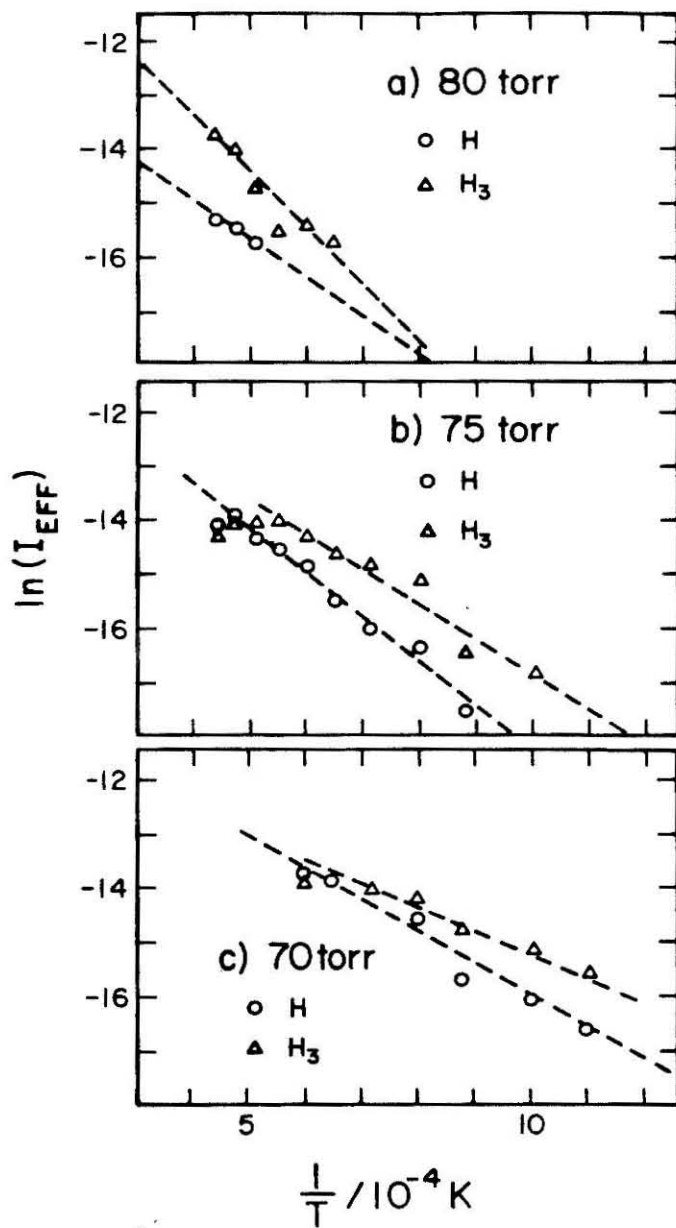


Figure 12

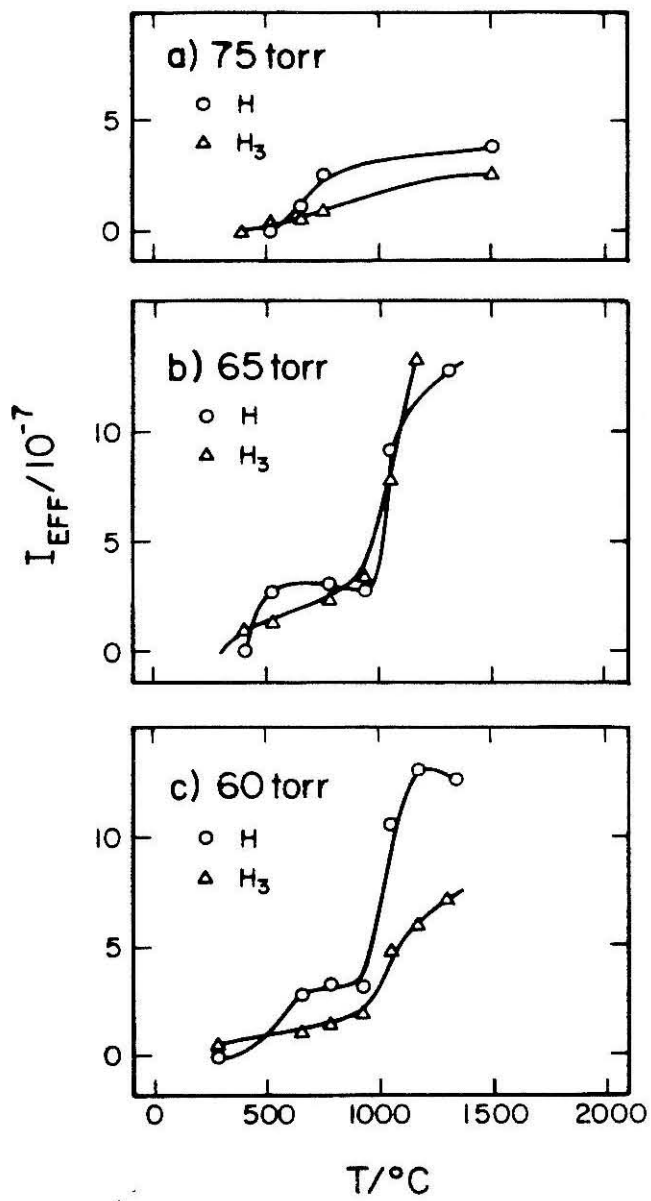


Figure 13

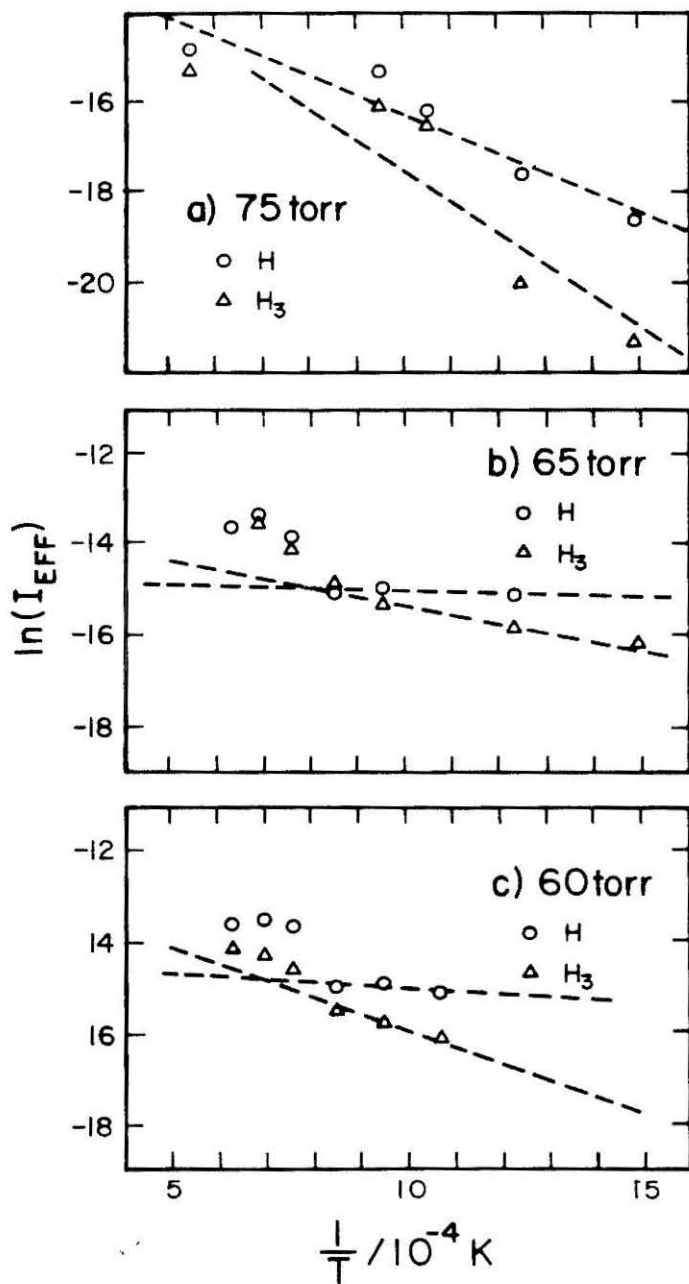


Figure 14

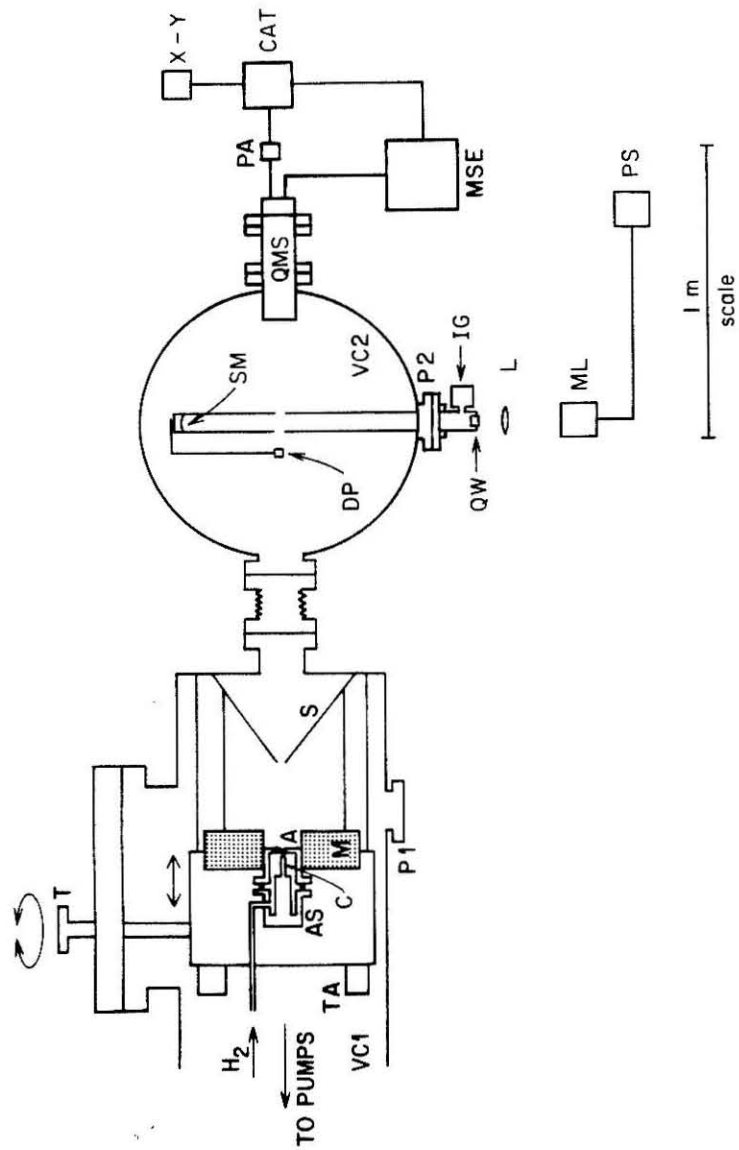
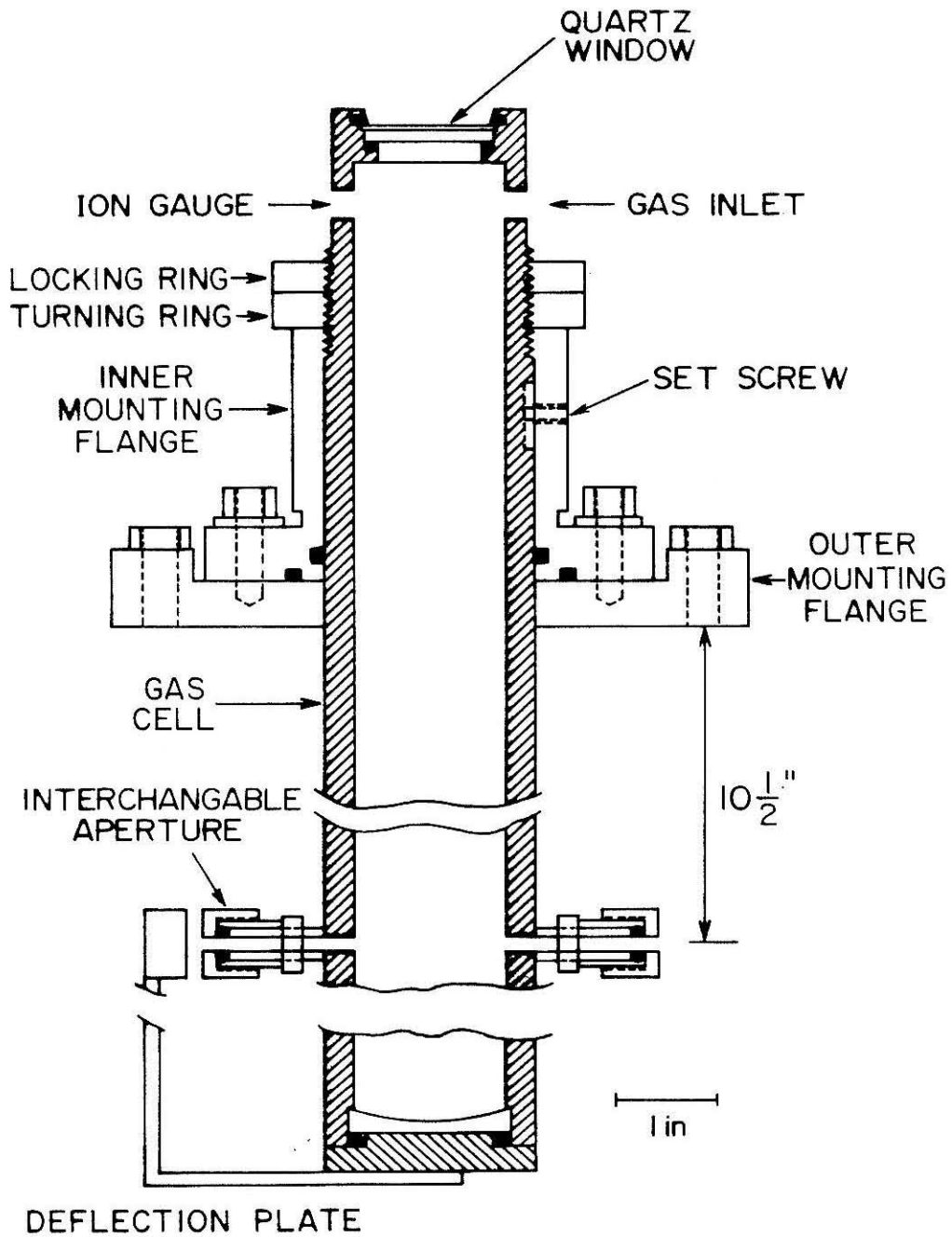


Figure 15

**Figure 16**

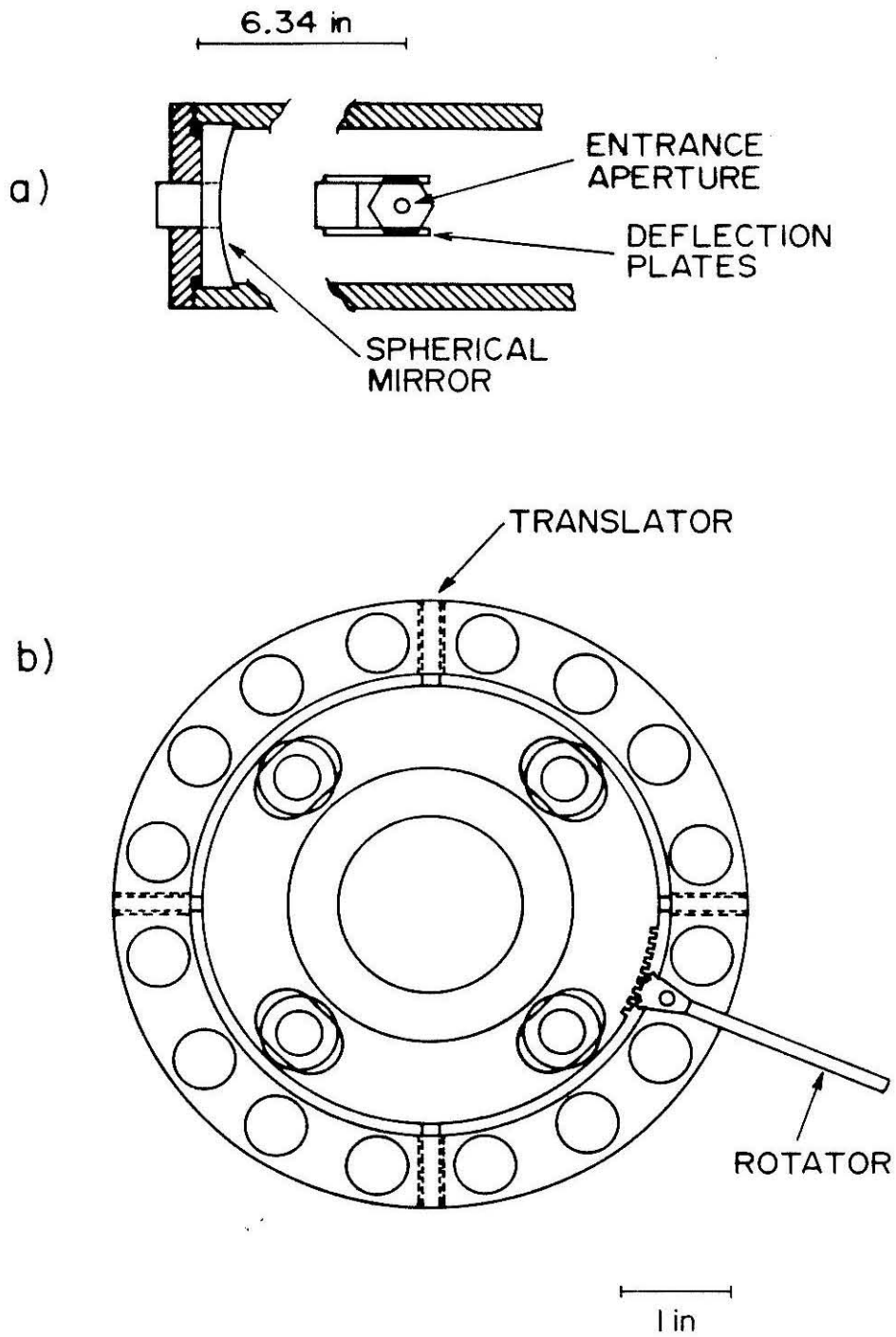


Figure 17

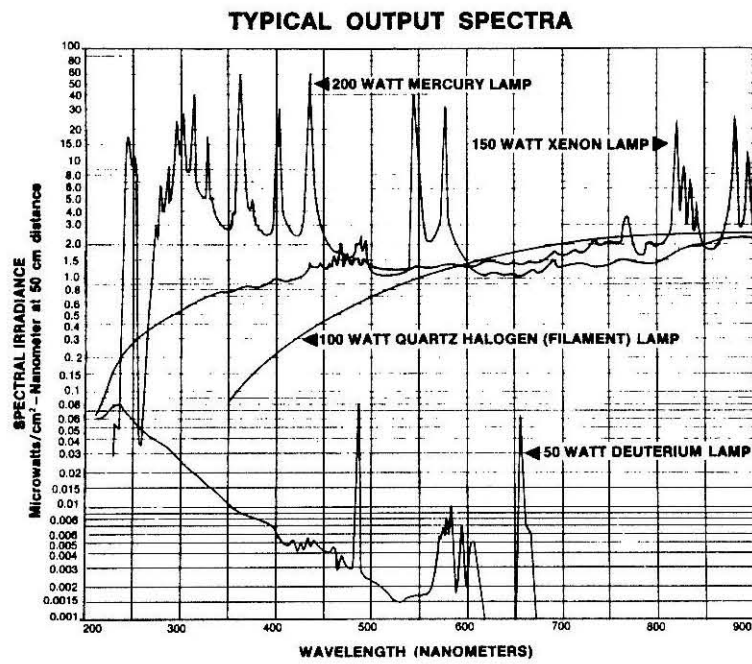


Figure 18

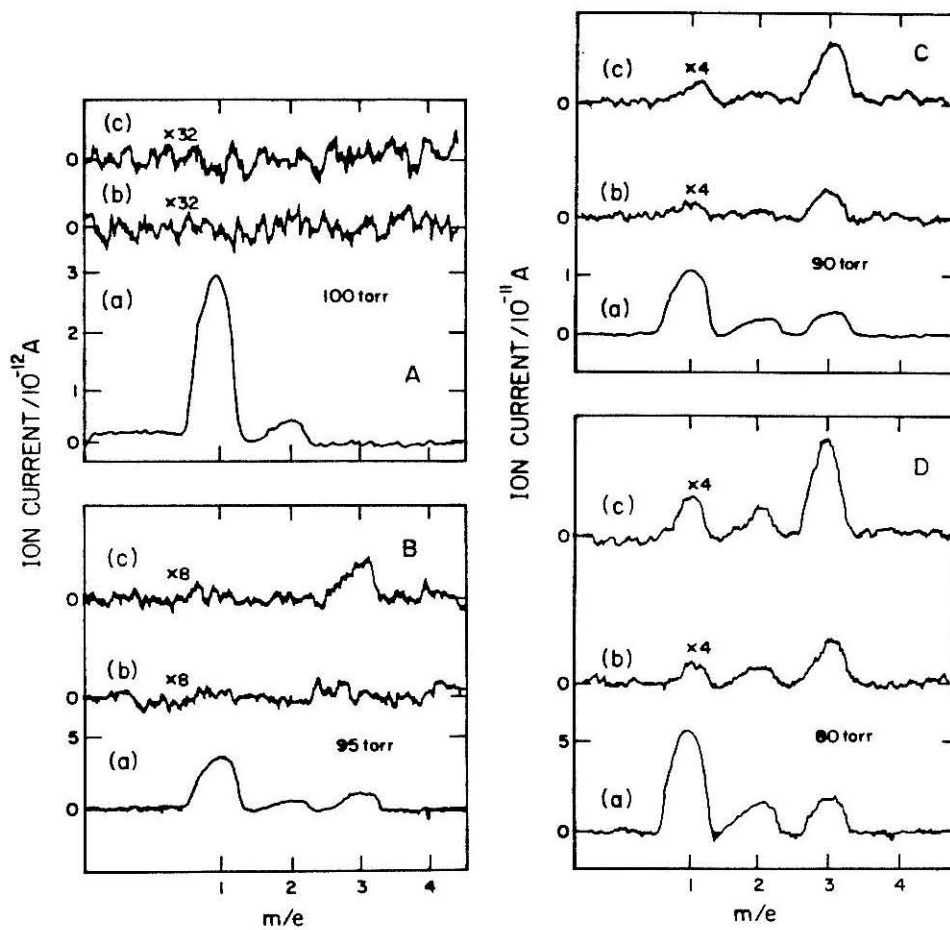
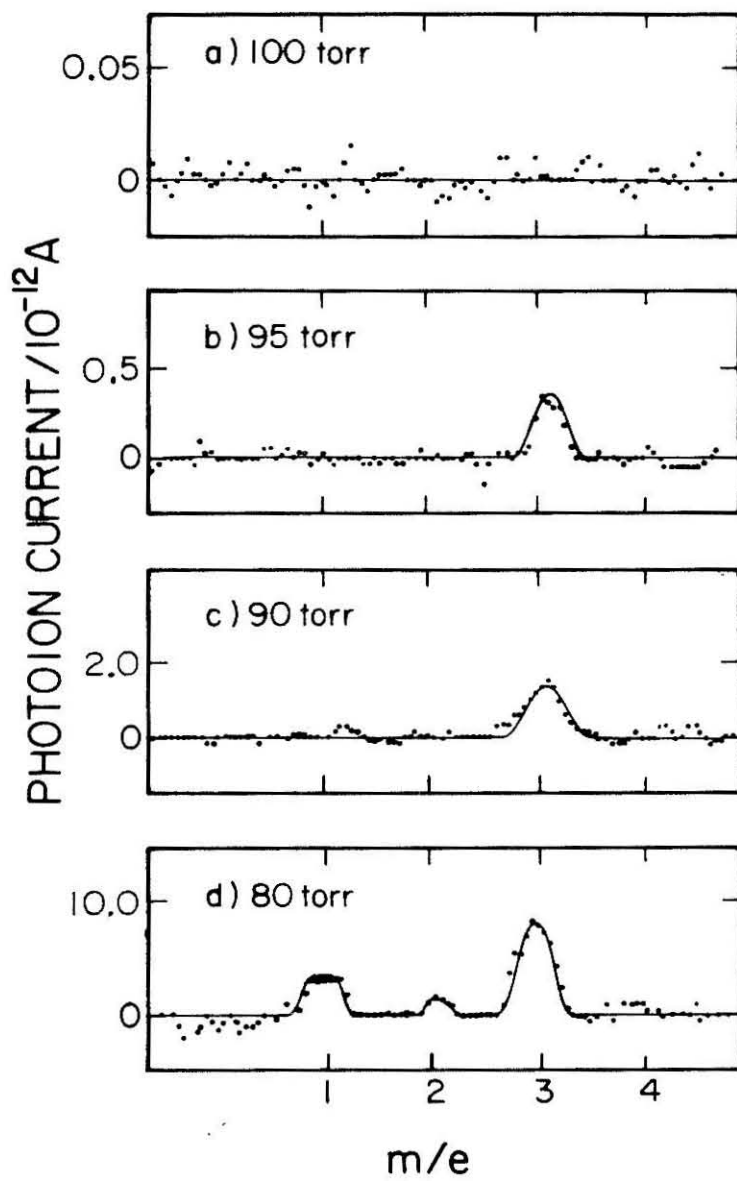


Figure 19

**Figure 20**

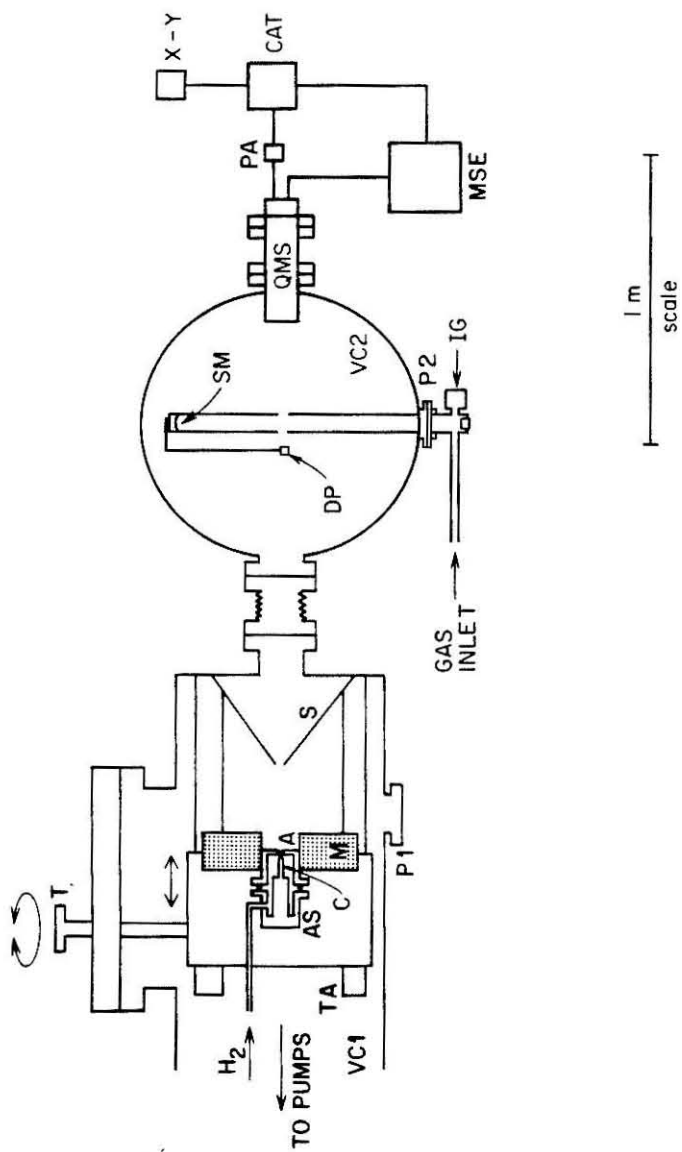


Figure 21

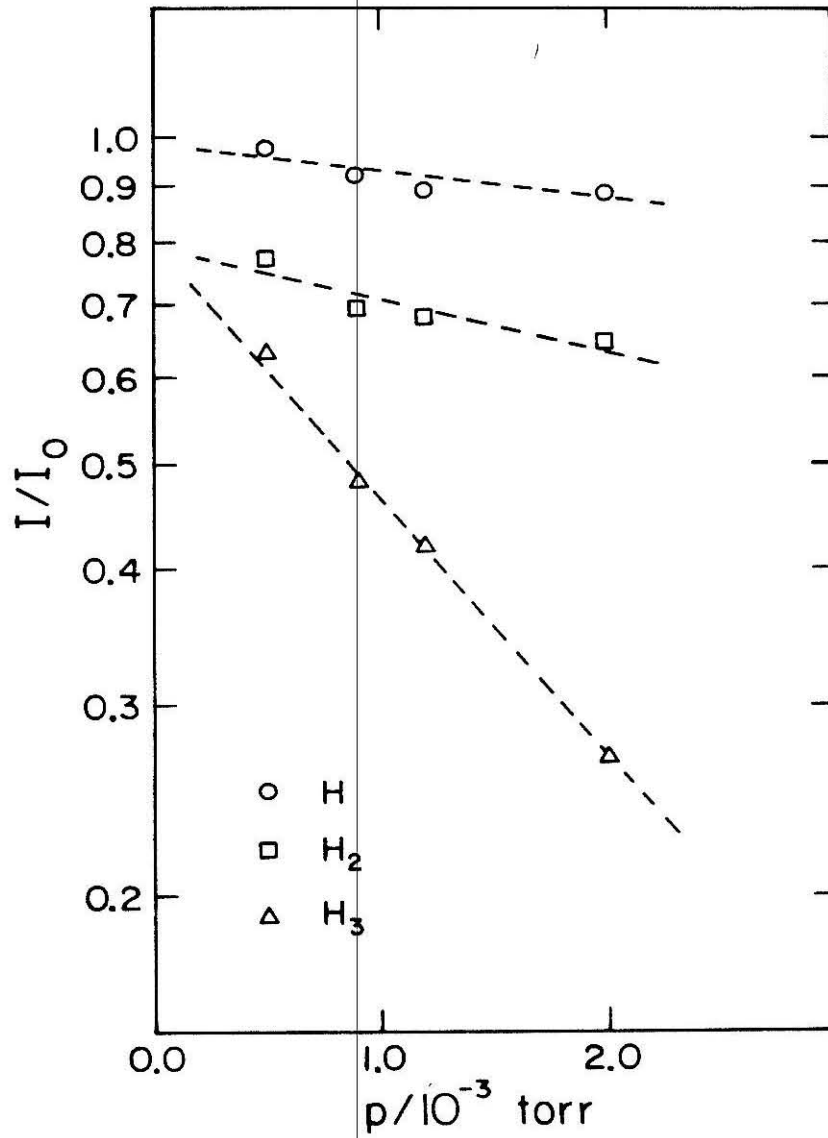
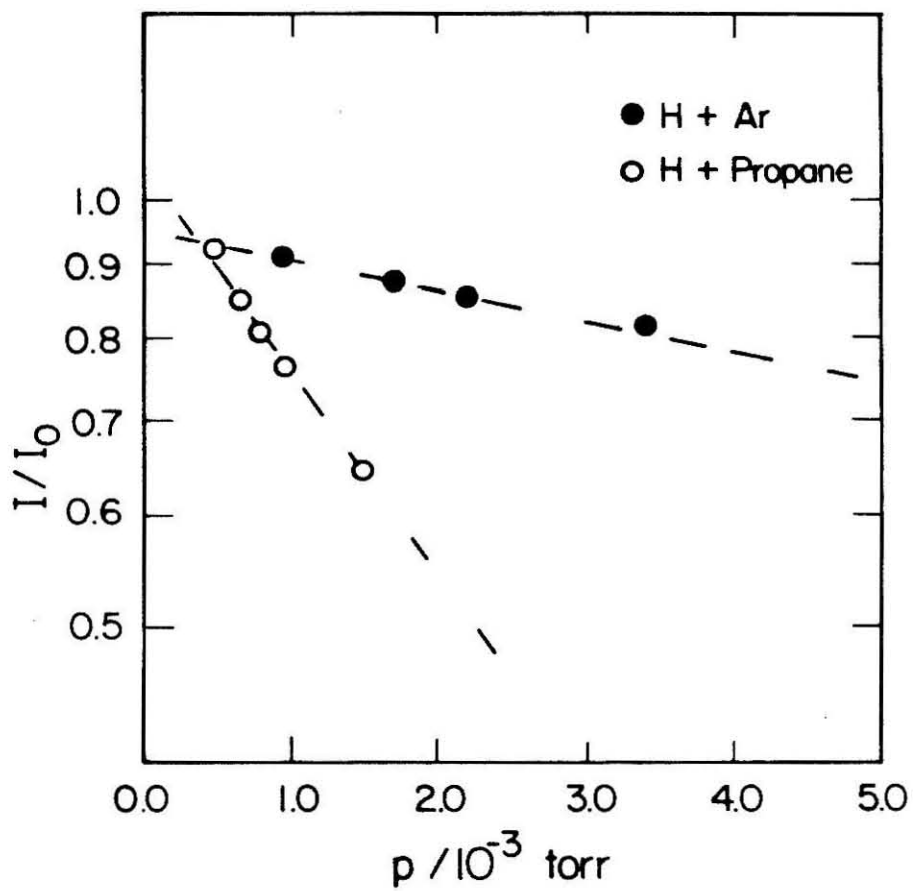


Figure 22

**Figure 23**

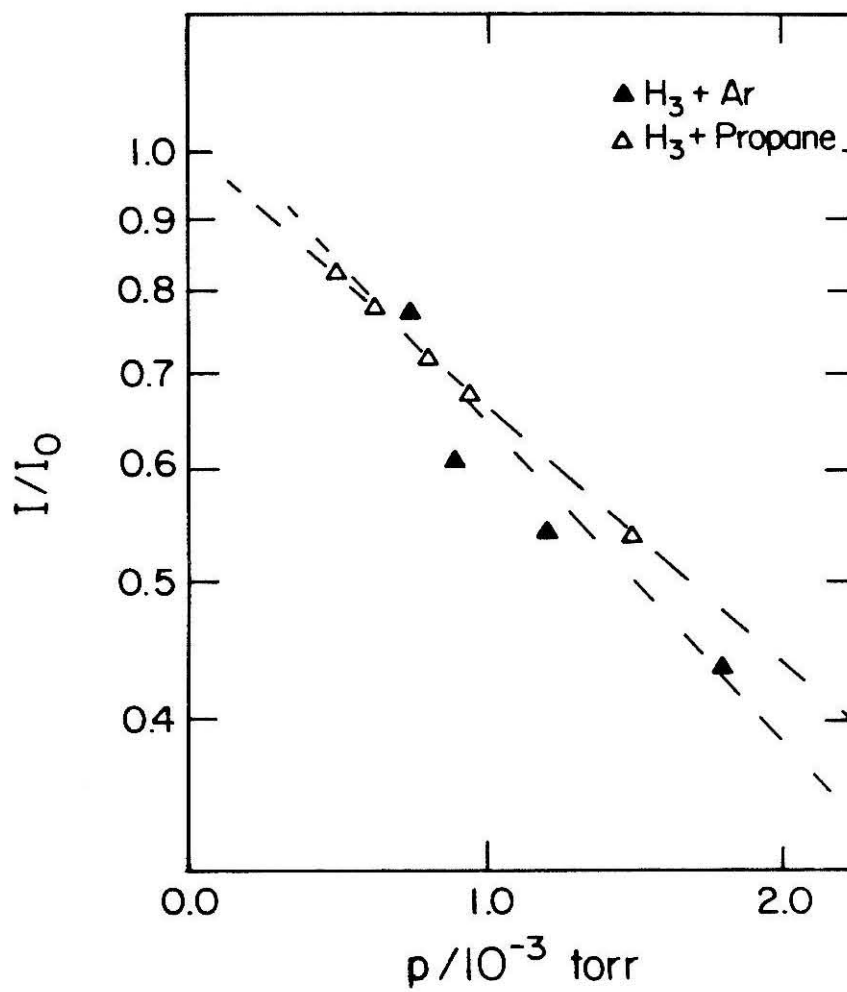


Figure 24

## 5. Results and Discussion for WH and WD Molecules

### 5.1 Introduction

One of the oldest techniques for the observation of emission spectroscopy from molecules and radicals is through excitation by an electric discharge. The first time this technique was employed to observe emission from a radical (defined here as a system with non zero spin<sup>1</sup>) was by Oldenberg<sup>2</sup> in 1934, when he observed OH in a discharge sustained through moist hydrogen. Since then electric discharges have been of great utility in the observation of the emission spectroscopy of excited species. In an attempt to characterize our hydrogen discharge we have observed the visible emission of the plasma plume which appears in front of our nozzle during normal operation of the arc. In the 6800 Å region of the spectrum, however, we observed very sharp transitions converging to two band heads. Bands usually have at one end a sharp edge, called a band head, where the intensity falls suddenly to zero, while on the other side the intensity falls off more slowly. In the case of this spectrum the two bands were shaded to the red.

It was clear from the first observation of these bands that they could not be due to H<sub>3</sub> emission since this structure was so sharp. In addition the rotational spacing of the peaks was too small for it to be attributed to that molecule. Likewise, all other spectral features which we have observed and assigned to H<sub>3</sub> show prominent intensity changes when the stagnation pressure is altered (Section 4.3). In contrast, these 6800 Å bands show no significant change in intensity in the region of 55 to 90 torr.

Throughout the operation of the arc discharge, considerable erosion from

the tungsten anode nozzle and copper holder has been observed. It was natural then to assume that the emission might be due to metal-containing species resulting from that erosion. Changing the discharge gas to deuterium creates a wavelength shift in the in the two bands that was consistent with what one would expect for a hydrogen-containing molecule. At this point we felt that the spectra we had observed were due to a metal hydride species. Attempts to assign this spectrum with known metal hydride spectra as well as other molecular species proved unsuccessful. However, tungsten hydride spectra have not been previously observed.

In order to further understand this spectroscopy we used the mass spectrometer to look for  $WH^+$  ions. We were capable of observing a signal in the range of its mass; however, due to poor resolution of our mass spectrometer in this high mass range we were unable to resolve its different isotopes.

In an attempt to determine the number of hydrogens which this candidate molecule contained we decided to run the discharge with a 50:50 ratio of  $H_2:D_2$  gas. If the molecule was a monohydride there would only be two emission spectra observed, one for the mono-hydride and one for the mono-deuteride. If it was a dihydride there would be three sets of spectra observed for  $WH_2$ ,  $WD_2$  and  $WHD$ . From these spectra we would then be able to deduce the number of hydrogens in the molecule. Performing this experiment we observed only two sets of spectra, the one which we had observed in running with pure  $H_2$  and another one we could also observe when running with pure  $D_2$ . On the basis of this experiment we felt we were observing the electronic spectrum of a monohydride. This working hypothesis was confirmed by the analysis of the spectra described below.

From these results it appears that this is the first observation of the electronic spectrum of  $WH$ . In the next section the analysis of both the  $WH$

and WD spectra is performed, and the rotational constants and bond distances of these species are derived. Due to relativistic terms in the electronic Hamiltonian the theoretical calculation of WH transitions energies has proved difficult to date. Recently a reliable potential for WH has been generated; our experimental bond distances will provide an important empirical check for theoretical calculations performed on this system.

## 5.2 Results and Analysis

Figure 1 shows a schematic of the apparatus. The nozzle was fully pulled back from the skimmer to permit an unobstructed view of the plume light through viewport P1. That light was focused onto the slits of a 0.5 meter Ebert scanning Jarrel-Ash monochromator by lens L, after being chopped at  $\sim 100$  Hz by C2. The wavelength scale of that spectrometer was calibrated before and with light from an Fe-Neon cathode discharge tube. The light, after dispersion by the monochromator, is detected by a photomultiplier tube whose output current is amplified by a Princeton Applied Research model 181 current sensitive preamplifier. The signal is then processed by a Princeton Applied Research model HR-8 lock-in amplifier which has been tuned to the chopping frequency of the chopper. The use of the lock-in provides excellent discrimination against any background or stray light originating after the chopper. The output of the lock-in is fed to a strip chart recorder and the monochromator is made to scan the desired spectral region smoothly. The signal intensity was sufficiently large for there never to be any difficulty in achieving good signal-to-noise resolution. In all cases the stagnation pressure was 60 torr. Figures 2 and 3 show, respectively, the emission spectrum obtained with  $H_2$  or  $D_2$  in the discharge. The observed spectral lines in wavenumbers are tabulated in Tables I and II and are accurate to one wavenumber.

The treatment of such spectra has been well characterized by Herzberg in his classic books<sup>1b,3a</sup>. We first start by solving the Schrodinger equation for the rigid rotator. The detailed calculation of its energy levels may be

found in Pauling and Wilson<sup>4</sup> and the result is

$$E_r = \frac{h^2}{8\pi^2\mu r^2} J(J+1) = \frac{h^2}{8\pi^2 I} J(J+1) \quad (5.1)$$

where  $\mu$  is the reduced mass,  $r$  is the bond distance, and  $J$  is the rotational quantum number which can assume the values 0, 1, 2, ... etc. In molecular spectroscopy the equation (5.1) is usually written in the form of term values, which are the energy values divided by  $hc$  and measured in  $\text{cm}^{-1}$ . We have

$$F(J) = \frac{E_r}{hc} = BJ(J+1) \quad (5.2)$$

where

$$B = \frac{h}{8\pi^2 c I} = \frac{h}{8\pi^2 c \mu r^2} \quad (5.3)$$

is called the rotational constant.

If the molecule is not completely rigid, there will be, on account of the centrifugal force, an increase in  $r$ , the internuclear distance, when the molecule is rotating. Equation (5.3) is then somewhat modified and takes, for a fixed vibrational state, the form

$$F(J) = BJ(J+1) - DJ^2(J+1)^2 + \dots \quad (5.4)$$

where  $B$  is as given in equation (5.3) and  $D$  is a small correction term approximated by

$$D = \frac{4B^3}{\omega^2} \quad (5.5)$$

where  $\omega$  is the vibrational frequency in  $\text{cm}^{-1}$ .

The rotational structure of a given electronic transition depends on the type of electronic states involved. For a  $\Sigma \rightarrow \Sigma$  type of transition the rotational selection rule is  $\Delta J = \pm 1$ . Transitions corresponding to  $\Delta J = +1$  are

designated as P branches while those transitions corresponding to  $\Delta J = -1$  are designated as R branches. However, both together form a simple series of lines which can be represented by one formula

$$\nu = \nu_0 + (B'_\nu + B''_\nu)m + (B'_\nu - B''_\nu)m^2 \quad (5.5)$$

where  $\nu$  is the transition frequency (in  $\text{cm}^{-1}$ , usually), and  $B'_\nu$  and  $B''_\nu$  are the rotational constants for the upper and lower states of a specific transition  $\nu$ , and  $\nu_0$  is called the band origin or the zero line. The band origin will be a constant for a specific transition. This formula can be represented graphically using the frequency of the transition as the abscissa and the quantity  $m$  as the ordinate where  $m = -J$  for the P branch and  $m = J + 1$  for the R branch. This representation was first used by Fortrat<sup>3b</sup>, and a parabola is generated which is naturally called a Fortrat parabola. As a result we see a simple series of lines whose separations change regularly. In most cases, owing to the quadratic term in equation 5.5, one of the branches will form a band head. This gives the appearance of one of the bands turning back.

If the upper and lower electronic states have different electronic angular momenta (such as in a  $\Pi \rightarrow \Sigma$  transition), then an additional rotational branch called a Q branch, corresponding to  $\Delta J = 0$ , exists. One of the first examples found of this was  $\text{AlH}^5$ . The lines of this third branch lie more closely together than for the P or R branches forming a different parabola. Therefore, a second head is generally present corresponding to this Q branch with the head lying very close to  $\nu_0$ . If the rotational constants of the upper and lower electronic states are near in magnitude the Fortrat parabola becomes nearly a straight line and the spacing between the spectral lines decreases, making the Q branch of the spectrum look almost like a single, very intense line whose intensity falls off at higher values of  $J$ . That is the case

observed for  $\text{BH}^6$ .

In the case of our observed emission bands for both the tungsten hydride and deuteride, two prominent band heads appear. This indeed makes the transition appear as if it is due to a  $\Pi \rightarrow \Sigma$  transition. Our assignments for the P, Q and R branches for both spectra appear at the top of Figures 2 and 3. We can now construct Fortrat parabolas, as outlined above, to examine how well our assignments fit. Figures 4 and 5 are the Fortrat parabolas for the hydride and deuteride, respectively.

With tungsten hydride having four d electrons and one s electrons valence electrons, one can expect that the electronic states involved will have sextet multiplicity (i.e.,  ${}^6\Pi \rightarrow {}^6\Sigma^{(+)}$ ). With high multiplicities many more P, Q, and R branches may be identified (again by the position of band heads). This is due to the different angular momenta in the molecule: electron spin, electronic orbital angular momentum and angular momentum of nuclear rotation all contribute to the total angular momentum of the molecule. These additional branches serve to complicate the interpretation of the spectra. Very few  $\Pi \rightarrow \Sigma$  systems have been studied with multiplicities greater than 3. The first to be analyzed in detail were done by Nevin: the first negative bands of oxygen which represent a  ${}^4\Sigma_g^- \rightarrow {}^4\Pi_u$  transition of  $\text{O}_2^+$  <sup>7-9</sup> and the MnH bands at 5677 and 6237 Å representing a  ${}^7\Pi \rightarrow {}^7\Sigma$  transition<sup>10</sup>. If Hund's case (a) (where it is assumed that the spin-orbit coupling is large, while the coupling of the rotation of the nuclei with the electronic motion is weak) strictly applied to the  $\Pi$  states, there would be 48 and 147 branches, respectively. The other important case is Hund's case (b) (where the coupling of the spin with the internuclear axis is weak and as a consequence the spin is coupled to the axis of rotation of the molecule) there would be only 12 and 21 main branches. In the case of the  $\text{O}_2^+$  bands Nevin identified 40 branches while for MnH

he identified 49. Also in the spectra of FeCl, a  ${}^6\Pi \rightarrow {}^6\Sigma$  and a  ${}^4\Pi \rightarrow {}^4\Sigma$  transition has been identified by Miescher<sup>11</sup> and Muller<sup>12</sup>.

Due to the observation of only two strong band heads (as shown in Figures 2 and 3) and due to our poor resolution, we were not able to deal fully with the multiplicity of the spectra. It should be noted that unassigned transitions that extended down to 6580 Å in the case of the hydride and down to 6620 Å in the case of the deuteride, appeared to be associated with the electronic transition. Whether these peaks are due to excited vibrational bands of this transition or are additional rotational branches due to the expected high multiplicity is unknown. The structure in this series of peaks could be fit to a parabola, but due to their low intensities and absence of any clear band head, assignment was made extremely difficult.

We then attempted to analyze the clear set of P, Q, and R branches as if the electronic transition had singlet multiplicity, in order to derive a rotational constant and bond distance for the upper and lower states. Historically, rotational constants are derived by the use of combination differences<sup>3c</sup>. Though useful for a preliminary analysis the method implicitly assumes that all measurement errors are associated with the state under analysis<sup>13,14</sup>. To avoid this source of error we utilized a program developed by Zare and coworkers<sup>14-16</sup> that employs all measured line positions and iteratively compares their values with those calculated from numerically diagonalized model Hamiltonians with adjustable molecular constants. Given approximate starting values from the molecular constants of a single band, Zare's program finds improved values using a nonlinear least-square fitting procedure. Estimates for the molecular constants are used as starting values for the fit. The molecular constants are then iteratively improved. Serious convergence and false-minima problems usually encountered in non-linear least-square fitting

do not occur with this technique if reasonable starting values are used.

The matrix elements used in the model Hamiltonians are those given by Zare and co-workers<sup>14-16</sup>. The upper and lower state Hamiltonians are diagonalized to yield a set of eigenvalues (term values) for each  $J'$  and  $J''$ . From these eigenvalues, calculated line positions are determined for the appropriate branches. Calculated line positions from the model Hamiltonians are compared to measured values of the line positions and new estimates of the molecular constants are made that reduce the sum of the squares of the residuals. This nonlinear least-squares subroutine is a modification of the program written by Meeter and Wolfe<sup>17</sup> and is based on the method of Marquardt<sup>18</sup> that combines the Gauss (Taylor series) method and the method of steepest descent. The molecular constants are iteratively improved until one of several specified convergence criteria are met. Upon convergence, the program provides as output the values of the band origin and the molecular constants for the upper and lower states as well as calculated line positions.

For our fit we chose to employ 5 molecular constants in the Hamiltonian:  $\nu_0$ , the origin of the band under study (namely, the difference between the rotationless, unsplit energy reference points of the upper and lower states), the B and D, the rotational constants and their centrifugal distortion for both the upper and lower states. The lines listed in Tables I and II were fit using this program. The molecular constants derived from the fit are listed in Tables III and IV. The numbers in parentheses in Tables I and II represent the difference between the calculated line position (by the program described above) and the observed line position. The curves in Figures 4 and 5 result from the Fortrat parabola generated by the calculated lines. We see that in both the WH and WD cases the general fit is satisfactory outside of an occasional line which may be due to misassignment of that line.

From the rotational constants listed in Tables III and IV we are able to calculate bond distances by using equation 5.4. Likewise, we are also able to crudely estimate the fundamental vibrational frequency of the metal hydride by using the centrifugal distortion constant and equation 5.5. These values are also listed in Tables III and IV.

We can now check the correctness of our assignments by comparing the WH and WD constants and evaluating the isotope effect. We first note that for WD  $\nu_o$  is  $9.4 \text{ cm}^{-1}$  to the red of the band origin for WH. One might expect these  $\nu_o$  to be the same. This is, however, not the case since the zero-point energy in the upper and lower states in general differs in magnitude for two isotopic molecules. As a result, an isotopic displacement for the 0-0 band is observed in many cases<sup>19-22</sup>.

We can expect to see a large isotope effect in the rotational constants caused by the large difference in the reduced mass of the two molecules. Since the internuclear distances in diatomic molecules are determined mainly by the electronic structure they should be very close to each other in isotopic molecules for the ground vibrational states. However, the rotational constants will be significantly different since it depends in addition on the reduced mass (see equation 5.3). Defining now  $B^i$  as the rotational constant of an isotopic molecule (distinguished from  $B$ , the rotational constant of the 'ordinary' molecule) we get, neglecting the small term in  $D$ ,

$$F^i(J) \sim B^i J(J+1) = \rho^2 B J(J+1) \quad (5.6)$$

where

$$\rho = \sqrt{\frac{\mu}{\mu_i}}. \quad (5.7)$$

We then see that the rotational constants of two isotopic molecules are related

**Table I****Transition Energies of WH (in  $\text{cm}^{-1}$ ) and their Assignments**

J	R	Q	P
0	14,844.2 (-3.2) <sup>a</sup>		
1	14,853.9 (-1.8)	14,833.8 (-3.0)	
2	14,861.0 (-1.7)	14,831.1 (-3.5)	14,820.0 (+4.2)
3	14,866.5 (-1.8)	14,828.6 (-2.6)	14,805.4 (+2.3)
4	14,870.9 (-1.7)	14,825.5 (-1.1)	14,788.7 (-0.7)
5	14,876.5 (+1.2)	14,822.7 (+1.9)	14,771.9 (-2.9)
6	14,883.5 (+7.3)	14,809.7 (+4.6)	14,758.7 (-4.7)
7	14,880.6 (+5.3)	14,809.7 (+4.6)	14,743.1 (+0.5)
8	14,873.4 (+0.9)	14,799.6 (+4.3)	14,727.3 (+2.3)
9	14,866.5 (-1.1)	14,781.6 (-2.2)	14,711.3 (+4.7)
10	14,857.8 (-2.6)	14,768.0 (-2.8)	
11	14,849.5 (-1.3)	14,749.5 (-6.4)	
12	14,840.9 (+2.4)	14,733.3 (-6.1)	
13		14,716.7 (-4.1)	
14		14,700.0 (-0.2)	
15		14,683.0 (+5.7)	

a) The numbers in parenthesis are the differences between the observed and fitted values. See text.

**Table II****Transition Energies of WD (in  $\text{cm}^{-1}$ ) and their Assignments**

J	R	Q	P
0	14,830.6 (-5.0) <sup>a</sup>		
1	14,838.4 (-1.6)		
2	14,843.7 (-0.2)		
3	14,849.1 (+1.5)		14,815.0 (+0.8)
4	14,853.3 (+2.5)	14,821.5 (-4.9)	14,808.5 (+1.2)
5	14,857.7 (+4.1)		14,803.8 (+4.2)
6		14,816.4 (-4.0)	14,791.1 (+0.3)
7	14,860.9 (+3.2)	14,812.6 (-3.6)	14,783.7 (+2.9)
8	14,862.9 (+4.2)	14,808.9 (-1.8)	14,770.1 (+0.7)
9		14,703.4 (-0.8)	
10	14,857.2 (-1.0)		
11	14,855.3 (-1.0)		
12	14,850.9 (-2.1)		
13	14,846.1 (-1.9)		
14	14,841.4 (+0.2)		
15	14,834.2 (+2.0)		

a) The numbers in parenthesis are the differences between the observed and fitted values. See text.

**Table III****Spectroscopic Constants of WH**

$$\nu_0 = 14,842.7 \text{ cm}^{-1}$$

	Upper State ( ${}^6\Pi$ )	Lower State ( ${}^6\Sigma$ )
$B/\text{cm}^{-1}$	4.72	5.29
$D/\text{cm}^{-1}$	$2.71 \times 10^{-3}$	$2.26 \times 10^{-3}$
$r_e/\text{\AA}$	1.89	1.78
$\nu/\text{cm}^{-1}$	394	512

**Table IV****Spectroscopic Constants of WD**

$$\nu_0 = 14,833.3 \text{ cm}^{-1}$$

	Upper State ( ${}^6\Pi$ )	Lower State ( ${}^6\Sigma$ )
$B/\text{cm}^{-1}$	2.33	2.53
$D/\text{cm}^{-1}$	$2.06 \times 10^{-3}$	$3.06 \times 10^{-3}$
$r_e/\text{\AA}$	1.91	1.83
$\nu/\text{cm}^{-1}$	156	233

by

$$B_e^i = \rho^2 B_e \quad (5.8)$$

but only holds rigorously for  $B_e$  since it is only the equilibrium internuclear distances which are nearly the same for two isotopic molecules. For other molecular constants they also have simple dependences on  $\rho$ . In the case of the centrifugal distortion constant, Dunham<sup>23</sup> has found that

$$D_e^i = \rho^4 D_e \quad (5.9)$$

to be a very good approximation. The investigation of the isotope effect in electronic band spectra has been extremely important in the early discovery of new isotopes of very small abundance<sup>24,25</sup>.

As a check of the correctness of our assignment of the spectra as due to tungsten hydride we can see how well the rotational constants obey equation 5.8. For tungsten hydride and deuteride we calculate a value of  $\rho$  of 0.50. Taking the ratio of the rotational constants from Tables III and IV we get for the ground state 0.48 and for the excited state 0.49. This agreement is reasonable and justifies our assignment.

We can now see from equation 5.6 that the band system of the heavier isotopic molecule is contracted compared to that of the lighter by a constant factor  $\rho^2$  which is less than one. This shift between consecutive lines is proportional to  $J + 1$ . To illustrate the magnitude of this effect in Figure 6 we have the Fortrat diagram for the computer fit for WH (solid curve) and WD (dashed curve). By superimposing the  $\nu_o$  of the two one is able to see the influence of the rotational isotope effect alone. As one might expect for the case of WH and WD the effect is quite large.

We wished to compare our data to other molecules in order to see if the constants were indeed reasonable. However, there have been no spectra

reported on with tungsten or molybdenum hydride and only spotty data on chromium hydride. Kleman and co-workers<sup>26</sup> and O'Connor<sup>27,28</sup> have reported the observation of CrH spectra. O'Connor analyzed the band at  $11611\text{ cm}^{-1}$  which he attributes to a  $A\ ^6\Sigma^{(+)} \rightarrow X\ ^6\Sigma^{(+)}$ . He was able to assign the twelve P and R branches and derive rotational constants such that he derived a bond distance of  $1.655\text{ \AA}$  for the ground state and  $1.787\text{ \AA}$  for the upper state, with vibrational frequencies of  $1581.2\text{ cm}^{-1}$  and  $1479.4\text{ cm}^{-1}$ , respectively. There has also been reported in the literature the observation of a complex band between 30075 and 30480 which was attributed to the  $B\ ^6\Pi \rightarrow X\ ^6\Sigma^{(+)}$  transition<sup>29</sup>. We see then that as we go down the periodic table the bonding of hydrides become weaker such that the bond distance increases and the vibrational frequency decreases. This pattern has been observed for the saline hydrides<sup>30</sup> as well as for the hydrogen halides<sup>31</sup>. Seeing this pattern with CrH and WH increases our confidence in the assignment of the spectra.

### 5.3 Future Work

One might feel that band spectra of the metal hydrides have been well characterized but there really still remain large gaps in their understanding. As of 1984 there were no hydride spectra<sup>32,33</sup> of the large majority of the lanthanides and actinides as well as of Y, Zr, Nb, Mo, Ru, Rh, Os and Ir. This information is summarized in Figure 7a. Of the known spectra about half have not been rotationally analyzed, a third have not been vibrationally analysed and about 15% are of uncertain identification<sup>32</sup>. Professor J. Beauchamp has suggested that it might be possible by adding metal carbonyls to the hydrogen gas which sustains the discharge to generate electronically excited metal hydrides whose emission might be observed. If this approach is successful it may permit the observation of additional metal hydrides not yet observed.

Another way of generating new metal hydrides might be through the use of different metals as nozzles. We have attempted to use a molybdenum nozzle but were unable to sustain a discharge due to rapid deformation of the nozzle under the high temperature conditions of the plasma.

In the case of metal nitrides (as of 1984)<sup>32,33</sup> there are very few systems which have been studied. The systems which have been observed are shown in Figure 7b. The Kunth type of discharge we have employed has also had great success in the generation of nitrogen atoms through the use of  $N_2$  as the discharge gas<sup>34,35</sup>. Metal nitride emission spectra from these sources have not been reported so far, but on the basis of our results it seems possible that attempts in this direction should be made. The only difficulty is that the stagnation temperature of the  $N_2$  sources seem to be colder than that for

hydrogen discharge, and the amount of electronically excited metal nitride which might be generated generated may be small.

Another possibility for use of these sources is the generation of metal clusters. Up to now in this thesis we have tried to minimize the amount of erosion from the tungsten electrodes, but conversely one can quite easily increase this erosion. If this was the case it might prove to be a valuable source of generating tungsten clusters. In attempting to stabilize his hydrogen discharge W. C. Stwalley<sup>36</sup> positioned, exterior to the nozzle, a sacrificial tungsten electrode. His observation was that this electrode was corroded eaten by the discharge. This technique could perhaps be employed for generating tungsten clusters.

Many possibilities exist for the utilization of this discharge source to generate novel molecular species. Due to the electronically hot medium of the plasma the possibility of observing emission spectroscopy also exists. It therefore may someday prove to be a very useful tool for the study of these novel molecules which otherwise are extremely difficult to produce.

## 5.4 References

1. G. Herzberg, *The Spectra and Structures of Simple Free Radicals, An Introduction to Molecular Spectroscopy*, Cornell University Press, Ithaca, a) p.1, b) p. 18. (1970).
2. O. Oldenberg, *J. Chem. Phys.*, **2**, 713 (1934).
3. G. Herzberg, *Molecular Spectra and Molecular Structure, I. Spectra of Diatomic Molecules*, D. Van Nostrand Company, Inc., N. Y., a) p. 66, b) p. 47, c) p. 168 (1950).
4. L. Pauling and E. B. Wilson, Jr., *Introduction to Quantum Mechanics*, McGraw-Hill, N. Y. (1935).
5. E. Bentgtsson-Knave, *Nova Acta Reg. Soc. Scient. Ups.* **8**, No. 4 (1932).
6. W. Lochte-Holtgreven and E. S. van der Vleugel, *Z. Physik*, **79**, 188 (1931).
7. T. E. Nevin, *Nature (London)*, **140**, 1101 (1937).
8. T. E. Nevin, *Phil. Trans. Roy. Soc., London*, **237**, 471 (1938).
9. T. E. Nevin, *Proc. Roy. Soc., London*, **174**, 371 (1940).
10. T. E. Nevin, *Proc. Roy. Irish Acad. A*, **48**, 1 (1942).
11. E. Miescher, *Helv. Phys. Acta*, **11**, 463 (1938).
12. W. Muller, *Helv. Phys. Acta*, **16** 3 (1943).
13. N. Aslund, *Arkiv for Fysik*, **30**, 377 (1965).

14. R. N. Zare, A. L. Schmeltekopf, W. J. Harrop, and D. L. Albritton, *J. Mol. Spectrosc.*, **46**, 37 (1973).
15. D. L. Albritton, W. J. Harrop, A. L. Schmeltekopf, R. N. Zare, and E. L. Crow, *J. Mol. Spectrosc.*, **46**, 67 (1973).
16. D. L. Albritton, A. L. Schmeltekopf, J. Tellinghuisen, and R. N. Zare, *J. Mol. Spectrosc.*, **53**, 311 (1974).
17. D. A. Meeter and P. J. Wolfe, *CO-OP Class/Index Code E2, CO-OP Organization Code WISC, Program Title GAUSHAUS*, University of Wisconsin Computing Center, Madison, Wisconsin (1966).
18. D. L. Marquardt, *J. Soc. Indust. Appl. Math.*, **11**, 431 (1963).
19. F. A. Jenkins and A. McKellar, *Physic Rev.*, **42**, 464 (1932).
20. R. de L. Kronig, *Z. Physik*, **50**, 347 (1928).
21. G. H. Dieke, *Physick Rev.*, **47**, 661 (1935).
22. J. H. Van Vleck, *Physic. Rev.*, **33**, 467 (1929).
23. J. L. Dunham, *Physic Rev.* **34**, 721 (1932).
24. G. H. Dieke and H. D. Babcock, *Proc. Nat. Acad. Amer.*, **13**, 670 (1927).
25. W. H. J. Childs and R. Mecke, *Z. Physik*, **86**, 344 (1931).
26. B. Kleman and B. Liljeqvist, *Arkif For Fysik*, **9**, 345 (1955).
27. S. O'Connor, *Proc. R. Ir. Acad.*, **50A**, 123 (1967).
28. S. O'Connor, *J. Phys. B.*, **2**, 541 (1969).

29. T. Smith, *Proc. R. Soc. Lon. A*, **332**, 113 (1973).
30. F. A. Cotton and G. Wilkinson, *Advanced Inorganic Chemistry*, Interscience Publishers, New York, p. 182 (1972).
31. R. S. Berry, S. A. Rice, and J. Ross, *Physical Chemistry*, John Wiley and Sons, New York, p. 312 (1980).
32. R. Grinfeld, *Proceedings of the Tenth Colloquium Spectroscopicum Internationale*, eds. E. R. Lippincott and M. Margoshes, Spartan Books, Washington, D. C. (1962).
33. K. P. Huber and G. Herzberg, *Molecular Spectra and Molecular Structure, IV. Constants of Diatomic Molecules*, Van Nostrand Reinhold Co. (1979).
34. R. L. Love, J. M. Herrmann, R. W. Bickes, jr., and R. B. Bernstein, *J. Am. Chem. Soc.*, **99**, 8316 (1977).
35. K. Tabayashi, S. Ohshima, and K. Shobatake, *J. Chem. Phys.*, **80**, 5335 (1984).
36. W. C. Stwalley, private communication.

## 5.5 Figures and Captions

Figure 1. A schematic view of the top of the machine: VC1, vacuum chamber one; AS, anode assembly; A, anode; C, cathode; M, magnet; Sm, water-cooled copper assembly; TA, Translation assembly; T, translator; P1, viewport; L, optical lens; C2, 150 Hz chopper; monochromator, 0.5 m Jarrell-Ash monochromator; PM, photomultiplier; CP, current preamp; LI2, lock-in amplifier; SCR2, stripchart recorder; VC2 vacuum chamber 2; C1, 10 Hz chopper; D, electric field deflectors; F, mechanical flag; QMS, quadrupole mass spectrometer; P2, port; PA, EAI preamplifier (ESA-75); LI1, lock-in amplifier; MSE, mass spectrometer electronics; SCR1, strip chart recorder.

Figure 2. Emission spectrum running hydrogen in the discharge. Assigned rotational transitions for WH appear above spectrum. The letters P, Q, and R refer to the corresponding spectral branches.

Figure 3. Emission spectrum running deuterium in the discharge. Assigned rotational transitions for WD appear above spectrum. The letters P, Q, and R refer to the corresponding spectral branches.

Figure 4. Fortrat diagram for WH. Open symbols represent assigned spectral lines while smooth curve represents the fit to those lines.

Figure 5. Fortrat diagram for WD. Open symbols represent assigned spectral lines while smooth curve represents the fit to those assigned lines.

Figure 6. Figure shows Fortrat diagram for computer fit for WH (solid curve)

and WD (dashed curve). The zero line of the  $\nu_0$  of the two bands have been superimposed to show the magnitude of the rotational isotope effect alone.

Figure 7. a) Diagram of periodic table where the dark rectangles correspond to the elements for which hydride band spectra are known.

Figure 8. b) Diagram of periodic table where the dark rectangles correspond to the elements for which nitride band spectra are known.



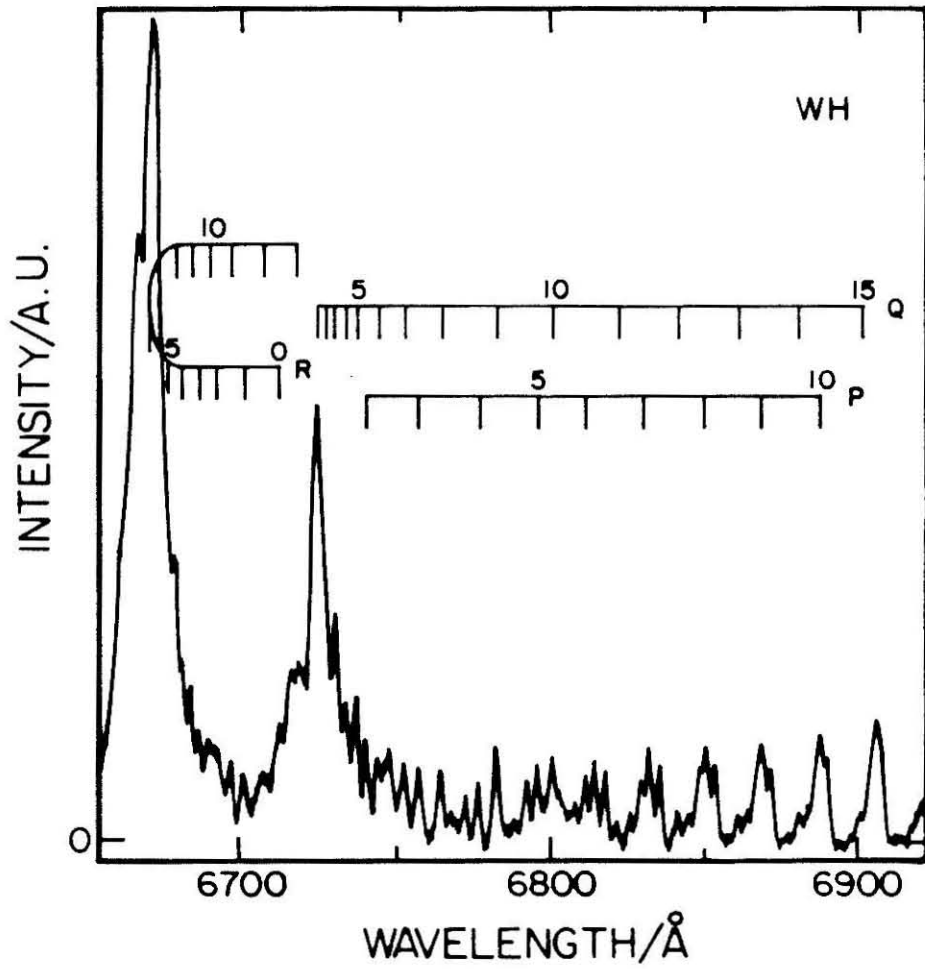


Figure 2

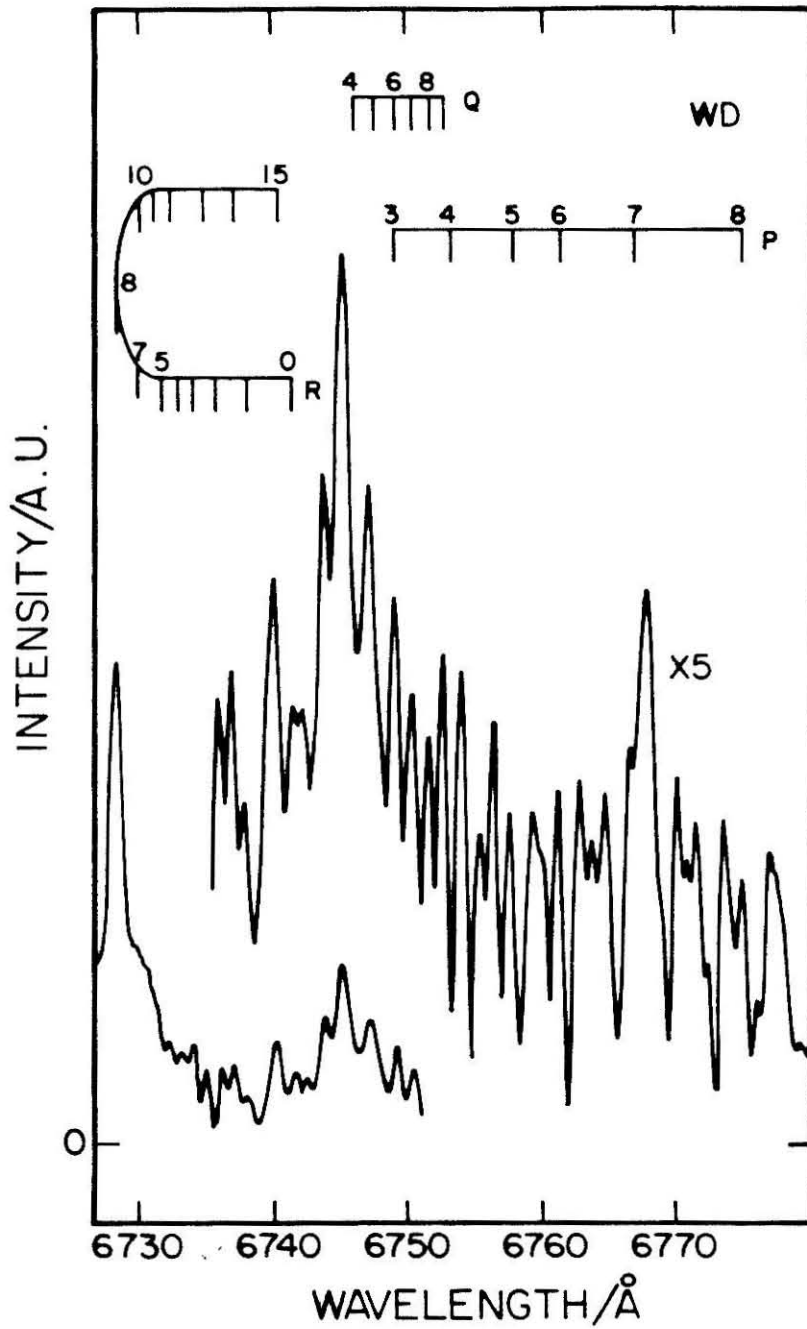


Figure 3

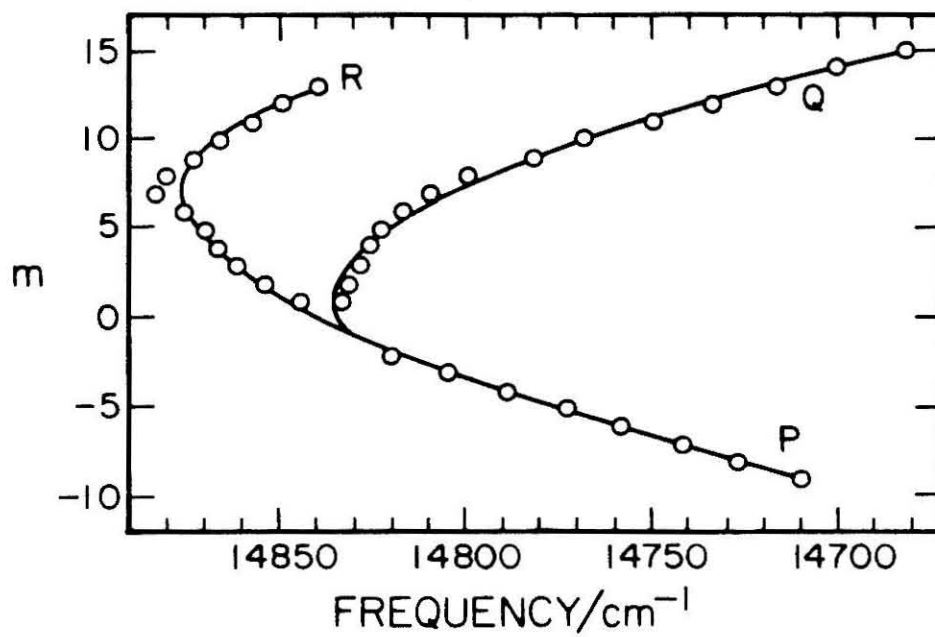
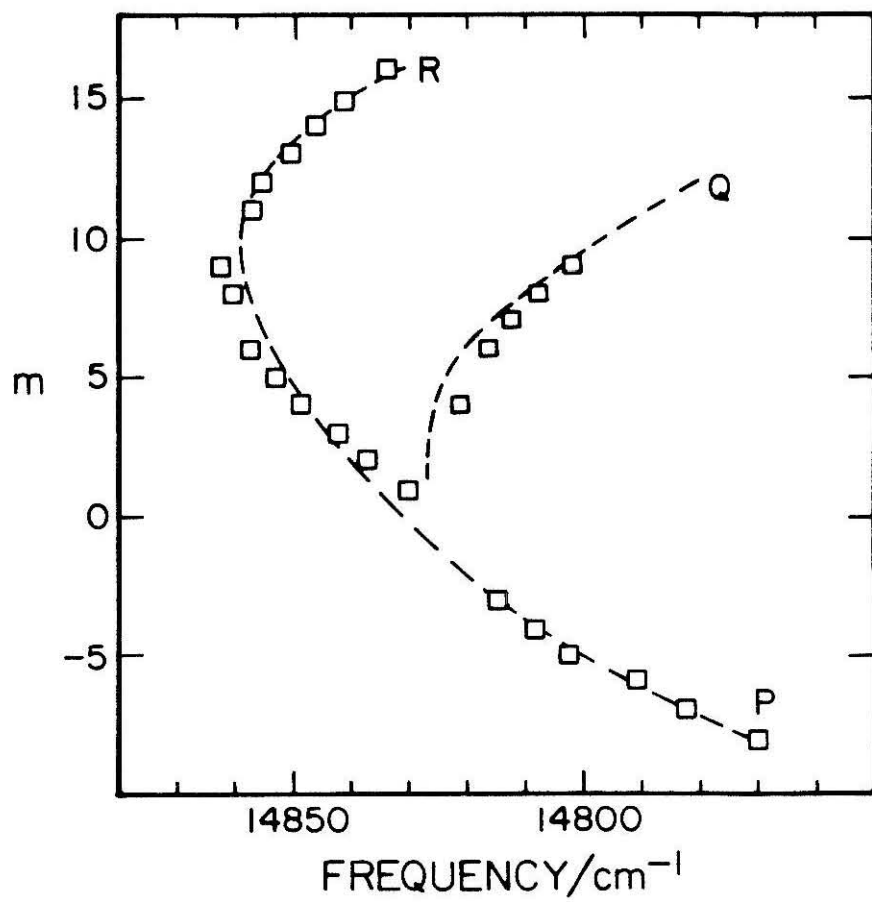


Figure 4



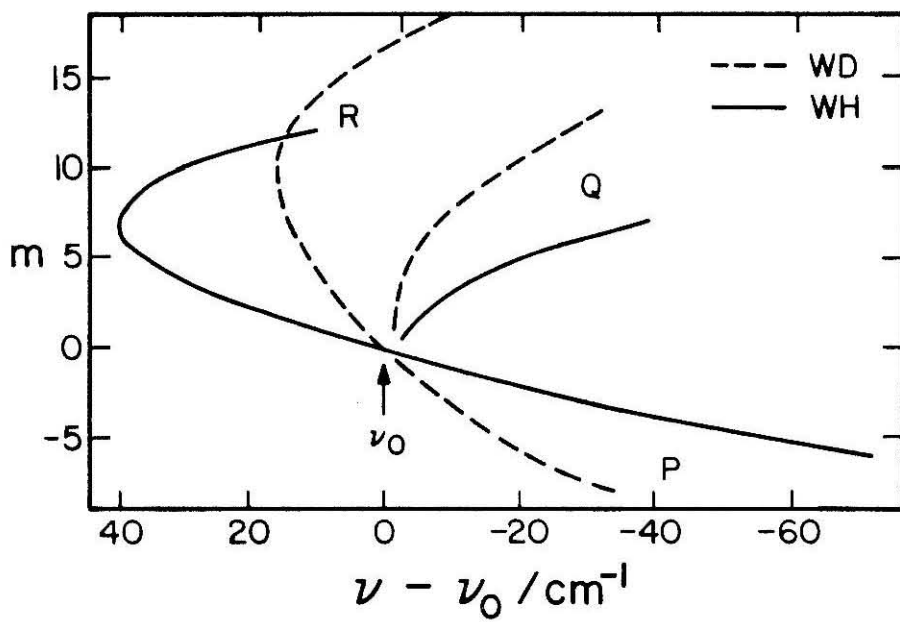


Figure 6

1 H 1.0079																	2 He 4.0026
3 Li 6.941	4 Be 9.0122											5 B 10.811	6 C 12.011	7 N 14.0064	8 O 15.9994	9 F 18.9984	10 Ne 20.1798
11 Na 22.9898	12 Mg 24.304											13 Al 26.9815	14 Si 28.0855	15 P 30.9738	16 S 32.06	17 Cl 35.453	18 Ar 39.948
19 K 39.0983	20 Ca 40.078	21 Sc 44.9559	22 Ti 47.88	23 V 50.9415	24 Cr 51.9961	25 Mn 54.938	26 Fe 55.845	27 Co 58.9332	28 Ni 58.6934	29 Cu 63.546	30 Zn 65.38	31 Ga 69.723	32 Ge 72.63	33 As 74.9216	34 Se 78.96	35 Br 79.904	36 Kr 83.80
37 Rb 85.4678	38 Sr 87.62	39 Y 88.9058	40 Zr 91.224	41 Nb 92.9064	42 Mo 95.94	43 Tc 98	44 Ru 101.07	45 Rh 102.9055	46 Pd 106.36	47 Ag 107.8682	48 Cd 112.411	49 In 114.818	50 Sn 118.710	51 Sb 121.757	52 Te 127.60	53 I 126.9055	54 Xe 131.29
55 Cs 132.9054	56 Ba 137.327	57-71 La-Lu 138.9055	72 Hf 178.49	73 Ta 180.9479	74 W 183.85	75 Re 186.207	76 Os 190.23	77 Ir 192.222	78 Pt 195.084	79 Au 196.9665	80 Hg 200.59	81 Tl 204.387	82 Pb 207.2	83 Bi 208.9804	84 Po (209)	85 At (210)	86 Rn (222)
87 Fr (223)	88 Ra (226)																
89 La (138.9055)	90 Ce (140.12)	91 Pr (140.9077)	92 Nd (144.24)	93 Pm (144.9128)	94 Sm (150.36)	95 Eu (151.964)	96 Gd (157.25)	97 Tb (158.9253)	98 Dy (162.50)	99 Ho (164.9303)	100 Er (167.259)	101 Tm (168.9304)	102 Yb (173.0547)	103 Lu (174.967)			
95 Ac (227)	96 Th (232.0377)	97 Pa (231)	98 U (238.0289)	99 Np (237)	100 Pu (244)	101 Am (243)	102 Cm (247)	103 Bk (247)	104 Cf (251)	105 Es (252)	106 Fm (257)	107 Md (258)	108 No (259)	109 Lr (260)			

\*Atomic weights are given on the <sup>12</sup>C scale. For artificial radioactive elements, the longest lived known isotope is given in parentheses

Figure 7

1 H 1.008																	2 He 4.0026																														
3 Li 6.941	4 Be 9.0122											6 C 12.011	7 N 14.007	8 O 15.999	9 F 18.998	10 Ne 20.179																															
11 Na 22.990	12 Mg 24.305											14 Si 28.086	15 P 30.974	16 S 32.06	17 Cl 35.453	18 Ar 39.948																															
19 K 39.098	20 Ca 40.078	21 Sc 44.956	22 Ti 47.88	23 V 50.942	24 Cr 51.996	25 Mn 54.938	26 Fe 55.847	27 Co 58.933	28 Ni 58.71	29 Cu 63.546	30 Zn 65.38	31 Ga 69.72	32 Ge 72.63	33 As 74.922	34 Se 78.96	35 Br 79.904	36 Kr 83.80																														
37 Rb 85.468	38 Sr 87.62	39 Y 88.906	40 Zr 91.224	41 Nb 92.906	42 Mo 95.94	43 Tc 98	44 Ru 101.07	45 Rh 102.905	46 Pd 106.4	47 Ag 107.868	48 Cd 112.412	49 In 114.818	50 Sn 118.710	51 Sb 121.757	52 Te 127.6	53 I 126.905	54 Xe 131.29																														
55 Cs 132.905	56 Ba 137.327	57-71 Lanthanides	72 Hf 178.49	73 Ta 180.948	74 W 183.85	75 Re 186.207	76 Os 190.23	77 Ir 192.22	78 Pt 195.084	79 Au 196.967	80 Hg 200.59	81 Tl 204.387	82 Pb 207.2	83 Bi 208.980	84 Po 209	85 At (210)	86 Rn (222)																														
87 Fr (223)	88 Ra (226)																																														
<table border="1"> <tr> <td>89 La 138.905</td> <td>90 Ce 140.12</td> <td>91 Pr 140.9077</td> <td>92 Nd 144.24</td> <td>93 Pm (145)</td> <td>94 Sm 150.4</td> <td>95 Eu 151.96</td> <td>96 Gd 157.25</td> <td>97 Tb 158.9254</td> <td>98 Dy 162.50</td> <td>99 Ho 164.9304</td> <td>100 Er 167.26</td> <td>101 Tm 168.9342</td> <td>102 Yb 173.054</td> <td>103 Lu 174.967</td> </tr> <tr> <td>104 Ac (227)</td> <td>105 Th (232)</td> <td>106 Pa (231)</td> <td>107 U 238.0289</td> <td>108 Np (237)</td> <td>109 Pu (244)</td> <td>110 Am (243)</td> <td>111 Cm (247)</td> <td>112 Bk (247)</td> <td>113 Cf (251)</td> <td>114 Es (252)</td> <td>115 Fm (257)</td> <td>116 Md (258)</td> <td>117 No (259)</td> <td>118 Lr (260)</td> </tr> </table>																		89 La 138.905	90 Ce 140.12	91 Pr 140.9077	92 Nd 144.24	93 Pm (145)	94 Sm 150.4	95 Eu 151.96	96 Gd 157.25	97 Tb 158.9254	98 Dy 162.50	99 Ho 164.9304	100 Er 167.26	101 Tm 168.9342	102 Yb 173.054	103 Lu 174.967	104 Ac (227)	105 Th (232)	106 Pa (231)	107 U 238.0289	108 Np (237)	109 Pu (244)	110 Am (243)	111 Cm (247)	112 Bk (247)	113 Cf (251)	114 Es (252)	115 Fm (257)	116 Md (258)	117 No (259)	118 Lr (260)
89 La 138.905	90 Ce 140.12	91 Pr 140.9077	92 Nd 144.24	93 Pm (145)	94 Sm 150.4	95 Eu 151.96	96 Gd 157.25	97 Tb 158.9254	98 Dy 162.50	99 Ho 164.9304	100 Er 167.26	101 Tm 168.9342	102 Yb 173.054	103 Lu 174.967																																	
104 Ac (227)	105 Th (232)	106 Pa (231)	107 U 238.0289	108 Np (237)	109 Pu (244)	110 Am (243)	111 Cm (247)	112 Bk (247)	113 Cf (251)	114 Es (252)	115 Fm (257)	116 Md (258)	117 No (259)	118 Lr (260)																																	

\* Atomic weights are given on the <sup>12</sup>C scale. For artificial radioactive elements, the longest-lived known isotope is given in parentheses.

Figure 8

## Appendix A : Magnetic Velocity Selector

### A.1 Introduction

Stwalley *et al.*<sup>1</sup> have reported a wide energy spread in their hydrogen atom beam. Our beam has also exhibited a wide range of energies as described in Section 3.3. It is of great interest to make this beam as monoenergetic as possible with respect to its translational energy, and to be able to select that energy over as wide a range of energy as possible. If this capability can be achieved with a sufficiently high beam intensity, it should be able to study the energy dependence of the dynamics of reaction of H atoms with other molecules. However, in order to achieve this goal, we cannot use mechanical-type velocity selectors. The median velocity transmitted through a multi-disc velocity selector is

$$v_m = \frac{2\pi R\omega L}{\Delta} = \frac{v_c L}{\Delta} \quad (A.1)$$

where  $v_c$  is the peripheral speed of the selector disc,  $\Delta$  is the offset of the exit slit from the entrance slit and  $L$  is the distance between the first and last discs<sup>2</sup>. From this equation it becomes apparent that as  $v_m$  becomes large either  $\omega$  or  $L$  must become larger and/or  $\Delta$  must decrease. As a result these velocity selectors become awkward for velocities of  $\sim 3 \times 10^5$  cm/sec and impractical above  $10^6$  cm/sec. However, the use of an inhomogeneous magnetic field can in effect give us the selection and resolution which is desired.

The technique was first used by Stern and Gerlach in 1921 to analyze a beam of silver atoms through an inhomogeneous magnetic field. Had  $\mu_{\text{eff}}$  been the classical component of the atomic magnetic moment, a continuous distribution of intensity at the detector would have been observed. The observation

of a double trace demonstrated for the first time the spatial quantization of angular momentum in an inhomogeneous magnetic field<sup>3-5</sup>. Since that experiment many other atoms have been studied using this technique<sup>6-10</sup> including paramagnetic molecules such as O<sub>2</sub><sup>1</sup>. It has also been used in the case of <sup>1</sup>Σ molecules for which there is no net electronic magnetic moment, making any deflection be due to the nuclear magnetic moment or the rotational magnetic moment. As a result H<sub>2</sub>, D<sub>2</sub>, and HD have been studied<sup>12,13</sup> and the rotational magnetic moment of H<sub>2</sub>O has been measured<sup>14</sup>.

These magnetic deflectors also have great application in the study of spin exchange processes<sup>15,16</sup> permitting the detection of changes in spin multiplicity<sup>17</sup>. This technique may also be used to study the anisotropy of an interatomic potential, for if one of the colliding atoms has a  $J > 1/2$  the dispersion interaction will be noncentral and can be observed through magnetic analysis<sup>18-20</sup>.

Perhaps the most interesting use of such a magnetic field has been as a velocity selector for hydrogen atoms<sup>21</sup>. An early analysis of such a technique was given by Cohen and Ellett<sup>22</sup> and later by Bederson and Rubin<sup>23</sup>. In Stwalley's experiment<sup>1</sup> he utilized a 25.4 cm-long inhomogeneous magnet, as had been described by Herm<sup>24</sup>, to characterize his superthermal hydrogen atom beam. In the course of the experiment the magnet was operated at a field strength of 14 kG and a gradient ( $\partial H/\partial z$ ) at beam position of 54kG/cm. Through the use of a bolometer, which could be translated perpendicular to the beam path, a deflection profile could be obtained of the hydrogen atoms after passing through the inhomogeneous field. The profile of the deflected beam was then inverted to give the velocity distribution of the hydrogen atoms. From this analysis he found that he could characterize his beam by a temperature ( $T = 25,000\text{K}$ ) and a Mach number ( $M = 0.3$ ).

The use of such an inhomogeneous magnetic field can possibly give us the tunability as well as the resolution we need to perform a reactive crossed beam experiment. As will be shown at the end of Section A.3, the expected H atom beam intensities will decrease, due to this magnetic selection, from about  $10^{22}$  atoms  $\text{s}^{-1}$  sterad $^{-1}$  to about  $10^{18}$  atoms  $\text{s}^{-1}$  sterad $^{-1}$ , and as shown in Section 3.5 this intensity should suffice to perform interesting reactive scattering experiments. Not only will the beam be resolved in terms of energy but also in spin states<sup>25</sup> such that spin-flip experiments might also be possible. The rest of this section will discuss the design and the recent construction of a Stern-Gerlach magnet for the energy selection of our superthermal hydrogen atom beam.

## A.2 Theory

The interaction potential of an atom having a magnetic moment  $\vec{\mu}$  with a magnetic field  $\vec{H}$  is given by

$$V = -\vec{\mu} \cdot \vec{H}. \quad (\text{A.2})$$

This atom will then feel a force

$$\vec{F} = -\vec{\nabla}V. \quad (\text{A.3})$$

Since the only significant dependence of  $V$  on position is through the spatial inhomogeneity of the field, we can write

$$\vec{F} = -\frac{\partial V}{\partial H} \vec{\nabla}H. \quad (\text{A.4})$$

The coefficient  $\partial V/\partial H$  differs for each of the  $2J + 1$  magnetic substates arising from the various possible orientations of the angular momentum vector  $\vec{J}$  of the atom in the magnetic field. If the inhomogeneity in the field occurs only in the  $z$  direction (see Figure 1 for coordinate system definition), then

$$F_x = F_y = 0 \quad (\text{A.5})$$

$$F_z = -\frac{\partial V}{\partial H} \frac{\partial H}{\partial z}. \quad (\text{A.6})$$

Many different types of deflection gradients have been devised<sup>14,24</sup>. Perhaps the best choice for our current purpose is the use of a focusing field, such as a hexapole array. These have been used<sup>25-28</sup> to produce a focusing of the beams which emerge at various angles from a source. The device may be considered as either a velocity selector, a rotational state selector or a

molecular orientation selector since the focal length of the rods is velocity dependent. A detailed design for its use as a spin filter has been given by Brash *et al.*<sup>29</sup>. An additional advantage to this field is that since the array acts as a focusing element, the rods may be made as long as needed since there will be no attenuation of the beam due to the  $1/r^2$  relation.

In the case of the hexapole array the magnetic field may be generated either by permanent magnets or electromagnetically. In the latter case, if a current  $i$  is passed through the array of conductors, each a distance  $R$  from the axis, the field generated is

$$B = \frac{3ir^2}{10\pi R^3} = B_o \left(\frac{r}{R}\right)^2 \quad (\text{A.7})$$

where  $B_o$  is the field strength at the pole tips in gauss and  $r$  is the displacement from the center of the array. The force acting on an atom a distance  $r$  from the center is given by

$$F = \frac{-2m_J g \mu_B B_o r}{R^2}. \quad (\text{A.8})$$

As a result the focal length of the rods can be given by

$$f = \pi v R \sqrt{\frac{M}{(2m_J g \mu_B B_o)}} \quad (\text{A.9})$$

where  $v$  is the velocity of the atoms travelling through the array. Although this type of inhomogeneous field appears to be highly attractive for our purpose, the fields necessary to generate velocity selection for our superthermal hydrogen atoms are not attainable. Using such an array to velocity select 1 eV atoms, we see from equation A.9 that even with high fields of 15 kG the focal length would be of the order of 250 cm. To be able to tune continuously from 0 to 5 eV with good resolution a hexapole array is unsuitable.

The design of greatest utility for our purposes is the 2-wire deflecting field<sup>30</sup>, which is a field created from two long parallel straight wires carrying

equal currents in opposite directions, as shown in Figure 2a. The field and gradient are completely calculable from the geometrical arrangement of the wires, as a result of the absence of ferromagnetic materials, and as a result this technique has become the standard for molecular beam deflecting magnets<sup>31</sup>

This derivation for the value of this field as a function of current is given in many textbooks. Using the coordinate system of Figure 1, the result is

$$H = 2I \frac{2a}{r_1 r_2} \quad (\text{A.10})$$

$$\frac{\partial H}{\partial z} = -2I \frac{2a}{r_1^3 r_2^3} (r_1^2 + r_2^2) z = H \frac{(r_1^2 + r_2^2)}{r_1^2 r_2^2} z \quad (\text{A.11})$$

where  $I$  is one-tenth the current in amperes,  $H$  is in gauss, distances are in cm and  $2a$  is the distance between the centers of the wires. The main advantage of this way of producing a field gradient is that this gradient is almost totally directed along the  $z$  axis with  $\frac{\partial H}{\partial z}$  being basically constant along the  $y$ -axis (over the region  $-0.7a$  to  $+0.7a$ ); therefore, one may use a tall ribbon beam directed along the  $y$ -axis, as shown in Figure 2a, and have it deflected sideways with very little vertical distortion. A main disadvantage of this method is that because of the high currents required a small field is generated. For example, a current of 100 amps in each wire will produce a field of 133 gauss and a gradient of 1,080 gauss per cm.

A way to get around this disadvantage and indeed produce a gradient just along the  $z$ -axis but at fairly high fields is to use the fact that for a 2-wire field the magnetic equipotentials are circles which pass through the center of the two wires. In Figure 2b we see that the field lines form sets of circles orthogonal to the equipotentials. If one now constructs an iron core electromagnet using poles which correspond to the equipotentials of a 2-wire field the magnet should produce a field in the air gap with virtually the same

lines of magnetic force as an equivalent 2-wire field. As long as saturation difficulties are avoided, the field produced by the magnet, like a 2-wire field, will have a nearly uniform gradient.

Due to the presence of iron in the magnet, the field no longer can be calculated from the excitation current. Though it is no longer possible to calculate the field, the ratio of the transverse field gradient to the field is determined solely by geometric parameters<sup>32</sup>:

$$\frac{1}{H} \frac{\partial H}{\partial z} = -\frac{r_1^2 + r_2^2}{r_1^2 r_2^2} z. \quad (\text{A.12})$$

For our beam directed along the midpoint between the poles (which has coordinates  $x, y=0, z$ ) we have  $r_2^2 = r_1^2 = a^2 + z^2$  from equation (A.12) and (A.6),

$$\frac{\partial H}{\partial z} = -H \frac{2z}{a^2 + z^2} \quad (\text{A.13})$$

and

$$F_z = H \frac{\partial V}{\partial H} \frac{2z}{a^2 + z^2}. \quad (\text{A.14})$$

It is now possible to calculate  $\frac{\partial V}{\partial H}$  for a hydrogen atom from equation (A.1) by obtaining first the magnetic moment of such an atom. From Dirac's relativistic treatment of the electron<sup>33</sup> it is known that the magnetic dipole due to the spin of a lone electron is

$$\vec{\mu}_e = -g_e \frac{e}{2mc} \vec{S} \quad (\text{A.15})$$

where  $g_e$  is the gyromagnetic ratio for the electron and  $\vec{S}$  is the spin angular momentum vector. Since our interest is only along the projection in the  $z$ -direction

$$(\mu_e)_z = -g_e \frac{e}{2mc} (m\hbar) = B_e = 9.27 \times 10^{-21} \text{ erg/G} \quad (\text{A.16})$$

where  $B_e$  is the Bohr magneton. It is only necessary to take into account the spin of the electron, because due to its orbital momentum in the ground state is zero and, due to the great mass difference between the electron and the proton, the magnetic moment associated with the proton is some three orders of magnitude less.

To calculate the amount of deflection caused by the magnet it is only necessary to combine equations (A.4) and (A.11) and get

$$F_z = -B_e H \frac{2z}{a^2 + z^2}. \quad (\text{A.17})$$

Again, using the coordinate system that is depicted in Figure 1 but now shifting the origin to the midpoint between the poles at the entrance to the magnet, Newton's equations give

$$z(t) = -\frac{1}{2} \frac{F_z}{m} t^2. \quad (\text{A.18})$$

It is now possible to see how the magnet will achieve velocity selection since

$$t = \frac{L}{v} = L \sqrt{\frac{m}{2E}} \quad (\text{A.19})$$

where  $v$  is the velocity of the hydrogen atoms,  $E$  their kinetic energy, and  $L$  is the length of the magnet. Substituting (A.13) into (A.12) we get, for the deflection at the exit of the magnet,

$$z = -\frac{1}{2} \left( \frac{F_z}{m} \right) \left( \frac{L}{v} \right)^2 = -\frac{1}{4} B_e \left( \frac{2z}{a^2 + z^2} \right) \left( \frac{HL^2}{E} \right) \quad (\text{A.20})$$

where the deflection of the ribbon beam is a function of the field, the kinetic energy of the hydrogen atom beam, and the square of the length of the magnet. Equation A.20 shows that the Stern-Gerlach magnet is really an energy selector. As a result, two different species (such as H and H<sub>3</sub>) with equal magnetic moment will be deflected by equal amounts if they have the same energy rather than the same velocity.

### A.3 Design

Our basic design is analogous to that of Herm and Herschbach<sup>22</sup>. For this type of selector the beam must be tightly collimated before it arrives at the entrance of the inhomogeneous magnet. To ensure this, the beam will be forced to pass through two adjustable slits before it reaches the magnet. Also between these two slits will be two high electrostatic fields perpendicular to each other to clean out any ions or electrons which may still remain in the beam as well as to quench any metastable 2s hydrogen atoms.

At this point a well collimated ribbon of neutral atoms will enter the magnet. In designing the poles of the magnet one attempts to maximize the magnetic field gradient as much as possible, thereby maximizing the resolution of the velocity selector, all within the constraints of machinable tolerances and physical reality. The compromise which was settled on is shown in Figure 3 and should give

$$\frac{\partial H}{\partial z} / H = 6 \text{ cm}^{-1}. \quad (\text{A.21})$$

As a result a tall, ribbon-shaped beam of hydrogen atoms passing through the center of the gap between the magnet poles will be deflected to either side. It should be noted that while  $\partial H / \partial z$  varies only slightly in the  $y$ -direction (the vertical direction in Figure 3) from these poles, a different geometry of pole tips will remove it totally. The shape of such poles, using the coordinate system defined in Figure 1, should satisfy the equation

$$z = \frac{1}{k} \ln \frac{1}{\cos ky} \quad (\text{A.22})$$

where  $k$  is a constant related to the pole gap and, for the gap of Figure 3, is equal to  $k = 1.5875 \text{ cm}$ . Pole pieces with such a shape have the property that

the force in the z-direction is independent of the y-coordinate of the particle. As a result, a thin-ribbon shaped beam of uniform velocity H-atoms remains rectangular as the beam is bent by the inhomogeneous magnetic field produced by those poles. This avoids the introduction of transverse aberrations that occur with the circular poles just discussed and also helps maximize the intensity of the energy-selected beam which emerges from the magnet. The disadvantage of this design is that it requires a computer-controlled milling machine for its manufacture. In order to permit the use of differently shaped pole pieces, we designed the Stern-Gerlach selector in such a way that the pole pieces may be interchangeable. Because of ease of construction we are first attempting to make the set of pole pieces with circular tips already described and at a later time will construct the logarithmic-cosine tips if necessary.

Due to physical constraints, we chose the length of the magnet as  $11 \frac{1}{4}$  inches. The hydrogen atoms, after passing through the magnet will be deflected to the left or right (depending on the component of their spin along the z direction) by an extent which depends on their velocity while any neutral contaminants with zero magnetic moment will pass through undeflected. To achieve the actual velocity selection there will be a Jarrell-Ash bilateral adjustable slit (as indicated in Figure 4) mounted to a translator positioned  $\frac{3}{8}$  of an inch from the exit of the magnet. The slit opening will be adjustable from 2 to 2000 microns and will help determine the energy resolution. Both the opening and closing of the slit as well as the moving of the slit left to right with respect to the exit of the magnet will be controlled from outside of the vacuum chamber. By then moving the exit slit transversally to the beam, at constant magnetic field, the energy spectrum of the hydrogen atoms will be scanned. Likewise, the size of the exit slit opening will establish how wide a slice of the energy spectrum is being transmitted. In other words, at constant

magnetic field the position of the slit will determine the energy selected while its width will determine the resolution.

Undoubtely the easiest mode in which to operate the selector is to keep the slit fixed .01 inch off the magnet center line and scan the energy of the beam not by moving the slit but by changing the energizing current for the magnet, thereby changing the field. We can expect with the parameters chosen that by scanning the magnetic field from 0 to 15 kilogauss we will scan an energy spectrum 0 to 5 eV. By changing the field and keeping the slit fixed, the opening of the slit must be continually changed in order to provide a constant resolution. Figure 5 shows what the slit opening must be as a function of energy to provide a constant resolution of 20, 40 or 60 meV. From this figure it appears that excellent resolution will be achievable in the 0 to 5 eV range provided there is sufficient beam intensity.

Because the eventual goal is to perform perpendicular crossed beam experiments, it is necessary to realize that because of the deflection of the beam the secondary beam must not be perpendicular to the center line of the magnet but rather to the actual direction of the deflected beam. As shown in Figure 4 the expected deflection will be of the order of 5 minutes of arc, and as a result, it is desirable that the whole velocity selector apparatus be mounted on a rotating plate to ensure that the beams cross perpendicularly.

As stated before, since the magnetic field cannot be known as a function of current nor, in view of the small pole gap, can the absolute field be easily measured<sup>22</sup>, it is necessary to provide some form of calibration for the magnet. It is therefore necessary to measure the energy of the transmitted beam by some independent method. This type of velocity analysis of the energy-selected beam can be accomplished by a cross-correlation method<sup>34-36</sup> which has been of great utility in low energy neutron diffraction studies<sup>34,37</sup>. It is

essentially a time-of-flight technique with the beam chopped such that it is modulated as white noise. The resulting signal in the detector is cross-correlated with the modulating sequence to produce the time-of-flight spectrum. The modulation is accomplished by using a correlation chopper with teeth spaced using a pseudo-random number generator. For each duty cycle of the chopper the beam is 'coded' by this random sequence and the molecules dephase according to their relative velocities as they travel to the detector. Once detected, the signal as a function of the time for that one duty cycle may be deconvoluted knowing the sequence of teeth widths of the chopper, yielding a velocity profile of the beam. The great advantage of this technique is that one achieves noise reduction by a factor of 7 over other signal averaging techniques, as well as providing velocity resolution of about 1% with a beam intensity approximately one-half that of the unmodulated beam.

In the case of our magnetic velocity selector we have available a correlation chopper 17 cm in diameter having 1023 pseudo-random spaced teeth, which can be rotated at frequencies up to 600Hz. A computer simulation analysis indicated that for an appropriate measurement in the crossed molecular beam apparatus available in our laboratory<sup>38</sup> energies up to 1 eV may be measured by extending the path from the chopper to the detector. To go to even higher energies would require a longer flight path, larger chopper or a faster motor. However, going up to 1 eV will provide the calibration necessary for the magnet. The electronic software and computer interface necessary for implementing this have already been designed by Jerry Winniczek<sup>39</sup>. A 255 tooth system was built and is being used by him.

The velocity selector and box will be fit into the existing 50" belljar such that reactive crossed beam experiments using the variable-angle mass spectrometer may be used. This configuration is shown in Figure 6. The source

and source chamber will remain outside of the large belljar and is mated through a 6" conflat flange into the bell jar. It will then enter the velocity selector box which is mounted on two oil diffusion pumping stacks, each having a rated speed of 400 l/sec. This will have the additional advantage that the box and velocity selector will be differentially pumped with respect to of the source chamber and the 50" bell jar. This will provide four regions of differential pumping: source to source chamber (60 torr to 500 microns), source chamber to velocity selector chamber (500 microns to  $10^{-5}$  torr), velocity chamber to 50" bell jar ( $10^{-5}$  torr to  $10^{-7}$  torr), and finally 50" bell jar to the cryopumped mass spectrometer ( $10^{-7}$  torr to  $10^{-9}$ ). Through this differential pumping, there should be an intense hyperthermal beam of energy selected hydrogen atoms capable of providing good signal-to-noise ratio in crossed beam experiments (see Section 3.5).

We can estimate the degree of attenuation of the beam by the velocity selector. Estimating the velocity distribution to be box-shaped and extending from 0 eV to 10 eV (Figure 6, section 3) to velocity select with 100 meV resolution would result in a drop in intensity of two orders of magnitude. To achieve this resolution the final slit will be open approximately 200 microns. This results in a solid angle of  $\sim 10^{-8}$  steradian, two order of magnitude smaller than discussed in Section 3.2 . As a result, the beam will be attenuated by two orders of magnitude, thus velocity selection will result in a drop of four orders of magnitude in intensity. This result is discussed in Section 3.5 of the thesis.

## A.4 Construction

The material of which the magnet is to be built is crucial in terms of optimizing the performance with respect to energy selection. Table I lists the magnetic properties of potential candidates for the construction of the magnet<sup>40</sup>. Armco electromagnet ingot iron<sup>41</sup> is quite popular for use in magnets in that it has reduced aging; that is, as a function of time the magnetic properties and hardness deteriorate slowly. For most magnetic materials the permeability will decrease by 25 to 50 % over the first year of operation while with Armco iron it will decrease by only 5 to 10 %. After machining the material it is then annealed at 1350° to 1880° F to minimize aging and improve the magnetic properties. However, the poles should be made out of a material that has high magnetic saturation compared with iron. To exceed the saturation of iron, an iron alloy containing up to 65% of cobalt is necessary; the highest values (about 24,200) are obtained by using 34.5% Co. Wider use of alloys containing between 25 and 50% Co is limited by the low resistivity and high hysteresis loss. With small additions of vanadium and chromium and special treatment in processing and annealing, high percentage Co alloys produce the best magnetic properties for both AC and DC applications. Because of these considerations we followed Herm and Herschbach<sup>22</sup> example and constructed the body of the magnet out of Armco iron and the poles out of an alloy which has high permeability at very high magnetic flux densities. Hiperc 50 (previously known as Permendur), made by Carpenter Technology, was the pole material<sup>42</sup>. It is composed of 48.7% cobalt and 1.9% vanadium, with the rest of the alloy composed of iron. With this material With it they reported a peak induction at the midpoint of the gap of about

**Table I****Characteristics of Magnetic Materials**

	Hiperco 50	Grain Oriented 50% Ni Iron	35%Co, 1%Cr, 64%Iron	Armco Iron
Permeability	6,000	150,000	10,000	5,000
Induction at max. perm. (gauss)	13,000	13,000	10,000	8,000
Saturation Value (gauss)	23,500	16,000	24,200	21,400
Resistivity (microhm-cm)	40	45	20	10
Density (gm/cm <sup>3</sup> )	8.15	8.25	8.00	7.88

**Table I cont.****Characteristics of Magnetic Materials**

	Hiperco 50	Grain Oriented 50% Ni Iron	35%Co, 1%Cr 64%Iron	Armco Iron
Residual Induct. (gauss)	10,000	14,500	11,000	7,700
Hysteresis Loss (ergs/cm <sup>3</sup> /cy)	1,500	450	2900	2700
Coercive Force (oersteds)	2.20	0.09	0.63	1.00

15 kilogauss with a transverse gradient of 90 kilogauss/cm. For best magnetic properties the Hiperco 50 must be annealed at 1625°F. Procurement of this material proved initially difficult since it is normally sold only under defense contracts, and then only in ton lots<sup>40</sup>. Luckily they were able to supply us with a small sample of the hot rolled unannealed Hiperco 50 which more than satisfied our requirements. Figure 7 shows the Armco body of the magnet with the inhomogeneous Hiperco 50 poles in place. As shown in this figure, brass spacers have been put along the top of the magnet. This was done to prevent any deformation of the air gap between the poles due to their natural attraction when the energizing current is turned on.

The energizing current and cooling water are carried by forty-two turns of 3/16" I.D. copper tubing wound about the magnet base twenty-one turns about each of the sides as shown in Figure 7. The coils and the base are insulated from each other. The energizing current will be furnished by a transistorized, regulated DC power supply capable of delivering 0-100 amps at 0-10 volts with little ripple.

Since both the body of the magnet and the poles must be annealed and since there was some uncertainty concerning how the material may deform with heating, it was decided to machine the parts and have them annealed together at 1625°F. In the initial rough machining enough material was left on the parts such that if there were any warpage it could easily be corrected. In machining the Hiperco 50 it was noted the material was very brittle and easily broke under pressing. Once machined, the poles were fastened back to back before annealing in order to minimize the warpage. After annealing there was considerable warpage but it was possible to remachine the poles such that the deviation of the male pole from linearity is no greater than is .0002" within tolerance and that of the female pole .0005".

The differential pumping chamber, which is to house the magnet within the bell jar, was modeled after the existing chamber which currently contains an He primary beam source. It is to be mounted over two of the mercury diffusion pumps. The chamber is built out of stainless steel, but since it is meant to only provide differential pumping its walls are 1/16" thick. The removable top providing easy access into the chamber is made out of aluminum which has been black anodized. On either side of the chamber are four 6" conflat flanges to allow electrical, water, and gas connections into the chamber.

Since the beams should intersect perpendicularly it is necessary to rotate the magnet and its assorted peripherals  $0^{\circ}5'$  off the primary beam direction. To accomplish this the magnet and everything except the final exit slit is mounted on top of two stacked plates as shown in Figure 8. The lowest plate is supported by three push-pull screws. These screws are engaged into three tapped pads which are welded onto the floor of the differential pumping chamber. Their function is to elevate the plate into a horizontal plane at a controlled distance below the beam centerline and to permit lateral movement of the plate into alignment with the beam source.

As shown in Figure 8, a ball bearing separator and a large bearing at the pivot point are between the lower plate and the upper plate which support the magnet, the two entrance slit assemblies, a beam cut-off flag, the pairs of electrically charged deflection plates and the velocity correlation disc and motor. Thus the upper plate can easily be rotated with respect to the fixed lower plate.

Originally proper alignment was to be achieved by positioning the magnet, closing the chamber, striking the beam and checking the alignment with the movable mass spectrometer, then judging the required relocation, relieving the vacuum, opening the system, making the change in the magnet location, and then repeating the procedure until alignment was acceptable. Because of

the time-consuming nature procedure of this it was decided to design the system such that it be would be possible to mechanically rotate the upper plate while the system was under vacuum. This has been done by the installation of a flex cable control which will permit the rotation, by the user, external to the chamber. The flex cable will extend through the differentially pumped magnet chamber and then through the 50" bell jar, providing external control of the rotation of the upper plate. An indication of the amount of rotation is given by a dial which measures the displacement of the front end of the upper plate with respect to the chamber center line. By displacing the exit end of the magnet .016" this will achieve the  $0^{\circ}5'$  expected deflection. The accuracy of the dial is .0001" which is more than sufficient for our purpose. The user will then directly monitor this dial while rotating the flex cable and have an accurate assessment of the position of the upper plate with respect to the center line. Doing this in conjunction with measuring the intensity of the beam with the mass spectrometer will provide a better understanding of the actual position and alignment of the beam.

What follows is a brief description of the components which are mounted on top of the upper plate, as shown in Figure 9. Working from back to front the first item is the entrance port [EP]. This will be attached to vacuum the pipe which connects the source chamber to the velocity selector chamber VSC. The actual functioning of this device is discussed later in this section. The beam will then enter the VSC and will encounter an adjustable slit [S]. Its function is to give the beam the shape needed for energy selection before it reaches the magnet. The slit size will be set (through a micrometer head, L. S. Starrett Co. T1463L) by the operator before the vacuum system is closed up and cannot be changed unless the vacuum is broken.

The beam will then pass through the mechanical flag region. This is a simple pneumatically activated metal flag [Fl] which can be used to interrupt

the beam by being inserted in its path. The beam will then pass through the correlation chopper region. In this region it will likewise be possible to position the teeth of the correlation chopper [CCh] in the path of the beam via a pneumatic valve. Here the chopper blade is mounted on an AC hysteresis synchronous motor (Globe indust. type; FC #75A1003-2) capable of rotating at 600 Hz at 115 volts (the same motor currently used by J. Winniczek in his correlation work<sup>37</sup>). The motor itself is mounted within a water-cooled casing to prevent overheating. To utilize the chopper it is necessary to be able to lock on its rotation frequency. This is provided by a single, deeper slit cut into the disc, deeper than the pseudo-random slits already present. With each revolution of the disc this deeper slit will pass through a photon coupler interrupter module (G.E #H13B1-H13B2), such that the signal frequency from this module will provide the lock-in frequency.

The beam will then pass through two sets of copper deflection plates [DP] set perpendicular to each other. These plates are like the set discussed in Section 3.1, and their purpose is to deflect any ions out of the beam as well as to quench any H metastables. Because the vacuum in this region is expected to be much greater than the one generated in our mass spectrometer test stand, it is expected that fields greater than 1000 V/cm can be generated. This was not possible in the test stand because of dielectric breakdown which caused extensive sparking between the edges of the deflection plates.

The beam will then pass through a second slit, just like the first, to further collimate it before entry into the magnet gap. The beam will then pass through the magnet, and H as well as H<sub>3</sub> will be deflected as a function of their energy.

The actual energy selection will be accomplished by the monochromator slit [MSl] mounted 5/16" away from the exit of the magnet. Ideally the slit should be positioned as far as possible from the exit of the magnet and, due

to the VSC size constraint, this was the largest distance possible. As discussed previously, the position of this exit slit with respect to the centerline of the magnet will in effect determine energy selection while its slit opening will provide the the energy resolution. The slit used for this purpose is a Jarrel-Ash bilateral monochromator slit continuously adjustable from 0 to 2000 microns. Since the slit needs to be translated with respect to the fixed magnet, it is mounted on an Instrument Industries #TC-100-M5 translator [ST]. This translator is mounted directly to the exit wall of the differential pumped chamber [VSC].

Both the opening and closing of the slit as well as its translation need to be performed while the system is under vacuum. This is accomplished by directly driving both the translator and slit with Rapidsyn stepping motors (23D-6102A). The motors themselves are controled by Rapidsyn bipolar motor drivers (model DMU-33-21). The slit opens  $200\mu$  for each complete revolution of the micrometer head. Each step of the corresponding motor turns the micrometer head by  $1.8^\circ$  (with a 5% accuracy and therefore 10 steps will open the slit by  $10\mu$ ). Likewise, the translator will move  $.025''$  per full revolution of its micrometer head. With the translator travel expected to be about  $.050''$  this will present no problem for the stepper motor, for both the translator and the slit microswitches have been placed to limit the extent of their travel.

One unresolved problem which exists is that the Jarrel-Ash slit is made out of magnetic material. Being only  $5/16''$  away from the exit of the magnet it may be affected when the magnet is energized. If such operating difficulties occur then successive magnetic components will be fabricated from non-magnetic stock.

Having now passed through the final exit slit the beam will exit the differentially pumped chamber and now enter the  $50''$  bell jar. In doing so it will be chopped by a modulator [Ch] which is mounted to the outside of the

VSC. The chopper is mounted on a motor (Globe 75A119-2, 115V, 1,200RPM) situated in a water cooled base. This modulation of the beam will permit the use of lock-in techniques in measuring the scattered signal. The beam can then reach the chamber center [CC] where it can interact with whatever molecules are in the secondary beam.

The one difficulty remaining in the construction of the system was in a mating flange which would provide a vacuum tight seal between the source chamber and the VSC. Due to the bell jar being in the down position when this mating was to be accomplished, it was necessary not to use any bolt fittings, due to their inaccessability. The design which was settled on is shown in Figure 10. The way it operates is as follows: the source chamber will be first correctly positioned with the flexible flange [F] removed; with the bell jar [BJ] in the up position the O-ring fitted disc is put in place on the entrance of the velocity selector chamber [VSC]. The bell jar will then be lowered into place; once down, the pipe which will provide the mating between the two chambers is placed within the port; by a fitted O-ring at the end of it, it is pushed into the fitted disc resulting in a vacuum-tight connection; at this point the flexible flange can then be put into place, completing the seal. To break vacuum all that is necessary is to reverse the above procedure and the discharge source chamber will never need to be moved.

## A.5 References

1. K. R. Way, S.-C. Yang and W. C. Stwalley, *Rev. Sci. Instrum.*, **47**, 1049 (1976).
2. M. A. D. Fluendy and K. P. Lawley, *Chemical Applications of Molecular Beam Scattering*, Chapman and Hall, London, p. 98 (1973).
3. O. Stern, *Zeits. f. Physik.*, **3**, 418 (1920).
4. Gerlach and O. Stern, *Ann. Physik.*, **74**, 673 (1924).
5. Gerlach and O. Stern, *Ann. Physik.*, **76**, 163 (1925).
6. J. B. Taylor, *Phys. Rev.*, **28**, 576 (1928).
7. U. Kurt, and T. E. Phipps, *Phys. Rev.*, **34**, 1357 (1929).
8. T. E. Phipps, and J. B. Taylor, *Phys. Rev.*, **29**, 309 (1927).
9. O. Specchia, *Nuovo Cimento*, **12**, 541 (1935).
10. W. Meissner, and H. Scheffers, *Phys. Zeits.*, **34**, 48 (1933).
11. R. Schnurmann, *Zeits. f. Physik.*, **85**, 212 (1933).
12. R. O. Frisch, and O. Stern, *Zeits. f. Physik.*, **85**, 4 (1933).
13. I. Estermann, and O. Stern, *Zeits. f. Physik.*, **85**, 17 (1933).
14. R. G. J. Fraser, *Molecular Rays*, Cambridge University Press, Cambridge, England (1931).
15. D. E. Prichard, and F. Y. Chu, *Phys. Rev. A.*, **2**, 1932 (1970).
16. D. E. Prichard, G. M. Carter, F. Y. Chu, and D. Kleppner, *Phys. Rev.*

- A., **2**, 1922 (1970).
17. K. Rubin, J. Perel, and B. Bederson, *Phys. Rev.*, **117**, 151 (1960).
  18. K. Berkling, C. Schlier, and P. Toschek, *Zeits. f. Physik.*, **168**, 81 (1962).
  19. M. A. D. Fluendy *J. Sci. Instr.*, **42**, 489 (1965).
  20. V. W. Cohen, and A. Ellett, *Phys. Rev.*, **51**, 65 (1937).
  21. B. Bederson, and K. Rubin, AEC Technical Report NYO-10, 117 (New York University, New York, February, 1962).
  22. R. R. Herm, and D. R. Herschbach, UCRL-10562, UC-34 Physics (October, 1962).
  23. G. Clausnitzer, *Nucl. Instr. and Meth.*, **23**, 309 (1963).
  24. I. I. Rabi, *Nature*, **123**, 163 (1929).
  25. H. Friedburg, and W. Paul, *Naturwissenschaften*, **37**, 20 (1950) and **38**, 159 (1951).
  26. H. Friedburg, and W. Paul, *Z. Phys.*, **130**, 493 (1951).
  27. M. I. Korsunskii, and Ya. M. Fogel, *J. Exp. Theor. Phys. (USSR)*, **126**, 760 (1951).
  28. R. Vauthier, *C. R. Acad. Sci. Paris*, **228**, 1113 (1949).
  29. H. M. Brash, D. M. Cambell, S. P. Farago, A. G. A. Rae, H. C. Siegmann, and J. S. Wykes, *Proc. Roy. Soc. Edin.*, **A68**, 158 (1969).
  30. I. I. Rabi, J. M. B. Kelloff, and J. R. Zacharias, *Phys. Rev.*, **46**, 157 (1934).
  31. P. Kusch and V. Hughes, *Handbuch der Physik*, **37** (Springer, 1959).

32. N. F. Ramsey, *Molecular Beams*, Oxford U. P., London, Appendix F (1956).
33. P. A. M. Dirac, *The Principle of Quantum Mechanics*, 4th ed., Oxford, New York (1958).
34. K. Skold, *Nucl. Instrum. Methods*, **63**, 114 (1968).
35. V. L. Hitschy and J. P. Aldridge, *Rev. Sci. Instrum.*, **42**, 381 (1971).
36. L. D. F. Allen, *Velocity Distributions by Correlation Techniques*, LA-5187, UC-34, Los Alamos Scientific Laboratory, New Mexico, April 1973.
37. T. E. Stern, A. Blaquiere, and J. Valat, *J. Nucl. Energy*, **16**, 499 (1962).
38. A. Kuppermann, R. J. Gordon, and M. J. Coggiola, *Faraday Discuss. Chem. Soc.*, **55**, 145 (1973). M. Keil, J. R. Slankas, and A. Kuppermann, *J. Chem. Phys.*, **70**, 541 (1979).
39. J. W. Winniczek, Ph.D thesis, California Institute of Technology (1985).
40. *Metal Handbook*, 8th edition, Vol 1, American Society for Metal, Metals Park, Ohio (1961).
41. Available through Armco Steel Corp., Dept. LE 9627, Box 600, Middletown, Ohio 45042.
42. Available through Carpenter Technology Corp., P.O. Box 662, Reading, Pa. 19603.

## A.6 Figure and Captions

Figure 1. Definition of coordinate system (taken from Ref. 20). The  $x$  axis point into the plane of the paper.

Figure 2. (a) Cross-section of two wire field holder and field wires. The direction of the beam is perpendicular to the plane of the paper. (b) Magnetic field lines around infinitely narrow two-wire field (full curves) and magnetic equipotentials (dashed curves) (both figures taken from Ref. 30).

Figure 3. Cross-section of design for pole pieces of magnet which effectively produces two-wire field with  $\frac{\partial H}{\partial z} / H = 6 \text{ cm}^{-1}$ . The direction of the beam is perpendicular to the plane of the paper. All units are in inches.

Figure 4. Schematic top view of H-atom beam and velocity selector coupled to the 50-inch bell jar. Angle of rotation (not to scale) is exaggerated for clarity.

Figure 5. Plots of calculated slit width as a function of selected energy for three energy resolutions; 20, 40, and 60 meV.

Figure 6. Side view of crossed beam apparatus using the H-atom beam as primary beam: VC1, vacuum chamber one; S, water-cooled copper skimmer; GV, pneumatic gate valve; F, flexible flange; BJ, 50-inch bell jar. Dashed lines indicate box within the bell jar which contains the magnetic velocity selector.

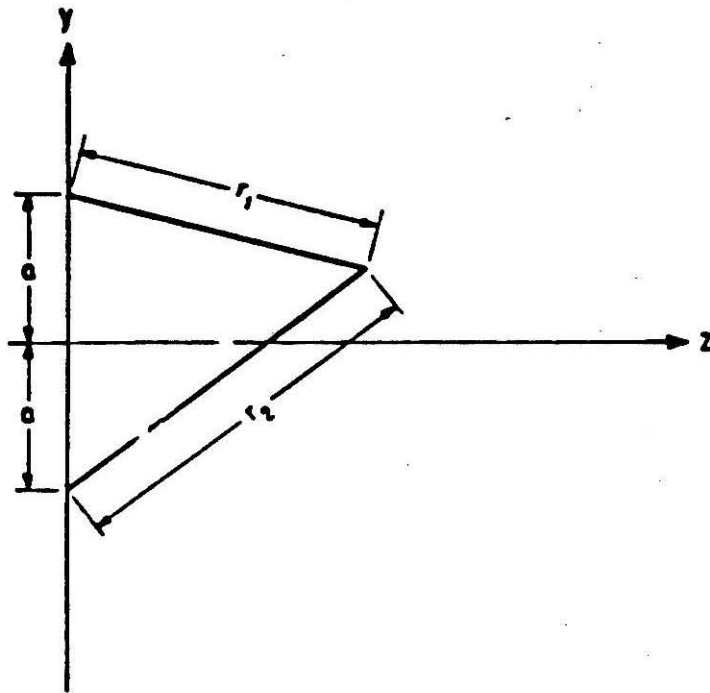
Figure 7. Side view of inhomogeneous magnet with circular pole tips in place.

Figure 8. Schematic view of magnet on top of positioning plate. (a) top

view, (b) side view: PP, pivot point; HA, height adjuster. (c) close-up of ball-bearing separator.

Figure 9. Top view of inhomogeneous magnet inside box: EP, entrance port; HA, height adjuster; S, adjustable slit; FL, flag; DP, deflection plates; CCH, correlation chopper; P, outside ports to velocity selector chamber; PP, pivot point; MB, magnet body; WC, water-cooling coils; MS1, motorized Jarrel-Ash slit; ST, motor for slit translator; CH, beam chopper for lock-in; CC, chamber center. Partially dotted line traced through the apparatus indicates undeflected path of hydrogen atom beam.

Figure 10. Side-view of coupling between VC1 and BJ: F, flexible flange; BJ, 50-inch bell jar; VSC, velocity selector chamber.

**Figure 1**

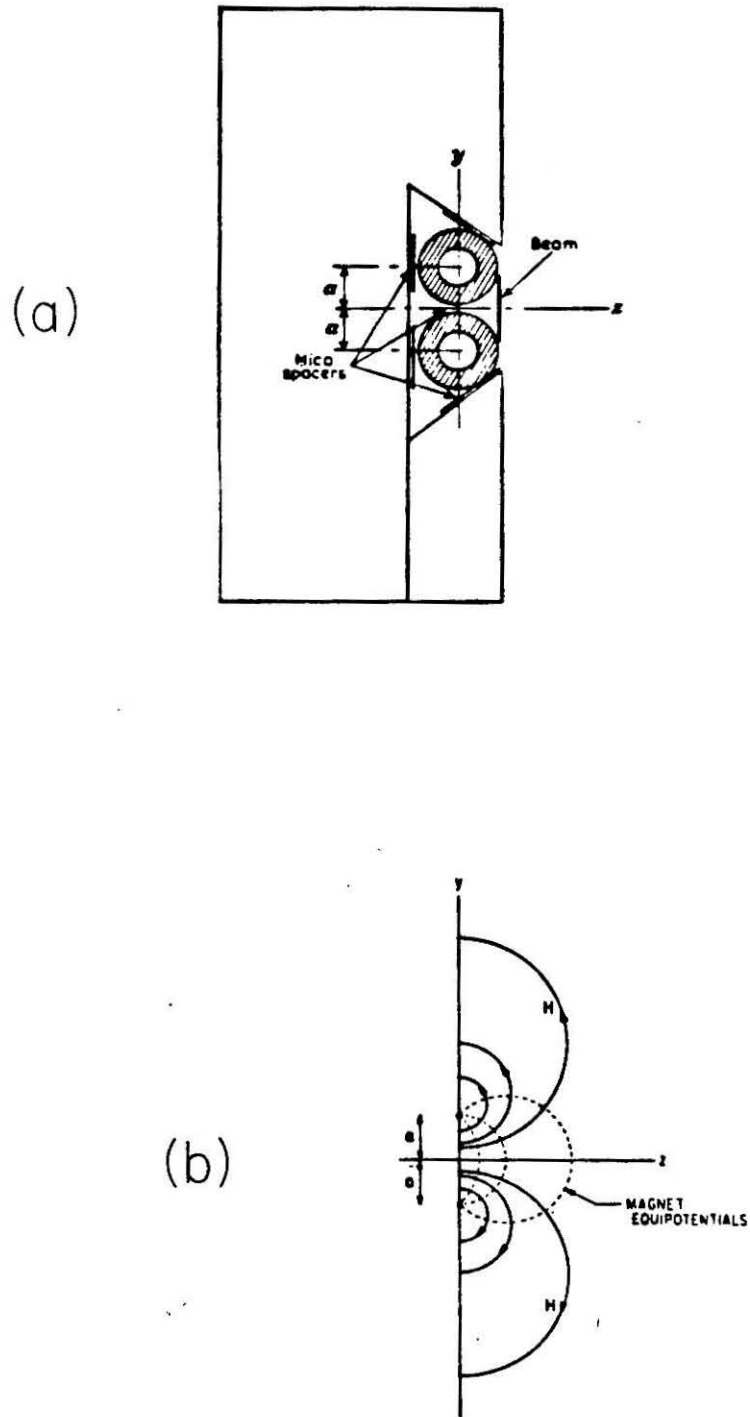
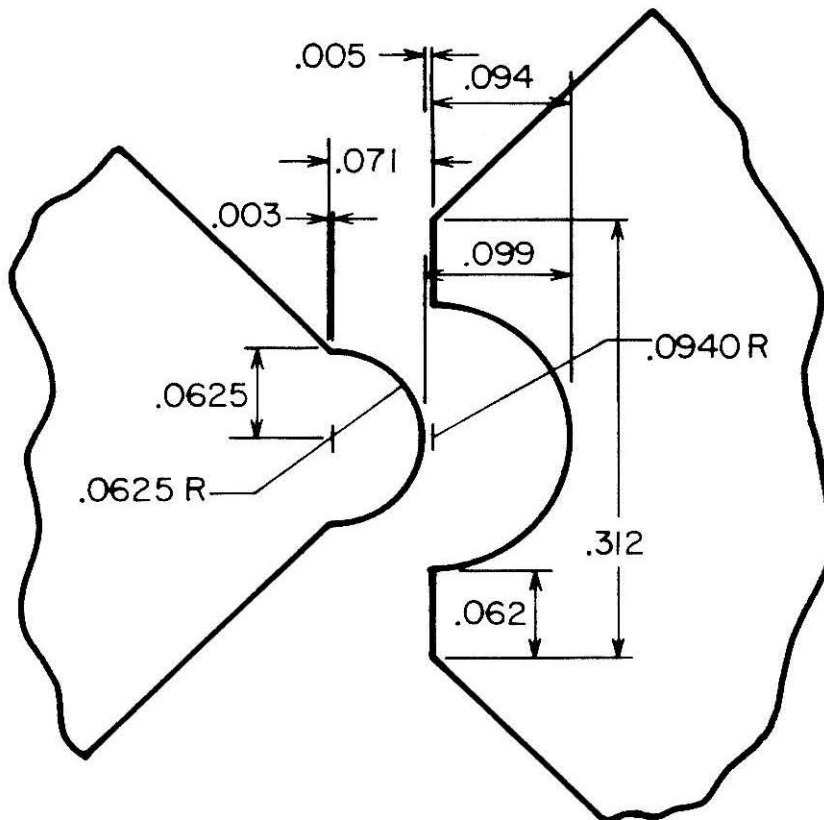


Figure 2

**Figure 3**

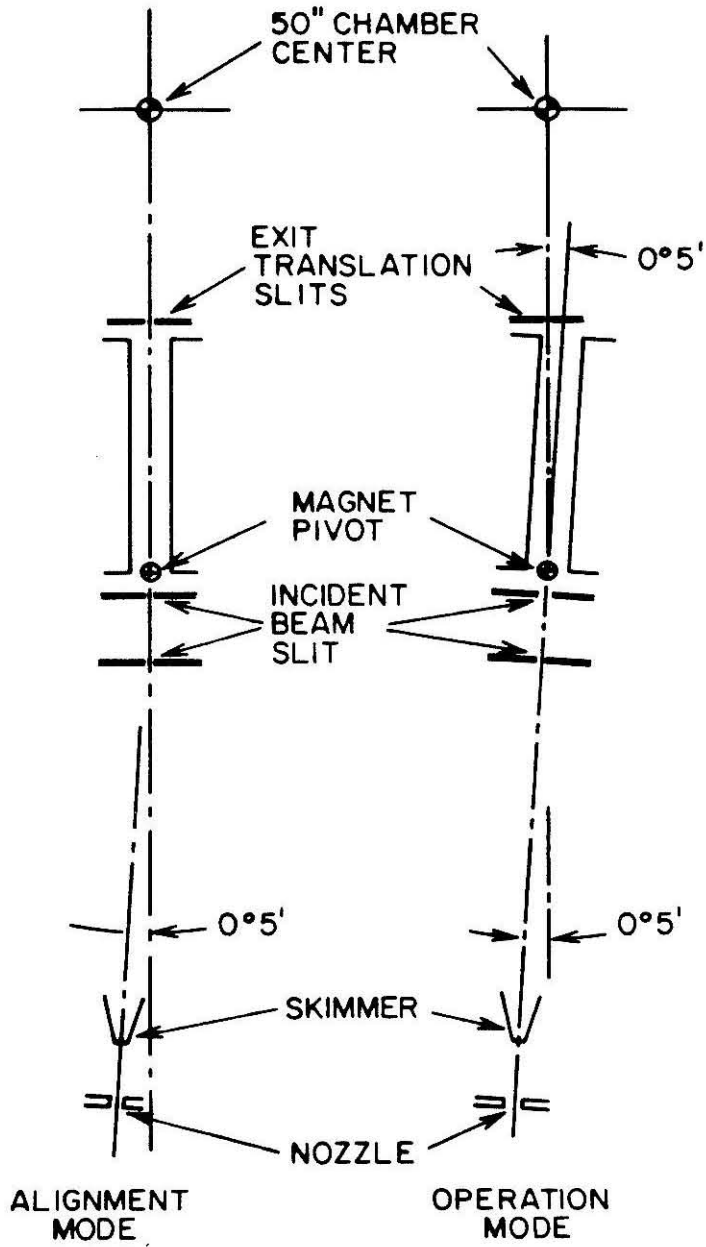
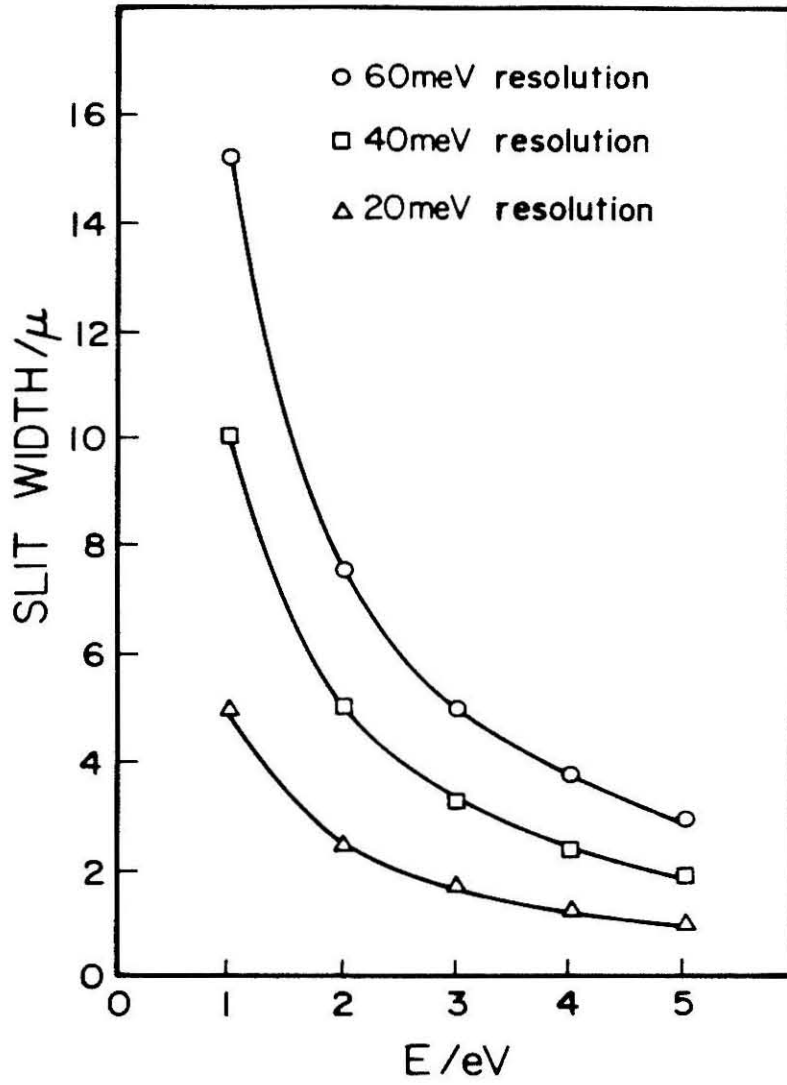


Figure 4

**Figure 5**

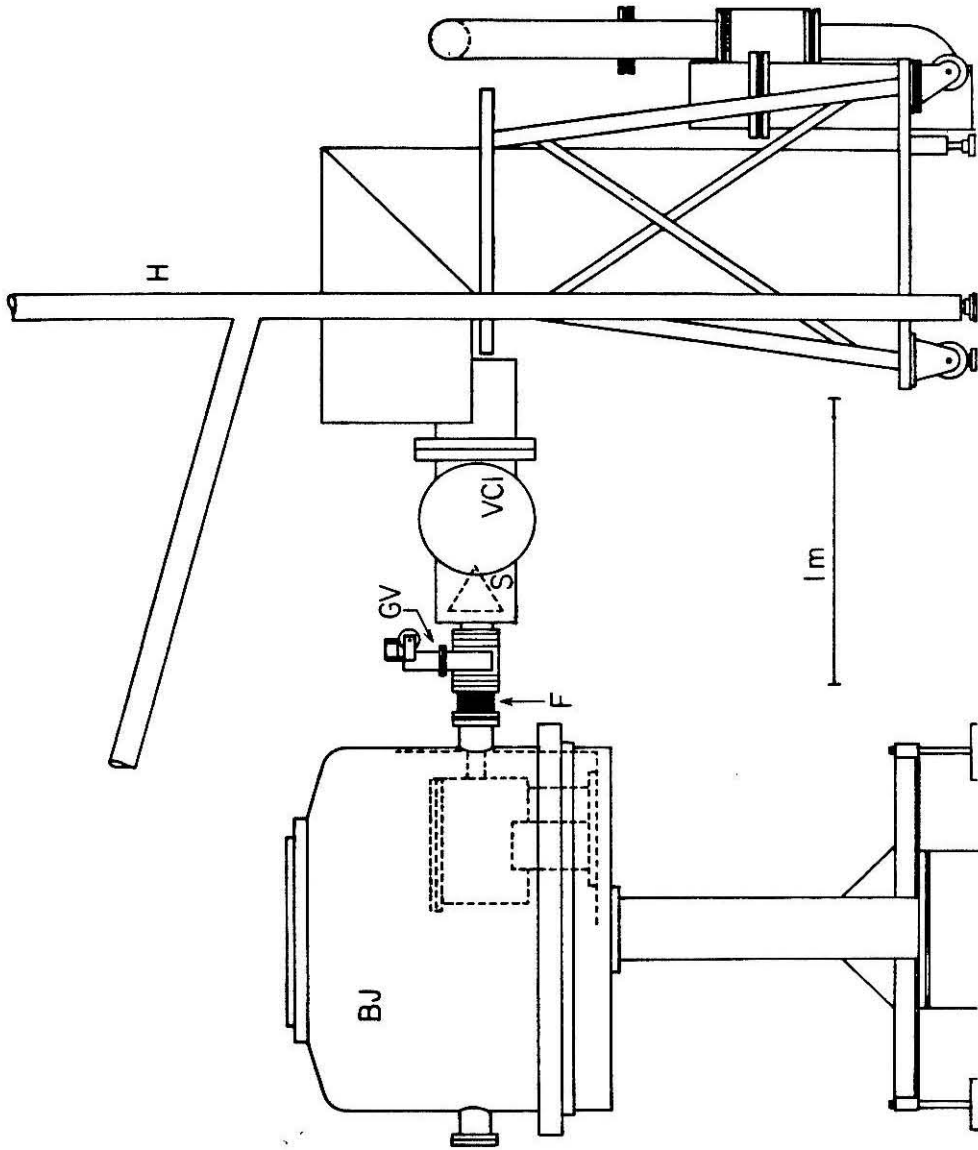
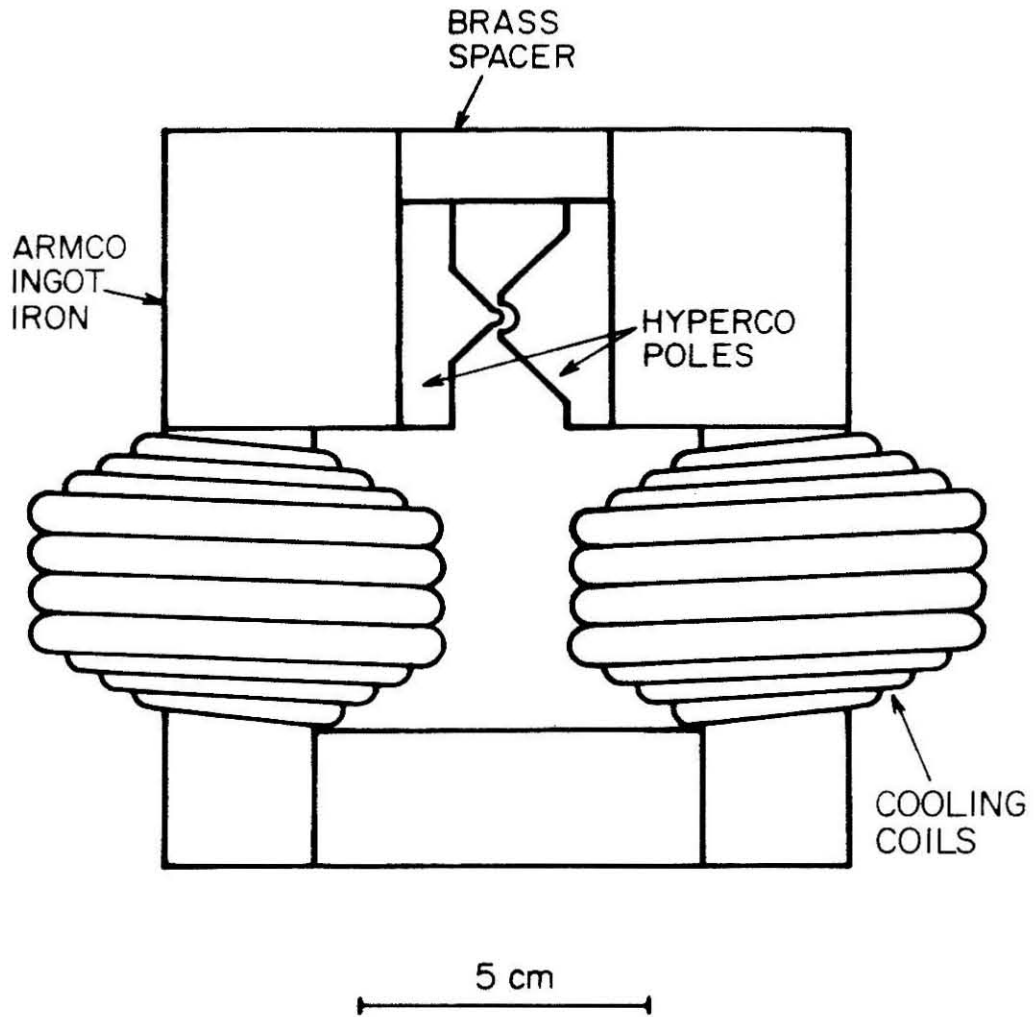


Figure 6

**Figure 7**

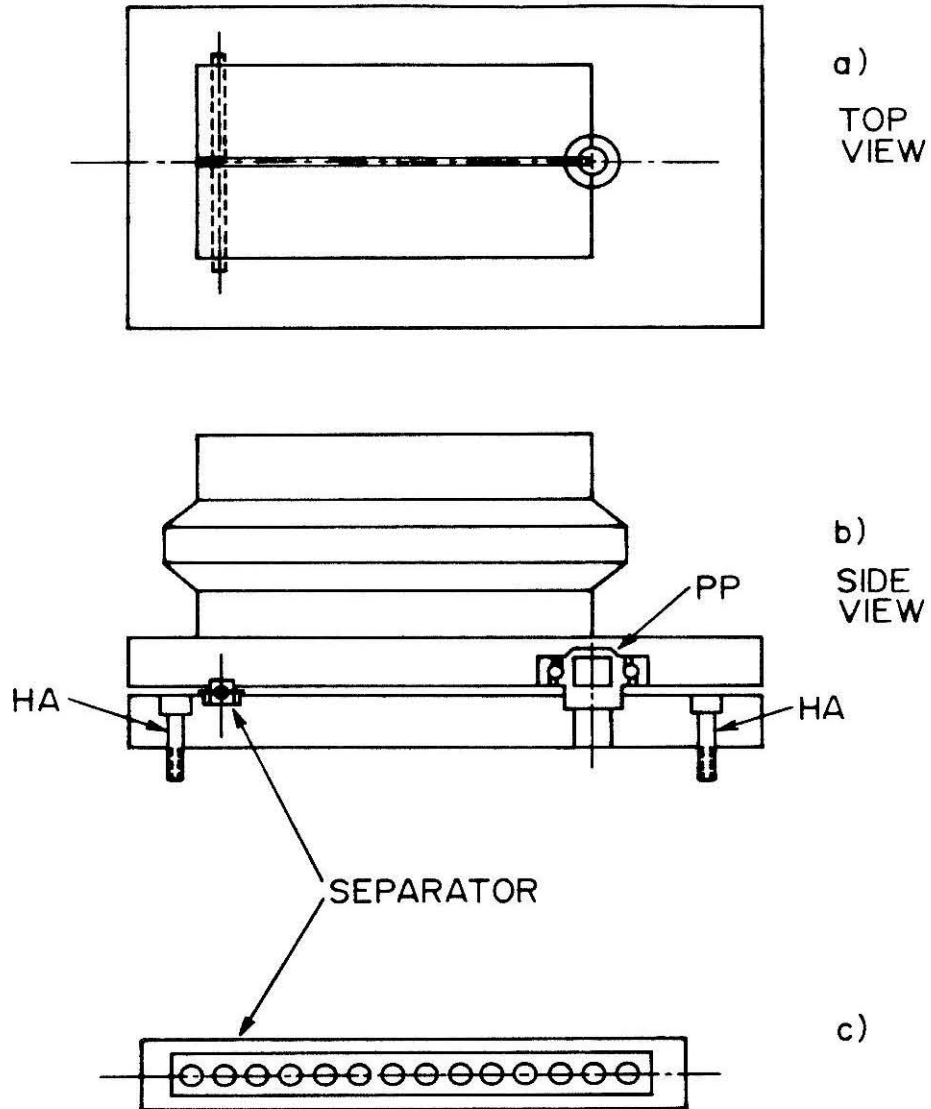


Figure 8

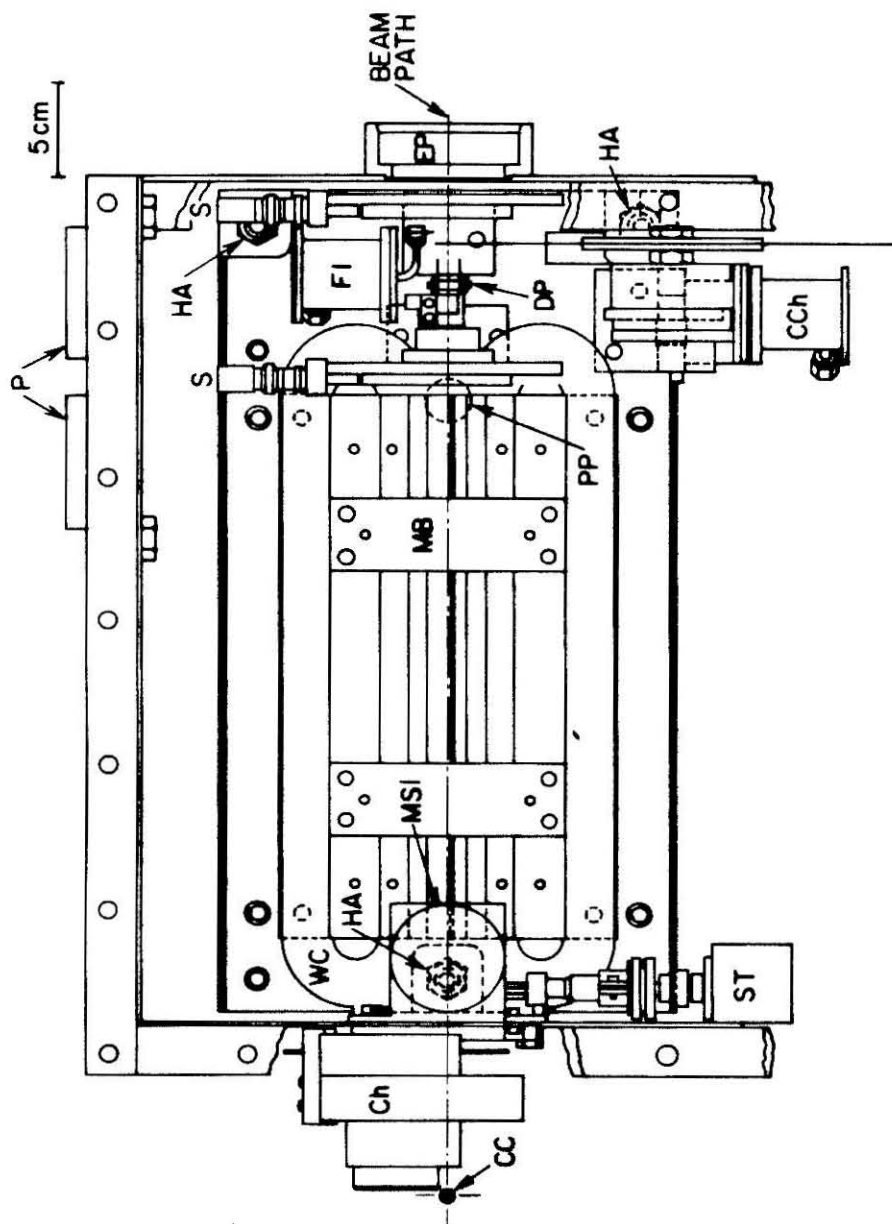
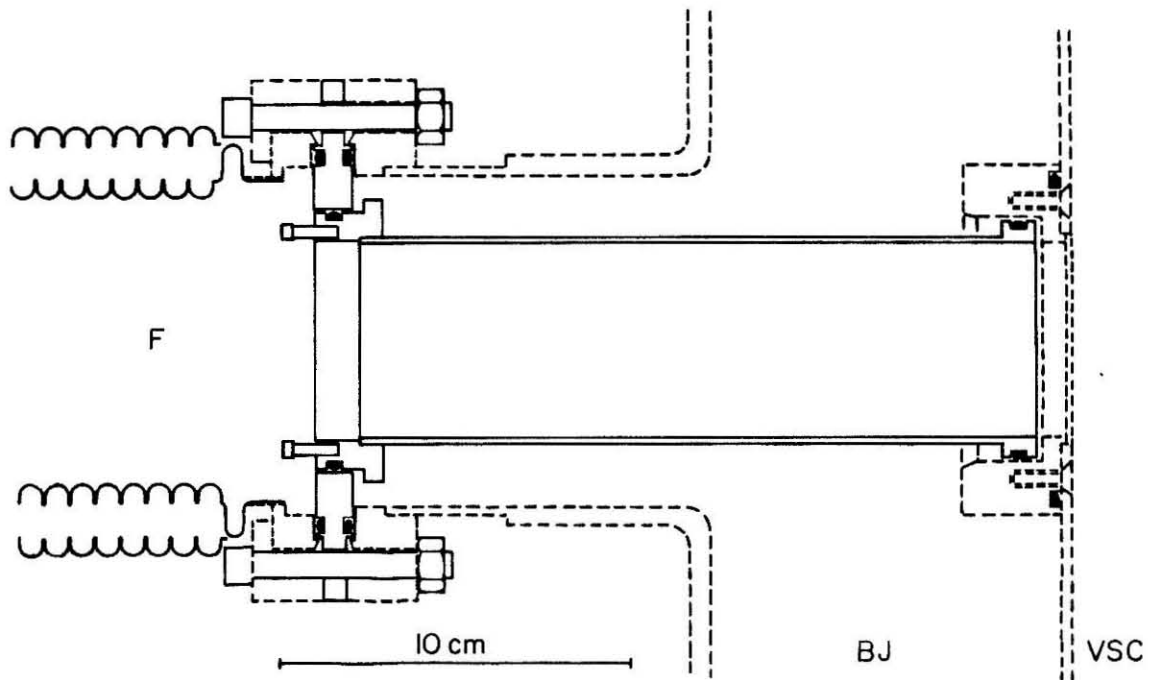


Figure 9

**Figure 10**

## Appendix B : Quantum Mechanical Study of the Collinear

### Reaction $\text{Be} + \text{FH}(v = 0, 1) \rightarrow \text{BeF}(v') + \text{H}$

#### B.1 Introduction

Over the past decade, there has been substantial interest in the reaction of alkaline earth atoms with hydrogen halides<sup>1-11</sup>



where  $\text{M} = \text{Ba}, \text{Ca}, \text{Sr}$  and  $\text{X} = \text{F}, \text{Cl}, \text{Br}, \text{I}$ . Of particular interest has been the way in which reaction rates and product state distributions vary with changes in the vibrational<sup>2-4</sup>, translational<sup>5,6</sup>, and rotational<sup>7-9</sup> state of the  $\text{HX}$  reagent excitation of the metal atom<sup>10,11</sup>.

A particularly important conclusion of these studies on the  $\text{Ba}, \text{Ca},$  and  $\text{Sr} + \text{FH}$  reactions is that little of the available product energy is channeled into the products vibrational energy. This result was found by Pruett and co-workers<sup>2</sup> for  $\text{Ba}$ . and was found for  $\text{Ca}$  and  $\text{Sr}$  by Karny and Zare<sup>3</sup>. Further work on this system<sup>5,6</sup> has now shown that with increasing collision energy the reagents' relative translational energy leads to increased excitation of the reaction products, and that excitation of the  $v = 1$  state of the reagent in the  $\text{Ba} + \text{HF}$  reaction leads to a reaction rate increase of a factor of three<sup>4</sup>.

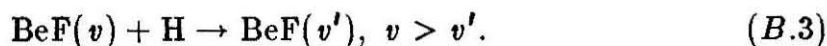
An accurate theoretical treatment of these reactions is difficult because the large number of electrons present makes calculation of potential energy surfaces prohibitively expensive. For this reason, substantial effort has been made to study the simplest  $\text{M} + \text{HX}$  reaction, that of  $\text{Be} + \text{FH}$ , considering only the collinear configuration,



Schor *et al.*<sup>12</sup> performed *ab initio* quantum mechanical calculations of the corresponding potential energy surface and used that surface (along with an extended LEPS<sup>13</sup> surface designed to mimic the saddle point region of the *ab initio* surface) in collinear quasi-classical trajectory calculations<sup>12,14</sup>. Diatomics-in-molecules surfaces have also been calculated for this reaction<sup>15-17</sup>, as well as for the reaction  $\text{Ca} + \text{HCl} \rightarrow \text{CaCl} + \text{H}$ <sup>18</sup>. Most recently, a three-dimensional potential energy surface for the  $\text{Be} + \text{FH}$  system has been calculated<sup>19</sup> and has been fit to a simple form in a three-dimensional quasi-classical trajectory calculation<sup>20</sup>.

In this work, quantum mechanical calculations are carried out on the collinear  $\text{Be} + \text{FH}$  reaction using the extended LEPS surface of Schor *et al.*<sup>12</sup>. This calculation was performed in two parts, the first being the calculation of reaction probabilities for  $\text{Be} + \text{FH}$ . Here the reaction probabilities and final energy distribution were examined as a function of the translational energy of the reagents. The effect of FH vibrational excitation ( $v = 0, 1$ ) on the reaction probabilities and on the vibrational energy distribution in the  $\text{BeF}$  product was examined and these results were then compared with the collinear quasi-classical calculation of Schor *et al.*<sup>12,14</sup>.

The second process of interest was the non-reactive vibrational deactivation of  $\text{BeF}$ :



For the above process total deactivation rates and their temperature dependencies were calculated. Also determined was whether deactivation occurred in 1-quantum or multi-quanta steps.

## B.2 Potential Energy Surface

The choice to employ the LEPS surface for this calculation was based on its simplicity and its availability. However, there exist some differences between the *ab initio* and the LEPS surfaces which should first be discussed.

The *ab initio* surface represents a set of discrete points which were interpolated using a 2-dimensional cubic spline. In Figure 1, the potential is shown in Delves mass weighted coordinates. There exist, however, many global fitting procedures which attempt to fit a potential surface of discrete points as a simple functional form<sup>15,21,22</sup>. Schor *et al.*<sup>12</sup> chose to approximate their *ab initio* potential using a LEPS fit as shown in figure 2. The LEPS is a simple valence-bond type surface which has been shown to give a remarkably good description of the  $F + H_2$  system<sup>23,24</sup>. The surface is easy to use for it employs few parameters to fit the entire surface outside of the asymptotic structural constants. The LEPS form requires 12 parameters: the three Morse parameters,  $D_e$ ,  $B$ , and  $r_e$  for each diatomic, taken from the literature values, and three Sato parameters to fit the potential such that the barrier height and location are the same on the LEPS as they are on the *ab initio* surface. These parameters are listed in Table I.

The LEPS and *ab initio* surfaces differ qualitatively in the following ways:

A) Even though both surfaces have their saddle points at extended geometries and have the same barrier height of 28 kcal, the minimal energy path on the LEPS surface curves smoothly up to it, while on the *ab initio* surface the approach is much more abrupt. As seen in Figure 3, the steepness in the rise to the saddle point for the LEPS potential is quite gradual.

**Table I****Parameters Used in LEPS Potential Surface<sup>12</sup>**

Parameter	HF	BeF	BeH
$D_e$ , kcal/mole	138.3	138.8	56.6
$R_e$ , a.u.	1.733	2.573	2.538
$\beta$ , a.u. <sup>-1</sup>	1.190	0.919	0.922
Sato parameter	-0.05	-0.06	-0.05

B) On the LEPS surface, because of the gradual rise to the saddle point, vibration is coupled very well to translation, yet on the *ab initio* surface they are very poorly coupled, a factor which might have an effect on the reaction dynamics.

C) The exoergicity of the LEPS surface is 0.5 kcal, while the exoergicity of the *ab initio* surface is 6.0 kcal. These differences point to the basic inflexibility of the LEPS surface. The success in the LEPS approximation in describing such systems like  $F + H_2$  stems from the fact that the system is covalent. In such a system where the two asymptotic regions smoothly rise to a saddle point, the LEPS will prove to be an adequate representation of the *ab initio* surface. However, in such a system as  $Be + FH$  where the system changes from a covalent to an ionic system as the reaction proceeds, the *ab initio* surface reflects the change in configuration as the nature of the bonding changes, while the LEPS cannot reproduce this.

Despite these differences, it is expected that, since the similarity in barrier height and channel width between the two surfaces is good, and since these characteristics should dominate the dynamics on the surface, a detailed quantum calculation on the LEPS surface will give results of a much more exact nature than the quasi-classical calculation<sup>12,14</sup> that have already been performed. As a result of comparison of these two separate results, any quantum effects on this LEPS surface will become that much more apparent.

### B.3 Calculation Parameters

The method used to calculate the collinear quantum reaction probabilities was the close-coupling propagation method of Kuppermann which has already been discussed in the literature<sup>25,26</sup>. In this method, the wavefunction is expanded in terms of a sum of a product of radial and vibrational wavefunctions. The calculation itself consists of solving this system of coupled differential equations. The results are then analyzed for unitarity. Poor unitarity occurs if the system has been inadequately described with respect to the number of basis functions, integration regions, step sizes, etc. The calculation is then optimized with respect to these numerical parameters. Eventually at high enough energy the approximation will break down due to lack of enough basis functions.

In this work, the translational energy regime was extended to 1.4 eV before the unitarity became unacceptable. This necessitated the use of between 24 to 27 basis functions for the higher energy points and 20 basis functions for the lower energy points. Unitarity for the whole calculation was better than 3 %, and at lower energy points having better unitarities. Once optimization of the calculation was completed, calculation of the entire energy regime took 27 hours of IBM 370/158 time. The positioning of the energy levels of HF and BeF is given in Table II where the common zero energy is the bottom of the HF well with the Be atom removed to infinity.

**Table II****Energy levels of HF and BeF in eV**

$v$	HF	BeF
0	0.28	0.075
1	0.77	0.23
2	1.24	0.38
3	1.69	0.53
4		0.68
5		0.82
6		0.97
7		1.11
8		1.28
9		1.39
10		1.52
11		1.66

## B.4 Results & Discussion

### B.4.1 $\text{Be} + \text{FH} (v) \rightarrow \text{BeF} (v') + \text{H}, v = 0, 1$

The collinear quasi-classical trajectory calculations of Schor *et al.*<sup>12,14</sup> display reaction probabilities which rise extremely sharply from threshold to unity, and which do not decrease with increasing energy in the range of energies studied. The dynamical threshold translational energies for the  $\text{Be} + \text{FH}(v) \rightarrow \text{BeF}(\text{all}) + \text{H}$  reaction is 1.06 eV for  $v = 0$  and 0.80 for  $v = 1$ . The exact quantum curves also rise from 0 to 1. The corresponding curves have a sigmoid shape, achieving the value of 0.01 at translational energies of 0.98 eV and 0.75 eV for  $v = 0$  and  $v = 1$ , respectively, and a value of 0.99 at 1.18 eV and 0.90 eV, respectively. Over the translational energy range of 1.23 eV to 1.5 eV the  $v = 0$  probability drops from 1.00 to 0.97 whereas the quasi-classical one remains equal to 1.00. These classical and quantum results for the same system are shown in Figure 4, in which the total reaction probability is plotted against reagent translational energy for  $\text{FH} (v = 0, 1)$ .

In summary, the quantum results for  $\text{FH} (v = 0)$  differ from the quasi-classical ones in that the reaction probabilities rise more gradually to unity with increasing energy, and then decrease slightly at higher energies. For  $\text{FH} (v = 1)$  the quantum mechanical probabilities rise more rapidly to unity than they do for  $\text{FH} (v = 0)$ . The phenomenological thresholds (defined as the translational energy at which the reaction probability equals 0.01) calculated in the quantum mechanical calculation were slightly lower than those in the trajectory calculations.

The difference between the quantum phenomenological thresholds for the  $v = 0$  and  $v = 1$  reactions is 0.23 eV. Since the spacing of these two vibrational

levels is approximately 0.49 eV, and the threshold reduction is only 0.27 eV, one sees that HF vibrational excitation is only partially (47 %) effective in promoting reaction. Such relative inefficiency is not too surprising given that the configuration of the saddle point is more similar to that of the reagents than that of the products. where the minimum energy path is still fairly narrow. Vibrational enhancement of reaction in this system is only slightly more than in the reaction



in which excitation of HF to  $v = 1$  was calculated to give a 0.22 eV reduction in the threshold to reaction<sup>27</sup>.

The disposal of energy in the products also shows both similarities and differences between the quasi-classical and quantum mechanical calculations. In Figure 5 the fraction of available energy going into product vibration ( $f_{\text{vib}}$ ) as a function of reagent translational energy is shown for these calculations. Both indicate that this fraction is approximately 0.35 for ground state reagents. For FH ( $v = 1$ ), both treatments furnish values of  $f_{\text{vib}}$  near 0.45 in the 0.9 to 1.00 eV translational energy range, although the quantum mechanical results start falling rapidly with decreasing energy at slightly higher energies.

Pronounced differences were observed between the BeF product vibrational state distribution in the two calculation, however. Histogram plots of these distributions at selected energies for ground (Figure 6 & 7) and vibrationally excited (Figure 8 & 9) states show these differences clearly. For  $v = 0$ , the quasi-classical distributions have sharp lower and upper cut-offs, whereas the quantum ones have a more gaussian-like shape. For  $v = 1$ , both the quasi-classical and quantum results are quite broad; the quasi-classical ones are slightly bimodal whereas the quantum ones are very clearly bimodal.

Bimodal distribution of product vibrational states have been seen in other

collinear quantum mechanical systems<sup>28-30</sup>, primarily in light-heavy-heavy (L-H-H) systems such as



Quasi-classical trajectory calculations have been seen to display less structure in their product state distributions<sup>31</sup>, as has also been observed here. Bimodal vibrational state product distributions have not been observed experimentally in these systems, although unusual distributions differing substantially from standard unimodal ones have been observed<sup>32,33</sup>. Recent work in converting one-dimensional probabilities to three-dimensional ones suggest that with properly energy- and state-selected reagents, bimodal vibrational state product distributions might well be observable in the three-dimensional world<sup>34</sup>.

As has been discussed previously<sup>35-37</sup>, the bimodal product-state distribution in the quantum-mechanical calculations is due to a Franck-Condon reflection pattern, where the state-to-state reaction probabilities have a close correspondence to the probability density distribution of the vibrationally excited reagent. Classically, one may interpret the bimodal product state distribution for  $v = 1$  reagents to be due to two different types of trajectories. The high vibrational state products come from trajectories. One type samples the repulsive wall at small values of  $R_\alpha$  and gives rise to high vibrational state products, whereas the other passes from the reagent to the product region leaving the saddle point to its left and producing lower vibrational energy products (see Figure 1). The latter type of trajectory does not occur for  $v = 0$  because for ground state reagents only the region of configuration space close to the minimum energy path is explored. These two regions are indicated as the shaded areas in Figure 10. As a result the  $v = 0$  reagent produces a unimodal product distribution corresponding to the one pathway available.

Summarizing these results:

1) Vibrational energy is only moderately (just under 50%) effective in promoting reaction.

2) Quantum mechanical and quasi-classical trajectory calculations give approximately equal values of the fraction of available energy going into product vibration (0.35 for  $v=0$ , 0.45 for  $v=1$ ), but the details of the product distributions differ markedly.

3) A bimodal BeF vibrational state distribution has been obtained for the vibrationally excited ( $v=1$ ) reagents. Similar distributions have been seen for L + HH reactions, the reverse of the H + HL reaction being considered here. A dynamical justification for this result is suggested.

#### B.4.2 $\text{BeF}(v) + \text{H} \rightarrow \text{BeF}(v') + \text{H}, v > v'$

Because of the unusual dynamics which the  $\text{BeF} + \text{H}$  surface had demonstrated we also examined the non-reactive vibrational deactivation of  $\text{BeF}$  in a collinear collision with  $\text{H}$ . Figure 11 shows the deactivation rate vs. initial vibrational energy for three different temperatures. At higher vibrational energies the rate of deactivation levels out to a constant value. This same effect is observed in Figure 12 where the activation energy for deactivation becomes lower for a higher initial vibrational energy. These results indicate that a higher initial vibrational state, sampling a much steeper portion of the potential, gives rise to a faster deactivation rate. As a result, since the vibrational spacing for  $\text{BeF}$  is small, there is little difference between high adjacent vibrational states, and the deactivation rate begins to approach a constant value for highly vibrationally excited  $\text{BeF}$ . In both these examples, the expected temperature dependence is observed; that is, at high temperatures, the deactivation rate increases and the activation energy decreases.

Because of the steepness of the barrier it is of interest to see if the vibrational deactivation occurs in 1-quantum or multi-quanta steps. To distinguish between these two processes, the rate for 1-quantum vibrational deactivation was calculated. Figure 13 shows the ratio of this rate with the rate for total deactivation as a function of temperature for several vibrational states. The results show that for a low vibrational state at a low temperature the process is almost exclusively 1-quantum deactivation, while at high temperature and high vibrational state the deactivation may be partially described as a multi-quanta deactivation.

## B.5 Future Work

Additional calculations are planned to include the exact quantum calculation on the *ab initio* potential surface. Future work could also include the streamlines and probability current densities for the LEPS surface. If the dynamical argument for the observed bimodality of the vibrational state distribution of BeF is correct, then the streamlines will convincingly show these two different pathways.

The calculations reported were performed on the IBM 370/158 computer at Ambassador College, Pasadena, California, for which we express our appreciation.

**B.6 References**

1. H. W. Cruse, P. J. Dagdigian, and R. N. Zare, *Faraday Disc. Chem. Soc.*, **55**, 277 (1973).
2. J. G. Pruett and R. N. Zare, *J. Chem. Phys.*, **64**, 1774 (1976).
3. Z. Karny and R. N. Zare, *J. Chem. Phys.*, **68**, 3360 (1978).
4. A. Torres-Filho and S. G. Pruett, *J. Chem. Phys.*, **72**, 6736 (1980); **72**, 740 (1982).
5. A. Gupta, D. S. Perro, and R. N. Zare, *J. Chem. Phys.*, **72**, 6237 (1980); **72**, 6250 (1980).
6. A. Siegel and A. Schultz, *J. Chem. Phys.*, **72**, 6227 (1980).
7. Z. Karny, R. C. Estler, and R. N. Zare, *J. Chem. Phys.*, **69**, 5199 (1978).
8. C.-K. Man and R. C. Estler, *J. Chem. Phys.*, **75**, 2779 (1981).
9. R. A. Altkorn, F. E. Bartoszek, J. DeHaven, G. Hancock, D. S. Perry, and R. N. Zare, *Chem. Phys. Lett.*, **98**, 212 (1983).
10. U. Brinkmann and H. Telle, *J. Phys. B.*, **10**, 133 (1977).
11. F. Engelke and K. H. Meiwes-Broer, *Chem. Phys. Lett.*, **108**, 137 (1984).
12. H. Schor, S. Chapman, S. Green, and R. N. Zare, *J. Chem. Phys.*, **69**, 3790 (1978).
13. P. J. Kuntz, E. M. Nemeth, J. C. Polanyi, S. D. Rosner, and C. E. Young, *J. Chem. Phys.*, **44**, 1168 (1966).

14. H. Schor, S. Chapman, S. Green, and R. N. Zare, *J. Phys. Chem.*, **83**, 920 (1979).
15. P. J. Kuntz and A. C. Roach, *J. Chem. Phys.*, **74**, 3420 (1981).
16. A. C. Roach and P. J. Kuntz, *J. Chem. Phys.*, **74**, 3435 (1981).
17. J. L. Schreiber and P. J. Kuntz, *J. Chem. Phys.*, **76**, 1872 (1982).
18. A. D. Isaacson and J. T. Muckermann, *J. Chem. Phys.*, **73**, 1729 (1980).
19. S. Chapman, M. Dupuis, and S. Green, *Chem. Phys.*, **78**, 93 (1983).
20. S. Chapman, *J. Chem. Phys.*, **81**, 262 (1984).
21. F. O. Ellison, *J. Am. Chem. Soc.*, **85**, 3540 (1963).
22. J. C. Tully, *J. Chem. Phys.*, **58**, 1396 (1977).
23. J. T. Muckermann, *J. Chem. Phys.*, **56**, 2497 (1972).
24. C. F. Bender, P. K. Pearson, S. V. O'Neil, and H. F. Schaefer, *J. Chem. Phys.*, **56**, 4626 (1972).
25. G. C. Schatz, J. M. Bowman, and A. Kuppermann, *J. Chem. Phys.*, **63**, 674 (1975).
26. A. Kuppermann, in *Theory of Scattering: Papers in Honor of Henry Eyring, Theoretical Chemistry Advances and Perspectives*, **6A**, Academic Press, New York (1981), and references therein.
27. J. A. Kaye, Ph.D Thesis, California Institute of Technology, 1982.
28. J. N. L. Connor, W. Jakubetz, and J. Manz, *J. Chem. Phys.*, **63**, 674 (1970).
29. J. K. C. Wong and P. Brumer, *Chem. Phys. Lett.*, **68**, 517 (1979).

30. J. N. L. Connor, W. Jakubety, A. Laganá, J. Manz, and J. C. Whitehead, *Chem. Phys.*, **65**, 29 (1982).
31. J. N. L. Connor, J. C. Whitehead, W. Jakubety, and A. Laganá, *Nuovo Cimento*, **63B**, 459 (1981).
32. A. M. G. Ding, L. J. Kirsch, D. S. Perry, J. C. Polanyi, and J. L. Schreiber, *Faraday Disc. Chem. Soc.*, **55**, 252 (1973).
33. B. Hildebrandt, H. Vanni, and H. Heydtmann, *Chem. Phys.*, **84**, 125 (1984).
34. W. Jakubetz, *Chem. Phys.*, **88**, 271 (1978).
35. D. R. Herschbach, *Faraday Disc. Chem. Soc.*, **55**, 233 (1973).
36. M. S. Child, *Mol. Phys.*, **35**, 759 (1978).
37. M. S. Child and K. B. Whaley, *Faraday Disc. Chem. Soc.*, **67**, 479 (1979).

## B.7 Figures and Captions

Figure 1. Contour plot of the *ab initio* potential energy surface for the collinear Be + FH reaction in Delves' scaled coordinates. The solid curves are equipotential contours spaced each by 0.2 eV taking the bottom of the FH well as the zero of energy. The dashed contours designate a negative energy with respect to the bottom of the FH well.

Figure 2. Contour plot of the LEPS potential energy surface for the collinear Be + FH reaction in Delves' scaled coordinates. The solid curves are equipotential contours spaced by 0.2 eV taking the bottom of the FH well as the zero of energy.

Figure 3. Schematic diagram of the potential energy function characteristics along the minimum energy path in Delves' coordinate space. The distance is measured along that path from the saddle point configuration, and  $V(s)$  is the corresponding potential energy. The horizontal lines indicate the vibrational energy levels of the bound states of the isolated diatoms.

Figure 4. Total Reaction probabilities for the reaction  $\text{Be} + \text{FH}(v) \rightarrow \text{BeF}(v = \text{all}) + \text{H}$ , as a function of reagent translational energy for the diatom reagent in its ground and first vibrationally excited states. The arrow on the abscissa indicates the energy of the barrier top with respect to the  $v = 0$  HF state. That with respect to HF ( $v = 1$ ) lies at 0.44 eV.

Figure 5. Energy disposal of the product for  $\text{Be} + \text{FH}(v) \rightarrow \text{BeF}(v') + \text{H}$ . Plotted is the percent product vibrational energy as a function of reagent translational energy for the diatom reagent in its ground and first vibrationally excited states. Open symbols represent the quasi-classical

trajectories of Schor *et al.*<sup>12</sup>, while the solid symbols represent the exact quantum treatment of this work.

Figure 6 & 7. Distribution among product vibrational levels for  $\text{Be} + \text{FH}(v = 0) \rightarrow \text{BeF}(v') + \text{H}$  for selected translation energies shown. Open bars represent the quasi-classical trajectories of Schor *et al.*<sup>12</sup>, while the solid bars represent the exact quantum treatment of this work.

Figure 8 & 9. Distribution among product vibrational levels for  $\text{Be} + \text{FH}(v = 1) \rightarrow \text{BeF}(v') + \text{H}$  for selected translation energies shown. Open bars represent the quasi-classical trajectories of Schor *et al.*<sup>12</sup>, while the solid bars represent the exact quantum treatment of this work.

Figure 10. Contour plot of the LEPS potential energy surface for the collinear  $\text{Be} + \text{FH}$  reaction in Delves' scaled coordinates. The solid curves are equipotential contours spaced by 0.2 eV taking the bottom of the FH well as the zero of energy. Contours corresponding to the isolated diatom FH in its ground and first vibrationally excited states are shown.

Figure 11. Total vibrational deactivation rate as a function of initial vibrational state of BeF and translation temperature.

Figure 12. Activation energy for the deactivation of vibrationally excited BeF as a function of initial vibrational state of BeF. Circles represent the low temperature regime (200-400K) while squares represent the high temperature regime (700-1000K).

Figure 13. Ratio of  $k_{v \rightarrow v-1}$  vs.  $k_{deact}$  as a function of inverse temperature for a variety of initial vibrational energies for BeF.  $k_{v \rightarrow v-1}$  is the rate for the 1-quantum non-reactive deactivation of BeF, while  $k_{deact}$  is the total vibrational deactivation rate.

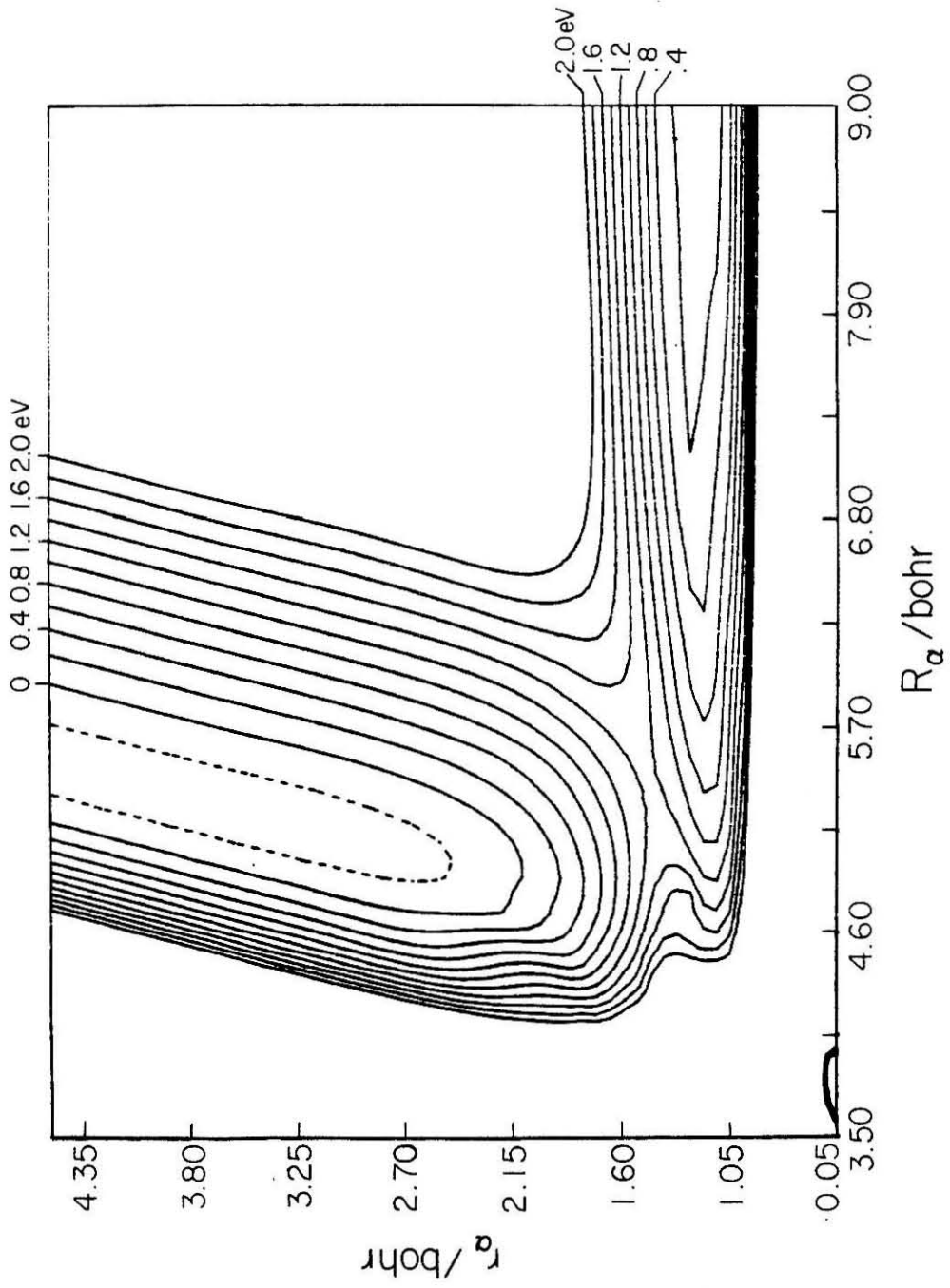


Figure 1

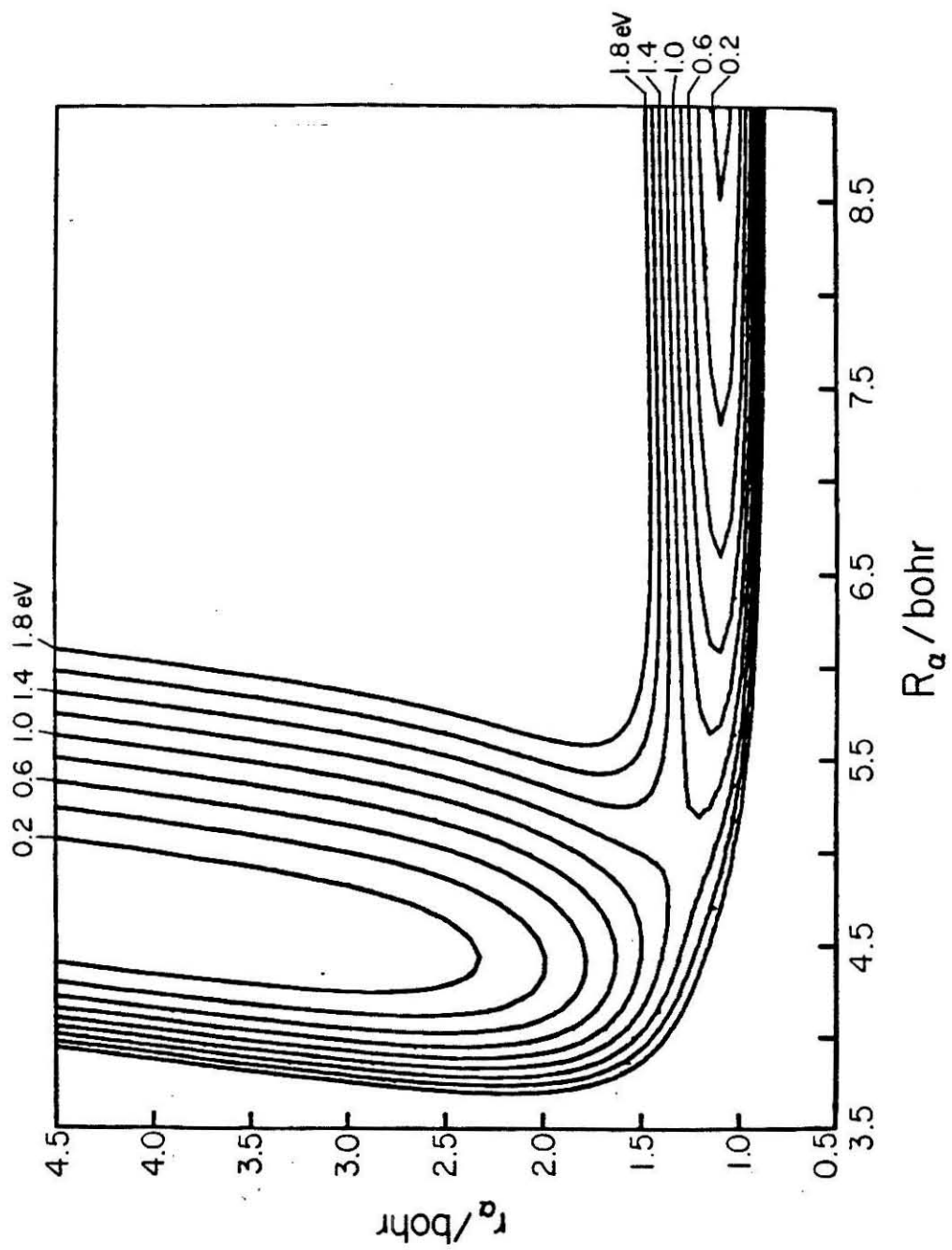


Figure 2

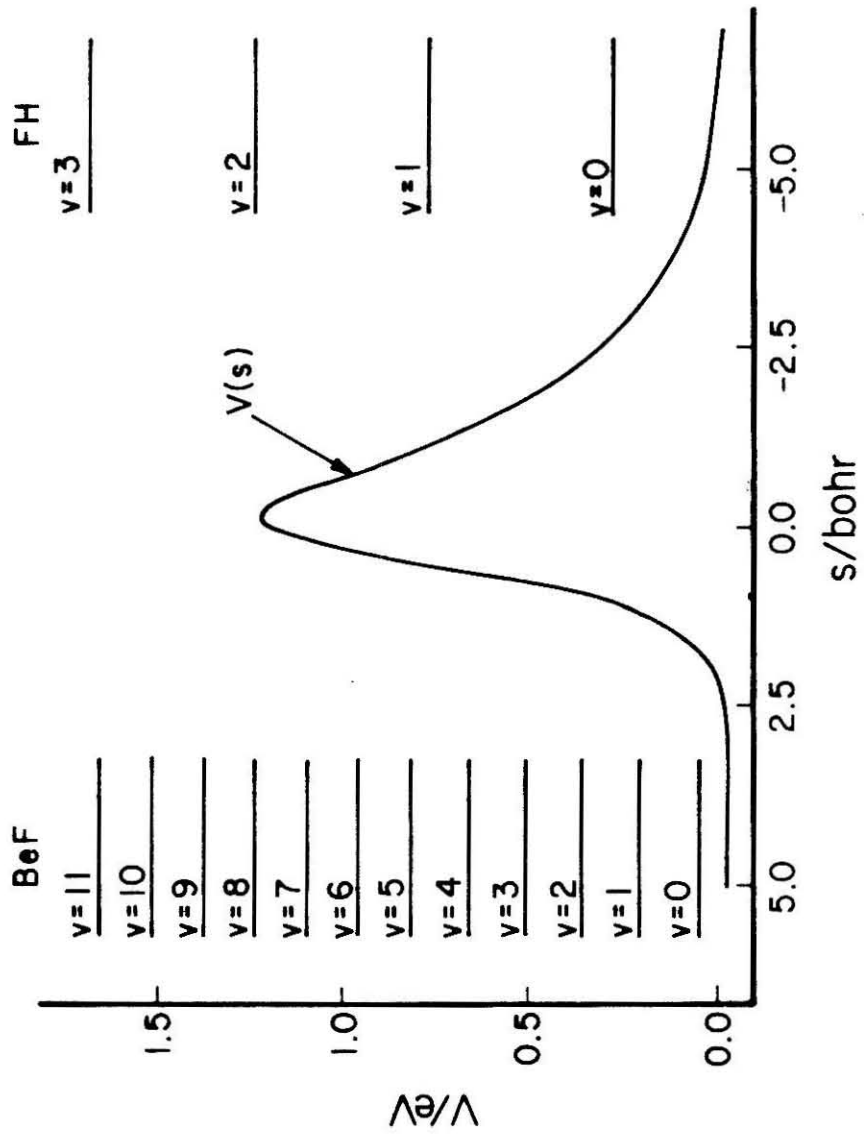


Figure 3

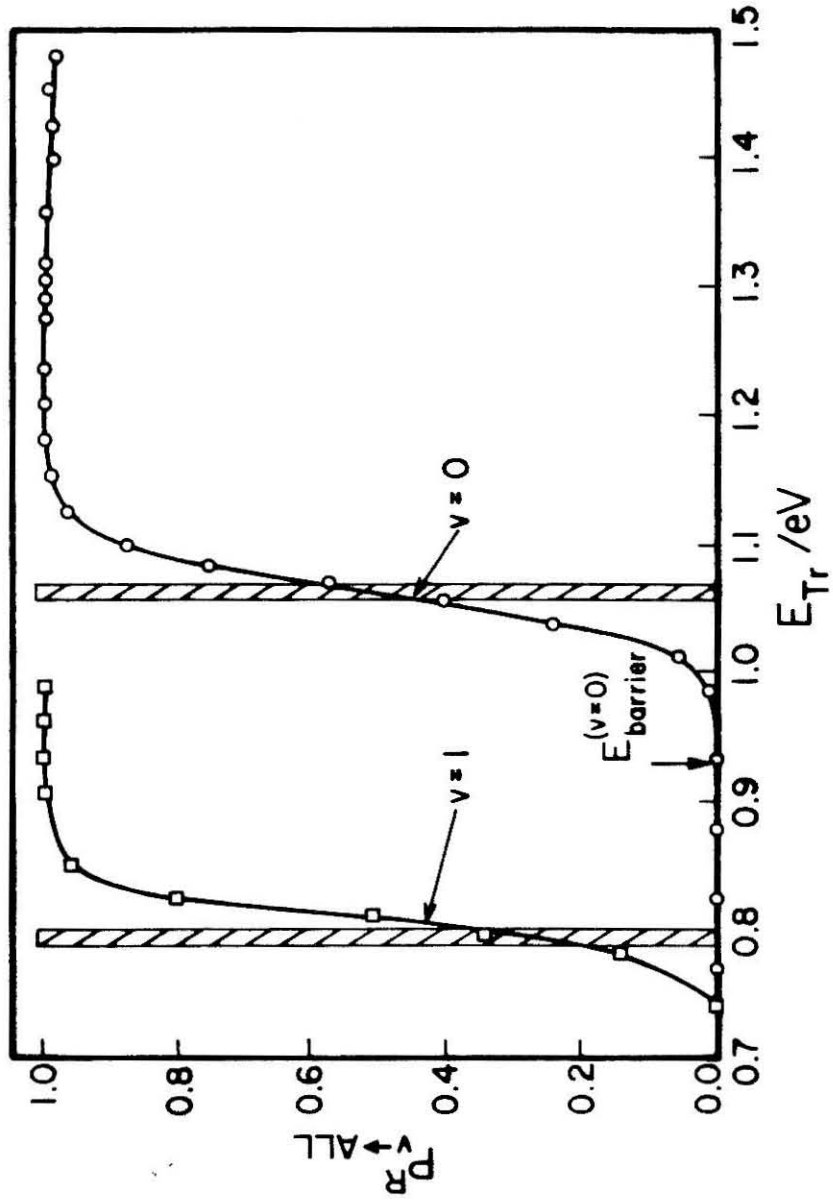


Figure 4

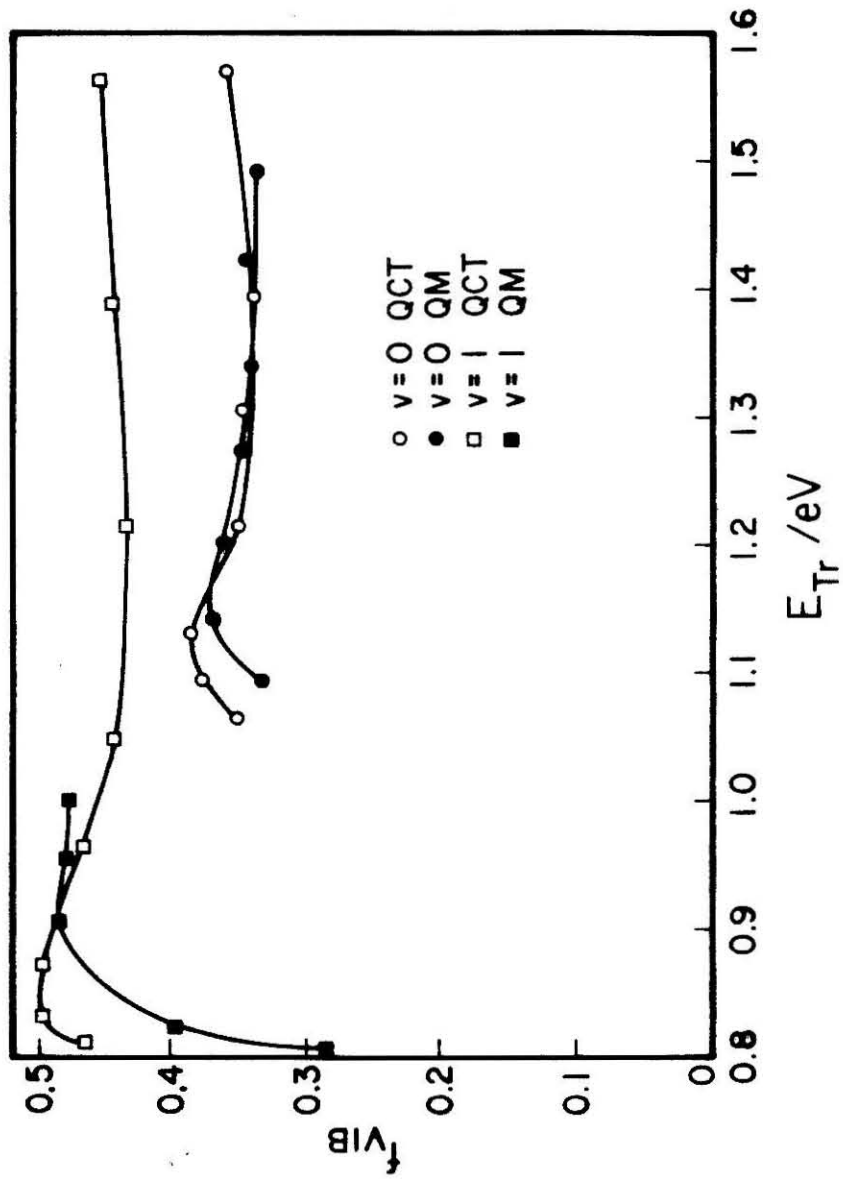


Figure 5

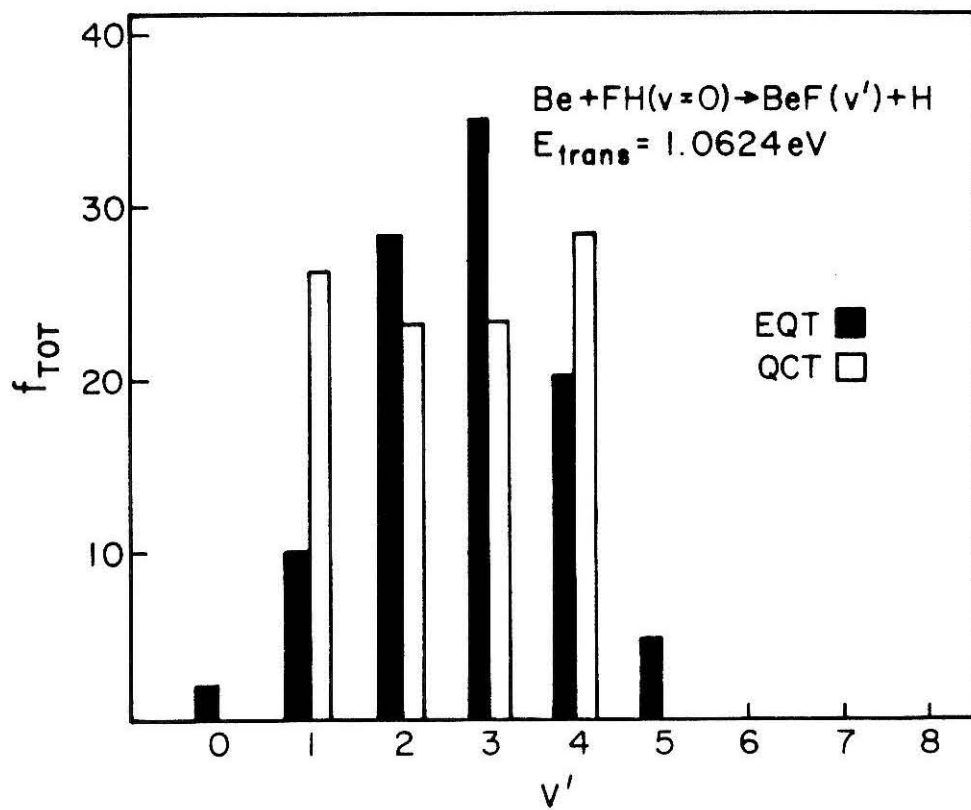


Figure 6

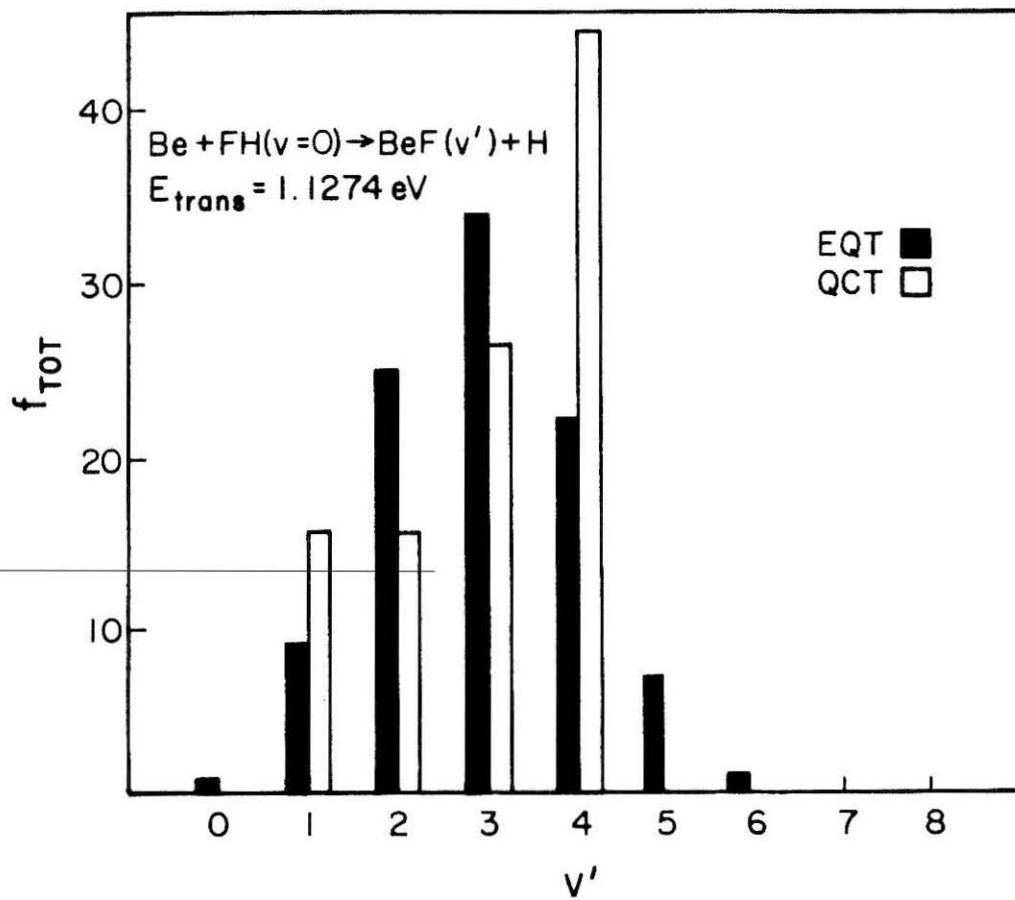


Figure 7

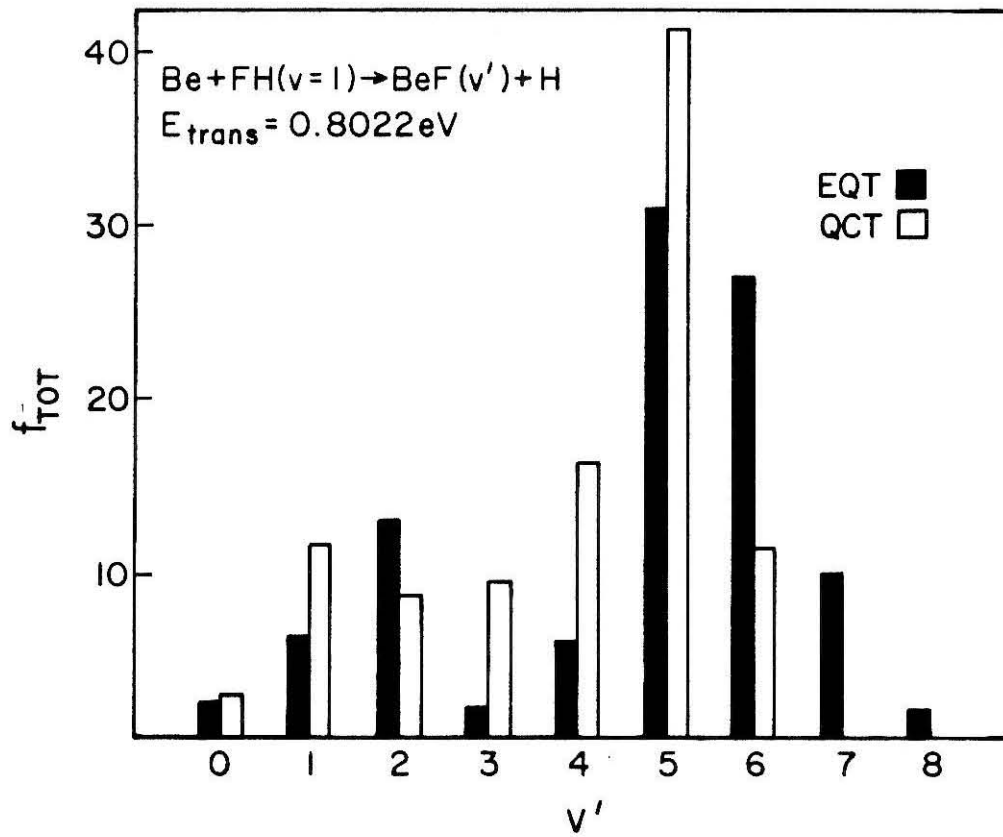


Figure 8

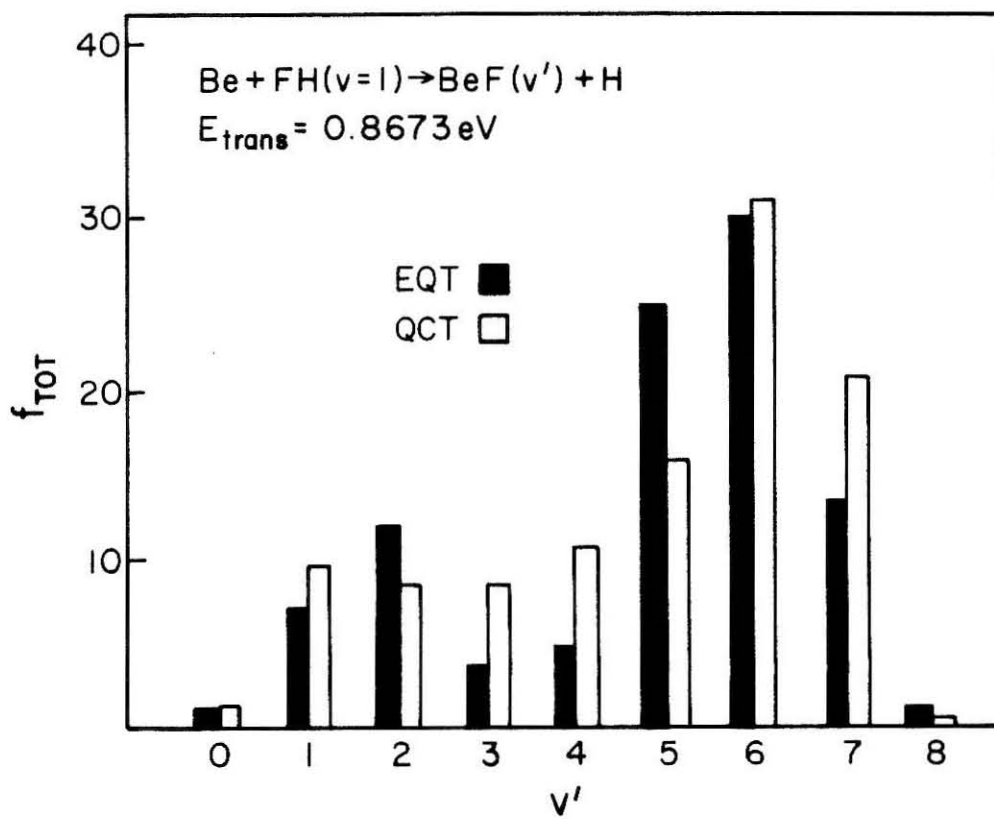


Figure 9

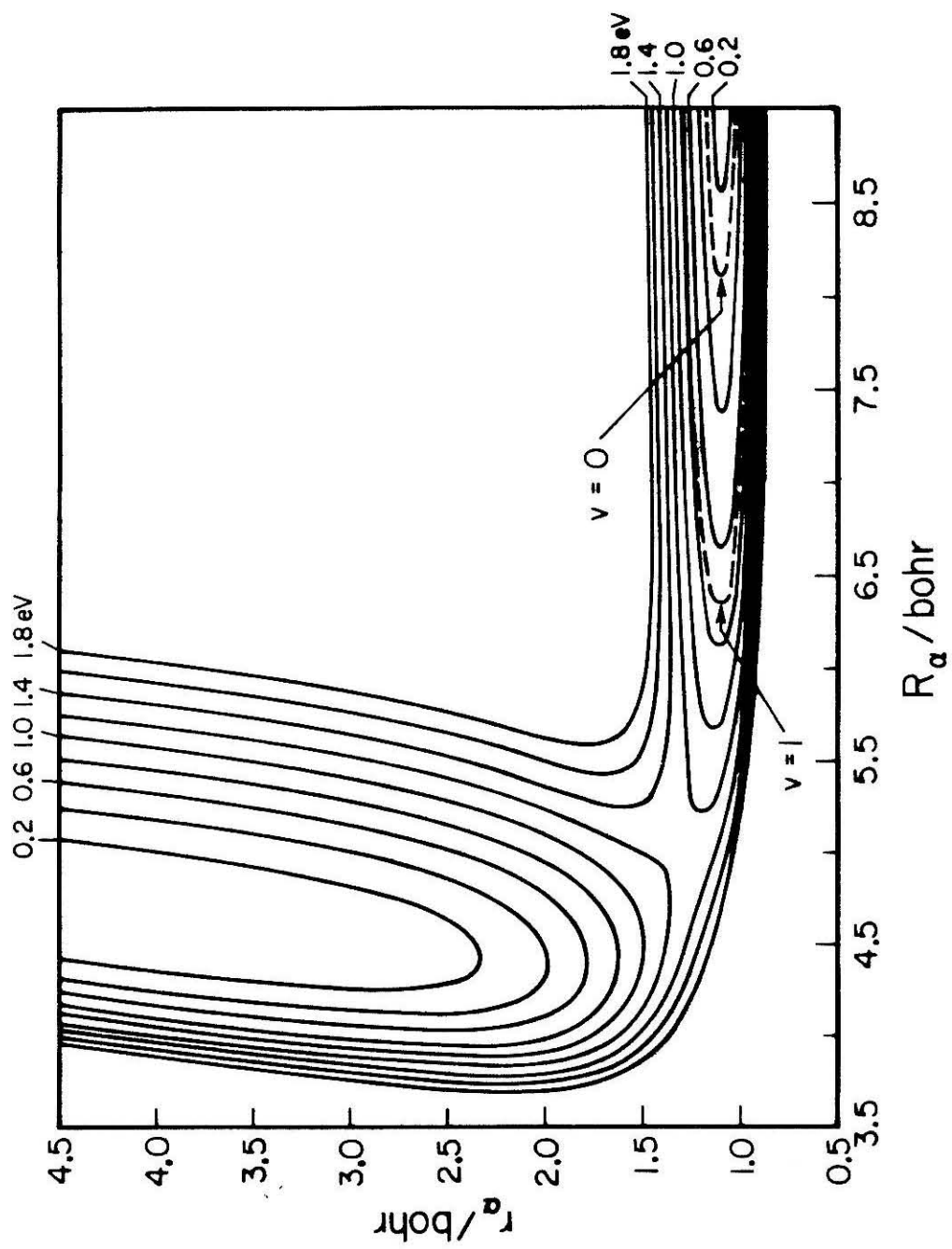


Figure 10

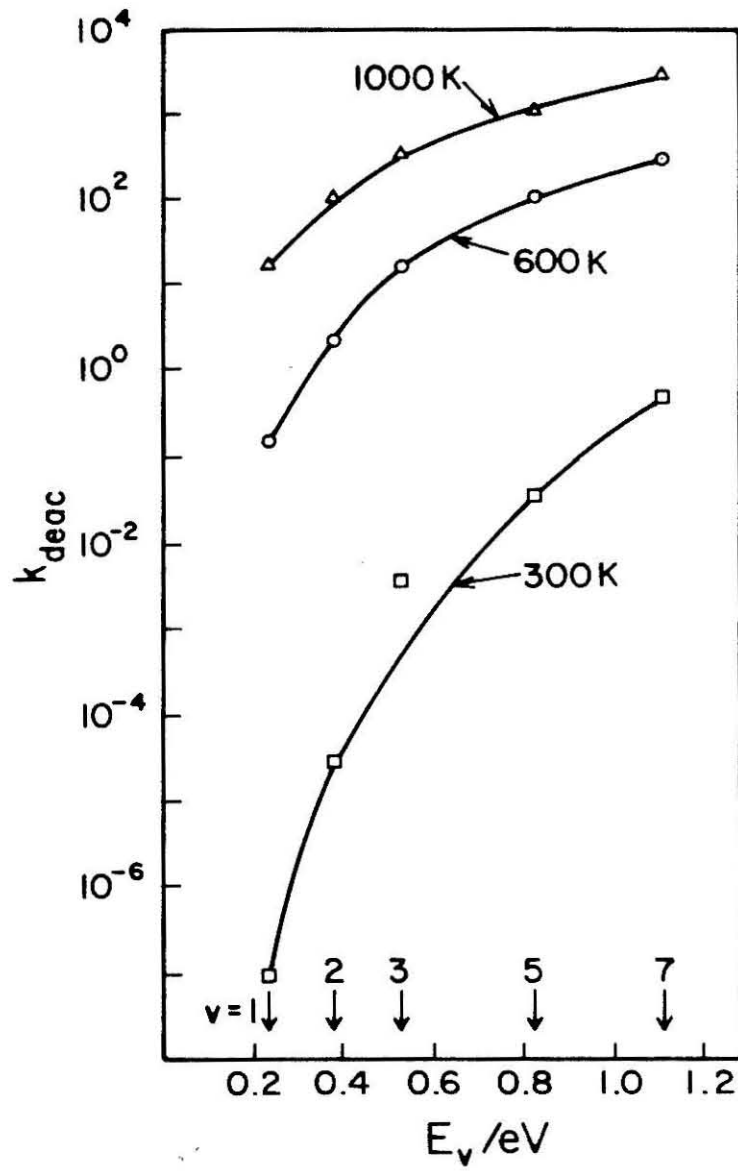


Figure 11

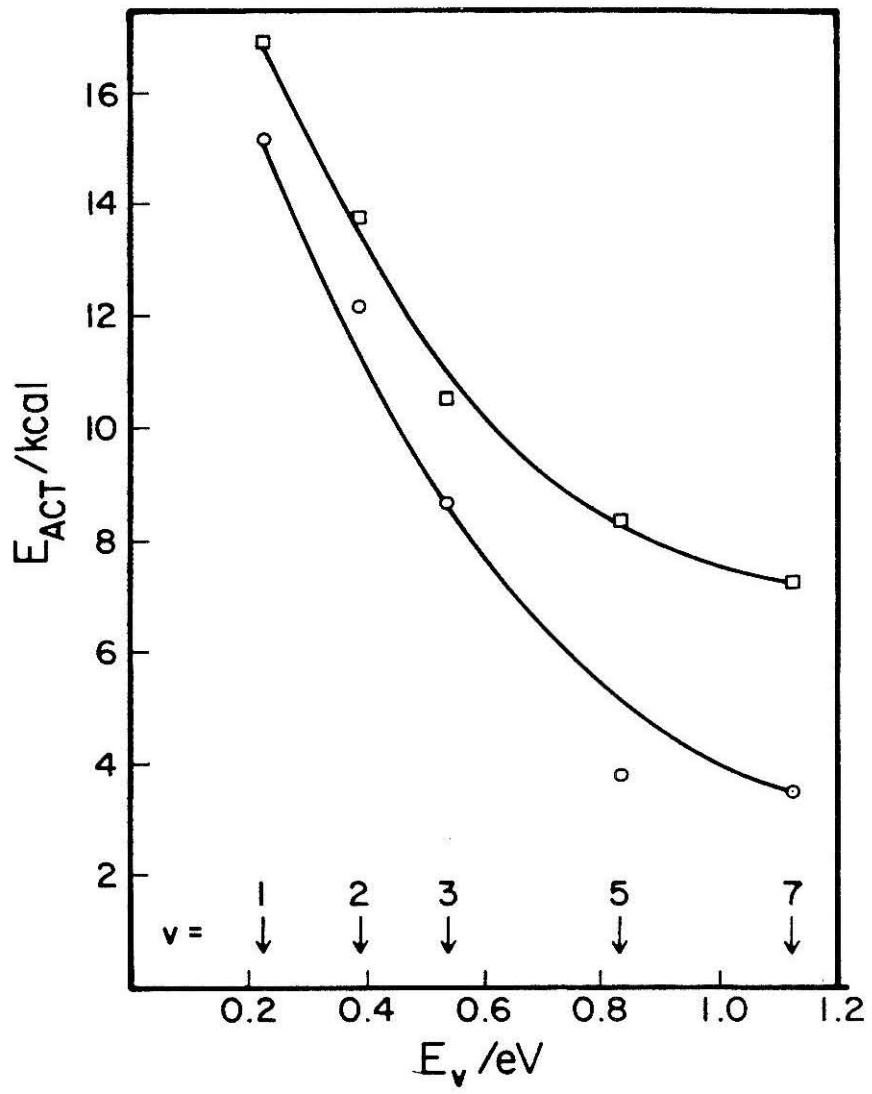


Figure 12

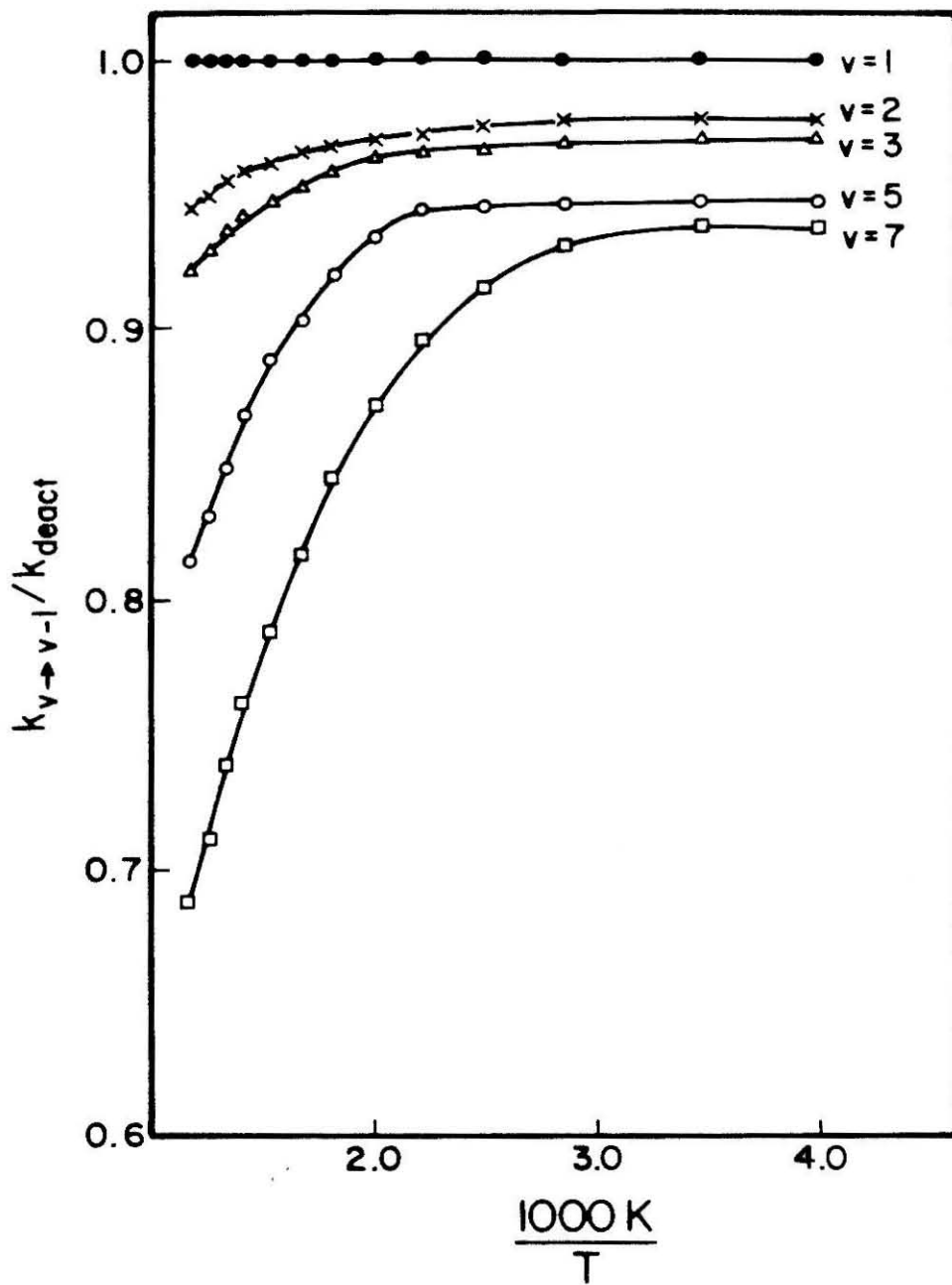


Figure 13

**PROPOSITION I:** Investigation of  $\text{H} + \text{H}_2$  Reaction Dynamics as a Function of Collision Energies Using Sychrotron Radiation

**Abstract:** Recently experiments have been performed which can determine the HD product internal state distribution formed by the reaction of fast H atoms with thermal  $\text{D}_2$  molecules. This is accomplished by irradiating a mixture of HI and  $\text{D}_2$  with a 266 nm laser pulse to dissociate the former, creating hydrogen atoms with a center-of-mass energy of  $\sim 1.30$  eV. It is proposed to repeat this experiment by using synchrotron radiation to dissociate the HI as well as to probe for the HD product. The tunability of the synchrotron radiation will allow probing the  $\text{H} + \text{D}_2$  dynamics as a function of translational energy of the reactant. The results will then allow detailed comparision with quantal calculations

The reaction of H with H<sub>2</sub>, the simplest bimolecular reaction involving neutral reagents, has been the subject of extensive investigation. Beginning with the early efforts of London, Eyring, and Polanyi<sup>1,2</sup> the reaction has been the focus of many theoreticians<sup>3,4</sup>. As a result, the system is the most accurately known<sup>5</sup> and is one of the few systems which has been treated exactly in three dimensions<sup>6-9</sup>.

Despite the over 50 years of theoretical investigation on this system there have been very few experiments performed. To date there have only been three molecular beam experiments which have been reported<sup>10-12</sup>. These experiments have been plagued by three basic problems. The first is that the reaction requires a large activation energy ( $\sim 0.33$  eV) such that to generate products the reactants will have to be moving quite fast. The second major problem is that the reaction cross section is quite low ( $\sim 1 \times 10^{-16}$  cm<sup>2</sup>) thus product yields will be low. Lastly, the reaction product, H<sub>2</sub>, is difficult to detect, especially in a quantum-state-specific manner.

It has only been recently that two groups independently have performed experiments which appear capable of measuring the internal state distributions for the H + D<sub>2</sub> system<sup>13-15</sup>. Both experiments have employed a laser-photolysis of HI to produce fast hydrogen atoms which react quickly with D<sub>2</sub> which is also present in the cell. The HD product is then detected by sensitive nonlinear spectroscopic techniques to determine the quantum state distribution for the HD product. Gerrity and Valentini<sup>13</sup> have used coherent anti-Stokes Raman spectroscopy (CARS) while Rettner, Marinero, and Zare<sup>14,15</sup> have employed multiphoton ionization (MPI).

Both generated their fast H atoms by photolyzing hydrogen iodide with the fourth harmonic of a Nd:YAG laser at 266 nm. A major problem with this generation is that at this wavelength there are two channels possible for

the HI;  $H + I (^2P_{3/2})$  and  $H + I (^2P_{1/2})$  with a  $\sim 2 : 1$  ratio of 'fast' to 'slow' H atoms<sup>16-19</sup>. The HD reaction products are then detected by two-photon resonance ( $X ^1\Sigma_g^+(v=0) \rightarrow E, F ^1\Sigma_g^+(v=0)$ ) three-photon ionization using tunable radiation in the 200-226 nm range. This is accomplished by using a YAG-pumped frequency-doubled dye laser which is then passed through a Raman shifter. This probe pulse is synchronized to the photolysis laser at a variable delay time ( $\sim 5 - 25$  ns). The timing between the photolysis and probe pulse is essential since any rotational relaxation of the HD during this delay would give a faulty final state distribution.

There are several limitations with this experiment. The biggest difficulty is that it is limited to a single collision energy. As a result this limits the amount of comparison which can be made with already existing theory. As has been shown by Schatz and Kuppermann<sup>20</sup> in their three dimensional calculation (for  $j = 0$ ), the first resonance which appears for the  $H + H_2$  system is at 0.975 eV with a 0.035 eV width. It would then be of great interest to perform this experiment in this energy region and see if these dynamical resonances could be observed.

It is proposed to extend this technique to a variety of collision energies by using the tunable radiation from a synchrotron source as the radiation for the photolysis of HI. The kinetic energy (in the lab coordinate frame) of the H atom produced by photolysis of a molecule HX is given by

$$E_t = \frac{(m_X)}{(m_{HX})} \times [hv - D_o(H - X) + E_{int}(HX) - E_{int}(X)]$$

where  $hv$  is the energy of the incident photons,  $D_o$  is the bond dissociation energy and  $E_{int}$  is the internal energy (including electronic excitation). For the case of HI  $D_o$  is 3.054 eV<sup>21</sup> and the energy for the transition  $I (^2P_{3/2} \rightarrow ^2P_{1/2}) = 0.943$  eV<sup>22</sup>. By having a source of tunable radiation, changing the frequency

of the photolysis pulse enables one to change the translational energy of the hydrogen atom produced.

A synchrotron is an ideal source for this radiation. Synchrotron radiation is emitted by charged particles moving circular orbits with highly relativistic velocities. The source gives off continuous radiation from the infrared to the X-ray region with pulse lengths which can go as low as 100 ps and with a repetition rate of usually 50 Hz <sup>23</sup>.

The major consideration of this experiment is whether there will be sufficient intensity from the synchrotron such that HI will be dissociated to a reasonable extent. If not, there may be too little HD generated to be observed. In the experiment of Marinero and co-workers<sup>14,15</sup> a 266 nm pulse of 10 mJ energy and 5 ns duration with 10 Hz repetition rate was used. This corresponds to approximately  $10^{17}$  photons per second. The synchrotron ring at Stanford (SPEAR) as of December 1979 is capable of currents of 300 mA though some European synchrotrons are capable of currents as high as 500 mA<sup>24</sup>. From this current we can expect  $3 \times 10^{14}$  photon  $s^{-1}$   $\text{\AA}^{-1}$   $\text{mrad}^{-1}$ .<sup>25</sup> Though this is some three orders of magnitude lower than used in the Marinero and co-workers experiment<sup>14,15</sup> it should be sufficient. Recently in our lab G. Parker <sup>26</sup> has shown that the experiment should be possible at  $10^{14}$  photons  $s^{-1}$ . Even if the intensity of the synchrotron is not sufficient it can be increased by using a multiple pass cell. It also can be increased by using a larger spectral bandwidth to dissociate the HI. By having a bandwidth of  $5\text{\AA}$  this will create an energy spread of  $\sim .03$  eV in the translational energy of the hydrogen atoms produced which is an acceptable decrease in the resolution. As a result we can expect that there will be sufficient hydrogen atom intensity with a tunable translational velocity of acceptable resolution.

The experiment will be performed as follows. The radiation from the

synchrotron will be split into two beams<sup>27</sup>, which will both be passed into separate monochromators<sup>28</sup>. The first monochromator will act as the pulse beam such that the frequency setting will correspond to a translational energy for the hydrogen atom generated. It will then pass into the gas cell containing D<sub>2</sub> and HI.

The second beam will act as a probe beam to multi-photon ionize the HD product and will serve to probe the product state distribution. In fact, using the synchrotron radiation for the probe will have several advantages over the laser radiation used by Marinero and co-workers<sup>14,15</sup>. It is important to delay the pump pulse with respect to the probe pulse by a short period of time to prevent rotational relaxation of the HD product with the bulk. With the Marinero and co-workers experiment<sup>14,15</sup> the best they could accomplish was a delay of  $\sim 5$  ns. In this synchrotron experiment the delay can be varied to as small a time as desired. This is due to the fact that since the pump and probe pulse radiate at the same source, they can be made to arrive at the reaction vessel at different times by having them travel different path lengths. By making the probe pulse travel a path length 1.5 m longer than the pump pulse, it will arrive at the reaction cell 5 ns after the pump pulse. By simply changing the path length the delay time will likewise be changed. As a result, this experiment will provide an important check of the Marinero and co-workers experiment<sup>14,15</sup>. By repeating their conditions but using a shorter delay time, any observed change in the final state distribution of the products means that they must have had some relaxation of the HD product in their experiment.

An additional advantage may be in the intensity of the synchrotron radiation. Their radiation was generated by a hydrogen Raman cell output which emitted  $\sim 10^{15}$  photons s<sup>-1</sup>. The intensity of the probe pulse from the

synchrotron will be equal to if not greater than the Raman cell output. If this is the case it will enhance the sensitivity of the measurement of the HD.

Lastly, if the HD signal intensity of this experiment should prove small it will be possible to raise the pressure of HI and D<sub>2</sub> in the cell. This is possible because we can make the delay time as short as we like. As a result, we can increase the pressure so there will be more collisions and more reaction, but we can also probe more quickly thus eliminating the chance of rotational deactivation of the product.

If this experiment proves successful it will prove to be a very powerful tool to probe H + D<sub>2</sub> reaction dynamics and possibly resonance phenomena as well. After the initial experiment is done with HI and D<sub>2</sub> it may prove advantageous to use a different molecule to generate the hydrogen atoms. Photolysis of HBr has been predicted to produce only Br atoms in the  $^2P_{3/2}$  state<sup>29</sup>. However, experiments have now shown that a small fraction of the Br atoms ( $\sim 0.15$ ) are in the  $^2P_{3/2}$  state<sup>30</sup> where the energy gap<sup>31</sup> between this and the ground state is  $\sim 3685 \text{ cm}^{-1}$ . We therefore see that the HBr when dissociated produces a smaller number of spin-orbit excited halogen atoms than HI. As a result the H atom spectrum of translational energies for HBr will be less bimodal than in the HI case.

**References**

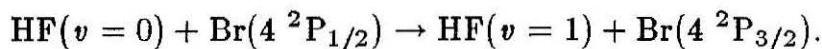
1. F. London, *Z. Elektrochem*, **35**, 552 (1929).
2. H. Eyring and M. Polanyi, *Z. Phys. Chem. Abt. B*, **12**, 279 (1931).
3. D. G. Truhlar and R. E. Wyatt, *Annu. Rev. Phys. Chem.*, **27**, 1 (1976).
4. M. Baer, *Adv. Chem. Phys.*, **49**, 191 (1982).
5. P. Sigebahn and B. Liu, *J. Chem. Phys.*, **68**, 2457 (1978).
6. G. C. Schatz and A. Kuppermann, *J. Chem. Phys.*, **62**, 2502 (1975).
7. G. C. Schatz and A. Kuppermann, *J. Chem. Phys.*, **65**, 4642-4668, (1976).
8. A. B. Elkowitz and R. E. Wyatt, *J. Chem. Phys.*, **63**, 702 (1975).
9. R. B. Walker, E. B. Stechel, and J. C. Light, *J. Chem Phys.*, **69**, 2922 (1978).
10. J. Geddes, H. F. Krause, and W. C. Fite, *J. Chem. Phys.*, **56**, 3298 (1972).
11. G. H. Kwei and V. W. S. Lo, *J. Chem. Phys.*, **72**, 6255 (1980).
12. R. Gotting, H. R. Mayne, and J. P. Toennies, *J. Chem. Phys.*, **80**, 2230 (1984).
13. D. P. Gerrity and J. J. Valentini, *J. Chem. Phys.*, **79**, 5202 (1983).
14. C. T. Rettner, E. E. Marinero, and R. N. Zare, *Physics of Electronic and Atomic Collisions* eds. J. Eichler, I. V. Hertel, and N. Stolterfoht, (North-Holland, Amsterdam), p. 51 (1984).

15. E. E. Marinero, C. T. Rettner, and R. N. Zare, *J. Chem. Phys.*, **80**, 4142 (1984).
16. J. Romand, *Ann. Phys*, **4**, 527 (1949).
17. R. Schmiedl, H. Dugan, W. Meier, and K. H. Welge, *Z. Phys. A*, **304**, 137 (1982).
18. G. N. A. van Veen, K. A. Mohamed, T. Baller, and A. E. de Vries, *Chem. Phys.*, **80**, 113 (1983).
19. R. D. Clear, S. J. Riley, and K. R. Wilson, *J. Chem Phys.*, **63**, 1340 (1974).
20. G. C. Schatz and A. Kuppermann, *Phys. Rev. Lett.*, **35**, 1266 (1975).
21. K. P. Huber and G. Herzberg, *Molecular Spectra and Molecular Structure. Constants of Diatomic Molecules*, Van Nostrand Reinhold, N. Y. (1979).
22. C. E. Moore, *Natl. Bur. Stand., Circ. 467*, **3** (1958).
23. C. Kunz *Synchrotron Radiation, Techniques and Application*, ed. C. Kunz, Springer-Verlag, Berlin, p. 1 (1979).
24. H. Winick, *Synchrotron Radiation Reserch*, eds. H. Winick and S. Doniach, Plenum Press, New York, p. 28 (1980).
25. J. P. Blewett (ed.), *Proposal for a National Synchrotron Radiation Light Source*, BNL Report 50595 (1977).
26. G. Parker, Candidacy report (1983).
27. V. Rehn, J. L. Stanford, A. D. Baer, V. O. Jones, and W. J. Choyke,

- Appl. Opt.*, **16**, 1111 (1978).
28. V. Saile, *Nucl. Instrument. Methods*, **152**, 59 (1978).
29. R. S. Mulliken, *J. Chem. Phys.*, **8**, 380 (1940)
30. F. Magnotta, D. J. Nesbitt, and S. R. Leone, *Chem. Phys. Lett.*, **83**, 12 (1981).
31. *JANAF Thermochemical Tables, 2nd Ed.*, NSRDS-NBS, 37 (1971).

**PROPOSITION II:** Study of Electronic to Vibrational Energy Transfer  
using Oriented Crossed Beams

**Abstract:** The quenching of electronic fluorescence has been extensively researched over the past years in a number of systems. However, in all these experiments the question of the importance of steric effect has not been investigated. It is proposed to study the effect of electronic to vibrational energy transfer through the use of oriented molecular beams. A system which has been of great interest is

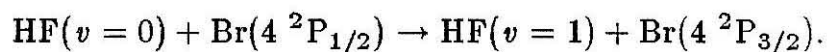


Since this process is nearly resonant it shows high efficiency. This experiment consists of orienting a molecular beam of HF (by applying appropriate electric fields) and crossing it with an atomic beam of electronically excited Br atoms. The steric dependence on the E→V energy transfer can then be examined by observing the amount of energy transferred as a function of orientation of the HF with respect to the Br.

Of all the energy transfer processes which have been examined, electronic to vibrational (E→V) energy transfer is the least understood. A fundamental understanding of these processes is of prime importance in understanding chemical reaction studies<sup>1</sup>, atmospheric modeling<sup>2</sup> and development of new laser systems<sup>3</sup>. These studies also serve to test approximate scattering theories as well as probes of potential curve crossing in chemically reactive systems.

Most studies have shown the importance of matching the vibrational energy of the quencher to the energy of the electronically excited atom<sup>4-6</sup>. This work was first shown in the work by Polanyi and co-workers<sup>7-9</sup> who in studying the quenching of Hg( $6^3P_1$ ) and Hg( $6^3P_0$ ) atoms by CO observed 30 - 50 % of the electronic energy was transferred into the  $v = 2$  state of CO.

This effect has been observed in other systems. The trend in the observed E → V energy transfer rates for Br\* to HF, HCl and HBr supports the idea that resonance plays an important role in these processes<sup>10</sup>. One system which has demonstrated resonantly enhanced E→V energy transfer in bulk<sup>11-13</sup> is the system



The spin-orbit splitting in Br ( $4^2P_{1/2} \rightarrow 4^3P_{3/2} = 3685 \text{ cm}^{-1}$ ) is highly resonant with several possible vibration-rotation transitions in HF ( $v(0 \rightarrow 1) = 3962 \text{ cm}^{-1}$ ) and has been used to explain the efficiency of Br relaxing HF ( $v = 1$ ) in recent shock tube experiments<sup>14</sup>. The rate for the quenching is extremely fast ( $(1.1 \pm 0.2) \times 10^6 \text{ s}^{-1} \text{ torr}^{-1}$ )<sup>15</sup> This corresponds to a cross section of  $(5.4 \pm 1.0) \times 10^{-16} \text{ cm}^2$  or for their experimental conditions 6 gas kinetic collisions.

It is proposed to study the energy transfer process for this system through

an oriented crossed beam experiment. By orienting the HF beam with respect to the electronically excited Br atomic beam one may compare the efficiency of energy transfer with the type of collision interaction. From this observation one will be able for the first time to see if there is a steric preference to energy transfer.

The experiment consists of first creating a supersonic HF beam, such that the molecules will be rotationally cooled and have a narrow velocity distribution. Once skimmed, they will pass through a rotational state selector to select out the  $j = 0$  state. For a polar symmetric top molecule one could employ a selector such as the one described by Bernstein<sup>16,17</sup>. By using an inhomogeneous electric field, a particular quantum state is selected. Once selected the molecules may then be oriented in a local electric field exterior to the inhomogeneous field produced by the hexapole array of rods. Thus one may align symmetric top molecules by first selecting only molecules in the proper  $j = 0$  state and then allowing them to fly into a weak uniform electric field aligning to them the laboratory coordinates. Alignment of molecules has been successfully achieved with  $\text{CH}_3\text{I}$ <sup>18</sup>, which having a dipole moment of 1.62D, gave very good alignment with the field. The molecules were calculated to have an average angle of  $10^\circ$ .

This selection of symmetric top molecules which possess a dipole moment occurs because the hexapole field applies a harmonic force upon the molecule for negative values of the effective induced electric dipole moment

$$\mu_{eff} = \frac{\partial W}{\partial E}$$

where  $W$  is the Stark energy and  $E$  the magnitude of the electric field. Molecules without angular momentum around their axis (e.g. diatomic with a closed electron shell) have positive electric dipole moments and it is very dif-

difficult to produce orientation short of using brute force (strong static electric field  $\sim 240$  kV/cm)<sup>19</sup>.

However, Friedmann<sup>20</sup> and Regenfus<sup>21</sup> have reported similar effects using a two-pole magnetic field<sup>22</sup>. It is therefore possible to use an electric two pole field for similar purposes with polar diatomics. Waech and co-workers<sup>23</sup> have reported the use of a ten-pole electric field (with two-pole symmetry) to separate and focus the states of diatomics with positive induced electric dipole moments. In the case of CsF and RbCl,  $J, M = 0$  states have been successfully focused.<sup>23</sup> However the net focusing is not as great as in the hexapole array system. This is because in the plane defined by the two parallel wires the particles are pushed away from the symmetry axis, whereas in the plane which is perpendicular to the first plane and contains the symmetry axis, the particles with positive effective dipole moment are pulled onto the axis of the field arrangement. Only in the latter plane is there a resultant focusing effect.

This disadvantage has been solved by Lubbert and co-workers<sup>24</sup> by putting a second two-wire field coaxially behind the first one. Thus, a particle that feels a diverging force in the first field is influenced by a converging force in the second field and *vice versa*<sup>25-27</sup>. Such a system is called an alternate gradient focusing system (AGF system). This AGF selector has been used to separate the rotational states of ICl with resultant 90% purity of the ( $J, M = 0$ ) state and with an improvement in intensity of a factor of four from the previous two pole field<sup>23</sup>.

In the proposed experiment the HF molecules are selected by the AGF array and then pass through a homogeneous electric field defined by a pair of electric plates. The field will then align the HF with respect to its polarity. Considering that HF has a large dipole moment of 1.90D, and by also using

a long path length for the plates, alignment should be achieved.

With the HF beam so prepared one would then cross it with a beam of supersonic Br atoms in the  $4^2P_{1/2}$  state. This beam would be movable such that it would cross the HF beam at different angles. Where the beams crossed,  $E \rightarrow V$  energy transfer would occur and the species would then scatter. It is then possible to estimate how much of this energy transfer occurred, through examination of a velocity profile of the HF molecules after the interaction. This would be done using a correlation chopper and a mass spectrometer as a detector. This technique was first pioneered by R. B. Bernstein and co-workers<sup>28</sup> for the case of  $D_2 + K$ .

To estimate the intensity of the signal which could be expected we used J. W. Winniczek experiment as a model. He is currently making inelastic collision measurements using a cross molecular beam in conjunction with a correlation chopper to observe the inelastic process<sup>29</sup>. Using his experimental parameters and the cross section for the  $E \rightarrow V$  process<sup>15</sup> we estimate that there will be an observable signal of vibrationally excited HF, with a signal-to-noise ratio of approximately 5.

One would first do the experiment by observing the HF velocity profile for the elastically and inelastically scattered HF with the Br in the electronic ground state. This would be done by generating the Br atoms by passing  $Br_2$  through a microwave discharge<sup>30</sup>. One could then see how the HF velocity profile changes using excited Br atoms. These Br atoms would be generated by passing the  $Br_2$  gas through the 4730 Å line of a frequency doubled  $Nd^{+3}$ :YAG laser<sup>31</sup> or even by flash photolysis of  $HBr$ <sup>32</sup>. From the shift of the velocity profile one could then gauge the amount of  $E \rightarrow V$  energy transfer that had occurred, due to the inelastic nature of the process.

Now using the advantage that the HF are aligned, one can rotate the Br

atom source (or conversely change the alignment of the HF via the homogeneous field) and see how the E→V energy transfer changes as a function of angle with respect to the aligned HF molecules. By this it will be possible to deduce which types of collisions are more effective in E→V energy transfer: those perpendicular to the HF or collinear; and if collinear, on the F side or on the H side.

In addition one could rotate the mass spectrometer detector and determine how the vibrationally excited HF molecules are scattered as a function of angle. Likewise, one could look at the E→V energy transfer of other systems, like HCl or HBr.

Should this technique of monitoring the amount of energy transfer via the velocity change in the beam prove insensitive it will still be possible to perform the experiment. R. N. Zare and co-workers have shown the great utility of laser-induced fluorescence in monitoring the product states. The technique involves irradiating the product molecules with a tunable laser and observing the total fluorescence as the laser-excited states return to the ground state. This can be used in the proposed experiment to observe the population of the HF ( $v = 1$ ) state as a function of the orientation of the electronically excited Br beam.

Though the experiment is quite difficult to initially set up there is the potential for the generation of an immense amount of data regarding exactly what factors are important in E→V energy transfer.

**References**

1. S. Lemont, G. W. Flynn, *Ann. Rev. Phys. Chem.*, **28**, 261 (1977).
2. G. H. Millman, *J. Atm. & Ter. Phys.*, **27**, 585 (1965).
3. J. K. Hancock, and W. H. Green, *J. Chem. Phys.*, **57**, 4515 (1972).
4. R. J. Donovan and D.J. Little, *J. Chem. Soc. Faraday Trans. 2*, 1837 (1973).
5. J. J. Ewing, D. W. Trainor, and S. Yatsiv, *J. Chem. Phys.*, **61**, 4433 (1974).
6. M. J. Bevan and D. Husain, *J. Phys. Chem.*, **80**, 217 (1976).
7. G. Karl and J. C. Polanyi, *Discuss. Faraday Soc.*, **33**, 93 (1962).
8. G. Karl and J. C. Polanyi, *J. Chem. Phys.*, **38**, 271 (1963).
9. G. Karl, P. Kruus and J. C. Polanyi, *J. Chem. Phys.*, **46**, 224 (1967).
10. A. B. Petersen, C. Wittig and S. R. Leone, *Appl. Phys. Lett.*, **27** 307 (1975).
11. I. H. Zimmerman, and T. F. George, *J. Chem. Phys.*, **61**, 2486 (1974).
12. G. P. Quigley, and G. J. Wolga, *J. Chem. Phys.*, **62**, 4568 (1975).
13. S. R. Leone, and F. J. Wodarzky, *J. Chem. Phys.*, **60**, 314 (1974).
14. J. A. Blauer and W. C. Solomon, *Proc. Intern. Symp. Combust.*, 14th University Park, PA (1973).
15. F. J. Wodarczyk and P. B. Sackett, *Chem Phys.*, **12**, 65 (1976).

16. T. G. Waech, K. H. Kramer, and R. B. Bernstein, *J. Chem. Phys.*, **48**, 3978 (1968).
17. P. R. Brooks, and E. M. Jones, *J. Chem. Phys.*, **45**, 3449 (1966).
18. P. R. Brooks, E. M. Jones, and K. Smith, *J. Chem. Phys.*, **51**, 3073 (1969).
19. S. Stolte, *Ber. Bunsenges. Phys. Chem.*, **86**, 413 (1982).
20. H. Friedmann, *Z. Physik*, **161**, 74 (1961).
21. G. Regenfus, thesis, University of Munich (1963).
22. F. Ramsey, *Molecular Beams*, Oxford University Press, London p. 431 (1956).
23. T. G. Waech, K. H. Kramer, and R. B. Bernstein, *J. Chem. Phys.*, **48**, 3978 (1968).
24. A. Lubbert, G. Rotzoll, and F. Gunther, *J. Chem. Phys.*, **69**, 5174 (1978).
25. D. Auerbach, E. A. Bromberg, and L. Wharton, *J. Chem. Phys.*, **45**, 2160 (1966).
26. F. Gunther and K. Schugerl, *Z. Phys. Chem.*, **80**, 155 (1972).
27. A. Lubbert, F. Gunther, and K. Schugerl, *Chem. Phys. Lett.*, **35**, 210 (1975).
28. A. R. Blythe, A. E. Grosser, and R. B. Bernstein, *J. Chem. Phys.*, **41**, 1917 (1964).

29. J. W. Winniczek, Ph.D thesis, California Institute of Technology (1985).
30. G. P. Quigley, and G. J. Wolga, *Chem. Phys. Lett.*, **27**, 276 (1974).
31. S. E. Harris, and R. W. Wallace, *Laser Focus*, **6**, 42 (1970).
32. R. J. Donovan, D. Husain, and C. D. Stevenson, *Trans. Faraday Soc.*, **66**, 2418 (1970).
33. R. N. Zare and P. J. Dagdigian, *Science*, **185**, 739 (1974).

**PROPOSITION III:** Bonding of  $\text{NH}_3$  and  $\text{H}_2\text{O}$  on Stepped Surfaces Investigated by ESDIAD

**Abstract:** Electron stimulated desorption ion angular distribution (ESDIAD) has been shown to be a useful tool for the elucidation of the bonding geometries of adsorbates on surfaces. It is proposed to apply this technique to  $\text{NH}_3$  and  $\text{H}_2\text{O}$  bonded to the stepped surface of a  $\text{W}(110)$  crystal in an attempt to understand how the stepping of the surface influences the adsorbed molecules. This will provide important information on the way molecules orient themselves on a 'corrugated' surface with implications for understanding catalytic processes since these terraced surfaces are much closer to the reality of a true catalytic surface than that of a single crystal. It is proposed to also perform the experiment utilizing  $\text{PH}_3$  and  $\text{H}_2\text{S}$  to see how larger size will affect the overall orientation of the molecules on the step.

A question of great importance to surface scientists is an understanding of the bonding between a metal surface and a molecule which is adsorbed to it. Conventional experimental techniques are capable of giving qualitative understanding of the interaction, but are woefully inadequate in answering questions concerning the geometrical structure of the adsorbed species, at what site the molecule is adsorbed, and its orientation with respect to the surface and other molecules adsorbed on that surface. Answers to these questions are essential to achieving a basic understanding of surface catalytic properties and how molecular orientation effects chemistry on a surface.

It is now well established that the electron stimulated desorption ion angular distribution (ESDIAD) method is capable of providing direct information about site location and geometrical structure of molecules on surfaces<sup>1-3</sup>. In this method, electronic excitation of surface molecules by a focused electron beam can result in desorption of atomic or molecular ions from the surface. These ions desorb in discrete cones of emission in directions determined by the orientation of the bond which is ruptured by the excitation. As shown in Figure 1A, ESDIAD of CO bound in a vertical configuration on a metal stepped surface will result in the the desorption of a  $O^+$  in the direction of the surface normal, while the same process applied to  $H_2O$  results in desorption of  $H^+$  in an off-normal direction. Measurement of the patterns of ion desorption provide a direct display of the geometrical structure of surface molecules in the adsorbed layer.

Two types of detection systems have been developed: an area detector with visual display and a scanning ion detector, as shown in Figures 1B and 1C. In the display type of apparatus<sup>4</sup> a focused electron beam (< 1mm diameter, 100 to 400 eV) bombards a single crystal sample prepared under a high vacuum ( $\sim 1 \times 10^{10}$  torr). In all these studies beam currents are kept

low to prevent any damage to the substrate. Typically the electron dose is kept below  $10^{-3}$  Coul/cm<sup>2</sup>. The ion beams which desorb via ESDIAD pass through a hemispherical grid and impinge on the front surface of a double microchannel plate assembly (MCP). The output from the MCP assembly (gain  $\sim 10^6$ ) is accelerated to a fluorescent screen where it is displayed and recorded. Typically a bias potential of 200 V is applied to 'compress' the ion trajectories so that all the beams are visible on the screen. In this case the total electron energy is the electron gun potential plus the bias potential, typically 300V. By reversing the potentials on the MCP assembly a LEED pattern of the surface is generated. In the present set up employed at NBS, a quadrupole mass spectrometer is used in conjunction with the MCP assembly to mass identify the ESDIAD ions.

Figure 1C shows a different type of detector set-up where a channeltron multiplier is mounted on a computer-driven goniometer as a movable detector for ESDIAD<sup>5</sup>. In this case the data, instead of being a photograph of a fluorescent screen, is a computer-generated plot of ion intensity vs. desorption angle. In addition if one pulses the electron beam, the ion mass may be detected by a time-of-flight method. A new technique has been recently developed which allows direct measurement of ESDIAD neutral specie. Feulner, Treichler and Menzel<sup>6</sup> have developed an improved mass spectrometer system which can detect low-level neutral signals at or near the thresholds for desorption.

There has been much theoretical work performed on ESDIAD<sup>7-10</sup>, concluding that the instantaneous force on a ESDIAD ion is repulsive in the direction of the original bond. That is, ESDIAD does image the initial state vibrational wave function and that the desorption impulse is along the bond direction. In a simple physical picture, electronic lifetimes ( $\sim 10^{-14}$  s) are

much shorter than the period of low-frequency bending vibrations ( $\sim 10^{-12}$  s), such that the electron beam samples a statistical array of surface oscillators "frozen" into a distribution of orientations. As a result the direction of the ESDIAD beam will contain information on the bond orientation and the profile of the beam will carry information about the surface vibrational dynamics. Asymmetric beam profiles have been observed for surfaces heated at large temperatures<sup>11</sup>. This phenomenon has also been observed in the case of bridging CO and is attributed to the different vibrational amplitudes of the CO for the in-plane and out-of-plane stretch<sup>12</sup>.

Whatever additional effects may change the beam width of the desorbed ions and cross section for the ionization process, the ion desorption angle observed is related to the surface bond angle and in particular it is found that the expected azimuthal angle of the surface bond is preserved in ESDIAD. As a calibration check ESDIAD results have been compared with systems that have had structural identification (measured by other methods (EELS, UPS, ARUPS, LEED)<sup>13-17</sup>) of molecules adsorbed on surfaces and in every case ESDIAD agreed with the previous result.

A useful example and perhaps the most interesting application of ESDIAD to date is the effect of  $\text{NH}_3$  and  $\text{H}_2\text{O}$  on  $\text{Ni}(111)$  and  $\text{Al}(111)$ <sup>18,19</sup>. Figure 2A is a LEED pattern for a clean surface of  $\text{Ni}(111)$  while 2b is the hydrogen ion ESDIAD pattern for  $\text{NH}_3$  on  $\text{Ni}(111)$  ( $\theta=0.25$  T=150K). The continuous halo of  $\text{H}^+$  desorption in a direction away from the surface normal is consistent with an array of  $\text{NH}_3$  molecules bonded via the N atoms with no preferred azimuthal orientation of the H atoms which point away from the surface (as if the  $\text{NH}_3$  is freely rotating about an axis normal to the surface of the crystal). However, if the surface is predosed with oxygen atoms (as small as  $\theta=0.03$ ) the halo pattern is broken and what is now observed is a

ESDIAD pattern with three-fold symmetry.

Similar results are observed for  $\text{H}_2\text{O}$  on  $\text{Ni}(111)$ . Figure 2d shows the ESDIAD pattern for  $\text{H}_2\text{O}$  for coverages less than saturation on  $\text{Ni}(111)$ . The less than distinct halo (as observed in Figure 2a for  $\text{NH}_3$ ) suggests the array of adsorbed hydrogen-bonded  $\text{H}_2\text{O}$  molecules contain a distribution of "tilt" angles with respect to the surface normal, as well as a random distribution of azimuthal angles. However a small dosage of oxygen atoms again produces a ESDIAD pattern of three-fold symmetry (Figure 2e) which upon heating to the onset of desorption disappears (Figure 2f).

A structural model to explain these results is presented in Figure 3. From LEED it is known that the oxygen atom on  $\text{Ni}(111)$  is adsorbed in threefold hollow sites<sup>20</sup>. If the O atoms are located in threefold hollows above the second-layer atoms, the  $\text{H}_2\text{O}$  can be bonded in top sites, and the  $\text{NH}_3$  in other threefold hollows, with the resulting ESDIAD pattern coming from the non-hydrogen bonded ligand. As a result the presence of a single oxygen atom can influence the azimuthal orientation of more than one molecule, consistent with the observation of Madix<sup>21</sup> and Kretzschmar<sup>22</sup>. This result has interesting implications in that such a small amount of oxygen atoms can indeed influence to such a great extent the orientation of the molecule adsorbed to the surface. These steric effects in co-adsorption may have profound implication for the understanding of the mechanisms by which catalyst promoters and poisoners function. It may be that these additives alter the reaction pathway by inducing the formation of a surface structure which in the absence of the additive would have a low probability of forming. Recent work has been performed on  $\text{NH}_3$  and  $\text{H}_2\text{O}$  on  $\text{Ru}(001)$  using ESDIAD<sup>23</sup>. In particular the effect Na has on the orientation of these molecules has also been studied<sup>24,25</sup> in hopes of gaining an understanding of the metal-electrolyte

interface.

I propose to use the technique of ESDIAD to study  $\text{H}_2\text{O}$  and  $\text{NH}_3$  on stepped surface such as  $\text{W}(110)$ . These stepped surfaces, unlike the 'smooth' surface of  $\text{Ni}(111)$ , have a regular array of terraced steps. Stepped surfaces have been shown in a variety of experiments to exhibit unique physical, chemical, and electronic properties<sup>26-28</sup>. Experimental work has shown enormous changes in the work function of the surface at the edges of the steps, contrasted to the flat plateau region of the crystal<sup>29</sup>. As a result, one would expect dramatic differences in the orientation of an adsorbed molecule on such a corrugated surface, differences which could only be detected through ESDIAD. An understanding of such effects will prove essential to appreciating the influence of any surface defects on an adsorbed layer of molecules. It should also be noted that these stepped surfaces are undoubtedly much closer to the reality of a rough catalytic surface, and an understanding of them is therefore crucial to begin to explain surface catalyzing effects.

To perform this study a polyhedral tungsten crystal containing a  $\text{W}(110)$  flat and 4 flats having orientations  $6^\circ$  and  $10^\circ$  off the  $(110)$  plane with rows of steps parallel to the  $[100]$  and  $[110]$  directions will be used. Besocke and Berger<sup>30</sup> point out the distinct advantages to using one polyhedrally shaped sample instead of many separately prepared crystals: (1) all surfaces are prepared on a single sample crystal with the same bulk impurity levels, (2) cleaning, heating and dosing of the sample is the same for all surfaces so that good relative measurements may be made.

This type of sample, as depicted in Figure 4(a), has been used previously to observe ESD of oxygen atoms<sup>31</sup>. Note that the nomenclature introduced by Lang<sup>32</sup> to describe the stepped surface ( $\text{W}(\text{S})[8(100)\times(112)]$ ) means a stepped tungsten surface; the average step contains 8 rows of atoms on a ter-

race of (110) orientation; the edge orientation is (112). Figure 4(b) shows the idealized, unreconstructed W(110) crystal surface showing the atomic structure of the steps which are parallel to the [100] and [110] direction respectively. By dosing the surface with either H<sub>2</sub>O or NH<sub>3</sub> and observing the ESDIAD pattern I would expect for the center facet the known ESDIAD pattern for that crystal face, while for each of the side facets two patterns would result. The first pattern would be the already observed ESDIAD pattern of the center facet while the second, weaker pattern would be due to ions desorbing from the step regions. By contrasting these two patterns as a function of step size a detailed picture would be observed for the molecular orientation at the edges. Also of interest would be the observation of the effect of oxygen dosing on the orientation of the molecules. In the case of 'flat' Ni(111) short range azimuthal order was observed, apparently through the creation of hydrogen bonds. However, the presence of steps may indeed interfere with this short range ordering due to steric effects.

In particular if these experiments on W(110) produce results, it would be useful to extend the technique to the study of H<sub>2</sub>O on the Ti(001) surface. H<sub>2</sub>O on Ti(001) has shown unusual dissociative behavior. On all other surfaces studied to date, H<sub>2</sub>O forms H and OH or dissociates to form O and H. Recent ultraviolet photoemission spectroscopy (UPS) of H<sub>2</sub>O on Ti(001) has shown that this terraced surface forms three species; O, H and OH<sup>33</sup>. This result may be indicative that the H<sub>2</sub>O is adsorbed at two sites, the edge and the plateau, such that at one site H and OH are produced, while at the other site H and O are formed. An ESDIAD study of this system, performed in the same manner of the previously discussed W(110), may shed light on this effect.

Finally, I also propose to study H<sub>2</sub>S and PH<sub>3</sub> of Ni(111) by ESDIAD.

$\text{H}_2\text{O}$  and  $\text{NH}_3$  have already been studied on this surface; however,  $\text{H}_2\text{S}$  and  $\text{PH}_3$  are  $\sim 0.4 \text{ \AA}$  larger and are significantly less polar than  $\text{H}_2\text{O}$  and  $\text{NH}_3$ . As a result it would be interesting to contrast the difference in bonding of  $\text{H}_2\text{S}$  and  $\text{PH}_3$  with  $\text{H}_2\text{O}$  and  $\text{NH}_3$  and explain any difference in their orientation on Ni(111) in terms of the molecular differences of the adsorbate.

It will then be extremely informative to see the effect small amounts of oxygen atoms will have on  $\text{H}_2\text{S}$  and  $\text{PH}_3$  azimuthal ordering. The large effects seen with  $\text{H}_2\text{O}$  and  $\text{NH}_3$  were explained as being presumably due to hydrogen bonding. In the case of  $\text{H}_2\text{S}$  and  $\text{PH}_3$ , hydrogen bonding should be far less pronounced due to the reduced electronegativity of the adsorbate, and one might expect differences in the ESDIAD pattern of these molecules as a function of oxygen atom coverage. This result will then be a measure of the importance of hydrogen bonding on a surface and may give some feeling for the nature of adsorbate-adsorbate interaction while bonded on a surface.

**References**

1. T. E. Madey in *Inelastic Particle-Surface Collisions*, Springer Series in Chemical Physics, Eds. E. Taglauer and W. Heiland (Spring-Verlag, Berlin), p.80 (1980).
2. T. E. Madey and J. T. Yates, Jr. *Surface Sci.*, **63**, 203 (1977).
3. T. E. Madey and R. Stockbauer, in *Methods of Experimental Surface Science*, Eds. R. C. Park and M. G. Lagally, in press.
4. T. E. Madey, J. J. Czyzanski, and J. T. Yates, Jr. *Surface Sci.*, **49**, 465 (1975).
5. H. Niehus and B. Krahl-Urban, *Rev. Sci. Instr.*, **52**, 68 (1981).
6. P. Feulner, R. Treichler, and D. Menzel, *Phys. Rev.*, **B24**, 7427 (1981).
7. J. I. Gersten, R. Janow, and N. Tzoar, *Phys. Rev. Lett.*, **36**, 610 (1976).
8. W. L. Clinton, *Phys. Rev. Lett.*, **39**, 965 (1977).
9. R. Janow, and N. Tzoar, *Surface Sci.*, **69**, 253 (1977).
10. E. Preuss, *Surface Sci.*, **94**, 249 (1980).
11. T. E. Madey, *Surface Sci.*, **79**, 575 (1979).
12. T. E. Madey, J. T. Yates, Jr., A. M. Bradshaw, and F. M. Hoffmann, *Surface Sci.*, **89**, 370 (1979).
13. G. E. Thomas, and W. H. Weinberg, *J. Chem. Phys.*, **70**, 1437 (1979).
14. H. Pfnur, D. Menzel, F. M. Hoffmann, A. Ortega, and A. M. Bradshaw, *Surface Sci.*, **93**, 431 (1980).

15. J. C. Fuggle, M. Steinkilberg, and D. Menzel, *Chem. Physics*, **11**, 307 (1975).
16. W. Erley, H. Wagner, and H. Ibach, *Surface Sci.*, **80**, 612 (1979).
17. G. Apai, P. S. Wehner, R. S. Williams, J. Stöhr, and D. A. Shirley, *Phys. Rev. Lett.*, **37**, 1497 (1976).
18. F. P. Netzer and T. E. Madey, *Phys. Rev. Lett.*, **47**, 928 (1981).
19. T. E. Madey and F. P. Netzer, *Surface Sci.*, **117**, 549 (1982).
20. L. D. Roelofs, A. R. Kortan, T. L. Einstein, and R. L. Park, *J. Vac. Sci. Technol.*, **18**, 492 (1981).
21. M. Bowker, M. A. Barteau, and R. J. Madiz, *Surface Sci.*, **92** 528 (1980).
22. K. Kretzschman, J. K. Sass, A. M. Bradshaw, and S. Holloway, *Surface Sci.*, **115**, 183 (1982).
23. C. Benndorf and T. E. Madey, *Surface Sci.*, **135**, 164 (1983).
24. D. L. Doering, S. Semancik, and T. E. Madey, *Surface Sci.*, **133**, 49 (1983).
25. C. Benndorf, and T. E. Madey, *Chem. Phys. Lett.*, **101**, 59 (1983).
26. H. Wagner, *Physical and Chemical Properties of Stepped Surfaces*, Springer Tracts of Modern Physics (Springer, Berlin) 1978.
27. M. Henzler, *Appl. Phys.*, **9**, 11 (1976).
28. C. S. McKee, M. W. Roberts, and M. L. Williams, *Advan. Colloid Interface Sci.*, **8**, 29 (1977).

29. B. Krahl–Urban, E. A. Nielisch, and H. Wagner, *Surface Sci.*, **64**, 52 (1977).
30. K. Besocke, and S. Berger in: *Proc. 7th Intern. Vacuum Congr. and 3rd Intern. Conf. on Solid Surfaces*, Vienna, 1977 Eds. R. Dobrozemsky *et al.* (Berger, Vienna) p. 893 (1977).
31. T. E. Madey, *Surface Sci.*, **94**, 483 (1980).
32. B. Lang, R. W. Joyner, and G. A. Somorjai, *Surface Sci.*, **30**, 440 (1972).
33. R. Stockbauer, D. M. Hanson, S. A. Flodstrom, and T. E. Madey, *Phys. Rev. B.*, **26**, 1885 (1982).

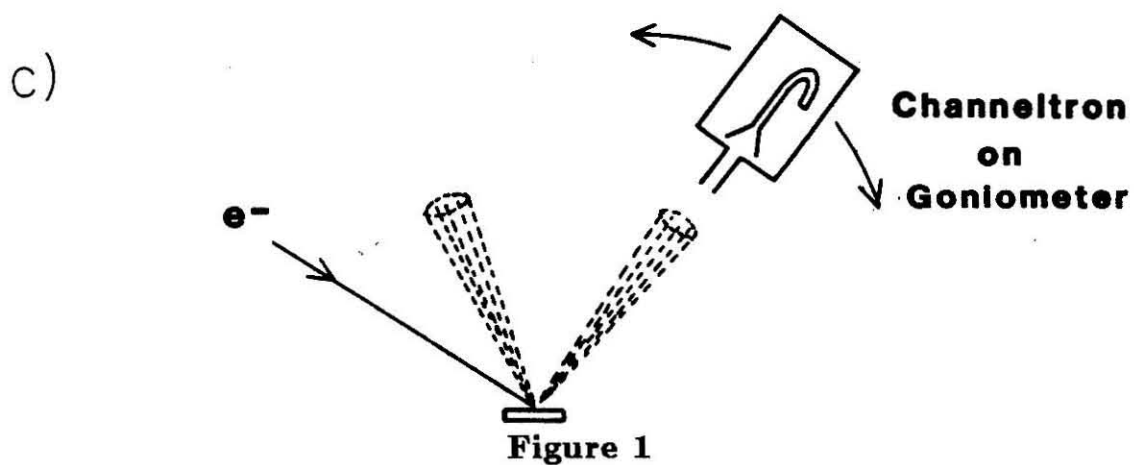
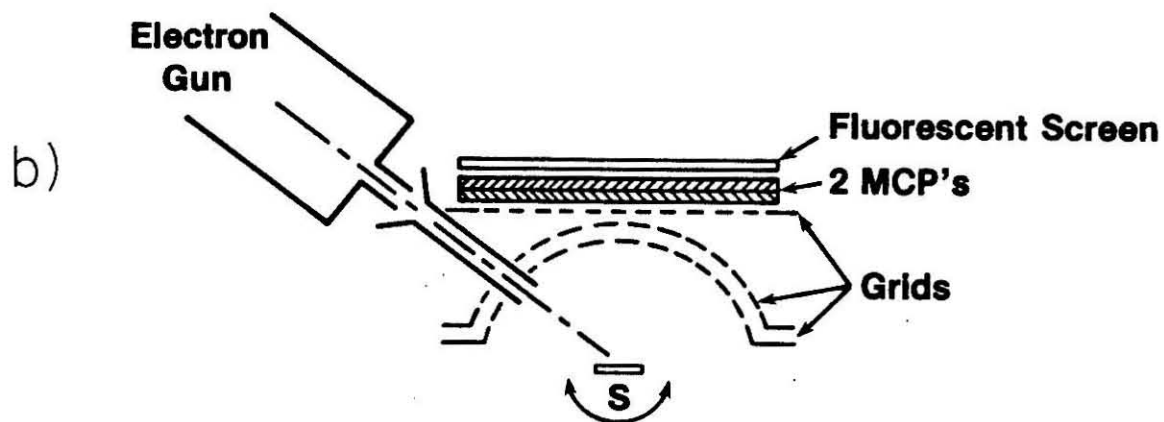
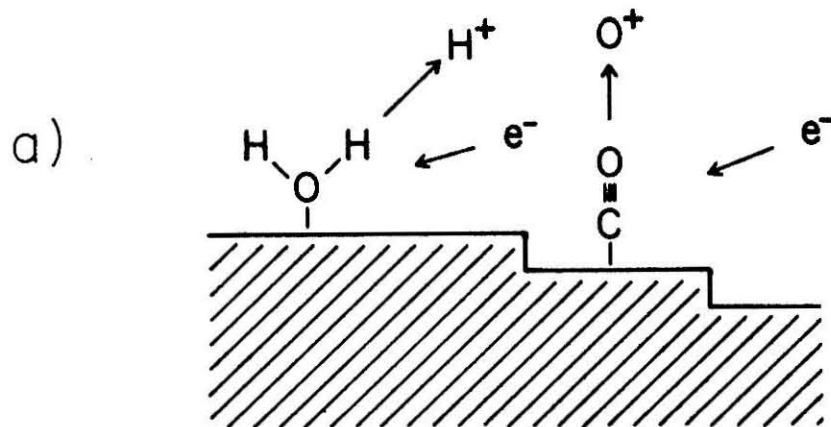
## Figure Captions

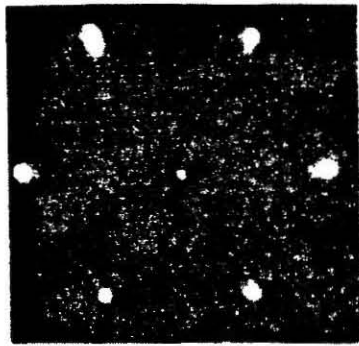
Figure 1. (a) Schematic bonding configurations for adsorbed CO and H<sub>2</sub>O, showing relationship between bond angle and ion desorption angle in ESDIAD. (b) Schematic of NBS ESDIAD apparatus. ESDIAD patterns are displayed using the grid–microchannel–plate–fluorescent screen detector array<sup>4</sup>. (c) Schematic of computer–driven moveable ion detector for ESDIAD<sup>5</sup>.

Figure 2. LEED and ESDIAD patterns for NH<sub>3</sub> and H<sub>2</sub>O on Ni(111): (a) LEED of clean Ni(111) surface, electron energy  $V_e=120$  eV. (b) H<sup>+</sup> ESDIAD pattern, NH<sub>3</sub> on clean Ni(111),  $V_e=300$  eV. (c) ESDIAD pattern, NH<sub>3</sub> on O/Ni(111),  $\theta_O \leq 0.05$  monolayer,  $V_e=300$  eV. (d) ESDIAD pattern, H<sub>2</sub>O on clean Ni(111) at 80 K,  $V_e=300$  eV. (e) ESDIAD pattern, H<sub>2</sub>O on O/Ni(111) at 80 K,  $\theta_O \leq 0.05$  monolayer,  $V_e=300$  eV. (f) ESDIAD pattern, H<sub>2</sub>O on O/Ni(111) after heating to 120 K,  $V_e=300$  eV. The arrows on the figure (c) and (e) are oriented along the  $[\bar{1}\bar{1}2]$  azimuths.

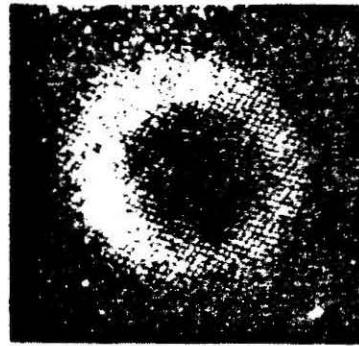
Figure 3. Schematic models for bonding of H<sub>2</sub>O and NH<sub>3</sub> to Ni(111) in the presence of oxygen. The dashed lines indicate hydrogen–bonding interactions.

Figure 4. (a) Schematic drawing of the polyhedral tungsten crystal to be used. (b) Drawing of ideal, unreconstructed tungsten (110) crystal surface showing the atomic structure of steps parallel to  $[100]$  and  $[110]$  direction.





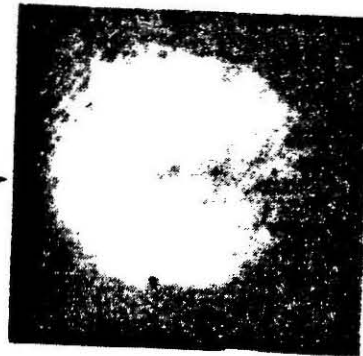
(a)



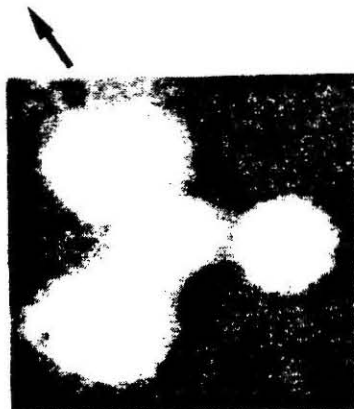
(b)



(c)



(d)



(e)



(f)

Figure 2

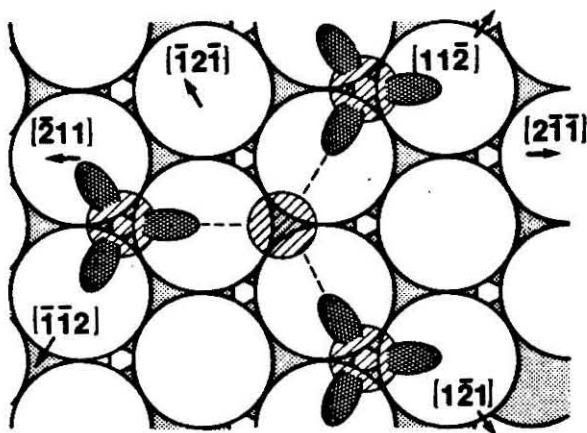
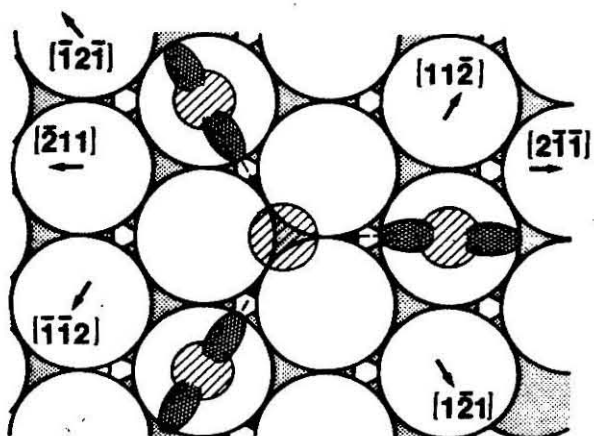
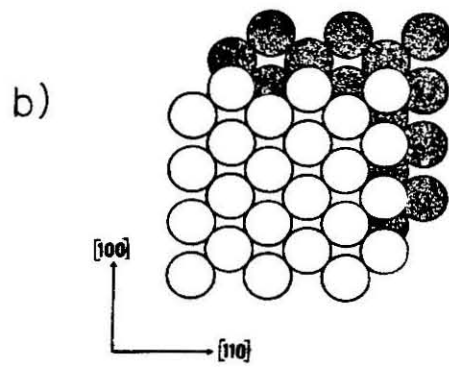
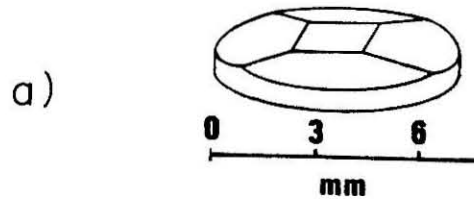
(a) Model for Orientation of  $\text{NH}_3$ (b) Model for Orientation of  $\text{H}_2\text{O}$ 

Figure 3



**Figure 4**

**PROPOSITION IV:** Effect of Magnetic Field on Organic Syntheses in the Plasma of Glow Discharges

**Abstract:** It has only been very recently that reactions of organic substances as a result of electron collisions in the cold plasma of glow discharges have been studied. These reactions are driven by inelastic collisions of high energy electrons with the neutral reactants generating quite often unique products. However, this process tends not to be selective and has proven only to be slightly preparatively useful. It is therefore proposed to study the influence of a magnetic field on the organic plasma discharge. This field should have the effect of containing the electrons to a greater extent. This in turn will increase the number of inelastic collisions and thereby increase the yield of the reaction without having to increase the temperature of the gas. It may also make reactions more selective since they will be able to operate at lower powers.

In attempts to produce new methods of syntheses chemists very early attempted to utilize plasma discharges to create organic compounds<sup>1-3</sup>. These first attempts resulted in only tarry or polymeric products due to their harsh conditions. As of late, due to improvements in experimental design, it has now become possible to use a plasma discharge as an efficient reactor for organic molecules<sup>4-7</sup>. It is also in the last few years that organic syntheses on the preparative scale have been successfully carried out in a plasma<sup>8</sup>.

Before discussing the types of reactions possible in a plasma discharge it is necessary to understand the nature of the plasma itself. Figure 1a shows a schematic of the instrument. A current flows between two electrodes that project into a vessel having a low gas pressure and that are connected to a source of direct current. Individual electrons are accelerated by the field and can excite or ionize atoms or molecules with which they collide. In a cool plasma, of the type useful for organic chemistry only a small fraction of the molecules are ionized at any instant ( $10^{-4}$  -  $10^{-1}$  A). As a result, the gas temperature is low enough that thermal decomposition of the organic molecules is avoided; the neutral molecules have temperatures  $< 100^{\circ}\text{C}$  while the electrons which are accelerated have typical temperatures of 10000K. Systems such as these where the temperature of the charged particles differ greatly from the temperatures of the neutral molecules are known as cold, or nonequilibrium plasmas.

It is inelastic collisions with these fast-moving electrons which trigger the reactions. This process has been likened to photolyses<sup>7</sup> where the electrons act as photons in the reaction medium. However, due to the nature of the plasma the dynamics are very complex with little understanding as to the processes involved. Most of the current mechanistic understanding of these plasma dynamics consists of realizing that these reactions are ideally limited

by electron impact such that the number of electrons and the distribution of electron energies determine reaction rates and paths.

Since these discharges occur only under reduced pressure all apparatus are of the flow type. Typical devices are shown in Figure 2. Figure 2a shows the simplest type of device where the discharge is across two metal electrodes where either a DC or low-frequency AC voltage of 20 - 50 V/cm is applied. In this case the electrodes must be protected by an inert gas since they would otherwise become coated with decomposition products<sup>9</sup> Other ways of generating the plasma consists of inductive or capacitive coupling to the plasma (2b and 2c), microwave discharge (2d) and having the current flow through the glass wall (2e).

In a typical experiment the residence time in the plasma zone is 50 ms, and the power is 50 W, though the plasma can be sustained at powers as low as 5 W. These condition will typically lead to conversion to products of about 50 %. Again the result of the reaction is highly dependent on the field strength, pressure, and vessel dimensions.

Many different types of reactions have been observed for these plasma reactors. One class consists of the extrusion of a small molecule from the reactant<sup>10</sup>. One example is the formation of benzocyclopropane from phthalide. Isomerizations are a second class of reactions which have been observed<sup>11-13</sup>. For example *trans*-stilbene can be converted to *cis*-stilbene with low conversion (~ 20%) but with 95% of the product being *cis*-stilbene<sup>14</sup>. A third family of reactions possible is cyanation reactions. This has some synthetic interest since methods for direct cyanation of aromatics and alkenes are not general. Plasma reactions tend to give considerable amounts of ipso-substitution products which are not found in solution-phase ICN photolyses<sup>15-18</sup>.

These examples serve to demonstrate the possibilities for synthesis with

a plasma. Despite the fact that several hundred organic compounds have already been investigated in glow discharges, there have been very few empirical studies on understanding the nature of the plasma chemistry. One such study examined the conversion of anisole to *o*-cresole, *p*-cresole and phenol as a function of flow rate and pressure<sup>19</sup> From the measurements a crude rate law was derived consistent with the idea that electron-impact reactions control the rate. This has been supported by the work of Bell and co-workers<sup>20,21</sup> who monitored the extent of reaction as a function of flow rate, pressure and power. These results showed that the rate of reaction and even the mix of products depend on power and inversely on the pressure.

This dependence again is explained by the electron densities since increasing the power increases the acceleration of the electrons while increasing the pressure increases the number of collisions with fewer of these collisions being above threshold. However, 1 cm<sup>3</sup> of the plasma zone normally contains about 10<sup>10</sup> - 10<sup>12</sup> electrons and ions as well as 10<sup>16</sup> neutrals. Though the electrons are in low concentration it is the presence of these particles and their ability to absorb energy from the electric field and transfer it to molecules via inelastic collisions that causes chemical reactions in the plasma. If it was possible to better control the electron density (than just through power or pressure) it may be possible to manipulate the plasma medium to produce a more efficient reactor.

We have observed in our lab what a large effect the presence of a magnetic field can have on a plasma discharge<sup>22</sup>. This effect has also been observed by Bernstein and co-workers<sup>23</sup> in that the discharge becomes greatly collimated with increasing magnetic field. Figure 3 shows the axial magnet which we use in our experiment. By passing a current through the coil of wire the magnetic field,  $\tilde{B}$ , passes through the center of the coil of wire. It is in the center of

the coil of wire that the plasma beam is generated. Any charged particle will experience a force

$$\vec{F} = q\vec{v} \times \vec{B}$$

where  $v$  is the velocity vector of the charged particle and  $q$  is the charge<sup>24</sup>. As a result any ions that attempt to leave the plasma will feel a perpendicular force to stay contained within. These particles will execute approximately helical motion such that the motion will tighten into a smaller helix the more intense the field. The field then effectively contains the plasma while increasing the density of charged particles within it.

It is proposed to use such a magnetic field to contain the plasma used for organic reactions. The benefit of such containment is that the electron density in the region of the reaction will be increased. Previously the only way to do this was to increase the power fed into the plasma. This then increases the temperature of the neutral molecules changing the plasma from a glow discharge into a arc discharge (Figure 1) As a result, the high temperature decomposes the reactants into tarry residue. With the magnetic field the gas molecules should remain cool, but the increase in electron density will increase the probability of inelastic collisions between the organic molecules and the electrons hence increasing the likelihood of reaction. As a result, the plasma should remain cool but with much greater yields of product due to the increased number of collision. There is also the possibility that new synthetic pathways opening due to the larger number of vibrationally and electronically excited molecules which are generated.

The initial system to investigate will be the *cis*-2-butene plasmolysis. The experiment will consist of utilizing a reaction vessel such as the one pictured in 2a (though it could conceivably be used with the other pictured there). The electromagnet (as pictured in Figure 3) will enclose the reactor

vessel between the anode and the cathode which sustain the discharge. This magnet will be capable of generating 0 - 1000 G by varying the current 0 - 20 A (as described in Section 2 of this thesis). *Cis*-2-butene is an instructive molecule to use for this initial study since there appears two competing pathways present in the plasma<sup>25</sup>. At low power the only pathway is isomerization to *trans*-2-butene and 1-butene with a low conversion rate. At high power, the only pathway is fragmentation to form propylene, acetylene and ethane with a high conversion rate. These results suggested that it was the electron density which regulated which pathway became important. As the authors noted, the plasma isomerization products were suggestive that the reaction was driven by an electronically excited intermediate<sup>26,27</sup>. The excited intermediate is formed by an inelastic collision of the reactant with a high energy electron. At very high power the electrons are accelerated to high energies where they fragment the molecule just as in a mass spectrometer.

The experiment will be to first set up conditions at low power where the *cis*-2-butene is converted to *trans*-2-butene at a low conversion rate. Then keeping power, pressure and flow rate constant the axial magnetic field will be turned on, and the products will be monitored as a function of field. As the field is increased one should expect greater conversion to the *trans* product as a function of field, without the fragmentation pathway playing any role. This will be due to the higher electron density electronically exciting more molecules without the high power which would normally fragment the molecules.

If this experiment proves to be successful it will give the chemist one more parameter with which to control the reactivity and selectivity of the plasmolysis. It may also be that the magnetic field interaction with the plasma may induce surprising pathways for unusual reaction. By further understanding

the mechanisms of such reactions the possibility of doing useful preparative chemistry with low-energy electrons in plasma may become feasible.

**References**

1. M. Berthelot, *C. R. Acad. Sci. Paris*, **67**, 1141 (1869),
2. R. W. Wood, *Proc. Roy. Soc. (London) A*, **97**, 455 (1920).
3. K. F. Bonhoeffer, *Z. Phys. Chem*, **113**, 119 (1924).
4. J. R. Hollahan, A. T. Bell, eds., *Techniques and Applications of Plasma Chemistry*, Wiley, New York (1974).
5. M. Shen, A. T. Bell, Eds., *Plasma and Polymerization*, American chemical Society, Washington, DC (1979).
6. B. Champman, *Glow Discharge Processes*, Wiley, New York (1980).
7. L. L. Miller, *Acc. Chem. Res.*, **16**, 194 (1983).
8. H. Shur, *Angew. Chem. Int. Ed. Engl.*, **11**, 781 (1972).
9. H. Schuler and L Reinbeck, *Z. Naturforsch*, **5a**, 657 (1950).
10. M. Tokuda, L. L. Miller, A. Szabo, and H. Suhr, *J. Org. Chem.*, **44**, 4504 (1979).
11. H. Shur and U. Schoch, *U. Chem. Ber.*, **108**, 3469 (1975).
12. H. Shur and R. I. Weiss, *Justus Liebigs Ann. Chem.*, **760**, 127 (1972).
13. M. Tezuka and L. L. Miller, *J. Am. Chem. Soc.*, **100**, 4201 (1978).
14. H. Shur and U. Schucker, *Synthesis*, 431 (1970).
15. L. L. Miller and A. Szabo, *J. Org. Chem.*, **44**, 1670 (1979).
16. N. B. H. Henis, Y. H. So, and L. L. Miller, *J. Am. Chem. Soc.*, **103**,

- 4632 (1981).
17. N. B. H. Henis and L. L. Miller, *J. Am. Chem. Soc.*, **104**, 2526 (1982).
  18. N. B. H. Henis and L. L. Miller, *J. Am. Chem. Soc.*, **105**, 2820 (1983).
  19. M. Tezuka and L. L. Miller, *J. Am. Chem. Soc.*, **78**, 4201 (1978).
  20. H. Kobayashi, M. Shen, and A. T. Bell, *J. Macromol. Sci. Chem.*, **8**, 373 (1974).
  21. L. C. Brown and A. T. Bell, *Ind. Eng. Fund.*, **13**, 203 (1979).
  22. J. F. Garvey, Ph.D thesis, California Institute of Technology (1985).
  23. R. W. Bickes, Jr. K. R. Newton, J. M. Herrmann, and R. B. Bernstein, *J. Chem. Phys.*, **64**, 3648 (1976).
  24. K. W. Ford, *Classical and Modern Physics, Vol. 2*, Xerox College Publishing, Lexington, Mass. (1973).
  25. J. G. Huntington and L. L. Miller, *J. Am. Chem. Soc.*, **98**, 8101 (1976).
  26. H. Suhr and U. Schucker, *Synthesis*, 431 (1972).
  27. L. L. Miller and J. G. Huntington, *Tetrahedron Lett.*, 1181 (1975).

**Figure Captions**

Figure 1. Plot of a current-voltage curve in a vessel 50 cm long filled with neon at 1 torr. The various types of discharge appear at various resistance values.

Figure 2. Simple forms of apparatus for reactions in glow discharges.

Figure 3. Magnet design currently used in hydrogen plasma described in thesis.

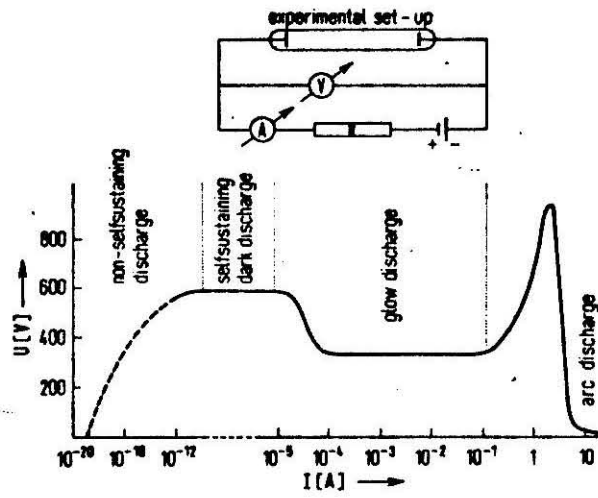
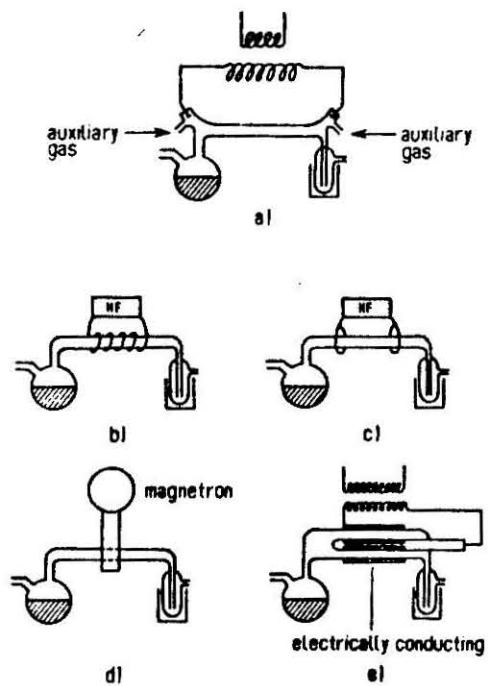


Figure 1

**Figure 2**

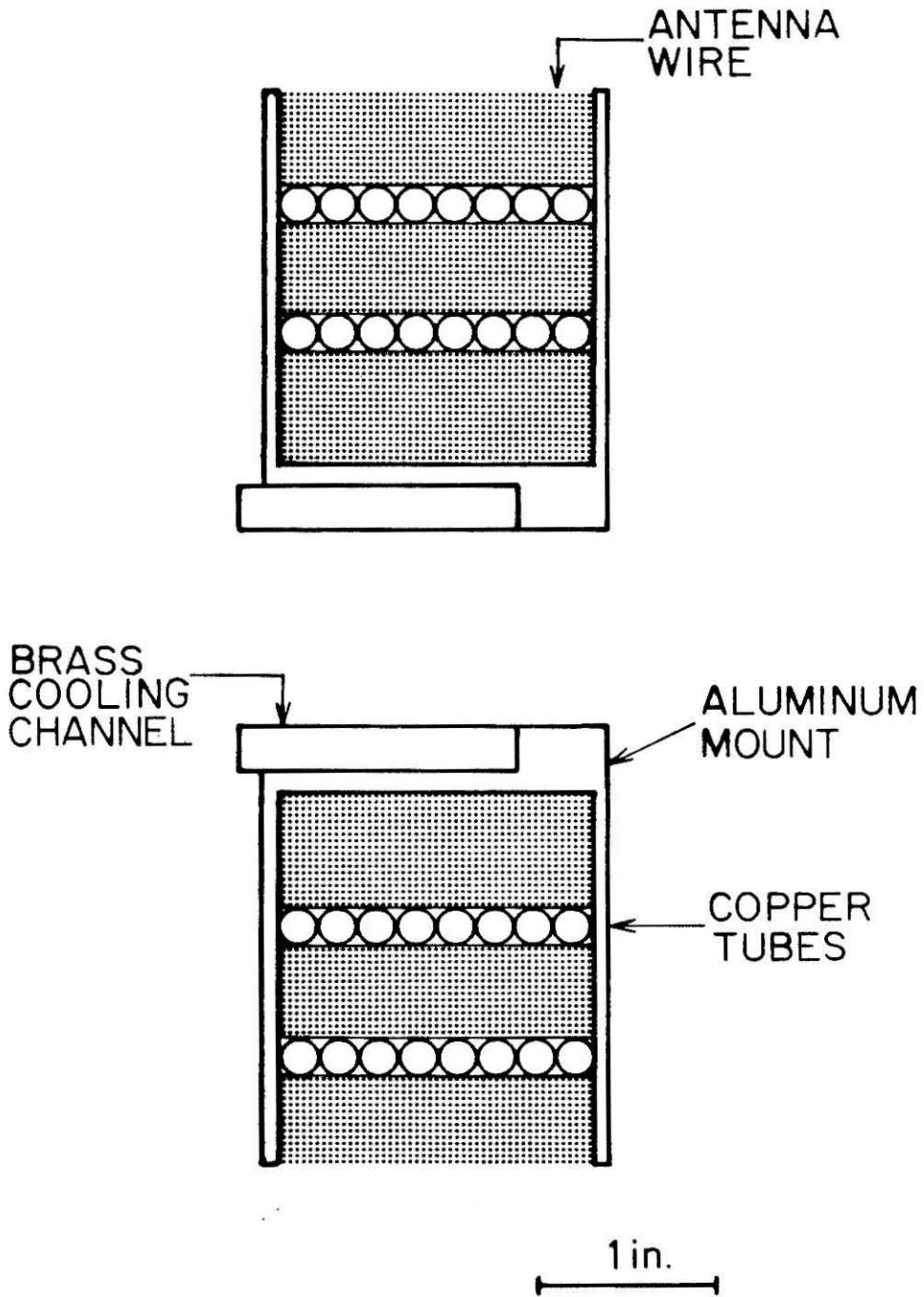


Figure 3

**PROPOSITION V: A Classical Determination of Vibrationally Adiabatic Barriers for the  $H + H_2$  as a Function of Delves' Angle**

It has recently been observed that the evaluation of periodic orbits for a classical collinear surface play a important role in resonance phenomena. It has been suggested that quantum resonances can be predicted via the location of these periodic orbits. It is proposed to utilize this technique as a systemmatic probe of the Porter-Karplus  $H + H_2$  potential. By observing how these orbits change as a function of Delves' angle, one will be able to see how the resonance structure changes as one goes from a light-light-light system to a heavy-light-heavy sytem. By understanding this effect it will lead to a more generalized understanding of the dynamics of the family of symmetric exchange reaction.

One of the most interesting developments of reactive dynamics has been the investigation of quantum resonances. These have been observed theoretically in exact quantum calculations for a variety of systems<sup>1-7</sup> which appear as sharp spikes in the reaction probability as a function of energy. These resonances represent quantum mechanical interference between direct reaction and dynamic resonance mechanisms in which the energy is trapped in internal degrees of freedom which creates an intermediate with a lifetime of the order of a few molecular vibrations. The mechanism of this trapping is of a dynamic nature involving a Feshbach process<sup>8,9</sup>. This process occurs if the system has more than one degree of freedom, such that the energy can be trapped in the internal coordinates. The system can separate only when the energy flows back into a translational degree of freedom. This suggests that resonances may correspond to the virtual state vibrational spectroscopy of the saddle-point region. As a result, understanding the positions of these resonances will lead to a detailed understanding of the saddle point regions of these potentials. However, the exact quantum calculation of these systems tend to be expensive especially for heavy-light-heavy systems. This is related to the very sharp and rapidly changing curvature of the minimum energy path of these systems in the strong interaction region of configuration space<sup>10-12</sup>.

One might expect that resonances may have a classical analog<sup>13</sup> but for systems like  $\text{H} + \text{H}_2$  the classical motion at the saddle point is unstable at all energies<sup>14</sup>. It has been observed recently for a classical collinear system that there can exist a periodic orbit dividing surface (PODS)<sup>15-17</sup>. These periodic orbits are defined as follows; for a coordinate system  $(u, v)$  the translation motion  $u$  is separable from the vibrational motion. These pods give rise to a adiabatic potential surface  $E_n(u)$  where  $n$  is a vibrational action which is strictly adiabatic. Suppose that  $E_n(u)$  goes through a maximum at  $u^*$ ,

$u^*$  corresponds to a barrier in the adiabatic surface such that a classical trajectory initiated at  $u^*$  with no momentum in the  $u$  direction and of energy  $E_n(u)$  will vibrate in the  $v$  direction indefinitely. If  $u^*$  is a minimum this will also correspond to a pods.

Schematically one can imagine the calculation of these pods in the following manner. One picks an energy and then moving along the equipotential corresponding to that contour release an appropriate reduced mass. For some of these points the motion will be classically periodic. For these periodic orbits one then find the associated action. This is then repeated for all other energies.

Pechukas was the first to recognise that these periodic orbits play a fundamental role in classical scattering phenomena<sup>18</sup>. As has since been shown in several papers<sup>19-23</sup> classical trajectories tend to be 'repulsive' or 'attractive' in the vicinity of the pods. This means that the pods define vibrationally adiabatic barriers and wells of a reacting system. These adiabatic barriers exist as an outcome of competition between the increase of potential energy and decrease of vibrational force constant along the reaction coordinate.

It was shown by Latham and co-workers that there is connection between the existence of wells in the adiabatic channel potentials and resonances<sup>24</sup>. They showed that surfaces which had no wells in the adiabatic channel potential did not exhibit resonance properties. Pollak and Child<sup>20</sup> have suggested that the quantum resonances can be explained in terms of energy transfer between adiabatic reactant and product channels. The classical condition for a resonance then appears to be that the action of the orbit over one period be an interger and that the energy at which this occurs be lower than the adiabatic barrier. These orbits are easy to find and are uniquely determined by the masses and the potential surface. Another way of looking at these orbits

is if one imagines the vibration of the reactant or product diatom as a local mode, when there is a matching of these frequencies a resonance will occur. This is numerically observed via a periodic orbit showing resonative energy transfer between the two modes. For the cases of  $\text{H} + \text{H}_2$  and its isotopic analogues as well as  $\text{F} + \text{H}_2$ , the above condition suffice for a prediction of the location of the quantal resonances within a 1 % accuracy.

It is proposed to use this technique to probe systematically the resonance structure via these classical calculations. The calculation will consist of taking the Porter-Karplus  $\text{H} + \text{H}_2$  surface<sup>25</sup> and calculating the pods while changing the skew angle and keeping the potential energy surface constant. As PODS are easy to find numerically<sup>26</sup>, the computational effort will be much less than the exact quantum treatment of such a system. As a result we will have the location of these pods for a variety of Delves angles for the Porter-Karplus  $\text{H} + \text{H}_2$  surface.

In the scaling transformation of Delves<sup>27,28</sup>, the collinear motion of a  $\text{A} + \text{BC}$  system is transformed to that of a single particle moving in two dimensions in a potential energy field. The skew angle is defined as

$$\theta = \tan^{-1} \left[ \frac{(m_B M)}{(m_A m_C)} \right]^{\frac{1}{2}}$$

where  $m_A$ ,  $m_B$ , and  $m_C$  are the masses of the three atoms and  $M$  the total mass. We see then by reducing the angle we are effectively moving from the regime of a light-light-light system to a heavy-light-heavy system.

In performing this calculation we will in effect be answering two questions. The first question is do the pods change in a predictable way as the surface is changed in a regular manner. One would expect this but it may be that they might exhibit some unusual behavior. The more important question which will be answered is how does the quantum resonance structure change

as one goes from a light-light-light system to a heavy-light-heavy system. By calculating where these periodic orbits are as a function of Delves' angle we will see what effect changing the mass of the particle has on the resonance structure. From this systematic approach one will be able to predict the resonance structure of any symmetric reactive system without having to perform the detailed quantum calculation. As mentioned earlier, systems with a light middle atom, such as  $I + HI$ , present grave difficulties in calculation due to the rapidly changing curvature of the minimum energy path.

This calculation will hopefully show how the resonance structure changes as a function of Delves' angle, giving detailed information on how the saddle point region of the surface is influenced by this parameter. By understanding this effect it may lead to a more generalized understanding of the dynamics of this family of symmetric exchange reactions

**References**

1. S. F. Wu, B. R. Johnson, and R. D. Levine, *Mol. Phys.*, **25**, 839 (1973).
2. G. C. Schatz, J. M. Bowman, and A. Kuppermann, *J. Chem. Phys.*, **58**, 4023 (1973).
3. J. N. L. Connor, W. Jakubetz, and J. Manz, *Mol. Phys.*, **29**, 347 (1975).
4. A. Kuppermann, *Potential Energy Surfaces and Dynamics Calculations*, ed. D. G. Truhlar, Plenum Publishing Co., p. 375 (1981).
5. A. Kuppermann, *Theoretical Chemistry: Advances and Perspectives*, **4A**, 79 (1981).
6. G. C. Schatz and A. Kuppermann, *Phys. Rev. Lett.*, **35**, 1266 (1975).
7. G. C. Schatz and A. Kupprmann, *J. Chem. Phys.*, **65**, 4624, 4642, 4668 (1976).
8. H. Feshbach, *Ann. Phys.*, **5**, 357 (1958).
9. H. Feshbach, *Ann. Phys.*, **19**, 287 (1962).
10. A. Kuppermann, *Proceedings of the Summer School on Chemical Photo-physics, Les Houches, France*, eds. J. S. Risley and R. Geballe, University of Washington Press, Seattle, p. 259 (1976).
11. C. C. Rankin and J. C. Light, *J. Chem Phys*, **51**, 1701 (1969).
12. G. Miller and J. C. Light, *J. Chen. Phys.*, **54**, 1635, 1643 (1971).
13. F. M. Chapman and E. F. Hayes, *J. Chem. Phys.*, **62**, 4400 (1975).
14. E. Pollak and M. S. Child, *J. Chem. Phys.*, **73**, 4373 (1980).

15. E. Pollak and P. Pechukas, *J. Chem. Phys.*, **69**, 1218 (1978).
16. P. Pechukas and E. Pollak, *J. Chem. Phys.*, **71**, 2062 (1979).
17. E. Pollak, M. S. Child and P. Pechukas, *J. Chem. Phys.*, **72**, 1669 (1980).
18. P. Pechukas, *Modern Theoretical Chemistry, Vol. 2, Dynamics of Molecular Collisions, Part B*, ed. W. H. Miller, Plenum, NY, Ch. 6 (1976).
19. M. S. Child and E. Pollak, *J. Chem. Phys.*, **73**, 4365 (1980).
20. E. Pollak and M. S. Child, *Chem. Phys.*, **60**, 23 (1981).
21. E. Pollak, *Chem. Phys.*, **61**, 305 (1981).
22. E. Pollak, *J. Chem. Phys.*, **74**, 5586 (1981).
23. E. Pollak, *J. Chem. Phys.*, **76**, 5843 (1982).
24. S. L. Latham, J. F. McNutt, R. E. Wyatt and M. J. Redmon, *J. Chem. Phys.*, **63**, 674 (1975).
25. R. N. Porter and M. Karplus, *J. Chem. Phys.*, **40**, 1105 (1964).
26. S. F. Wu and R. D. Levine, *Mol. Phys.*, **22**, 881 (1971).
27. L. M. Delves, *Nucl. Phys.*, **9**, 391 (1959).
28. L. M. Delves, *Nucl. Phys.*, **20**, 275 (1960).